Advances in Materials Science and Engineering

Natural Fiber Reinforced Polymer Matrix Composites

Lead Guest Editor: Ravichandran M
Guest Editors: Vinayagam Mohanavel, V Anandakrishnan, and Alokesh Pramanik

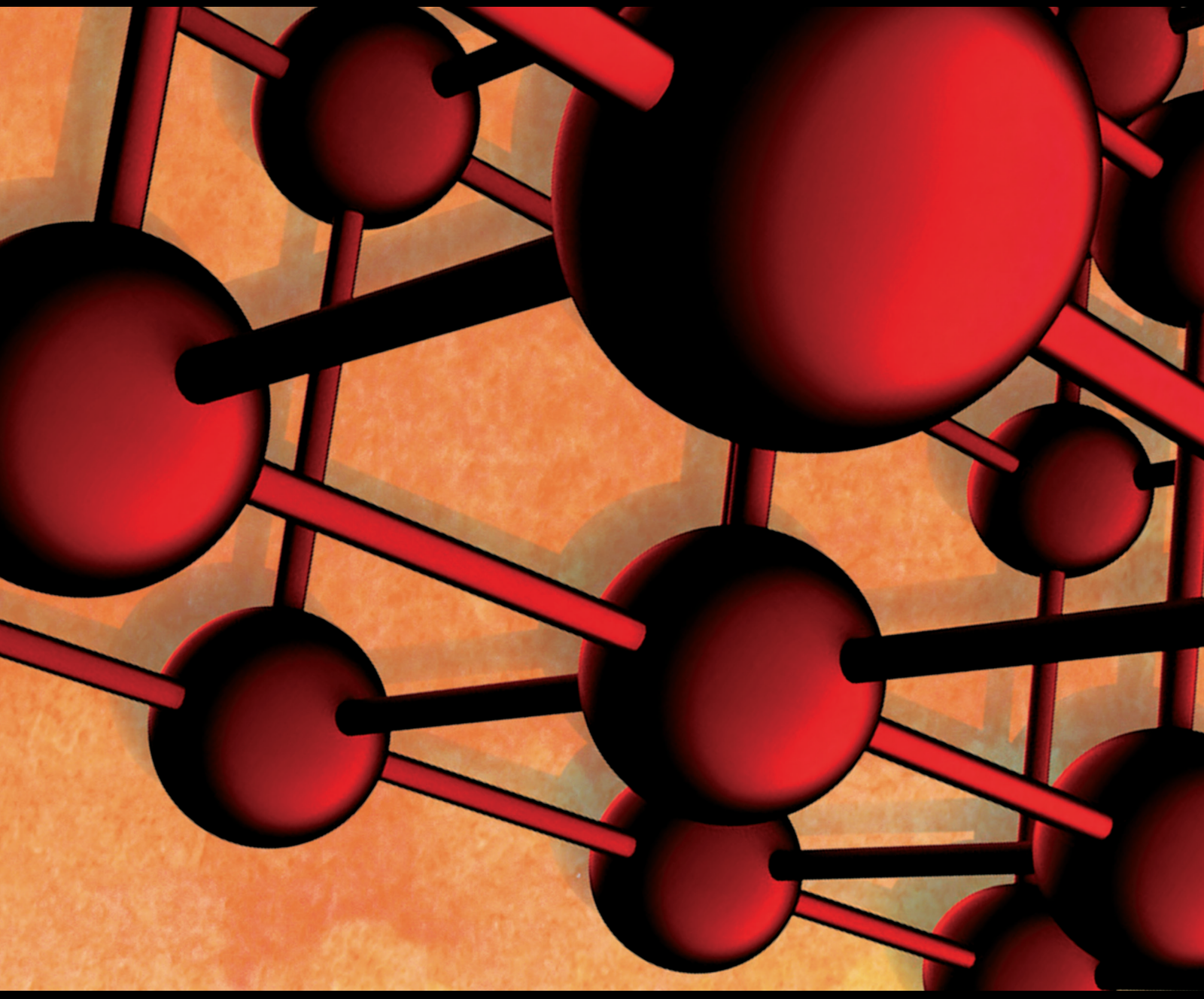

Natural Fiber Reinforced Polymer Matrix Composites

Advances in Materials Science and Engineering

Natural Fiber Reinforced Polymer Matrix Composites

Lead Guest Editor: Ravichandran M
Guest Editors: Vinayagam Mohanavel, V Anandakrishnan, and Alokesh Pramanik

Contents

Hindawi
Advances in Materials Science and Engineering
Volume 2022, Article ID 2158210, 8 pages
https://doi.org/10.1155/2022/2158210

Research Article

Artificial Neural Network Modeling of Abrasion Loss and Surface Roughness of Crab Carapace Impregnated Coir Vinyl Ester Composites

S. Rajamuneeswaran,[1] S. Jayabal,[2] N. Nagaprasad,[3] G. Veerappan,[4] Leta Tesfaye Jule,[5,6] and Ramaswamy Krishnaraj[6,7]

[1]*Department of Mechanical Engineering, Pandian Saraswathi Yadav Engineering College, Sivagangai 630 561, Tamil Nadu, India*
[2]*Department of Mechanical Engineering, Government College of Engineering, Sengipatti 613 402, Tamil Nadu, India*
[3]*Department of Mechanical Engineering, ULTRA College of Engineering and Technology, Madurai 625 104, Tamil Nadu, India*
[4]*Department of Mechatronics, Sri Krishna College of Engineering and Technology, Kuniyamuthur, Coimbatore 641008, Tamilnadu, India*
[5]*Department of Physics, College of Natural and Computational Science, Dambi Dollo University, Dambi Dollo, Ethiopia*
[6]*Centre for Excellence-Indigenous Knowledge, Innovative Technology Transfer and Entrepreneurship, Dambi Dollo University, Dambi Dollo, Ethiopia*
[7]*Department of Mechanical Engineering, Dambi Dollo University, Dambi Dollo, Ethiopia*

Correspondence should be addressed to Ramaswamy Krishnaraj; prof.dr.krishnaraj@dadu.edu.et

Received 31 August 2021; Accepted 29 March 2022; Published 13 April 2022

Academic Editor: Akbar Heidarzadeh

Roughness plays an important role in determining how an object would be related with its environment. In tribology, rough surfaces easily obtain wear more quickly and have higher friction coefficients than smooth surfaces. Roughness is often a good analyzer of the performance of a mechanical component. This investigation is aimed to study the abrasion loss and surface roughness behaviors in crab carapace-filled coir fiber reinforced vinyl ester composites. The development of filler-impregnated fiber-polymer composites in recent years necessitated the evaluation and prediction of tribological behaviors in fiber reinforced composites. The composite fabrication was planned by varying the three fabrication parameters with three levels such as fiber length (10 mm, 30 mm, and 50 mm), fiber diameter (0.1 mm, 0.18 mm, and 0.25 mm), and content of crab carapace fillers (0%, 2%, and 4%) as per Design of Experiments (DOEs) in this current investigation. Low velocity integrated wear loss tests on composite samples were carried out, and also the average surface roughness is measured in the fabricated composites. Nonlinear regression equations were developed to study the correlation between tribological behaviors and fabrication parameters. The interaction effect of fabrication parameters was studied using ANOVA two-tail test and validated using response surface plots. In order to forecast abrasion loss and surface roughness behaviors, artificial neural network (ANN) models were constructed, and it was discovered that the produced ANN models effectively predicted the abrasion loss as well as surface roughness behavior within the given ranges.

1. Introduction

Composites are materials that are made up of a strong load-bearing element (known as reinforcement) contained in a weaker substance (known as matrix material). Reinforcement contributes to the strength and rigidity of a structure, allowing it to withstand structural loads. The matrix or binder (organic or inorganic) is responsible for keeping the reinforcement in its proper location and orientation. Despite the fact that the constituents of the composites maintain their separate characteristics, such as physical as well as chemical properties, they work together to produce a mix of

traits that would be impossible for any one of the constituents to produce alone. Fiber-reinforced composites (FRCs) are created by mixing fibers and polymer resin, and they are also known as fiber composites (FRCs). Fiber reinforced composites are made up of fibers that are excellent in strength, lightweight, and toughness, and they are placed in a matrix that has unique interfaces between the fibers. Traditional materials such as steel and aluminum are isotropic in nature, whereas fiber reinforced composites exhibit anisotropic behavior. The majority of composites currently in use in the industry are composed of polymer matrices. The term "polymer" refers to a long-chain molecule that is composed of a huge number of repeating units with the same structural characteristics as one another [1]. The role of the matrix is to distribute the load to the fibers and also give a barrier towards an adverse environment as well as to protect the surface of the fibers against mechanical wear. Fillers are used in natural fiber reinforced composites to generate the required mould shape in sheet mould compounds (SMCs) and also to decrease the manufacturing costs of the composites. Fillers are used in natural fiber reinforced composites to produce significant mould shapes in sheet mould compounds (SMCs) and to decrease the manufacturing costs of the composites [2]. Despite the presence of filler, the mechanical characteristics of the coir/epoxy micro-composites are not significantly altered after their formation. When compared with NEU and NE, the NET exhibits a significant increase in flexural strength and flexural modulus. Despite the presence of filler, the mechanical characteristics of such coir/epoxy micro-composites are really not significantly altered after their formation. Tensile and fatigue tests were used to examine the material [3]. The surfaces of the fractured samples were investigated in order to evaluate the fracture mechanisms. Results reported a reduction in fatigue life of composites when imposed larger stress because of bonding interfacial, which was not acceptable. Most of the works in natural fiber reinforced polymer composites were concentrated on the characterization of composites, and the predictive modeling of behaviors was limited in literature [4]. In several of the production experiments on glass fiber reinforced composites, response surface methodology and neural network technologies were utilized in conjunction with each other [5]. Shukla and Tambe evaluated the surface roughness and kerf widths in abrasive water jet cutting of Kevlar composites utilizing the neural network. The result reveals that the that NN model was able to effectively forecast the two kerf widths as well as the surface roughness, with the predicted values closely matching the observed values in the experimental data [6]. Antil et al. demonstrated that the *S* form woven glass fibers reinforced polymer matrix composites (PMCs) can be used to investigate bonding behavior between reinforcement and matrix when subjected to the natural abrasive slurry. For the purpose of determining the effect of different erosion variables on erosion resistance, the response surface methodology is used. Compared with other techniques, response surface methodology (RSM), as well as artificial neural network (ANN) simulations, demonstrates good conformity with the erosion behavior of polymer matrix composites strengthened with glass fiber [7]. Subhrajit et al. analyzed the erosion performance of glass-epoxy composites loaded with marble waste with the help of an artificial neural network. The rate of erosion wear in composites lowers as the amount of filler in the composites increases. It was found that the results of the predictive model, which is based on artificial neural networks, are in good agreement with the values of the practical model [8]. In another prevailing study, Zain et al. used artificial neural network to predict surface roughness by end milling machining operations. They concluded that by varying the amount of layers as well as nodes in the hidden layers of the ANN network structure, the framework for surface roughness in the milling process could be enhanced, especially for estimating the value of the surface roughness efficiency measure, which is important in the manufacturing process [9].

Shaikh et al. investigated the manufacturing, characterization, statistical analysis, and application of rice husk ash strengthened aluminium matrix composites. Based on the comparison of experimental and anticipated outcomes, it can be concluded that a properly trained ANN model is an effective tool for forecasting tribological behavior [10]. Recently, artificial intelligence-based models have emerged as the favored trend, and most academics are utilizing these models to construct a model for near-optimal machining settings [11–15]. Vinod et al. studied thermo-mechanical characterization of *Calotropis gigantea* added in jute fiber reinforced epoxy composites. It was shown that 10 weight percentages of filler improved the mechanical properties such as ultimate tensile, ultimate flexural, and ultimate compressive strengths compared with unfilled ones [16]. Vijay et al. evaluated spent *Camellia sinensis* seed and *Azadirachta indica* seed powders as bio-fillers in the jute epoxy composites. The results showed that the morphological and physical properties of the fillers play a major role in improving the thermal and mechanical properties of the composites [17]. Dinesh et al. found that Rosewood dust and Padauk wood dust were used as fillers in the jute fiber epoxy composites. They have analyzed for mechanical, thermal, water absorption, and biodegradation characteristics. It was found that Padauk wood dust filler had improved the ultimate tensile strength, ultimate flexural strength, ultimate compressive strength, impact strength, and hardness properties to compare Rosewood dust filler composites [18]. Hayajneh et al. investigated thermo-mechanical characteristics of treated and untreated *Portunus sanguinolentus* shell filler used in jute fiber reinforced epoxy composites. The result showed that 10 wt% treated filler powder improved tensile, flexural, compressive, shear, impact, and hardness properties. Through the establishment of an expert system, it is also considered to be an effective strategy for modeling the machining process in order to anticipate performance measurements in the manufacturing process [19]. It is an expert system when a computer program performs expert-like functions in the context of solving some certain type of problem employing a knowledge base, inference engine, and user interface. A model based on artificial neural networks

(ANNs) is capable of learning, adapting to changes, and mimicking the human thought process with minimal human input [16–20]. The FL model operates on linguistic variables instead of on discrete values, as opposed to the conventional approach [10, 21, 22]. In this study, the abrasion loss and surface roughness in crab carapace-coir vinyl ester composites and predicting model create using the regression model and artificial neural network.

2. Materials and Methods

2.1. Materials. Crab carapace has been selected as filler material because it is abundantly available and being wasted as sea dumps. After removing their flesh, the obtained crab shells were washed with sodium hydroxide solution for numerous times to remove impurities, protein residues, and so on. The pigment constituents were removed by quenching the crude shells in the pure ethanol for 6 h at room temperature, followed by filtration and washing. The obtained crab shells were then dried at 100°C to remove the external water and then grinded via a ball-milled using a ball grinding mill. The grounded particles were used as filler for coir vinyl ester composites. The major compositions of crab carapace were carbon 37.77%, oxygen 29.86%, and calcium 32.37% [23].

2.2. Design of Experiments. A factorial design may also be called a fully crossed design. Such an experiment allows studying the effect of each factor on the response variable, as well as the effects of interactions between factors on the response variable. A 3^3 full factorial design with a total of 27 experimental was carried out. Composites of filler-impregnated coir and vinyl ester were constructed using three-level full factorial designs of fiber characteristics, including fiber length, diameter, and filler loading. The composites were prepared for a maximum thickness of three millimeters (mm). Table 1 lists the fiber properties as well as the levels that were chosen for them.

2.3. Experimental Procedure. It was determined that natural coir fiber would be the most effective reinforcement material in this experiment. The matrix substance was untreated vinyl ester resin, and the filler material was crab carapace, and they were both employed in the construction. The hand lay-up technique was employed to fabricate the filler-impregnated coir vinyl ester composites used in this study. Before the fabrication process began, a releasing agent made of poly vinyl acetate (PVA) was added to the surface. Previously, the coir fibers were pre-impregnated with a matrix composition comprising of unsaturated vinyl ester resin-crab carapace filler, N-dimethylaniline accelerator, methyl ethyl ketone peroxide catalyst, and cobalt naphthenate promoter in a proper ratio. A resin matrix (360 mm × 360 mm) was used to hold the impregnated layers in place before they were removed by applying a lot of pressure (1000 N). After 1 hour, the fabricated composites were removed from the mould and allowed to cure at room temperature (28 degrees Fahrenheit) for 24 hours. Figure 1 depicts a photographic view of produced carapace filler-filled coir fiber reinforced composites sheets with a coir fiber reinforcement structure [24].

Table 1: Parameters and their levels.

Parameter	Low	Medium	High
Fiber length (mm)	10	30	50
Fiber diameter (mm)	0.1	0.18	0.2
Filler content (%)	0	2	4

2.4. Abrasion Loss Testing. Experiments on abrasion loss as well as surface roughness were carried out on specimens that were cut from the produced composite and completed to the standard size with a compact handsaw machine and emery paper. The abrasion loss test was carried out in accordance with ASTM D5963-04 (2019). The test was carried out with the help of an Abrasion Resistance Tester. Figure 2 depicts a photographic view of an abrasion test specimen under examination.

2.5. Surface Roughness Testing. Surface roughness is essential in various fields and also has significant significance in the study of surface accuracy as well as the formulation of the ISO 1997 norm for surface roughness. In accordance with the workpiece random orientation of fiber and percentage of filler material, the variation of surface roughness showed that the surface roughness fluctuated among different fiber orientations. Figure 3 shows a photograph of a surface roughness analyzer (Mitutoyo SJ-310) taken using a digital camera.

3. Results and Discussion

3.1. Impact of Fiber Parameters on Abrasion Loss of Carapace Filler-Filled Coir Vinyl Ester Composites. The relationship between fiber parameters (length, diameter, and filler content) and abrasion loss is illustrated in Figure 4 (mm^3). It was possible to get very low abrasion loss using a 50-mm fiber length, 0.18-mm fiber diameter, and a 0 percent carapace filler content, whereas the greatest abrasion loss was achieved using a 30-millimeter fiber length, 0.25-mm fiber diameter, and a 0 percent carapace filler content. The SEM images of carapace filler-filled coir vinyl ester composites after abrasion test are illustrated in Figure 5. The filler reinforced composite is characterized as being composed of fillers suspended in a matrix; it can have virtually any shape, size, or configuration. Filler is used in fiber reinforced composites to enhance the properties [25, 26].

3.2. Effect of Fiber Parameters on Surface Roughness of Carapace Filler-Filled Coir Vinyl Ester Composites. The association between fiber parameters (length, diameter, and filler content) and surface roughness (microns) is depicted in Figure 6. In 50 mm fiber length, 0.18 mm fiber diameter, 2 percent carapace filler percentage, and maximum surface roughness, the extremely low surface roughness was achieved. The fibers had a length of 30 mm, a diameter of 0.18 mm, and a filler concentration of 4% carapace filler. The

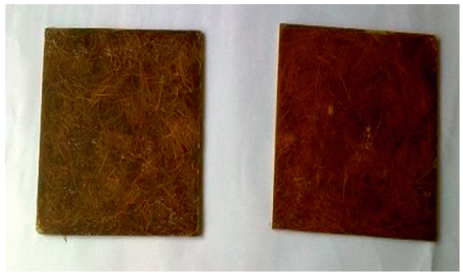

Figure 1: Photographic image of fiber reinforced sheet.

Figure 2: Photographic image of abrasion test specimen.

Figure 3: Surface roughness tester photographic picture (Mitutoyo SJ-310).

SEM images of carapace filler-filled coir vinyl ester composites after roughness test are shown in Figure 7.

Experimental results (abrasion and surface roughness) for carapace filler-filled coir vinyl ester composites are shown in Table 2.

3.3. Regression Models. Design Expert 8.0.4 statistical software was used to model the tribological phenomena, including surface roughness and abrasion loss. The letters f_1 and f_2 refer to fiber length and diameter, respectively, whereas the term f_3 refers to the amount of filler present. These are the mathematical models of surface roughness (SR) and abrasion loss (A_1), which have been created, and are shown in equations (1) and (2).

$$\begin{aligned} \mathrm{SR} = {} & 0.34606 + 0.016024 f_1 + 5.69038 f_2 + 0.026597 f_3 - 0.013760 f_1 f_2 + 1.2437510^{-3} f_2 f_3 \\ & - 0.037771 f_1 f_3 - 1.9583310^{-4} f_1^2 - 13.80688 f_2^2 + 9.0833310^{-3} f_3^2, \end{aligned} \tag{1}$$

$$\begin{aligned} A_1 = {} & 687 + 5.18 f_1 - 745 f_2 - 22.9 f_3 - 0.122 f_1^2 + 2492 f_2^2 + 1.59 f_3^2 - 3.28 f_1 f_2 \\ & + 24.4 f_2 f_3 + 0.294 f_1 f_3. \end{aligned} \tag{2}$$

3.4. Artificial Neural Network (ANN). A neural network is composed of a number of artificial neurons that are connected to one another and that process data using a connectionist technique to computation. Because the capabilities of a single neuron are restricted, complicated functions can be achieved by linking a large number of

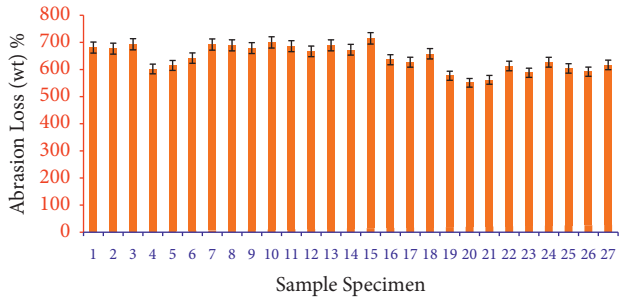

Figure 4: Impact of fiber parameters on abrasion loss.

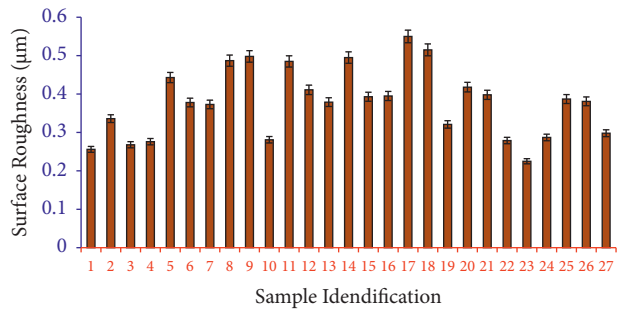

Figure 5: SEM images after the abrasion test.

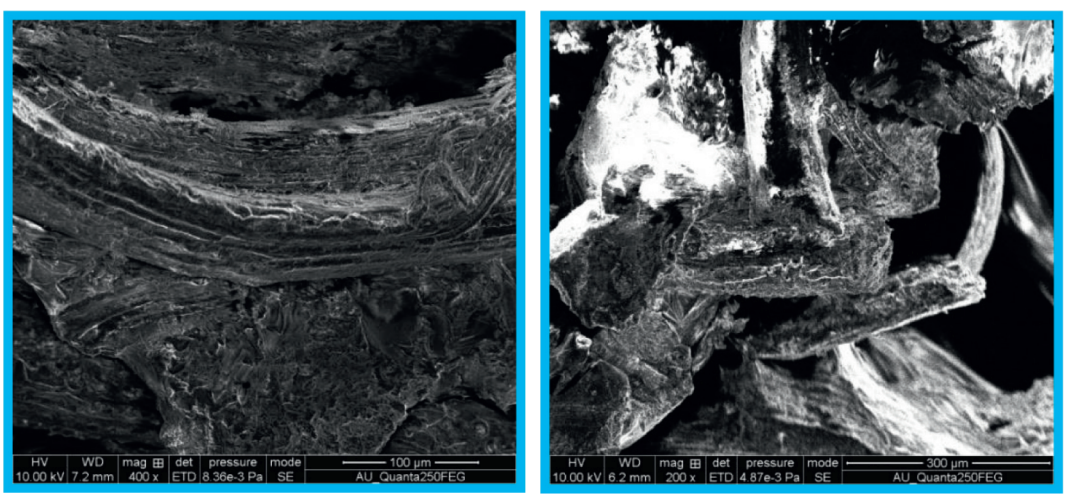

Figure 6: Effect of fiber parameters on the surface roughness test.

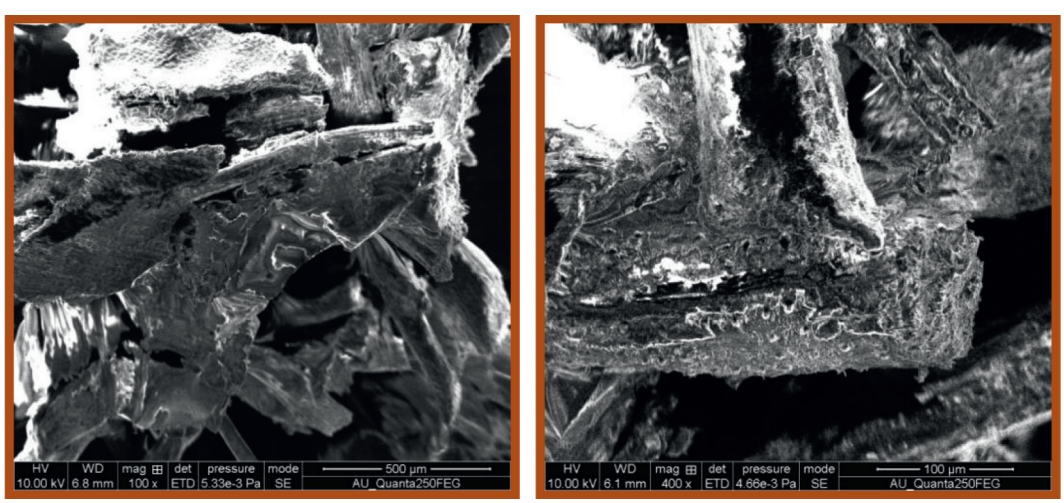

Figure 7: SEM images after the surface roughness test.

Table 2: Experimental results for carapace filler-filled coir vinyl ester composites.

Sample specimen	Fiber length (mm)	Fiber diameter (mm)	Filler content (%)	Abrasion loss	Surface roughness
1	10	0.1	0	680	0.256
2	10	0.18	0	675	0.336
3	10	0.2	0	690	0.268
4	10	0.1	2	598	0.276
5	10	0.18	2	610	0.443
6	10	0.2	2	636	0.378
7	10	0.1	4	685	0.373
8	10	0.18	4	681	0.487
9	10	0.2	4	670	0.498
10	30	0.1	0	690	0.281
11	30	0.18	0	675	0.485
12	30	0.2	0	655	0.411
13	30	0.1	2	676	0.379
14	30	0.18	2	659	0.495
15	30	0.2	2	700	0.393
16	30	0.1	4	620	0.395
17	30	0.18	4	610	0.55
18	30	0.2	4	640	0.515
19	50	0.1	0	558	0.321
20	50	0.18	0	531	0.418
21	50	0.2	0	541	0.398
22	50	0.1	2	591	0.279
23	50	0.18	2	565	0.225
24	50	0.2	2	603	0.287
25	50	0.1	4	579	0.387
26	50	0.18	4	566	0.381
27	50	0.2	4	590	0.298

neurons together in series. According to a large body of evidence, the topography of a neural network, the demonstration of data, the simplification of inputs and outputs, and the appropriate choice of activation functions all seem to have a considerable impact on the effectiveness and performance of a trained neural network.

3.5. Training the Artificial Neural Network. The training was carried out using the MATLAB software package. It is demonstrated in this paper that the ANN module can be used to estimate the abrasion loss as well as the surface roughness of carapace filler-impregnated coir vinyl ester composites. The features fiber length, fiber diameter as well as filler content are used as inputs, while the outputs are abrasion loss and surface roughness, which are used in the training of neural networks to determine the effectiveness of the network. Randomly generated weights among the input layer and the hidden layer and weights between both the hidden layers with the output layer are generated for the network topology that has been specified. An artificial neural network was trained using the feed forward back propagation technique, with a total of 27 patterns being employed in the training process. All of the ANN's training were accomplished without the introduction of almost any permissible error. The patterns that will be used for testing and training the ANN are chosen. These carefully chosen designs were normalized such that they fall between 0 and 1 on the scale. Performance curve for abrasion loss values and roughness values is depicted in Figures 8 and 9.

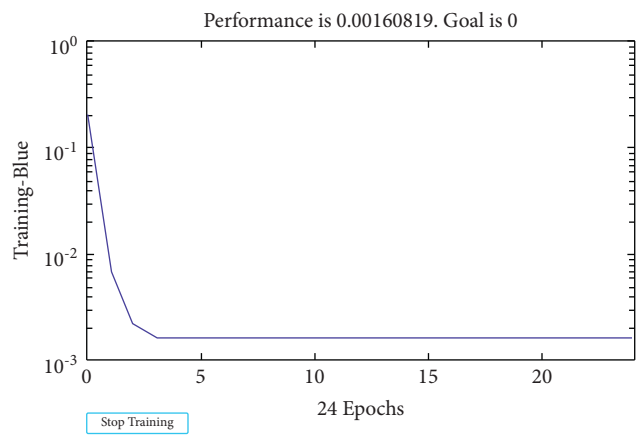

Figure 8: Performance curve for abrasion loss values.

The normalization of the inputs and outputs is performed by

$$X_i = \frac{X_i}{X_{\max}}. \quad (3)$$

The difference between the value of a characteristic and its maximum value is denoted by X_i and $X_{\max}$.

3.6. Validation of Abrasion Loss Test Result. Experiments were carried out to confirm the optimal conditions for eight different sets of variables. The differences between the

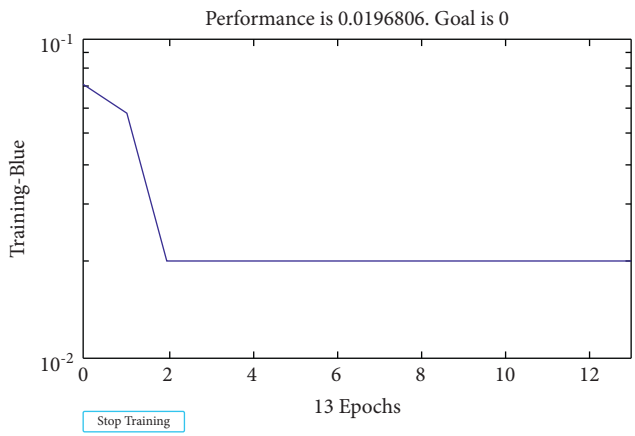

Figure 9: Performance curve for surface roughness values.

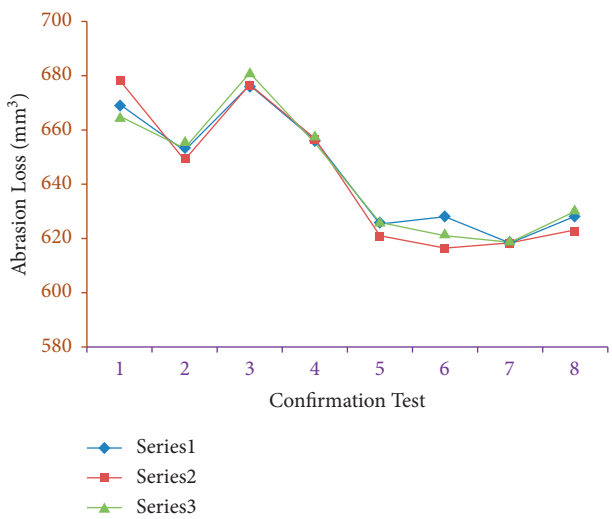

Figure 10: Comparison of predicted and experimental abrasion loss values.

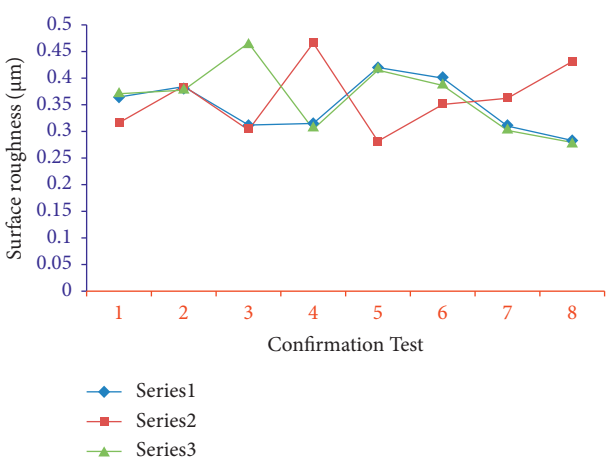

Figure 11: Comparison of predicted and experimental surface roughness values.

experimental and expected values are as shown in Figures 10 and 11; there is a comparison between anticipated and experimental abrasion loss as well as surface roughness values. Series 1 indicates the experimental value, Series 2 indicates the mathematical modeling value, and Series 3 indicates the predicted value.

4. Conclusion

In this experiment, the abrasion loss and surface hardness of carapace filler-filled coir vinyl ester composites were measured. Over a wide variety of situations, the regression and artificial neural network (ANN) models were constructed to forecast abrasion loss and surface roughness. Between the expected and experimental results, there was a high degree of agreement seen. The ANN-based models may be used to forecast the surface roughness as well as abrasion loss behaviors of carapace filler-coir vinyl ester composites, and they have proven to be useful. Surface roughness and abrasion loss were predicted by artificial neural network models with average absolute error percentages of 0.04 and 0.041, respectively, which are lower than the predictions made by regression models. The better abrasion loss was obtained for the fiber length of 30 mm, fiber diameter of 0.2 mm, and filler content of 2%, and high surface roughness was obtained for the fiber length of 30 mm, fiber diameter of 0.18 mm, and filler content of 4%. The result reveals that decrease in the fiber length and increase in filler content in the composites lead to reduction in the abrasion loss and surface roughness.

Data Availability

The data used to support the findings of this study are included within the article.

Disclosure

This study was performed as a part of the employment of the authors.

Conflicts of Interest

The authors declare that there are no conflicts of interest.

References

[1] P. K. Mallick, *Fiber-Reinforced Composites: Materials, Manufacturing, And Design*, CRC Press, Boca Raton, FL, USA, 2007.

[2] S. Harish, D. P. Michael, A. Bensely, D. M. Lal, and A. Rajadurai, "Mechanical property evaluation of natural fiber coir composite," *Materials Characterization*, vol. 60, no. 1, pp. 44–49, 2009.

[3] B. Latha and V. S. Senthilkumar, "Fuzzy rule based modeling of drilling parameters for delamination in drilling GFRP composites," *Journal of Reinforced Plastics and Composites*, vol. 28, no. 8, pp. 951–964, 2009.

[4] B. Latha and V. S. Senthilkumar, "Analysis of thrust force in drilling glass fiber-reinforced plastic composites using fuzzy logic," *Materials and Manufacturing Processes*, vol. 24, no. 4, pp. 509–516, 2009.

[5] S. Jayabal and U. Natarajan, "Regression & neuro fuzzy models for prediction of thrust force and torque in drilling of

glass fibre reinforced composites," *Journal of Scientific and Industrial Research*, vol. 69, pp. 741–745, 2010.

[6] M. Shukla and P. B. Tambe, "Predictive modelling of surface roughness and kerf widths in abrasive water jet cutting of Kevlar composites using neural network," *International Journal of Machining and Machinability of Materials*, vol. 8, no. 1-2, pp. 226–246, 2010.

[7] S. K. Antil, P. Antil, S. Singh, A. Kumar, and C. I. Pruncu, "Artificial neural network and response surface methodology based analysis on solid particle erosion behavior of polymer matrix composites," *Materials*, vol. 13, no. 6, p. 1381, 2020.

[8] R. A. Y. Subhrajit, A. K. Rout, and A. K. Sahoo, "A study on erosion performance analysis of glass-epoxy composites filled with marble waste using artificial neural network," *UPB Sci. Bull. Ser. B*, vol. 80, pp. 181–196, 2018.

[9] A. M. Zain, H. Haron, and S. Sharif, "Prediction of surface roughness in the end milling machining using artificial neural network," *Expert Systems with Applications*, vol. 37, no. 2, pp. 1755–1768, 2010.

[10] M. B. N. Shaikh, S. Raja, M. Ahmed, M. Zubair, A. Khan, and M. Ali, "Rice husk ash reinforced aluminium matrix composites: fabrication, characterization, statistical analysis and artificial neural network modelling," *Materials Research Express*, vol. 6, no. 5, Article ID 056518, 2019.

[11] M. R. H. Mohd Adnan, A. Mohd Zain, and H. Haron, "Prediction of surface roughness in the end milling machining using fuzzy rule-based," *Applied Mechanics and Materials*, vol. 421, pp. 244–249, 2013.

[12] J. Sheikh-Ahmad and J. Twomey, "ANN constitutive model for high strain-rate deformation of Al 7075-T6," *Journal of Materials Processing Technology*, vol. 186, no. 1-3, pp. 339–345, 2007.

[13] F. J. Pontes, A. P. d. Paiva, P. P. Balestrassi, J. R. Ferreira, and M. B. d. Silva, "Optimization of Radial Basis Function neural network employed for prediction of surface roughness in hard turning process using Taguchi's orthogonal arrays," *Expert Systems with Applications*, vol. 39, no. 9, pp. 7776–7787, 2012.

[14] K. Siva Prasad and G. Chaitanya, "Experimental study on surface roughness and dimensional accuracy of hole machining process on GFRP composites using abrasive water jet technique," *Materials Today Proceedings*, vol. 23, pp. 651–658, 2020.

[15] Y. Şahin and F. Şahin, "Effects of process factors on tribological behaviour of epoxy composites including $Al2O_3$ nano particles: a comparative study on multi-regression analysis and artificial neural network," *Advances in Materials and Processing Technologies*, pp. 1–15, 2021.

[16] A. Vinod, R. Vijay, and D. L. Singaravelu, "Thermo mechanical characterization of calotropis giganteastem powder-filled jute fiber-reinforced epoxy composites," *Journal of Natural Fibers*, vol. 15, no. 5, pp. 648–657, 2018.

[17] R. Vijay, A. Vinod, R. Kathiravan, S. Siengchin, and D. L. Singaravelu, "Evaluation of Azadirachta indica seed/spent Camellia sinensis bio-filler based jute fabrics-epoxy composites: experimental and numerical studies," *Journal of Industrial Textiles*, vol. 49, no. 9, pp. 1252–1277, 2020.

[18] S. Dinesh, P. Kumaran, S. Mohanamurugan et al., "Influence of wood dust fillers on the mechanical, thermal, water absorption and biodegradation characteristics of jute fiber epoxy composites," *Journal of Polymer Research*, vol. 27, no. 1, pp. 1–13, 2020.

[19] M. Hayajneh, A. M. Hassan, A. Alrashdan, and A. T. Mayyas, "Prediction of tribological behavior of aluminum–copper based composite using artificial neural network," *Journal of Alloys and Compounds*, vol. 470, no. 1-2, pp. 584–588, 2009.

[20] M. Younesi, M. E. Bahrololoom, and M. Ahmadzadeh, "Prediction of wear behaviors of nickel free stainless steel-hydroxyapatite bio-composites using artificial neural network," *Computational Materials Science*, vol. 47, no. 3, pp. 645–654, 2010.

[21] R. Ramprasath, S. Jayabal, and S. Sathiyamurthy, "Optimization of mechanical behaviors of red mud p coir-vinyl ester composites using intuitive analysis based on response surface methodology and simulated annealing," *Transactions of the Indian Institute of Metals*, vol. 67, no. 6, pp. 971–977, 2014.

[22] S. Sathiyamurthy, A. S. A. Thaheer, and S. Jayabal, "Mechanical behaviours of calcium carbonate-impregnated short coir fibre-reinforced polyester composites," *Proceedings of the Institution of Mechanical Engineers-Part L: Journal of Materials: Design and Applications*, vol. 226, no. 1, pp. 52–60, 2012.

[23] C. Velmurugan, R. Subramanian, S. Thirugnanam, and B. Anandavel, "Experimental study and prediction using ANN on mass loss of hybrid composites," *Industrial Lubrication & Tribology*, vol. 64, no. 3, pp. 138–146, 2012.

[24] T. U. Siddiqui, M. Shukla, and P. B. Tambe, "Optimisation of surface finish in abrasive water jet cutting of Kevlar composites using hybrid Taguchi and response surface method," *International Journal of Machining and Machinability of Materials*, vol. 3, no. 3-4, pp. 382–402, 2008.

[25] N. Ramdani, J. Wang, X.-y. He et al., "Effect of crab shell particles on the thermomechanical and thermal properties of polybenzoxazine matrix," *Materials & Design*, vol. 61, pp. 1–7, 2014.

[26] P. Kumaran, S. Mohanamurugan, S. Madhu et al., "Investigation on thermo-mechanical characteristics of treated/untreated Portunus sanguinolentus shell powder-based jute fabrics reinforced epoxy composites," *Journal of Industrial Textiles*, vol. 50, no. 4, pp. 427–459, 2020.

Hindawi
Advances in Materials Science and Engineering
Volume 2022, Article ID 6123160, 8 pages
https://doi.org/10.1155/2022/6123160

Research Article

Experimental study on removal of phenol formaldehyde resin coating from the abrasive disc and preparation of abrasive disc for polishing application

P. Sabarinathan,[1] V. E. Annamalai,[2] K. Vishal,[2] M.S. Nitin,[2] L. Natrayan,[3] Dhinakaran Veeeman,[1] and Wubishet Degife Mammo[4]

[1]*Centre for Additive Manufacturing, Chennai Institute of Technology, Chennai, Tamilnadu, India*
[2]*Department of Mechanical Engineering, Sri Sivasubramaniya Nadar College of Engineering, Chennai, Tamilnadu, India*
[3]*Department of Mechanical Engineering, Saveetha School of Engineering, Chennai, Tamil Nadu, 602105, India*
[4]*Mechanical Engineering Department, Wollo University, Kombolcha Institute of Technology, kombolcha, Amhara, Ethiopia*

Correspondence should be addressed to P. Sabarinathan; sabarinathanp@citchennai.net and L. Natrayan; natrayanphd@gmail.com

Received 28 August 2021; Accepted 8 January 2022; Published 23 February 2022

Academic Editor: Anandakrishnan V

In the automotive and aerospace industry, abrasive products lodge the major portion of the machining applications. Among that, the coated abrasive disc is used for a finishing application. Once the disc is fully consumed, the disc is unused and considered waste. The present work focuses on removing phenol-formaldehyde resin coating, and the fiber backing is reused for the same coated abrasive disc production application as flexible fiber backing. A sandblasting technique removes phenol-formaldehyde resin coating and embedded abrasive grains. During the fiber backing recovery process, the experimental parameters such as abrasive pressure, abrasive type, abrasive size, and orientation of the disc are varied to find out the optimal surface roughness value for reusing the produced coated abrasive discs. The results highlight that the recovered backing has an abrasive size of 120 mesh pressure of 0.20 MPa, an abrasive type of garnet, and a standoff distance of 1 mm. Surface features such as surface roughness and micrographs of the eroded surface are analyzed. Finally, the recovered backing was reused in the coated abrasive disc production, and the performance of the recovered disc was compared with the standard discs. The recovered fiber backing disc product was similar to a standard fresh disc.

1. Introduction

Abrasive products are energy-intensive materials and are mainly used to machine the high volume of material removed. Recycling abrasive products open up economic and environmental benefits to abrasive product manufacturers and society [1]. Bonded and coated abrasives are the two types of abrasives product. Authors have previously attempted to recycle connected abrasive products such as vitrified [2], resinoid [3] grinding wheels from the flange portion of the spent grinding wheel. Recovering the abrasive grains from the part adds wealth in terms of economics. The abrasive grains are sharp and potentially reused in the same abrasive applications. Various separation methods are available to recover the abrasive grains from the bonded products. But in the case of coated products, a tiny layer of abrasive grains is deposited on the fiber backing. So, the recovery of abrasive grains is not possible, but recovering the fiber backing from the spent portion is possible. This recycling of fiber backing from the spent abrasive discs reduces raw material cost by 30% for the coated abrasive disc production. Based on the 3R policy, every material should be reused somewhere as a resource [4]. Spent-covered abrasive consists of phenol-formaldehyde resin coat and fiber backing. Improper disposal of this waste adds up to the more serious environmental problems such as pollution and water

hampering. Recovery of fiber backing is necessary for abrasive product consumers and producers for the ecological benefits.

Researchers are attempting to recover the fiber backing from the coated abrasive disc using the chemical method [5]. The results highlighted that utilizing chemical solutions affects fiber quality in fiber entanglement. So more suitable manner such as the mechanical erosion method has opted for the backing recovery process. Many studies concentrate on the sandblasting or shot peening method for improving the bonding characteristics of materials.

Djokovic et al. studied the peel strength of the carbon fiber-reinforced epoxy composite. The effect of the composite surface structure was optimized concerning varying the blasting time, nozzle distance. The results highlight that increasing the blasting intensity leads to an increase in the surface roughness and increases the higher peel of strength of the composites [6]. Sabari Nathan et al. studied the abrasion resistance property of the grinding wheel rejects included concrete. The results highlight that addition of grinding wheel waste has increased the abrasion resistance of the concrete up to 40% [7]. Okada et al. has studied the sandblasting experiment on the yttria-stabilized tetragonal zirconia polycrystals. The investigation was conducted with different pressure, standoff distance, and particle size. The optimal sandblasting condition for the yttria-stabilized tetragonal zirconia polycrystals is the pressure of 0.25-0.30 MPa with a sandblasting time of 10 s [8]. Li et al. studied the adhesion performance of aluminum-lithium alloy joints using a sandblasting technique. The results show that increases in the abrasive particle size and sandblasting pressure have increased the substrates' surface roughness, which results in improved shear strength of the joints [9].

Coated abrasive products offer a massive market potential in a variety of applications. Coated abrasives are composed of three layers deposited on the backing material: a base layer, a raincoat, and a size coat [10], and based upon the type of backing, the product was classified as a sheet, cloth, and discs. The fiber backing is costlier and is used for heavy-duty applications. The primary element in the coated products is a type of support. Based on this, the product was classified. Among the various coated products, the recovery of support material is recovered for the fiber backing type only. Many types of research are done to recover the fiber from the spent materials. Senophiya et al. has recovered fiber from the spent printed circuit boards. So, there is more research on fiber backing recovery by using the chemical separation method [11]. This present work concentrates on removing phenol-formaldehyde resin coat by sandblasting technique and can be further reused to make coated abrasive discs.

Recycling is the critical element of the 5R principle. The cost imparted to the recycling process is useless [12]. So, the recovered fiber backing is reused to prepare coated abrasive discs. Currently, there are limited researches on the usage of coated abrasives for the finishing application.

Kuo et al. studied the multiple criteria optimizations for the coated abrasive grinding of titanium alloy using the minimum quantity lubrication (MQL) technique. The experiment was conducted by varying the grit number, loading pressure, and grinding speed: the general rapid abrasive and adhesive wear on the coated abrasive discs using coarse abrasive grits. In the case of fine abrasives, abrasive wear and clogging will have occurred at the higher grinding speed [13].

In this current work, vulcanized fiber backing is recovered using the sandblasting technique, and the recovered support is used to make the coated abrasive discs. The experimental approach was carried out to determine the surface roughness of the fiber backing recovered by sandblasting technique. After recovering fiber backing, the discs are used for the coated abrasive disc production. The performance of the standard and newly developed coated abrasive discs are analyzed, and the experimental results got reported. The optical microscopic technique studied surface characterization of the performance evaluated coated abrasive discs.

2. Materials and methods

2.1. Raw materials:. Spent coated abrasive discs of 120 grit were selected as the raw material for the backing recovery process. The coated abrasive disc comprises resin, abrasive grain, and fiber backing. Possibilities of recycling paper and cloth are complex, in case of recovering of fiber backing is possible. At the end of usage of coated abrasive discs, the support is left and thrown off as waste. The backing comprises of maker resin coat and blunted abrasive grains. Direct coating of the next layer of abrasive grains can cause a peel of the resin and abrasive grains from the fiber backing. To maintain the uniformity of the surface of the fiber discs, the fiber backing should be sandblasted to remove the maker coat from the fiber backing. Figure 1 shows the schematic layout of the fiber backing recovery experiment and again reused for the coated abrasive disc production.

They have selected a mechanical sandblasting erosion process to remove the resin coat from the fiber backing surface. The experiments are conducted in the sandblasting machine with the portable suction type (Make: Vegan controls, Coimbatore, India). The experiments are conducted with various experimental conditions, shown in Table 1. During the sandblasting experiment, an abrasive particle is mixed with high-pressure compressed air, blasted on the target material. The mixed air is passed through the workpiece through the nozzle of diameter 1 mm.

2.2. Experimental procedure. The backing recovery experiments selected the spent coated abrasive discs of 120 grit. While several diameters are available, chose a disc of 127 mm for this study. Because commercially, this 127 mm diameter has higher market potential and sales than 178 mm and 101 mm discs. To analyze the impact of each parameter, the experiment was conducted by maintaining all the parameters constant and changing the respective responsive parameter.

Initially, the coated abrasive discs are clamped at an angle of 60o, and the experiment was conducted with an

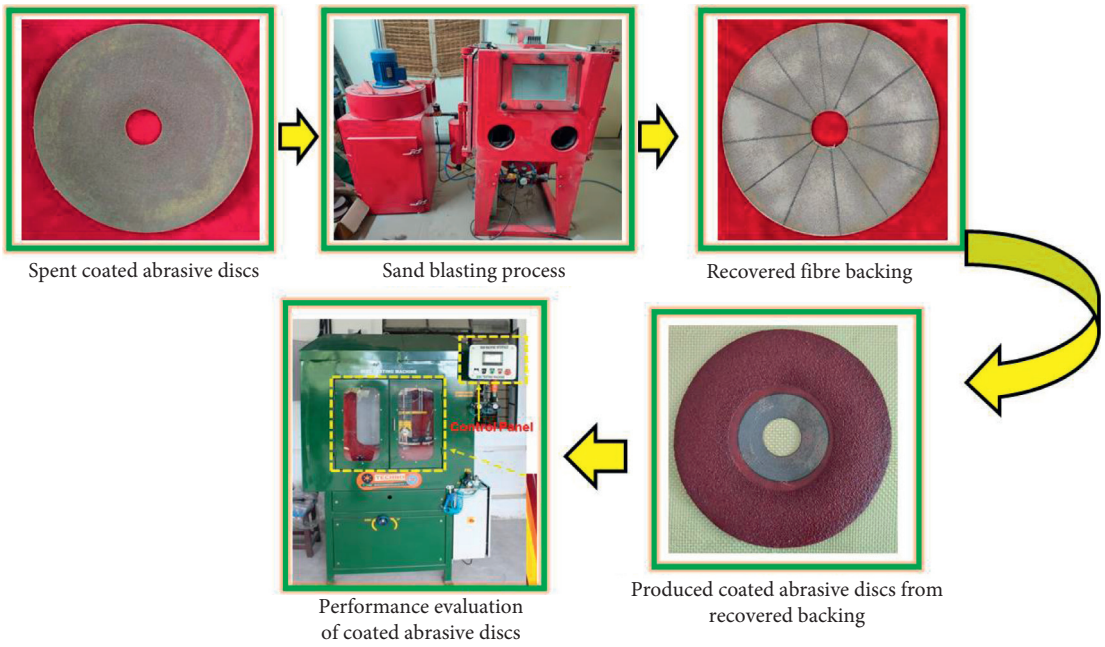

Figure. 1: Schematic layout of fiber recovery and coated abrasive disc production

Table 1: Parameter and its experimental range for the sandblasting experiment.

Parameter	Unit	Range
Blasting pressure	MPa	0.2, 0.5, 0.8
Abrasive	-	Silicon carbide, Alumina, Garnet
Size of abrasive	Mesh	80, 100, 120
Standoff distance	Mm	1, 3, 5

experimental condition for 10 minutes. The measurable output response such as surface roughness is considered as output response for the sandblasting experiments. Surface roughness such as average roughness value (Ra) of the sandblasted abrasive discs are measured by using contact type stylus profilometer (Mitutoyo Surftest SJ-301) with a cut off length of 8 mm. Recovered backing surface and newly developed coated abrasive discs to be analyzed by using an optical microscope (Make: Olympus, Japan).

2.3. Production of coated abrasive discs. In the present work, the coated abrasive discs are produced in the individual disc coating setup. The standard and recovered fiber backing is used for the coated abrasive disc production. In the first abrasive disc production, the resin was coated on the fiber backing surface utilizing the spin coating technique. Brown alumina abrasive grains of 60 grits are coated on the abrasive discs by grain coating using electrostatic projection to coat the fiber backing. The final resin coat is applied on the abrasive disc as the sizer coat for the abrasive holding in the discs.

The electrostatic grain coating technique uses the 60 grit abrasive grains on the fiber backing. Used standard and recovered backing for the fiber disc production and compared the performance of both the discs to evaluate the suitability of the usage of the discs. Produced discs are cured in the furnace, and it's flexed 5-7 times to introduce the flexibility of the produced discs.

Performance analysis of standard and recovered fiber backing used coated abrasive discs:

The performance of the produced coated abrasive disc is analyzed by using the coated abrasive performance evaluation machine (Make: Techno Machine Products, India). Specification of the performance evaluation machine is tabulated in Table 2. we tested the performance of the produced coated abrasive discs by maintaining the constant machining parameters output Calculated material removal rate based upon the formula (1).

$$\text{Material Removal rate} = \frac{\text{Weight of material removed}}{\text{time taken for machining}}. \quad (1)$$

For every 5 minutes, the workpiece weight and disc weight were measured using a digital weighing balance of 0.001 accuracies. The experiment is repeated five times to understand the deviation in the experimental results.

The machined surface of the coated abrasive discs is characterized in the optical microscope to analyze the chance of metal clogging and built-up in the coated abrasive discs.

3. Results and discussions:

The mechanical erosion process opted to recover the fiber backing compared with other recovery processes. Due to it doesn't affect the quality of the abrasive discs like fiber tangling and bending of the fiber. The response value such as surface roughness is considered output for the recovery experiment.

Experimental approach and its effect of various process parameters of mechanical erosion process:

Table 2: Specification of performance evaluation machine

Parameter	Range
Angle grinder size	5 inch
Maximum Loading RPM	11,000
Machine displacement	200 mm
Maximum depth to cut	4 to 5 mm
Tilting angle	15 to 25°

3.1. Impact of blasting pressure:. The experimental result clearly shows the effect of blasting pressure concerning the value of surface roughness of the recovered fiber backing. The experiment was carried out with different blasting pressure of 0.2, 0.5, and 0.8 MPa. Figure 2 shows the experimental output results of the surface roughness value concerning erodent pressure. The results highlight that the increases in the blasting pressure show increases in the surface roughness of the surface of the fiber backing. The maximum surface roughness value of 4.512 μm was observed on the highest blasting pressure of 0.8 MPa. At higher blasting pressure, there is a chance of high-impact energy. There is a chance of penetration of abrasive particles on the backing surface, which increases the surface roughness of the fiber backing [14]. The optimal blasting pressure for the recovery of fiber backing by using a mechanical erosion process is 0.2 MPa.

3.2. Effect of abrasive type. The experimental results of various abrasives are shown in figure 3. The experiments are carried out with three different abrasives: alumina, silicon carbide, and garnet. The results clearly show that the usage of silicon carbide abrasive shows the highest surface roughness value of 4.131 μm, followed by alumina of 3.66 μm, and garnet of 2.947 μm. from the results, the lowest surface roughness was observed on the garnet abrasive grains. This is due to higher hardness abrasive which can penetrate faster, and higher depth, which results in more elevated surface roughness value observed on the SiC abrasive grain used recovery process [15].

The optimal abrasive grain for the recovery of fiber backing will be garnet abrasive grain.

3.3. Effect of abrasive size. Figure 4 shows the surface roughness value of the sandblasted coated abrasive disc concerning the variation in the abrasive particle size. The experimental results clearly show that an increase in the abrasive particle size decreases the surface roughness for the surface of recovered fiber backing. For conducting experiments, various abrasive particle sizes of 80,100 and 120 mesh are considered. The results show that the experimental surface roughness concerning 80 grit abrasive grain will be 3.731 μm, followed by 100 grit of 3.32 μm and 120 grit of 2.724 μm. The lower surface roughness at the lower grit number is due to the smaller particle size. The interaction of particles and grooves production is smaller than other two-particle measures such as 80 and 100 grit. [16]. The optimal parameter for the abrasive particle size for the recovery of fiber backing will be 120 grits.

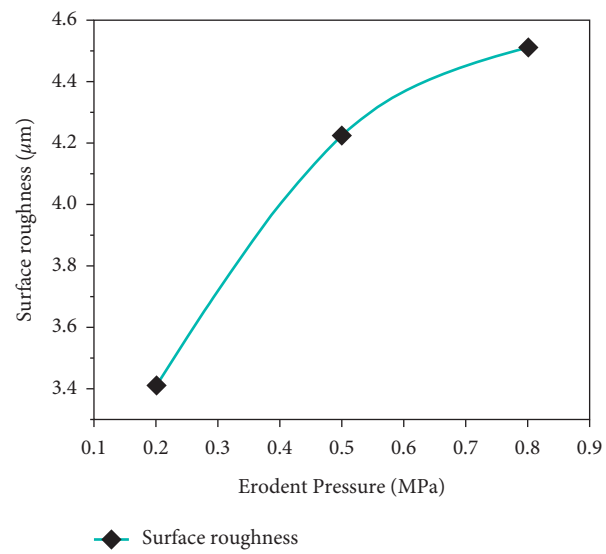

Figure 2: Effect of blasting pressure concerning surface roughness value.

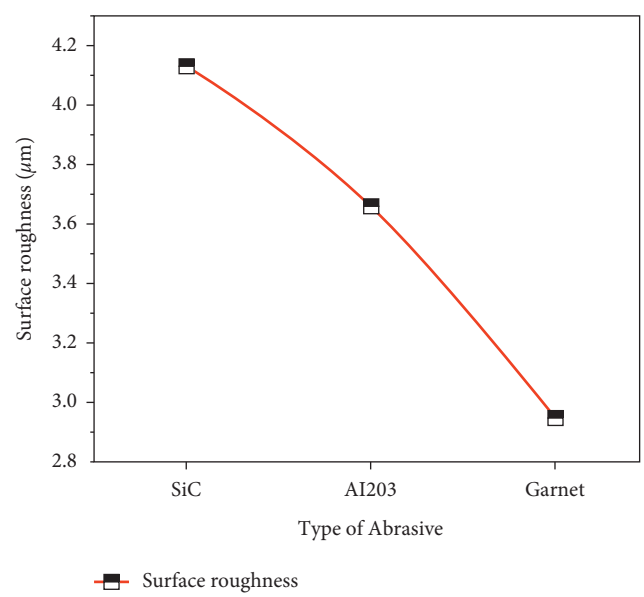

Figure 3: Effect of various abrasives with respect to surface roughness value.

3.4. Effect of standoff distance. Figure 5 (a) shows the surface roughness analysis of recovered fiber backing results for variation in the standoff distance. The experiment was conducted by varying the standoff distances of 1, 3, and 5 mm. The results show that increases in the standoff distance have increased the surface roughness value. The maximum surface roughness value of 3.972 μm was observed on the highest standoff distance of 5 mm, followed by 3.744 μm at 3mm and 3.445 μm at a 1 mm distance from the workpiece nozzle. The reason for the increase in the surface roughness by increasing the standoff distance is that the jet energy was lower at a higher space, which results in improper removal of resin from the backing surface [17]. The optimal standoff distance value for obtaining a lower surface roughness value will be 1 mm.

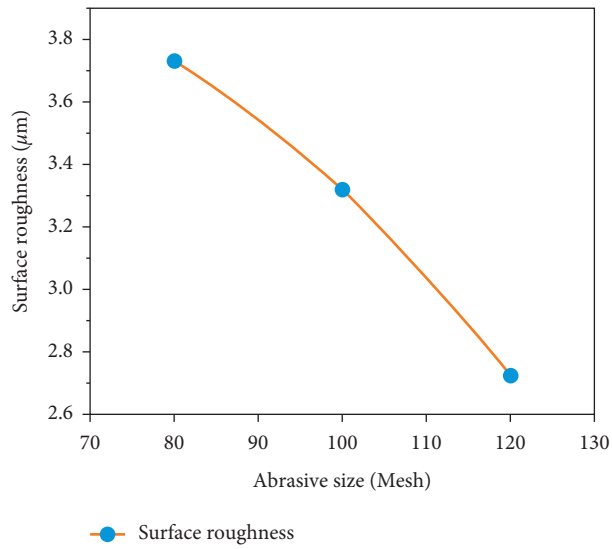

Figure 4: Effect of abrasive size with respect to surface roughness value.

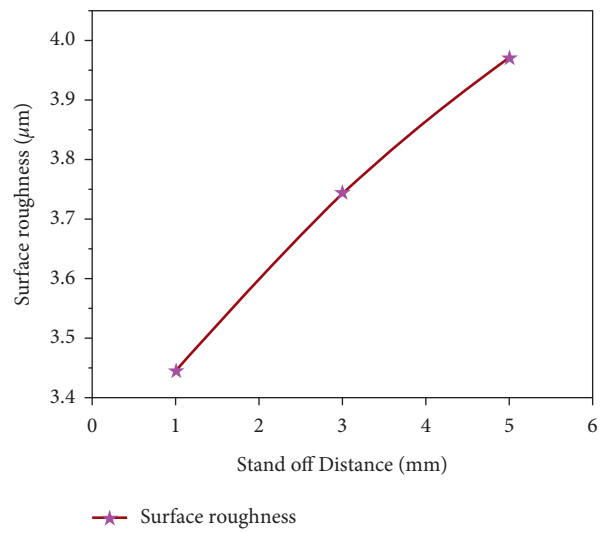

(a)

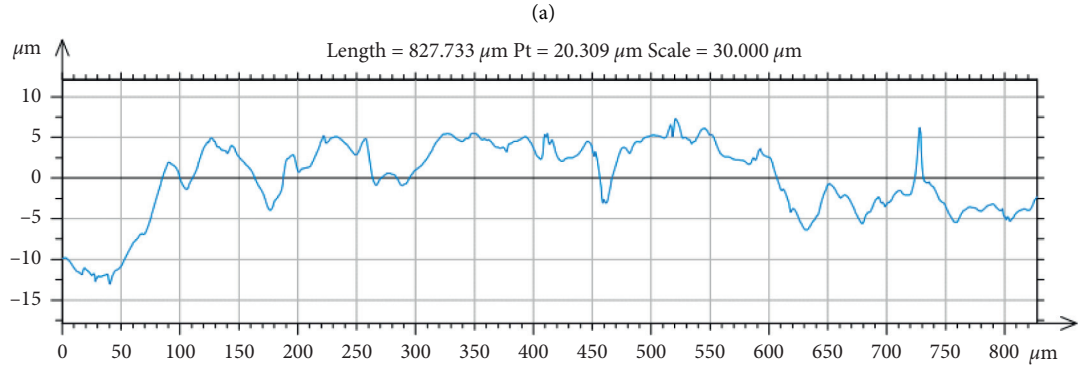

(b)

Figure 5: (a) Effect of standoff distance concerning surface roughness.(b)Surface roughness profile of the optimized condition for the recovered fiber backing.Performance analysis of reused fiber backing in coated abrasive application

3.5. Optimal combination for the recovery of fiber backing:. From the overall experimental results, the optimal combination for the recovery of fiber backing will be basting pressure of 0.2 MPa, abrasive type of garnet, abrasive size of 120 mesh, and standoff distance of 1 mm. Based on the experimental results, underwent the optimal combination

Table 3: Characteristics of coated abrasive discs for the current experiment

Backing Type	Grit size	Type of coating	Grit type
Standard	60	Electrostatic	Alumina
Recovered	60	Electrostatic	Alumina

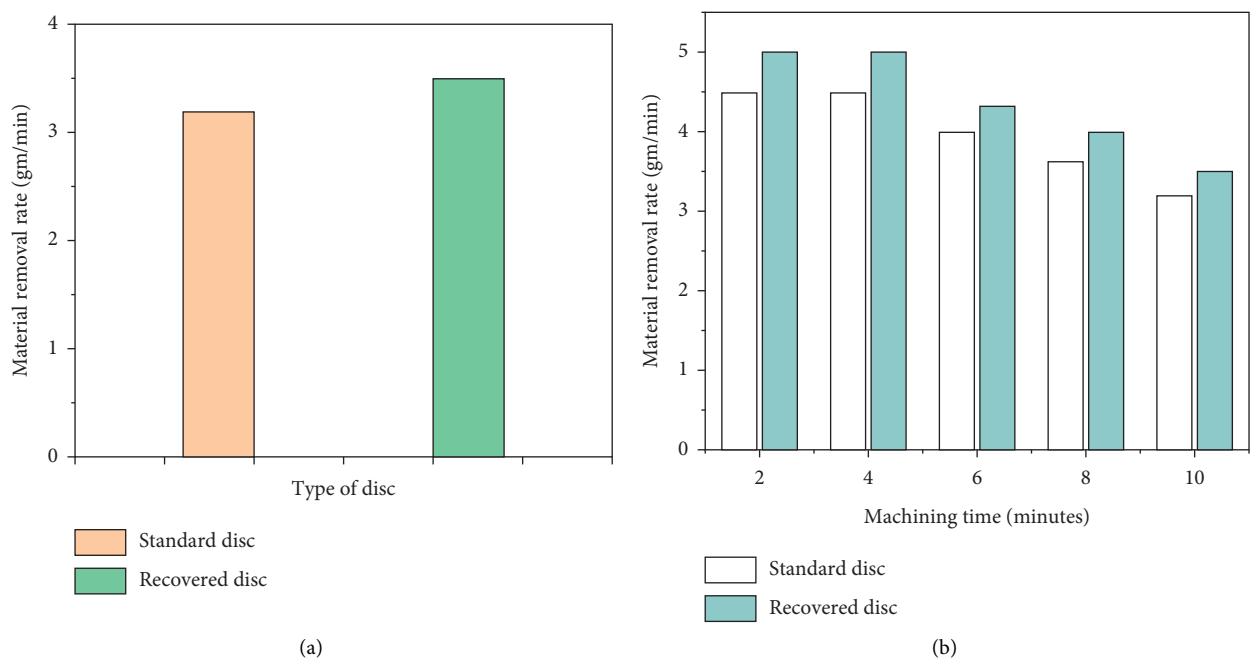

Figure 6: Material removal rate of performance results of coated abrasive discs

for the testing process, and the average surface roughness observed on the surface of the fiber backing will be 1.635 μm. It is observed from figure 5 5(b).

3.6. Production of coated abrasive discs. The recovered fiber backing is reused in the production of coated abrasive disc. The present work used standard brown alumina of 60 grit as abrasive for the coated abrasive disc production. Two different types of backings, such as standard and recovered backings, were selected for the backing material. Phenol formaldehyde resin was used as a resin for the base and topcoat. Table 3 shows the detailed characteristics of coated abrasives used for the experiments.

Produced coated abrasive discs as per industrial standards. Initially, the backing material was weighed and placed the disc in the maker unit. The primary coating of coated disc production is maker coat, which is necessary for sticking grain on the surface of the fiber backing during grain coating. Electrostatic projection of grains was utilized for the better anchorage of the grains. The grains were moved uniformly using the belt conveyor in the electrostatic unit. Due to applied voltage, the grains jump upwards and adhere to the resin surface of the fiber discs with sharp edges facing away from the backing. Then cured the discs in an oven.

A Sizer coat is the final coating process in which the coated grains are covered with a single layer of sizer resin. The sizer coat locks the abrasive grains during machining operations. Then cured the discs in an oven. The cured discs were placed in a humidity chamber for one day to improve their properties. Finally, the discs were flexed up and down using a roller flexing machine. The performance of the flexed discs was evaluated using an automatic performance evaluation machine. A squared rod of 50 mm^2 mild steel was used as a workpiece for the performance evaluation test.

Figure 6 6(a) shows the material removal rate of coated abrasive discs of standard and recovered backings. The recovered backing shows similar results and a better material removal rate from the experimental observation. This may be due to the formation of crater and valley during abrasive blasting, leading to better anchoring of resin bond with fiber backing and abrasive grain. This will be evident from the 3D surface roughness images shown in figure 6. Figure 6 6(b) shows the material removal rate for every 2 minutes of interval. The result shows that for the first 2 minutes, both the standard and recovered used backing discs show a higher material removal rate than the 4th, 6th, 8th, and 10th minutes. This may be attributed to the adhesive wear of the eroded metal piece that clogged on the coated abrasive surface.

Figure 7 (7a-b) shows new abrasive discs of standard and recovered backing before starting machining. Figure 7 (7c-d) shows the used disc of recovered backing at the 6th and 10th minutes during performance evaluation. Optical images depict that at the 10th minute, abrasive

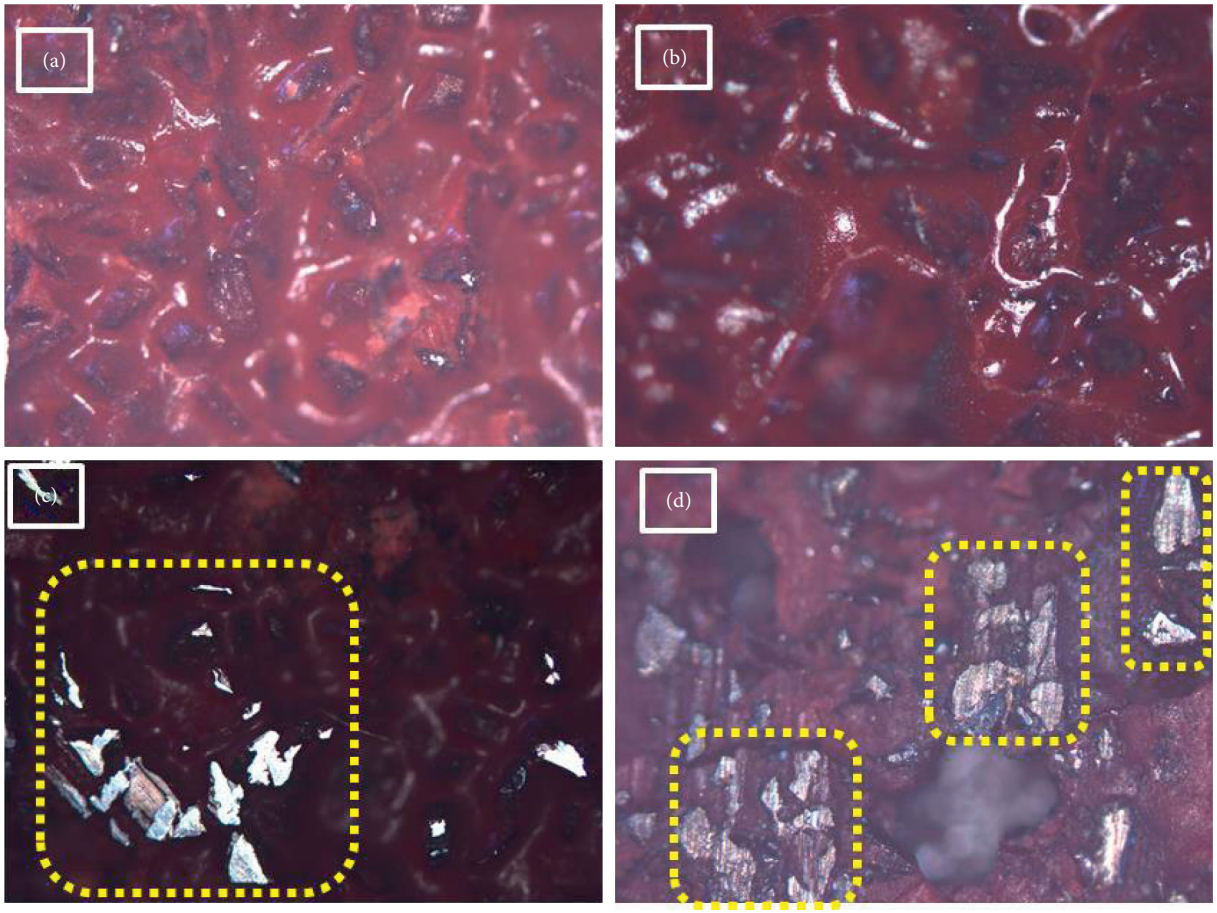

Figure 7: Optical images of produced coated abrasive discs (a) Standard disc (b) Recovered disc, (c) Performance evaluated recovered coated disc at 6th minute, and (d) Performance evaluated recovered coated disc at 10th minute.

discs show more metal clog than the 6th minute. This results in a decrease in material removal rate during the grinding operation.

In both cases, an increase in the machining time shows a decrease in the material removal rate. The experimental results indicate that the recovered backing has similar cutting action to the standard backing disc. This confirms that it is possible to reuse the recovered backing in coated applications.

4. Conclusions

The mechanical erosion process is employed to recover the fiber backing in this research work. Then the recovered fiber backing is used to prepare the coated abrasive discs. The present study of places is the impact of various experimental conditions such as blasting pressure, abrasive type, abrasive size, and standoff distance. From the experimental results following conclusions are made.

- Compared with the chemical method of fiber backing mechanical erosion method, which recovers the fiber backing similar to new disc as appearance entirely. The discs are free from damage, and the surface can be resin coating.
- The optimal combination for the recovery of fiber backing will be basting pressure of 0.2 MPa, abrasive type of garnet, abrasive size of 120 mesh, and standoff distance of 1 mm.
- Coated abrasive discs re-manufactured with the recovered fiber backing show similar performance results with the standard discs.
- This shows it is possible to reuse the recovered backing on the same coated abrasive disc production.
- Such a method will reduce the cost of coated abrasive discs and reduce the need for sending the used fiber backing to landfills.

Data Availability

The data used to support the findings of this study are included in the article. Should further data or information be required, these are available from the corresponding author upon request.

Conflicts of Interest

The authors declare that there are no conflicts of interest regarding the publication of this paper.

Acknowledgments

The authors thank Chennai Institute of Technology, Sri Sivasubramaniya Nadar College of Engineering, Chennai, and Saveetha School of Engineering, SIMATS, Chennai, for the technical assistance. The authors appreciate Wollo University's support, Kombolcha Institute of Technology, Ethiopia.

References

[1] B. Linke, *Life Cycle and Sustainability of Abrasive Tools*, Springer International Publishing, Midtown Manhattan, New York City, 2016.

[2] P. Sabarinathan, V. E. Annamalai, S. S. Kumar, and A. Xavier Kennedy, "A study on recovery of alumina grains from spent vitrified grinding wheel," *Journal of Material Cycles and Waste Management*, vol. 21, no. 1, pp. 156–165, 2019 Jan 22.

[3] P. Sabarinathan, V. E. Annamalai, and A. Xavier Kennedy, "On the use of grains recovered from spent vitrified wheels in resinoid applications," *Journal of Material Cycles and Waste Management*, vol. 22, no. 1, pp. 197–206, 2020 Jan.

[4] L. Liu, Y. Liang, Q. Song, and J. Li, "A review of waste prevention through 3R under the concept of circular economy in China," *Journal of Material Cycles and Waste Management*, vol. 19, no. 4, pp. 1314–1323, 2017.

[5] P. Sabarinathan, V. E. Annamalai, R. Balakrishnan, and A. C. Kuriakose, "Process optimization for recovery of fiber backing from coated abrasive disks," *Chemical Engineering Communications*, vol. 208, no. 6, pp. 893–902, 2021 May 3.

[6] E. Njuhovic, A. Witt, M. Kempf, F. Wolff-Fabris, S. Glöde, and V. Altstädt, "Influence of the composite surface structure on the peel strength of metallized carbon fibre-reinforced epoxy," *Surface and Coatings Technology*, vol. 232, pp. 319–325, 2013.

[7] P. Sabarinathan, V. E. Annamalai, and P. Sangeetha, "Mechanical and abrasion resistance properties of concrete containing recycled abrasive waste as partial replacement of fine aggregate," *Arabian Journal for Science and Engineering*, pp. 1–0, 2021 Apr 19.

[8] M. Okada, H. Taketa, Y. Torii, M. Irie, and T. Matsumoto, "Optimal sandblasting conditions for conventional-type yttria-stabilized tetragonal zirconia polycrystals," *Dental Materials*, vol. 35, no. 1, pp. 169–175, 2019 Jan 1.

[9] J. Li, Y. Li, M. Huang, Y. Xiang, and Y. Liao, "Improvement of aluminum lithium alloy adhesion performance based on sandblasting techniques," *International Journal of Adhesion and Adhesives*, vol. 84, pp. 307–316, 2018 Aug 1.

[10] S. N, A. K. S, P. A, and G. S, "Studies on semi-crystalline poly lactic acid (PLA) as a hydrophobic coating material on kraft paper for imparting barrier properties in coated abrasive applications," *Progress in Organic Coatings*, vol. 145, Article ID 105682, 2020 Aug 1.

[11] J. Senophiyah-Mary, R. Loganath, and T. Meenambal, "A novel method for the removal of epoxy coating from waste printed circuit board," *Waste Management & Research: The Journal for a Sustainable Circular Economy*, vol. 36, no. 7, pp. 645–652, 2018 Jul.

[12] M. Gautam and M. Agrawal, "Greenhouse gas emissions from municipal solid waste management: a review of global scenario," *Environmental Footprints and Eco-design of Products and Processes*, vol. 9, pp. 123–160, 2021.

[13] C. Kuo, Y. Hsu, C. Chung, and C.-C. A. Chen, "Multiple criteria optimisation in coated abrasive grinding of titanium alloy using minimum quantity lubrication," *International Journal of Machine Tools and Manufacture*, vol. 115, pp. 47–59, 2017 Apr 1.

[14] S. Palaniyappan, V. E. Annamalai, S. Ashwinkumaran, D. Thenmuhil, and D. Veeman, "Utilization of abrasive industry waste as a substitute material for the production of fireclay brick," *Journal of Building Engineering*, vol. 45, Article ID 103606, 2022 Jan 1.

[15] P. Andrzej, "Experimental research into alternative abrasive material for the abrasive water-jet cutting of titanium," *International Journal of Advanced Manufacturing Technology*, vol. 97, no. 1-4, pp. 1529–1540, 2018 Jul 1.

[16] K. Balaji and N. Yuvaraj, *Influence of different abrasives mixtures on abrasive water jet drilling of die steel Innovative Design Analysis and Development Practices in Aerospace and Automotive Engineering 2021*, pp. 511–519, Springer, Singapore, 2021.

[17] P. Sabarinathan, V. E. Annamalai, and K. Rajkumar, "Sustainable application of grinding wheel waste as abrasive for abrasive water jet machining process," *Journal of Cleaner Production*, vol. 261, p. 121225, 2020 Jul 10.

Hindawi
Advances in Materials Science and Engineering
Volume 2022, Article ID 3533143, 10 pages
https://doi.org/10.1155/2022/3533143

Research Article

Effect of Moisture Content on Mechanical Properties of AAM Natural Fiber-Reinforced Isophthalic Polyester Composites

T. Ramakrishnan,[1] **S. Senthil Kumar**,[2] **Samson Jerold Samuel Chelladurai**,[3] **S. Gnanasekaran**,[4] **N. K. Geetha**,[5] **Ramesh Arthanari**,[6] **and Baru Debtera**[7]

[1]*Department of Mechanical Engineering, Sri Eshwar College of Engineering, Coimbatore, Tamilnadu, India*
[2]*Department of Mechanical Engineering, RMK College of Engineering and Technology, Puduvoyal 601206, India*
[3]*Department of Mechanical Engineering, Sri Krishna College of Engineering and Technology, Coimbatore, Tamilnadu, India*
[4]*Department of Mechanical Engineering, Sri Shakthi Institute of Engineering and Technology, Chinniyampalayam, Coimbatore, Tamil Nadu, India*
[5]*Department of Mathematics, Dayananda Sagar College of Engineering, Bangalore 560078, India*
[6]*Department of Mechanical Engineering, Chennai Institute of Technology, Chennai, Tamil Nadu, India*
[7]*Department of Chemical Engineering, College of Biological and Chemical Engineering, Addis Ababa Science and Technology University, Addis Ababa, Ethiopia*

Correspondence should be addressed to T. Ramakrishnan; ramakrishnankct@gmail.com and Baru Debtera; baru.debtera@aastu.edu.et

Received 26 October 2021; Revised 16 December 2021; Accepted 5 January 2022; Published 28 January 2022

Academic Editor: Ravichandran M

Composite fiber reinforcement is one such proficient material that substitutes for useful applications for conventional and polyester blends where little weight and thus less energy conservation is required. This study highlighted the importance of recently discovered Agave Angustifolia marginated (AAM) fibers extracted by a manual process from AAM plants. This paper observes the various properties of the mechanical and moisture intake characteristics of AAM fiber and compares these to other naturally occurring fibers. Using isophthalic polyester resin, the mixed chopped AAM fiber-reinforced composite is prepared and detailed preparation techniques are presented. During physical composite testing, fiber pull-outs on the broken samples were investigated. Additionally, the experimental evidence demonstrates that increasing the volume fraction helps to increase the tensile, bending, and modulus of the AAM fiber composite. The chopped fiber isophthalic polyester reinforcement reaches its improved tensile strength and modulus at a 25% Vf about the 20 mm length of the fiber.

1. Introduction

The global economy is rapidly progressing through the process of energy conservation and reduction. Typically, natural fibers are used to reduce the weight of components; i.e., the fibers are strengthened with the appropriate matrix. Natural plant fibers offer numerous benefits over synthetic fibers in terms of cost, sustainability, renewable resources, and biodegradability. In the field of natural fibers, several authors have conducted their investigations. Natural plant fibers have numerous advantages over synthetic fibers in terms of cost, sustainability, renewable, and biodegradability. In the field of natural fibers, several authors have conducted their investigations into the topic [1]. Natural fibers are typically used in order to decrease the components' weight and increase their strength. The ASTM standards explored the relationship between filler loading (3 to 12% by weight) and the mechanical and physical properties of hybrid composite materials. The tensile strength of the polymeric material was found to be 34% higher than polyester, and the impact strength was determined to be 3.87 significantly greater [2]. These include tensile, compressive, and impact strength as well as tribological properties. Interfacial bonding is the main determinant of mechanical and tribological properties. Plant fiber thermoset composites' wear and friction

characteristics can be regulated by fillers and reinforcement orientation [3]. The innovation propels have prompted the present another age of specialized and keen materials. These new high-esteem materials can be created by surface treatment, synthetic uniting, 3D design, and nanotechnologies [4]. Advances in nanotechnology have permitted the plan of new materials with explicit properties since they offer the likelihood to control their morphological attributes [5]. The interfacial attachment was observed to be an overwhelming component regarding mechanical and tribological properties [6]. Wear and frictional attributes of plant fiber-based thermoset composites can be controlled utilizing appropriate fillers and support direction. A conversation on interfacial attachment and its impact on composite execution have likewise been incorporated [7, 8]. Because the present technology cannot reduce the weight of materials, increase spans, or build thin constructions, the search for new composite materials is sparked. Polymer-based reinforcement with fibers (FRP) has a high strength-to-weight ratio while being less weight when the use of FRP encourages civil engineers to reinforce and repair deteriorated RC structures [9, 10]. For variable boundary conditions, geometric parameters, and material qualities, the theory is used to quantify the impacts of axial distributed load/terminal force and temperature fluctuation on free vibration and buckling. At a very low computing cost, the current theory can accurately estimate the natural frequencies and buckling capabilities of multilayered beams [11–18]. The composite's mechanical characteristics are scrutinized for quality and durability. With the inclusion of nanoclay, the mechanical characteristics of the coir fiber epoxy composite were significantly improved at a reduced cost, making it an attractive alternative to glass fibers for several applications [19–53].

2. Materials and Experimental Methods

2.1. Fiber Materials. A width range of 30 cm to 150 cm is observed among the AAM plants cultivated throughout the field. The AAM leaf and the sand are washed with acetone before plucking. The leaves' green exteriors (stamps) are carefully removed. To remove the plant's secondary and tertiary walls, the plants are immersed in water for four days. Afterward, they are used in a biodegradable platform that allows the fibers to be harvested continuously. The unpasteurized AAM is then chopped into many thicknesses, such as 05 mm, 50 mm, 80 mm, 110 mm, and 140 mm, for polymer sample preparation.

2.2. Synthetic Polyester Resin. The study employed an isophthalic monosaturated polyester resin. To cure the resin, both the accelerator, Ketone Peroxide and Methyl Ethyl, and the catalyst, Cobalt Naphthalene, are used in combination [15]. When compared to other resins, thermoset polyester resin is one of the most cost-effective choices owing to its extremely low water absorption capacity, better mechanical strength, and outstanding bonding ability, among other properties. To enhance the bonding strength 2 : 1 mix ratio of resin-hardener by volume used, the isophthalic polyester resin exhibits a number of unique characteristics, which are listed in Table 1.

2.3. Polyester Resin Reinforced Composite Materials Sample Preparation. The AAM fibers are obtained from the water after four days, after which their moisture content is removed by placing the fibers in inhaled sunlight for eight hours. After they have been heated to 120°C for 60 minutes, the fibers are transferred to the hot air oven. To make the composites, the fibers are first sliced. A simple hand lay-up method provided composite specimens with volume concentrations of 10 wt.%, 15wt.%, 20wt.%, 25wt.%, and 30wt.%. To cure isophthalic polyester resin, 1% catalyst and 1% accelerator have been used. Composite specimens are made with preparation steel dies. The releasing agent is first applied to the male and female die sections to help remove the samples after phase transformation. Fibers are then spread across the die, and the surfaces are left to dry for 15 minutes.

In order to maintain the total fiber orientation and homogeneity, steel roller rolls are used to roll the composite into the isotypic properties of the material so that most of the air bubbles are removed. The closed mold is held on the hydraulic press for 8 hours, under compressive pressure, while curing. To prepare the desired composite plate, the resin is injected to reinforce these same fibers to a total of 4 millimeters. Once the composite plate has been postcured for one hour in an oven, it is ready for use.

2.4. Examination of the Fiber and Composites

2.4.1. Single Fiber Tensile Testing. To determine the tensile properties of an unremitting AAM fiber over a long length, an ASTM D3379-75 appropriate testing method that used the Instron Universal Testing machine was used as per the ASTM D3379-75 standard. Each fiber's gauge length was set to 100 mm, and a 1000-gram load cell was carried out to perform the test at various levels. The grippers' speed was set to 5 mm/min, and this acceleration was maintained all through the testing. In this study, twenty-five tests were performed, In this experimental study, the failure/break, tensile modulus, and tensile strength average values were obtained [16].

2.4.2. Tensile Strength of the PRC Materials. An electronic tensometer was used to test the composite specimen's tensile properties. The dog bones samples were made to ASTM D 638 standards. At the gauge length of 50 mm, the samples remained machine-cut to a fixed size of 165 mm, 13 mm, and 4 mm. The tensometer utilized a load cell with a capacity of 5 kN to test for this. In order to track which specimen goes with which number, five identical test samples (S1, S2, S3, S4, and S5) were used for each test. The composites' tensile strength, tensile load, elongation at break, and elastic modulus were all measured in this experiment [17].

2.4.3. Flexural Strength of the PRC Composite. The spring-mass testing machine was also used to conduct three-point flexural testing in accordance with ASTM D 790 standards.

Table 1: Effects of the isophthalic Synthetic Polyester Resin.

S. No	Properties	Unit	Range
1	Density	kg/m³	1125
2	Flexural strength	MPa	30
3	Flexural modulus	GPa	1.2–1.5
4	Shrinkage	%	0.004–0.008
5	Tensile modulus	GPa	0.8–1.1
6	Compressive strength	MPa	90–250
7	Tensile strength	MPa	18
8	Specific gravity	—	1.1–1.46

The samples were cut to 125 mm, 12 mm, and 4 mm in size. The samples were tested and the span to depth ratio was determined to be 16 : 1. A 6 kN load cell was employed in this experiment, with a speed (crosshead) of 2.5 mm/min. Five equal test specimens were made for each flexural test and labeled F1, F2, F3, F4, and F5. The displacement of the samples was measured using a computerized dial gauge, and the composites' flexural parameters such as strength properties, modulus of elasticity, flexural load, and displacement at breaks were analyzed. Five equal samples were broken between the gauge length and the tensile testing during the experiment [18].

2.4.4. Moisture Absorption Test Procedure. According to ASTM standards, flexural and tensile specimens were to be cut from the fabricated plate. In order to absorb the moisture, the surfaces of the test samples were bonded using polyester resin and placed in a warm atmosphere. The first specimens were dried in an air oven at 60°C. After conditioning the PRC specimens, they were immersed in distilled water at 30°C for about five days. The samples were gradually separated from the water and dried using filtrate to eliminate excess moisture from the surface, before being quantified using a weighing scale with a range of 0.01 mg. Once saturation limit was reached, the samples were placed in water so that sorption could continue until absorption was complete. To avoid evaporation errors, the measurement was finished in thirty seconds. We used ASTM D570 for 5 days, the sample had been measured, and the process is repeated.

3. Results and Discussion

3.1. Mechanical Characteristics of the AAM Fiber. The raw single AAM fibers are intricate for tensile testing with an appropriate gauge span of 100 mm. The twenty-five samples were used to determine the fiber tensile properties based on the average value of load and area. Table 2 compares tensile strength values of AAM fiber to those of other available natural fibers. The fiber diameter was varied from 493 mm to 500 mm. Density is an important parameter to consider when designing lightweight materials. The density of the AAM fiber was clearly lower than that of the other natural fibers in the table. However, it was slightly more than that of spatha rachilla, rachis fibers, elephant grass, and petiole bark. AAM fiber had a higher average tensile strength than other natural fibers such as petiole bark, spatha rachilla, rachis fibers elephant grass, kenaf, root, and coir fibers. The maximum load at break was somewhat greater than that of many other natural fibers. On the basis of the available qualities, it is obvious that the AAM fiber is a viable alternative to natural fibers in the future.

The percentage elongation at break was slightly higher than that of elephant grass, petiole bark, pineapple leaf, date, and bamboo, but it was the same as that of flex, banana, hemp, and jute. Based on the available properties, it is clear that the AAM fiber is one of the future natural fiber alternatives [18, 19].

3.2. Effect of Tensile Behavior of AAM-PRC Materials. Compared to different fiber volume fractions, the tensile characteristics of sliced AAM-PRC materials are anticipated to be identical to those of fibers with varying volume concentration and lengths. As illustrated in Figure 1, the material's strength fluctuates with the difference in fibers volume concentration as the various fiber lengths are altered. If the length of the fiber is increased from 5 to 140 mm, the tensile strength typically decreases from 19.15 to 16.25 MPa. Very little fiber accumulation is found in the composite, resulting in a 15.8% increase in the present case between both the higher and lower tensile strengths.

A similar linear drop in tensile strength can be seen up to 25%. The tensile strength increases by 15% between both the maximum and minimum are 10.85%. Due to the more accumulation of fiber in the composite, the Vf has been reduced by 10 percent. As well, the amount of efficiency was further reduced to 09.33 percent for 20% Vf. Tensile forces are exerted at a fiber length of 20 mm in the current project, and it is calculated for a proportionate volume concentration of 25%. The 25% Vf tensile strength improvement percentage is 11.49%. Compared to the previous figure of 20%, the new percentage is higher. Since the accumulation of fibers in the composite is more than in the composition, the fibers in the composite have more fibers with higher fiber ends than the 140 mm in the composition.

The tensile strength of a fiber is significantly influenced by the ends of the fiber. When the percentage volume fraction reaches 30, the tensile strength of the material drops rapidly to 13.02–9.85 MPa for a variety of fiber lengths as illustrated in Figure 2. The results show that there is substantially less stress and pressure on the fiber because of the lower volume content in the matrix of composites. The composite's tensile strength, as determined by fiber length, ranges between 20 and 50 mm. For 20 mm and 50 mm fiber lengths, there was a 39.99% improvement from 10% Vf to 25% Vf. The composite's tensile strength rises as the fiber content rises. In order to experience a good load transfer, you must see the fibers and the matrix separate from each other. Increased fiber length and volume fraction reduce tensile strength.

3.3. Flexural Properties of AAM Fiber-Reinforced Composites. The flexural property is a significant parameter in a composite material that is particularly helpful in structural applications. Figure 3 depicts the variance in flexural strength

Table 2: Difference between the tensile behavior of AAM fiber with numerous natural fibers.

Fiber name	Density (kg/m^3)	Diameter (um)	Tensile strength (MPa)	Tensile modulus (GPa)	% Elongation
Cotton	1600	—	287–597	5.5–12.6	3–10
Ramie	1500		220–938	44–128	2–3
Flax	1500	—	345–	27.6–80	1.2–3.2
Hemp	1480	—	550–900	70	1.6
Jute	1460	—	393–800	10–30	1.5–1.8
Sisal	1450	50–300	227–400	9–20	2–14
Pineapple	1440	20–80	413	34.5–	0.8–1
Leaf			1627	82.5	
Kenaf	1400	81	250	4.3	—
AAM fibers	1608	49.3–500	512	38.71	1.6

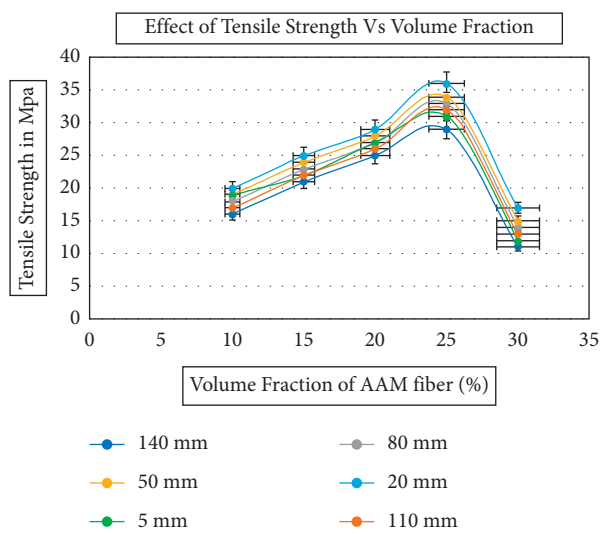

Figure 1: Effect of Tensile strength versus volume fraction of AAM fiber through different fiber lengths.

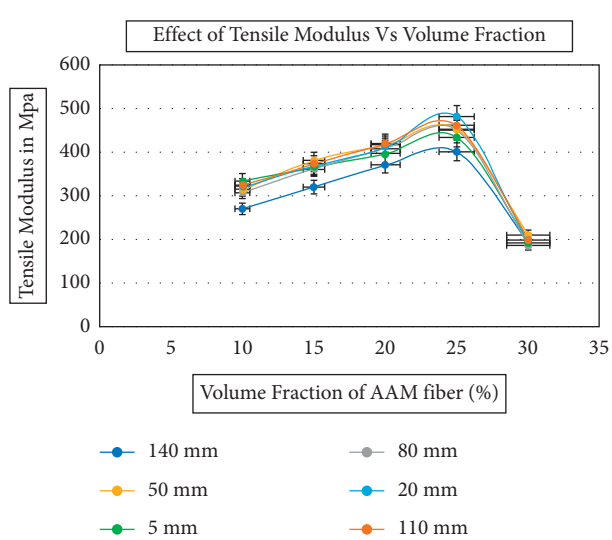

Figure 2: Effect of tensile modulus versus volume fraction of AAM fibers of various lengths.

values as the volume fractions increase by a percentage. It is discovered that the flexural values eventually increase close to 20% Vf. The flexural strength of a composite increases

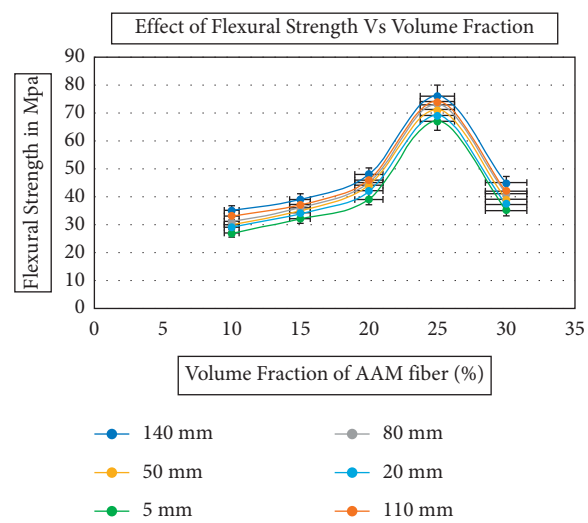

Figure 3: The relationship between flexural strength and the volume fraction of AAM fiber is explored through the use of different fiber lengths.

dramatically once the Vf of the fiber exceeds 20%. When the Vf of fiber in the composite is 30%, the increasing trend abruptly reverses and the flexural strength is drastically reduced. If the fiber content is greater than 30% Vf during matrix composites, it results in minimal filling of the matrix into the encircling fibers. A 10% Vf composite has a flexural strength of 32.45 MPa. In addition, the variation of fiber concentration and the flexural strength increases by 11.01%.

By increasing the fiber content of the composite by 15%, the maximum flexural strength increases to 37.14 MPa, and the flexural strength varies widely by 5.87 percent depending on the fiber content of the composite. The increase in flexural strength value persists, as in prior situations, up to a maximum of 25 percent Vf. The length of fiber is 140 mm, and a 25 percent Vf composite has a maximum flexural strength of 74.27 MPa. The volume fraction of the fiber content in the composite is 30 percent; the increasing trend abruptly declines to 48.54 MPa. For a 25 percent Vf material, the maximum flexural strength is determined by the length of the fibers used in the composite; in this study, 110 and 140 mm were the fiber lengths used in the material. Additionally, flexural strength is influenced by the fiber content and length of the fiber. Extensive testing has revealed that

perhaps the lengthy fiber carries the greatest flexural load compared to the short fiber.

In Figure 4, you can see the range of flexural modulus values for different AAM fiber volume concentrations. Once again, the flexural modulus significantly increases as the volume concentration rises. Although this shows an increase to 25% overall, this results in a 14.78 GPa flexural modulus when the fiber length is 140 mm. It is readily apparent that a fluctuation in the flexural modulus occurs when the fiber content of the substantive changes. When the volume of fiber content in the composites is 30, one of the mechanical properties of the composites such as flexural strength reduced up to 5.72 GPa. Based on Figure 4, there are different stress and strain curves for different fiber weight fractions when using a tensile test at 20 mm length. This finding concludes that the optimum flexural modulus of the composite is acquired when the fiber length is 140 mm and the percentage of Vf is 25 percent. From validating all of the results (Figures 3 and 4), it is apparent that isophthalic polyester resin reinforced composite with the addition of 25 wt.% chopped AAM fiber improved several mechanical properties such as flexural strength and modulus, tensile strength, and modulus. For the application of loads at volume fractions of 25% or greater, the fiber-reinforced effect is a challenging phenomenon for improving strength and modulus. At volume concentrations between 25% and 75%, the crack formation initiation is high. Expanding fiber volume fraction leads to an increase in the flexural and tensile modulus values.

To understand how sliced fiber-reinforced strength is determined by multiple factors, we examine how various factors (e.g., fiber strength, modulus, fiber length, the volume of fiber, fiber content, fiber content, and fiber positioning) enhance the mechanical properties of the sliced fiber-reinforced composite. In addition to such elements, the preparedness of the composite should indeed be considered. When in the matrix resin, sliced fibers have relatively high portions that are aligned in greater alignment. The presence of fibers-direct load transfer is observed, which results in an enhancement in the mechanical characteristics of the composite.

Natural fibers can be wider or narrower depending on the length of the fibers. Therefore, making an attempt to directly compare the composite properties of a composite object would be a difficult endeavor. At equal volume ratio and reinforcement type, this is among the easiest ways to prepare composite material. It is one of the straightforward approaches that have significant value in teaching comprehension.

3.4. Effect of Moisture Absorption Characteristics. The effects of fiber content on the composite specimen's moisture absorption behavior are shown in Figures 5–7. The absorption of moisture increased in all cases with increased fiber content. This is explained by improving the formation of microbial in the resin matrix [28]. Figure 5 illustrates the outcome of fiber concentration on the first day and then the fifth day of humidity absorption of composite fiber of

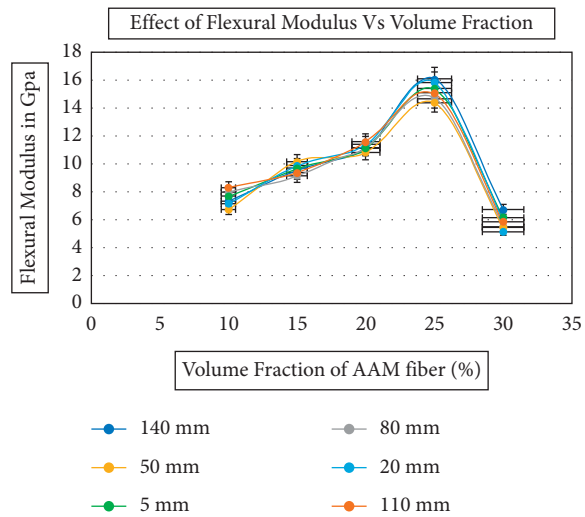

Figure 4: The relationship between the flexural modulus and the volume fraction of AAM fibers with varying fiber lengths.

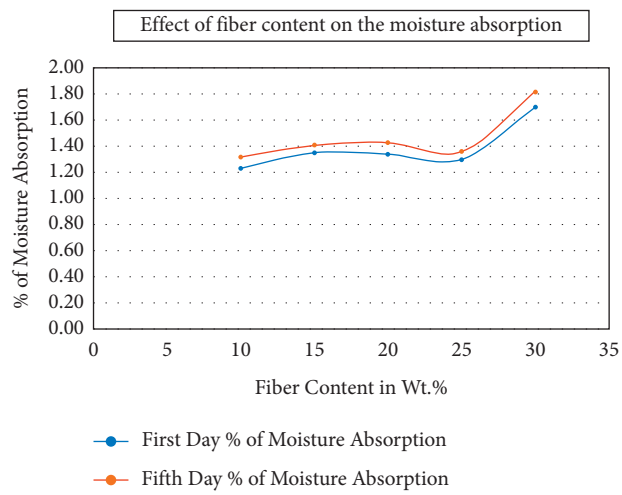

Figure 5: Moisture absorption of 20 mm fiber composites with different fiber volumes.

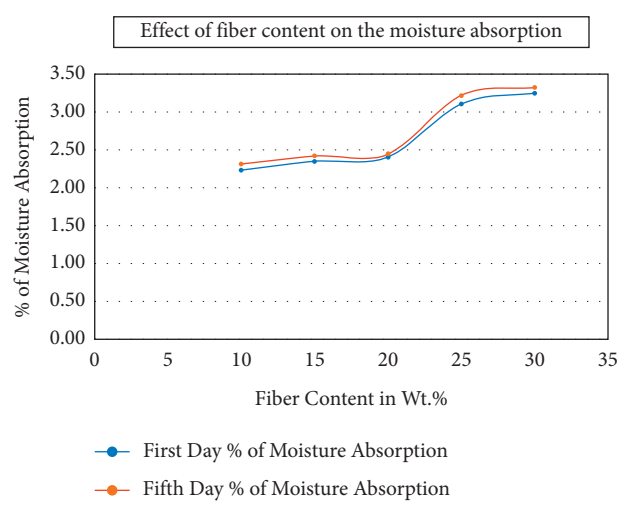

Figure 6: Water absorption of 140 mm length of fiber composite with varying fiber concentrations.

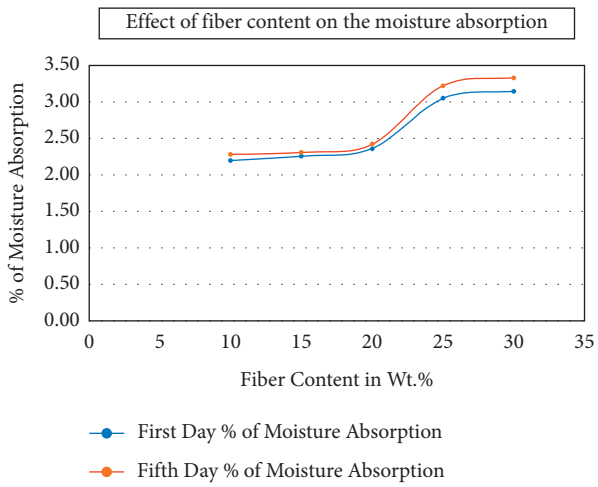

Figure 7: Water absorption of 100 mm length of fiber composite with varying fiber concentrations.

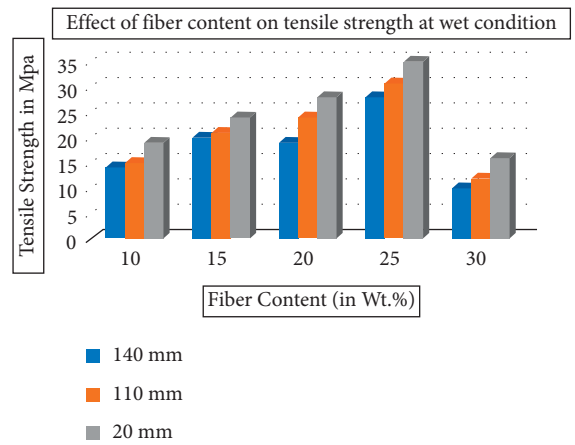

Figure 8: Tensile behavior of dry and wet conditions of composites with respect to the fiber content.

20 mm. The moisture absorption frequency was identified for the first and fifth days. 10wt.% of the composite observed moisture content up to 75%. Similarly, 20wt.% observed up to 85%, 30wt.% observed up to 85%, and 35wt.% observed up to 89%. Figure 7 showcases the analysis of the fiber content on water intake of the 100 mm length of fiber-reinforced composites during the above-stated days.

The water absorption assortment increased almost all the weight percentages of the composites during the first and fifth days of testing. The result produced for 10 wt.% of the composite was absorbed up to 34.3%, 20wt.% moisture intake percentage was 39.89%, and 30 wt.% of the composite was absorbed up to 43.82. Figure 6 shows the effect of fiber content at the end of the first and fifth days on moisture content of composite fibers of 140 mm. At 10wt percent for the first day and for the fifth day, 20wt percent and 30wt percent of fiber composites stood at 27.6%, 32.1%, and 41.1%. When the content of fibers increased, the absorption of humidity increased. The third, fourth, and fifth days of humidity absorption were almost identical: 10 wt.% and 100 mm and 20 wt.% and 100 mm. The components were also found in 10 wt.% and 140 mm and 30 wt.% and 140 mm. These components were found. The 150 mm length of the composite absorbed more moisture content when compared to other lengths of the AAM fibers, such as 50 mm and 100 mm. One of the most important findings from these studies is that increasing the amount of fiber and the length of the fiber will increase moisture absorption.

3.5. Tensile Strength Is Influenced by Moisture Absorption. The mechanical properties of the AAM fiber-reinforced polyester composites will affect the various consequence such as interphase of the region, interfaces of the fiber/matrix, fiber content or quantity, and directions of the fiber kept in the composite in the reinforcement. The varying fiber quantity and length in the AAM fiber-reinforced composite examined in both the dry and wet conditions are shown in Figure 8. In dry conditions, the tensile strengths of the composites with 10 weight percent and 20 mm, 20 weight percent and 20 mm, and 30 weight percent and 20 mm were 31.5 MPa, 40.2 MPa, and 47.4 MPa, respectively, in both directions. From ten percent to thirty percent, there is a 49.6 the maximum. At dry conditions, the 10 wt.% with 100 mm length of the fiber resulted in 39.7 Mpa tensile strength. Similarly, 20 wt.% with the same length of the composite tensile strength was 43.6 Mpa. The 30 wt.% of the composite with 100 mm length had a tensile strength of 51.5 Mpa. From ten percent to thirty percent, there was a 27.7% increment. At dry conditions, the tensile strength of 10 wt percent and 140 mm length of composite is 47.1 Mpa, that of 20 wt percent and 140 mm length of the composites is 49.9 Mpa, and that of 30 wt percent and 140 mm composites was 57.7 Mpa. From ten percent to thirty percent, there was a 21.0 percent improvement. The higher fiber content and the exact length of the composite in dry conditions had provided increased tensile strength. However, as fiber length and content increased, the percentage of betterment decreased. At wet conditions, the 10wt.% of 20 mm length composite tensile strength was 29.1 Mpa. Similarly, 30 wt.% with 20 mm length of the composite tensile strength was 42.1 Mpa. When compared to plain samples, the reductions were 6.1 percent and 10.7 percent, respectively. In moisture conditions, the tensile strengths of 30 wt.% with 20 mm length fiber, 30 wt.% with 100 mm length fiber, and 30 wt.% with 140 mm length fiber composites samples were tested decreased by 10.7 percent, 14.8 percent, and 22.5 percent, respectively. In wet conditions, the enhancement of the tensile modulus and strength of the tested composite sample continued to increase because the fiber content and length continued to increase. However, in moisture consumed samples, the variation of increment in mechanical properties of all lengths of fibers with different wt.% was less. This could be because the soaking of composites samples in moisture affected the bonding of the fiber-matrix reinforcement, causing the delamination and reduction in the mechanical behavior of the composite materials. In general, it was anticipated that when higher fiber wt.% composites were submerged in water, the tensile behavior composites were

decreased when compared with the dry samples. It is worth noting that the wet tensile strength of 20 wt.% and 20 mm composites samples was almost identical to that of 10 wt.% and 100 mm composites samples (36.3 MPa and 35.7 MPa). The fiber content was higher in 20 wt percent and 20 mm composites samples than in 10 wt percent and 100 mm composites samples, and fiber length was shorter in twenty weight percentage and length of 20 mm specimen composites than in 10 wt percent and 100 mm composites samples. The tensile behavior for the 20 weights% with 100 mm fiber length was 44.6 Mpa. The dry sample composite tensile strength of 30 weight% with 150 mm length fiber was 44.9 Mpa.

This became directly related to the amount of moisture absorbed in 30 weights% with 140 mm length of composites samples. The cellulose fibers swelled when the fiber content interface was exposed to moisture from the atmosphere. As a result of this, shear stress developed at the interface, resulting in fiber delamination, interlaminar, and structural rigidity loss, as shown in Figure 8. Immersion in water thus had an effect on composite strength.

3.6. Impact on Flexural Strength due to Moisture Absorption. The flexural properties seem to be another prominent and frequently analyzed property due to their various applications in composite materials. The flexural properties of AAM polyester composites containing 10–30 weight% fiber content at different fiber lengths are shown in Figure 9. At dry conditions, due to the increased content of fiber and its length, the flexural strength increased. In dry condition, the 10 wt.% with 20 mm length of fiber flexural strength was 50.3 Mpa. Similarly, 30 wt.% with 20 mm fiber length was 63.1 Mpa. The increased percentage difference is 23.91 Mpa when compared to both samples. In dry conditions, the tensile strength of 10 wt.% and 100 mm length of composite sample increased by 22.5% and 10.2% correspondingly, for 10 wt.% with 100 mm length of fiber to 30 wt.% with 100 mm length of composites. In dry conditions, the highest flexural strength achieved 30 wt.% with 100 mm fiber length of the composites. At the wet conditions test, the flexural properties of the composites with 10 wt.%, 20 wt.%, and 30 wt.% with the length of 20 mm had the tensile strength of 47.4 Mpa, 50.1 Mpa, and 55.6 Mpa. When compared to the dry samples, the reduction in percentages was 4.7, 7.6, and 9.3%. At we condition, the flexural behavior of composites of 10 wt.%, 20 wt.%, and 30 wt.% with 100 mm length of fiber had the following flexural properties 51.8 Mpa, 52.5 Mpa, and 61.5 Mpa. The percentage reductions were compared with dry samples that were 7.9%, 11.4%, and 11.8%, respectively. The 10 weight % with 140 mm length of the fiber, 20 wt.% with 140 mm fiber length, and 30 wt.% 140 mm fiber length flexural strength were 52.7 Mpa, 54.4 Mpa, and 60.9 Mpa. When compared to dry samples, the reduction percentages were 11.4%, 17.5%, and 20.7 Percent.

At wet conditions, due to the increased length and quantity of the fiber, the flexural behavior of the composites was increased. However, as higher quantity in the composites and increased length of fiber present in the composite

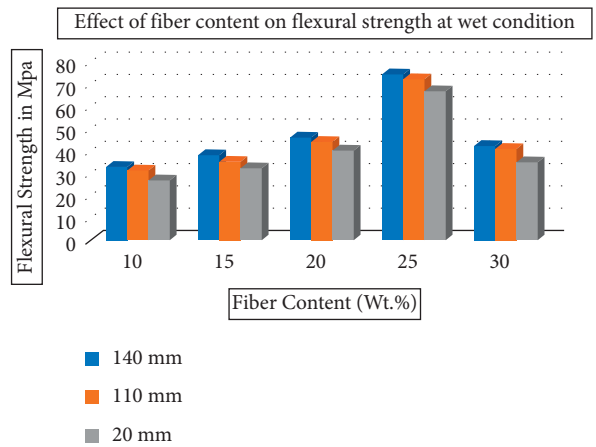

Figure 9: Flexural behavior in dry and wet conditions with varying fiber content.

were reduced, the strength properties increased in the samples [32].

The 10–30 wt.% fiber content with various lengths of the test samples of dry and wet state composites showed a huge expansion in flexural strength. Under dry conditions, the 30 wt.% with 20 mm fiber length composites had increased flexural behavior when compared with 20wt.% with 10 mm fiber length of composites. There were two cases of fiber: one was increased fiber content with the length of fiber being less and another case [33] was the fiber content and length of the fiber also being high. It was noted that the 30 wt.% with 100 mm length of the composites was higher strength when compared with increased length of fiber present in the composites such as 30wt.% and 140 mm fiber length.

The composite reinforcement was dragged to rupture due to the deflection during the bending of the sample test shown in the figure. Due to the low fiber content, the fiber pull-out from the matrix was observed. It was identified that the debonding, delamination, fiber breakage, and matrix failure occurred during the bend testing (Figure 9). Due to expanded moisture content in the composites, the flexural properties decreased incrementally in wet conditions, and the length of fiber content and volume also increased. The poor fiber-matrix interfacial bonding causes a diminished flexural behavior after the absorption of the moisture. The development of the hydrogen bond in the cellulose of fiber and in water molecules resulted in diminished mechanical behavior due to high moisture absorption. The natural fiber observed only the less amount of moisture content when it presents in the more OH group %. The huge accumulation of the moisture in the composites was caused by dimensional variations in the composites, lack of interfacial bonding, and strength between the fiber matrix. Because of the above issues, the mechanical properties were gradually reduced [34]. It was identified that the flexural behavior was equal in many of the weight percentages of the composites with varying lengths. The proportion ratio, humidity, and manufacturing methods of the composites influenced the moisture behavioral characteristics. The volume fraction and all other techniques decided the porosity of the composite.

The importance of the fiber-matrix adhesion on flexural strength was further highlighted in the figure (Figure 9).

4. Conclusions

(i) The new AAM fiber has improved mechanical properties and accessibility over other conventional materials. These conclusions have been reached based on a considerable amount of experimental testing.

(ii) AAM fibers have a higher tensile strength and modulus of elasticity than other natural fibers. In comparison to other fibers, the AAM fiber has a very low density.

(iii) With different fiber volume fractions and fiber lengths, the flexural and tensile behavior of Agave Angustifolia Marginata isophthalic (polyester) composite is significantly improved. Improved fiber content resulted in an increase in the tensile behavior of the composites. The chopped fiber isophthalic polyester reinforcement reaches its improved tensile strength and modulus at a 25% Vf about the 20 mm length of the fiber. Overall, decreased fiber lengths have greater strength and a greater number of fiber ends, which accumulate in the composite.

(iv) To achieve the increased flexural characteristics and modulus of the carved fiber isophthalic polyester composite, which reached 25% Vf for 110 mm and 140 mm fiber lengths, the maximum flexural strength and modulus of the sliced fiber isophthalic polyester composite are obtained at 25% Vf. However, the values have been significantly improved by an increase of 140 mm.

(v) The impact of moisture absorption behavior on the mechanical characteristics of AAM fiber-reinforced hybrid polyester composites was explored in this research, and the outcomes have been linked to composites containing dried fibers.

(vi) Flexural and tensile strength increased as fiber content and length increased in dry conditions. Tensile and flexural strength are greatly reduced when the material is wet. At both dry and wet conditions, the impact strength decreased as the fiber content and length increased.

(vii) The degradation of the fiber-matrix interface caused by moisture exposure resulted in a significant drop in mechanical properties.

(viii) To achieve the positive hybrid effect and develop an optimized material system, it is necessary to understand the moisture absorption characteristics of natural fiber-reinforced hybrid composite materials.

Data Availability

The data used to support the findings of this study are included within the article.

Disclosure

The publication is only for the academic purpose of Addis Ababa Science and Technology University, Ethiopia.

Conflicts of Interest

The authors declare that there are no conflicts of interest regarding the publication of this paper.

References

[1] B. J. Manujesh, M. R. Prajna, M. P. Sham Aan, C. V. Majida, and P. J. Antony, "Flexural characterization of foam cored E-glass reinforced smart materials using artificial neural network," *Materials Today Proceedings*, vol. 5, no. 10, pp. 21305–21313, 2018.

[2] L. Prasad, G. Singh, and M. Pokhriyal, "A comparative study on physical and mechanical behaviour of functionally graded composite materials reinforced with natural fillers," *Materials Today Proceedings*, vol. 5, no. 9, Article ID 16990, 2018.

[3] V. Chaudhary and F. Ahmad, "A review on plant fiber reinforced thermoset polymers for structural and frictional composites," *Polymer Testing*, vol. 91, Article ID 106792, 2020.

[4] K. Viswanath Allamraju, "Study of mechanical behaviour of hybrid jute nano fiber composite," *Materials Today Proceedings*, vol. 5, no. 9, Article ID 20750, 2018.

[5] S. J. Sbai, A. Boukhriss, S. Majid, and S. Gmouh, "Chapter 20 - the Recent Advances in Nanotechnologies for Textile Functionalization," in *Advances in Functional and Protective Textiles*, S. ul-Islam and B. S. Butola, Eds., Woodhead Publishing, Sawston, Cambridge, pp. 531–568, 2020.

[6] M. Mazumder, R. Ahmed, A. Wajahat Ali, and S.-J. Lee, "SEM and ESEM techniques used for analysis of asphalt binder and mixture: a state of the art review," *Construction and Building Materials*, vol. 186, pp. 313–329, 2018.

[7] S. S. Todkar and S. A. Patil, "Review on mechanical properties evaluation of pineapple leaf fibre (PALF) reinforced polymer composites," *Composites Part B: Engineering*, vol. 174, Article ID 106927, 2019.

[8] G. Saravanan, G. B. Bhaskar, E. Kaviyarasan, B. Naveen, S. Prabakaran, and S. Rajesh, "Experimental investigation of mechanical behavior of Bauhinia racemosa - based glass fiber reinforced composite," *Materials Today Proceedings*, vol. 16, pp. 758–765, 2019.

[9] Y. H. Mugahed Amran, R. Alyousef, R. S. M. Rashid, H. Alabduljabbar, and C.-C. Hung, "Properties and applications of FRP in strengthening RC structures: a review," *Structures*, vol. 16, pp. 208–238, 2018.

[10] C. Sowmya, V. Ramesh, and D. Karibasavaraja, "An experimental investigation of new hybrid composite material using hemp and jute fibres and its mechanical properties through finite element method," *Materials Today Proceedings*, vol. 5, no. 5, pp. 13309–13320, 2018.

[11] B. Han, W.-W. Hui, Q.-C. Zhang et al., "A refined quasi-3D zigzag beam theory for free vibration and stability analysis of multilayered composite beams subjected to thermomechanical loading," *Composite Structures*, vol. 204, pp. 620–633, 2018.

[12] R. Parhi, "16 - Nanocomposite for Transdermal Drug Delivery," in *Applications of Nanocomposite Materials in Drug Delivery*, Inamuddin, A. M. Asiri, and A. Mohammad, Eds., Woodhead Publishing, Sawston, Cambridge, pp. 353–389, 2018.

[13] K. Deepak, N. S. Reddy, and T. V. S. Naidu, "Thermosetting polymer and nano clay based natural fiber bio- composites," *Procedia Materials Science*, vol. 10, pp. 626–631, 2015.

[14] B. N. Raju, K. Ramji, and V. S. R. K. Prasad, "Mechanical properties of glass fiber reinforced polyester ZnO Nano-Composites," *Materials Today Proceedings*, vol. 2, no. 4, pp. 2817–2825, 2015.

[15] N. Dubey and G. Agnihotri, "Flexural and impact properties of midrib of coconut palm leaves reinforced polyester," *Materials Today Proceedings*, vol. 4, no. 2, pp. 3422–3430, 2017.

[16] A. Gnanavelbabu, P. Saravanan, K. Rajkumar, P. Sabarinathan, and S. Karthikeyan, "Mechanical strengthening effect by various forms and orientation of glass fibre reinforced isopthalic polyester polymer composite," *Materials Today Proceedings*, vol. 5, no. 13, Article ID 26850, 2018.

[17] V. Puri, P. Chakrabortty, S. Anand, and S. Majumdar, "Bamboo reinforced prefabricated wall panels for low cost housing," *Journal of Building Engineering*, vol. 9, pp. 52–59, 2017.

[18] N. Belayachi, D. Hoxha, and B. Ismail, "Impact of fiber treatment on the fire reaction and thermal degradation of building insulation straw composite," *Energy Procedia*, vol. 139, pp. 544–549, 2017.

[19] K. Sudha Madhuri, H. Raghavender Rao, and B. Chandramohan Reddy, "Experimental investigation on the mechanical properties of Hardwickia Binata fibre reinforced polymer composites," *Materials Today Proceedings*, vol. 5, no. 9, Article ID 19899, 2018.

[20] M. A. Fuqua, S. Huo, and C. A. Ulven, "Natural fiber reinforced composites," *Polymer Reviews*, vol. 52, no. 3, pp. 259–320, 2012.

[21] O. Faruk, A. K. Bledzki, H.-P. Fink, and M. Sain, "Progress report on natural fiber reinforced composites," *Macromolecular Materials and Engineering*, vol. 299, no. 1, pp. 9–26, 2014.

[22] S. V. Joshi, L. T. Drzal, A. K. Mohanty, and S. Arora, "Are natural fiber composites environmentally superior to glass fiber reinforced composites?" *Composites Part A: Applied Science and Manufacturing*, vol. 35, no. 3, pp. 371–376, 2004.

[23] X. Li, L. G. Tabil, and S. Panigrahi, "Chemical treatments of natural fiber for use in natural fiber-reinforced composites: a review," *Journal of Polymers and the Environment*, vol. 15, no. 1, pp. 25–33, 2007.

[24] V. Mohanavel, T. Sathish, M. Ravichandran, K. Arul, and R. Subbiah, "Mechanical properties of waste silk fibre reinforced PLA bio composites manufactured through hand layup method," *Journal of Physics: Conference Series*, vol. 2027, no. 1, Article ID 012016, 2021.

[25] K. Rajkumar, N. Vinoth, R. Santhosh Kumar et al., "Mechanical and water absorption behaviour of palm seed particles based hybrid bio-composites," *Journal of Physics: Conference Series*, vol. 2027, no. 1, Article ID 012006, 2021.

[26] P. J. Herrera-Franco and A. Valadez-González, "A study of the mechanical properties of short natural-fiber reinforced composites," *Composites Part B: Engineering*, vol. 36, no. 8, pp. 597–608, 2005.

[27] M. J. John and R. D. Anandjiwala, "Recent developments in chemical modification and characterization of natural fiber-reinforced composites," *Polymer Composites*, vol. 29, no. 2, pp. 187–207, 2008.

[28] V. Mohanavel, T. Sathish, M. Ravichandran, P. Ganeshan, M. M. Ravi Kumar, and R. Subbiah, "Experimental investigations on mechanical properties of cotton/hemp fiber reinforced epoxy resin hybrid composites," *Journal of Physics: Conference Series*, vol. 2027, no. 1, Article ID 012015, 2021.

[29] R. Subbiah, B. K. Kumar, T. Sathish et al., "Wear properties of waste silk fibre reinforced PLA bio composites using taguchi technique," *Journal of Physics: Conference Series*, vol. 2027, no. 1, Article ID 012012, 2021.

[30] A. Valadez-Gonzalez, J. M. Cervantes-Uc, R. Olayo, and P. J. Herrera-Franco, "Effect of fiber surface treatment on the fiber-matrix bond strength of natural fiber reinforced composites," *Composites Part B: Engineering*, vol. 30, no. 3, pp. 309–320, 1999.

[31] L. Kerni, S. Singh, A. Patnaik, and N. Kumar, "A review on natural fiber reinforced composites," *Materials Today Proceedings*, vol. 28, pp. 1616–1621, 2020.

[32] B. Biswas, N. R. Bandyopadhyay, and A. Sinha, "Mechanical and dynamic mechanical properties of unsaturated polyester resin-based composites," in *Unsaturated Polyester Resins*, pp. 407–434, Elsevier, Chennai, Tamilnadu, 2019.

[33] V. Mohanavel, T. Raja, A. Yadav, M. Ravichandran, and J. Winczek, "Evaluation of mechanical and thermal properties of jute and ramie reinforced epoxy-based hybrid composites," *Journal of Natural Fibers*, vol. 1, pp. 1–11, 2021.

[34] C. A. Chairman, M. Ravichandran, V. Mohanavel et al., "Mechanical and abrasive wear performance of titanium dioxide filled woven glass fibre reinforced polymer composites by using taguchi and EDAS approach," *Materials*, vol. 14, no. 18, Article ID 5257, 2021.

[35] R. R Niranjan, S. J Kokan, R. S Narayanan, and R Sridhar, "Fabrication and testing of abaca fibre reinforced epoxy composites for automotive applications," *Advanced Materials Research*, Trans Tech Publications Ltd, vol. 718, 2013.

[36] G. Kalusuraman, I Siva, J. T. W Jappes, G Xiao-Zhi, and S. C Amico, "Fibre loading effects on dynamic mechanical properties of compression moulded luffa fibre polyester composites," *International Journal of Computer Aided Engineering and Technology*, vol. 10, pp. 157–165, 2018.

[37] K. N. Keya, fnm au, N. A. Kona et al., "Natural fiber reinforced polymer composites: history, types, advantages, and applications," *Materials Engineering Research*, vol. 1, no. 2, pp. 69–87, 2019.

[38] F. Sarasini and V. Fiore, "A systematic literature review on less common natural fibres and their biocomposites," *Journal of Cleaner Production*, vol. 195, pp. 240–267, 2018.

[39] A. V. Oskouei, M. Bazli, H. Ashrafi, and M. Imani, "Flexural and web crippling properties of GFRP pultruded profiles subjected to wetting and drying cycles in different sea water conditions," *Polymer Testing*, vol. 69, pp. 417–430, 2018.

[40] A. Dhanola, A. S. Bisht, A. Kumar, and A. Kumar, "Influence of natural fillers on physico-mechanical properties of luffa cylindrica/polyester composites," *Materials Today Proceedings*, vol. 5, no. 9, pp. 17021–17029, 2018.

[41] T. Ramakrishnan, R. S. Kumar, S. Balasubramani, R. Jeyakumar, S. J. S. Chelladurai, and R. Ramamoorthi, "Experimental investigation of the effect of various chemical treatments on Agave angustifolia Marginata fibre," in *Green Materials and Advanced Manufacturing Technology*, pp. 173–190, CRC Press, FA, USA, 2020.

[42] R. S. Kumar, T. Ramakrishnan, and S. Balasubramani, "Multiobjective optimization of BSL 165 aluminium composite for aeronautical applications," in *Green Materials and Advanced Manufacturing Technology*, pp. 217–236, CRC Press, FA, USA, 2020.

[43] S. Balasubramani, N. Balaji, T. Ramakrishnan, R. Sureshkumar, S. J. S. Chelladurai, and S. J. S Chelladurai,

"Defect identification in casting surface using image processing techniques," in *Green Materials and Advanced Manufacturing Technology*, pp. 191–198, CRC Press, FA, USA, 2020.

[44] S. Ganeshkumar, V. Thirunavukkarasu, R. Sureshkumar, S. Venkatesh, and T. Ramakrishnan, "Investigation of wear behaviour of silicon carbide tool inserts and titanium nitride coated tool inserts in machining of EN8 steel," *International Journal of Mechanical Engineering & Technology*, vol. 10, no. 1, pp. 1862–1873, 2019.

[45] T. Ramakrishnan and S. Pavayee Subramani, "Investigation of physico-mechanical and moisture absorption characteristics of raw and alkali treated new Agave angustifolia Marginata (AAM) fiber," *Materials Science*, vol. 24, no. 1, pp. 53–58, 2018.

[46] T. Ramakrishnan and P. S. Sampath, "Dry sliding wear characteristics of new short Agave angustifolia Marginata (AAM) fiber-reinforced polymer matrix composite material," *Journal of Biobased Materials and Bioenergy*, vol. 11, no. 5, pp. 391–399, 2017.

[47] R. Jeyakumar, P. S. Sampath, R. Ramamoorthi, and T. Ramakrishnan, "Structural, morphological and mechanical behaviour of glass fibre reinforced epoxy nanoclay composites," *International Journal of Advanced Manufacturing Technology*, vol. 93, no. 1-4, pp. 527–535, 2017.

[48] T. Ramakrishnan and P. S. Sampath, "Experimental investigation of mechanical properties of untreated new Agave Angustifolia Marginata fiber reinforced epoxy polymer matrix composite material," *Journal of Advances in Chemistry*, vol. 13, no. 4, pp. 6120–6126, 2017.

[49] R. Ramamoorthi, R. Jeyakumar, and T. Ramakrishnan, "Effect of nanoparticles on the improvement of mechanical properties of epoxy based fiber – reinforced composites - a review," *International Journal for Science and Advance Research in Technology*, vol. 3, no. 11, pp. 1251–1256, 2017.

[50] T. Ramakrishnan, P. S. Sampath, and R. Ramamoorthi, "Investigation of mechanical properties and morphological study of the alkali treated Agave angustifolia Marginata fiber reinforced epoxy polymer composites," *Asian Journal of Research in Social Sciences and Humanities*, vol. 6, no. 9, pp. 461–472, 2016.

[51] T. Ramakrishnan and P. S. Sampath, "Thermogravimetric analysis (TGA) and the effect of moisture absorption on the mechanical properties of new Agave angustifolia Marginata fiber (AAMF) reinforced epoxy polymer composite material," *International Journal of Printing, Packaging & Allied Sciences*, vol. 4, no. 5, pp. 3245–3256, 2016.

[52] T. Ramakrishnan, K. Sathish, P. S. Sampath, and S. Anandkumar, "Experimental investigation and optimization of surface roughness of AISI 52100 alloy steel material by using Taguchi method," *Advances in Natural and Applied Sciences*, vol. 10, no. 6, pp. 130–138, 2016.

[53] S. Gnanasekaran, S. J. S Chelladurai, T Ramakrishnan et al., "Optimizing the characteristics of the laser hardfacing process parameters to maximize the wear resistance of Ni-based hardfaced deposits using the RSM technique," *Advances in Materials Science and Engineering*, vol. 2021, Article ID 3665631, 15 pages, 2021.

Hindawi
Advances in Materials Science and Engineering
Volume 2022, Article ID 9222003, 10 pages
https://doi.org/10.1155/2022/9222003

Research Article

The Wound Healing Effect of Nanoclay, Collagen, and Tadalafil in Diabetic Rats: An *In Vivo* Study

Allahyar Noori Ordeghan,[1] Danial Khayatan,[2] Mohammad Reza Saki,[1] Mostafa Alam,[3] Kamyar Abbasi,[4] Hossein Shirvani,[1] Mohsen Yazdanian,[5,6] Reza Sayyad Soufdoost,[7] Haidar Taimouri Raad,[5,6] Ali Karami,[5,6] and Hamid Tebyaniyan[8]

[1]*Exercise Physiology Research Center, Life Style Institute, Baqiyatallah University of Medical Sciences, Tehran, Iran*
[2]*Faculty of Pharmacy, Tehran Medical Sciences, Islamic Azad University, Tehran, Iran*
[3]*Department of Oral and Maxillofacial Surgery, School of Dentistry, Shahid Beheshti University of Medical Sciences, Tehran, Iran*
[4]*Department of Prosthodontics, School of Dentistry, Shahid Beheshti University of Medical Sciences, Tehran, Iran*
[5]*Research Center for Prevention of Oral and Dental Diseases, Baqiyatallah University of Medical Sciences, Tehran, Iran*
[6]*School of Dentistry, Baqiyatallah University of Medical Sciences, Tehran, Iran*
[7]*Imam Khomeini Clinic of Dentistry, Tehran, Iran*
[8]*Islamic Azad University, Science and Research Branch, Tehran, Iran*

Correspondence should be addressed to Mohsen Yazdanian; myazdaniandr@gmail.com and Hamid Tebyaniyan; tebyan.hamid@yahoo.com

Received 23 September 2021; Revised 21 November 2021; Accepted 2 January 2022; Published 15 January 2022

Academic Editor: Ravichandran M

The diabetic wound is the most challenging one to manage, which is associated with microvascular and macrovascular dysfunction, and novel strategies such as using hydrogels demonstrate their promising prospect in treatment and management approaches of the diabetic wound. This study aimed to investigate the effect of collagen/nanoclay/tadalafil hydrogel on wound healing in diabetic rats under HIIT exercise. Hydrogel was synthesized, and then biocompatibility and antibacterial tests were performed. The therapeutic effect of collagen/nanoclay/tadalafil hydrogel was assessed after induction of diabetes in the rat model, and wound healing was evaluated with macroscopic and microscopic tests. The result of the MTT test showed no significant cytotoxicity of collagen/nanoclay/tadalafil hydrogel. Furthermore, the inhibitory effect of hydrogel was detected on *E. coli* and *S. aureus*. The macroscopic results demonstrated that the wound contraction was considerable in the hydrogel/HIIT exercise and hydrogel groups compared with the HIIT exercise and control groups during 21 days. The microscopic results showed that the presence of fibroblasts, the amount of collagen, the epidermis density, and the formation of hair follicles were increased in the hydrogel/HIIT exercise group compared with other groups in the diabetic rate model. It can be concluded that collagen/nanoclay/tadalafil hydrogel with HIIT exercise could accelerate diabetic wound healing and can be an appropriate candidate for skin regeneration in medical applications.

1. Introduction

Diabetes has also known as a comprehensive metabolic disorder that impacts about 340 million people worldwide. Also, diabetic wounds have been developed in approximately 20% of people with diabetes. Hyperglycemia causes the most microvascular and macrovascular dysfunctions that entangle the process of wound healing. One of the common wound types is a diabetic foot ulcer that is widespread among all age groups and is more common in individuals more than 65 years with an incidence of about 3% and a prevalence of near 1% of the world population. About 2.5 to 15 percent of the world's annual health expenditure is spent on diabetes, and diabetic ulcers account for a large proportion of it. The World Health Organization reports that diabetes will be the 7th leading cause of death in

2030 [1, 2]. Diabetic wound treatments involved pressure off-loading, debridement of wound, infection management with topical antiseptics and topical antibiotics, and revascularization, which are the main principles of diabetic wound therapeutic approaches. There are various approaches to debridement such as surgical procedures, wet to dry dressing, biosurgery, preparations of enzymes, hydrogels, and dextranomer polysaccharide paste or polysaccharide beads. When wound dressings change the wound from moist to dry, they supply nonselective debridement, thus cleaning the wound with necrotic tissue removal. It is suggested that wounds be evaluated at every dressing change. Moisture-retentive dressings involving foams, hydrocolloids, hydrogels, films, hydrofibers, and alginates are helpful in different clinical settings [3].

HIIT (High-Intensity Interval Training) is based on the principle of exercise intensity that is a more sufficient modifier constituent of exercise causing adjustment in the human body system containing nervous [4], cardiovascular [5], and skeletal muscle [6] system. HIIT has been known as a time-efficient exercise method that is well described as short durations of high-intensity exercise (more than 80–85% peak oxygen uptake), alternating with active or passive rest periods [7]. Recently, HIIT has received great consideration for its impact on improving superior vascular function improvements compared to continuous training with moderate intensity in healthy people and several clinical patients containing metabolic syndrome, heart failure, and obesity [8]. Despite HIIT improvement effects on vascular function in a patient with systemic limited cutaneous sclerosis [9], its special effects on skin remain untested. New therapeutic approaches such as extracellular matrix proteins, bioengineered skin substitutes, negative pressure wound therapy, and growth factors have been indicated as adjunctive treatments for wounds [10]. Different biomaterials are also used in clinical wound therapy. For example, oxidized regenerated collagen/cellulose was primarily indicated to facilitate wound closure in a diabetic model in mice and acute wounds in rats. Different biomaterials are being produced in the regeneration of tissue to emerge as scaffolds where the cells are implanted or as vehicles for specified drug release. These scaffolds illustrate the source of tissue topology and provide cues that are topological and promote tissue regeneration. Many synthetic or natural polymers, also named hydrogels, are being progressed and investigated in preclinical researches. Biodegradable films are made of hydrogels or hydrocolloids and thus, by regeneration, can be integrated into the wound of patients [11]. One of the phosphodiesterase type 5 (PDE5) inhibitors is tadalafil which reduces cGMP (cyclic guanosine monophosphate) destruction and afterward increases the NO (nitric oxide) vasodilation effect. Usually, tadalafil has been utilized for controlling pulmonary arterial hypertension and erectile dysfunction through inhibition of NO collapse-driven cGMP in platelets aggregation and vascular smooth muscle, which impact vasodilation of peripheral blood vessels. Tadalafil also can preserve tissues, for instance, lung, skin, and brain against ischemia [12]. Furthermore, some animal studies have demonstrated that PDE5 inhibitors promote wound healing [13]. Inhibitors of PDE5 also upregulate iNOS (inducible nitric oxide synthase) by the pathway of NO-cGMP and develop the wound and fractures healing procedure [14]. Till now, there is no reported side effect in animal models when tadalafil is used in the wound healing process. Nanocomposite hydrogels of nanoclay would be provided easily and conveniently and demonstrated mechanical properties, biocompatibility, good swelling properties, and optical properties. Also, findings demonstrated that hydrogels composed with nanoclay could promote the connection of dermal fibroblasts of human on the surface of the hydrogels [15, 16]. Collagen is responsible for supporting the integrity of the cells and tissue structures that are the most protein and exist naturally. Skin collagen has been synthesized by myofibroblasts and fibroblasts that are arranged in the fibril forms of cutaneous tissue, bone, and tendons, which consistently undergo tensile and shear stresses. Type I collagen is found in the tendons, fasciae, and dermis and is the most important component in scar tissue. Collagen is also utilized in synthesizing skin substitutes that are also present in beaded structures, fibril surfaces, or transmembrane proteins composition [17]. Despite the fact that collagen, nanoclay, and tadalafil have been investigated individually in wound healing experimental studies, no evaluation exists to evaluate the effect of collagen/nanoclay/tadalafil combination on wound healing *in vivo*. This study aimed to assess the effect of collagen/nanoclay/tadalafil hydrogel on complete wound healing in type I diabetic rats under HIIT exercise.

2. Materials and Methods

2.1. Materials. Hydrochloric acid and tadalafil were purchased from Sigma-Aldrich (Germany). The solvents, chloroform, and methanol were obtained from Sigma-Aldrich (USA) and Carlo Erba (Italy). Collagen type I was obtained from Medzist and TAB Nano (Iran). The nanoclay was purchased from Southern Clay Products, Inc. *Staphylococcus aureus* (ATCC 25923) and *Escherichia coli* (ATCC 25922) strains and human embryonic kidney cells (HEK293) were gifted. MTT Kit was purchased from Bio Idea (Iran). DMSO (dimethyl sulfoxide) was purchased from Sigma-Aldrich (Germany). FBS (fetal bovine serum), DMEM (Dulbecco's modified Eagle's medium), PBS (phosphate-buffered saline), trypsin, ascorbic acid 3-phosphate, alkaline phosphatase kit, dexamethasone, beta-glycerol, and antistreptomycin were obtained from Gibco.

2.2. Synthesis of Hydrogel. To acquire collagen/nanoclay/tadalafil hydrogel, 10% w/v collagen solution was provided in 1% v/v acid acetic solution (pH = 2) and stirred well (40 rpm, 4°C, 24 hours). Then, pH was adjusted to 7 (by adding 0.5 M of NaOH under stirring for neutralizing the hydrogel). After preparation of the solution, tadalafil powder (30 mg/ml) was added to the solution of collagen while stirring (4°C, 2 hours). The obtained nanoclay (170 mg/ml) was centrifuged, washed (three times with DW and

lyophilized), and added progressively to the solution. The acquired homogeneous suspension was kept at 4°C.

2.3. Cell Culture. HEK293 were cultured in DMEM involving 10% FBS, streptomycin sulfate (10 mg/ml), and penicillin G sodium (10 units/ml) in a humidified incubator (5% CO_2, 90% humidity, 37°C). The culture medium was refreshed every 48 hours to achieve the confluence of 80%. The second passage of cells was utilized for the next step.

2.4. Biocompatibility Test. The MTT (methyl thiazolyl tetrazolium) test was performed straightforwardly according to the ISO 10993-5 standards. The cell culture plate serves as the negative control (without cytotoxicity). MTT assay was conducted to investigate the hydrogel cytotoxicity. For the aim, 20,000 HEK 293 cells were added to the culture medium (50 μL), including serum, and then cultured on the hydrogel. After 3 hours, the culture medium was added to each well. The culture medium was removed, and then, MTT solution (100 μL, 0.5 mg/mL) was added to each well. The supernatant solution was eliminated after 4 hours. Afterward, DMSO (100 μl) was added to dissolve the formed purple formazan crystals. The solution optical density was read at 570 nanometers wavelength in an ELISA reader (Convergent EL-Reader 96X). Outcomes were displayed as a percentage (100% = control value), and the assays were conducted in triplicate to obtain accurate results. The viability of cell was measured using the following equation:

$$\text{cell viability } (\%) = \frac{\text{value of therapy sample}}{\text{value of ample control}} \times 100. \quad (1)$$

2.5. Antibacterial Analysis. Staphylococcus aureus (Gram-positive bacteria) and *Escherichia coli* (Gram-negative bacteria) were utilized to evaluate the antibacterial activity of the collagen/nanoclay/tadalafil hydrogel. LB agar (Luria–Bertani agar) and LB broth (Luria–Bertani broth) were conducted as nutrient sources for the cell culture medium. *Staphylococcus aureus* and *Escherichia coli* were added to the LB broth and incubated in a shaking incubator (24 hours, 5% CO_2, 37°C). The bacteria concentration in the culture medium was 10^6 CFU mL^{-1} (colony-forming units per milliliter). The hydrogel was incubated in LB broth (24 hours, 37°C). Afterward, the viable bacteria number was calculated to investigate the antibacterial activity. Also, the inhibition zone was evaluated, and ciprofloxacin was performed as the standard antibiotic disc (control).

2.6. In Vivo Wound Healing in Diabetic Rats. To investigate the ability of collagen/nanoclay/tadalafil hydrogel in full-thickness wound healing, 36 adults male rats (white Wistar rats, 165 ± 15, aged 6–8 weeks) were utilized. Also, rats were bought from Animal Research. Furthermore, rats were divided into 4 groups ($n = 3$ for each time (7, 14, and 21 days)), control and test groups (hydrogel, hydrogel with HIIT exercise, and only HIIT exercise) accidentally. The rats were housed in wire-topped cages with sterile rice husk as bed material and kept at standard conditions (22–25°C, 65–75% humidity, 12 hours of light/dark cycles, fed with pellets and water ad libitum). All animal tests were examined based on the guidelines correlated with the Care and Use of Laboratory Animals. For induction of experimental type I diabetes in overnight fasted rats, single intraperitoneal injections of STZ (streptozotocin) and nicotinamide were used. First, nicotinamide was dissolved in sterile water and injected (110 mg/kg). After 15 minutes, STZ, dissolved in cold citrate buffer (pH = 4.5, 0.1 M), was injected (50 mg/kg). After 72 hours, diabetes was confirmed by measuring glucose of the tail vein blood using a glucometer (Bayer Contour TS Blood Glucose Monitor). After three weeks, rats with blood glucose levels >250 mg/dL were examined as diabetic and used for the *in vivo* studies [18].

2.7. Wound Model. Anesthesia is induced by IM (intramuscular) injection of ketamine (50 mg/kg, ketamine 10%) and xylazine (10 mg/kg, 2%). Dorsal skin was shaved and then sanitized using ethanol. Afterward, incisions (8 mm) were created by the circular punch. All diabetic rats were tested in four groups: Group 1: control (untreated), Group 2: HIIT exercise, Group 3: hydrogel, and Group 4: hydrogel/HIIT exercise during 21 days.

2.8. High-Intensity Interval Training Program. HIIT program was considered as three times a week on a treadmill [19]. To summarize, the program of HIIT contained a warm-up (5 minutes) and cooling section (a 40% double-speed), and the major part comprised one-minute intense running (5–7 sessions, at 80–90% of the maximum intensity of running speed test) and in rest rotations with 55% with zero slopes of the treadmill. The HIIT program details are presented in Table 1. The MERT is utilized in the first week before the beginning of the training protocol and at the end of the three-week program for finding out the maximum training intensity and capacity [20].

2.9. Macroscopic Evaluation. For measuring the contraction of the wound, the images were taken from wounds on days 7, 14, and 21. The average wound area was measured using ImageJ software (NIH, Maryland), and the percentage of wound contraction was calculated using the following method:

Table 1: High-intensity interval training protocol.

	Warm-up	Main seasons		Cold own	Total time (min)
		Intense periods	Rest		
Week 1		5 × 1 min (80% MERT)	5 × 1 min (55% MERT)		20
Week 2	5 min (40% MERT)	6 × 1 min (80% MERT)	6 × 1 min (55% MERT)	5 min (40% MERT)	22
Week 3		7 × 1 min (80% MERT)	7 × 1 min (55% MERT)		24

MERT: maximum running sprint test; min: minute.

$$\text{wound contraction } (\%) = \frac{\text{initial wound size} - \text{specific day wound size}}{\text{initial wound size}} \times 100. \quad (2)$$

2.10. Microscopic Evaluation. Tissue sampling was analyzed on days 7, 14, and 21 for each group. The thick part of the skin around the wound was dissected, disinfected with normal saline solution, placed in formalin solution (10%, 24 h), and fixed in paraffin using a tissue processor. The tissue sections (5 μm) were sliced to the wound surface perpendicularly, embedded on a slide, and stained with Hematoxylin and Eosin (H&E) and Trichrome-Masson reagents for histopathological studies. The wound healing of samples was investigated by a light microscope (Leica Microsystems, Wetzlar, Germany).

2.11. Statistical Analysis. Data were analyzed using SPSS (Kruskal–Wallis (nonparametric)), and Mann–Whitney test was used for comparing the groups. The p value was considered statistically significant ($p < 0.05$).

3. Results

3.1. In Vitro Biocompatibility of the Hydrogels. Biocompatibility was studied by culturing HEK 293 cells on hydrogels and control (tissue culture plate) for 24, 48, and 72 h. The developed hydrogel with collagen/nanoclay/tadalafil was prepared and investigated for wound healing in diabetic wounds with and without HIIT exercise. The MTT test showed no significant cytotoxicity, and the percentage of cell viability was more than 90% for 24, 48, and 72 h (Figure 1).

3.2. Antibacterial Analysis. The antibacterial activity of the collagen/nanoclay/tadalafil hydrogel was investigated by two bacterial species, *Staphylococcus aureus* (Gram-positive bacteria) and *Escherichia coli* (Gram-negative bacteria). The quantitative results of antibacterial activity showed that CFU (colony-forming unit) of *S. aureus* was 140×10^6 and CFU of E. *coli* was 95×10^6 in the collagen/nanoclay/tadalafil hydrogel, while the CFU of S. *aureus* and E. *coli* was 260×10^6 and 240×10^6 in the control group, individually. However, the number of bacteria was reduced in the collagen/nanoclay/tadalafil hydrogel. Therefore, this result revealed that the hydrogel might conduct an antibacterial effect on the healing process of the wound. Also, the size of hydrogels inhibition zones was estimated against *E. coli* and *S. aureus* as the principal species for infections of the wound as demonstrated in Table 2; ciprofloxacin standard disc was selected as the control group in comparison with the collagen/nanoclay/tadalafil hydrogel inhibitory action. Both *E. coli* and *S. aureus* were susceptible to the ciprofloxacin discs (the control group). The collagen/nanoclay/tadalafil hydrogel displayed an inhibition zone in comparison with the standard antibiotic disc because of the presence of nanoclay in the hydrogel.

3.3. Macroscopic Evaluation. Results of macroscopic evaluation showed significant changes in the percentage of wound healing of the HIIT exercise, hydrogel, and hydrogel/HIIT exercise groups compared with the control group in 14 and 21 days (Figure 2). The contraction rate of the wound in the hydrogel and hydrogel/HIIT exercise groups was more than that in the control group. Also, the percentage of wound contraction rate was remarkably increased in the hydrogel/HIIT exercise group, although the rate of wound contraction was enhanced in each group during 21 days. The healing rate of hydrogel was more than that of the HIIT exercise group, and the healing rate of hydrogel/HIIT exercise was more than that of the control group (Figure 3). These findings indicated the ability of hydrogel and HIIT exercise in the regeneration of diabetic wounds. The evaluation of diabetic wound healing rate was measured by ImageJ in this study. The results displayed that diabetic wound healing rate in 21 days of study with a hydrogel which is loaded with collagen has changed significantly (Table 3). The wound contraction rate in the hydrogel/HIIT exercise group was more than that in the HIIT exercise and hydrogel groups on days 14 and 21, respectively. Moreover, the contraction rate of the hydrogel group was much higher than that of the HIIT exercise and control groups. The results showed that hydrogel could heal diabetic wounds with HIIT exercise.

3.4. Microscopic Evaluation. Histopathological samples were used in microscopic analyses that estimate the wound healing in the granulation tissues collected during 21 days. Tissue sections were stained with H&E and Masson's trichrome stain. Early stages of cellular activities and wound healing through H&E staining were observed (Figures 4 and 5). Deposition and formation of collagen were evaluated using Masson's trichrome staining qualitatively (Figures 6 and 7). In the control group, the microscopic evaluation showed no substantial changes in the rate of wound healing

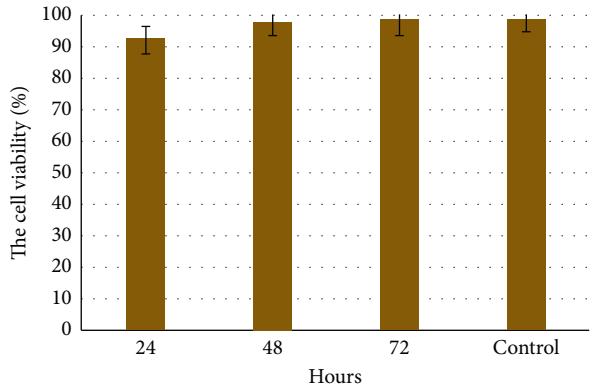

Figure 1: The cell viability study of the collagen/nanoclay/tadalafil hydrogel on HEK 293 cells for 24, 48, and 72 h three independent tests was conducted ($p < 0.05$).

Table 2: The antibacterial activity of collagen/nanoclay/tadalafil hydrogel against *E. coli* and *S. aureus*.

Samples	Inhibition zone	
	Staphylococcus aureus	*Escherichia coli*
Collagen/nanoclay/tadalafil hydrogel	10.2	14.5
Ciprofloxacin disc	26.7	27.3

All samples were tested three times in independent experiments ($p < 0.05$).

Figure 2: Macroscopic evaluation of the control, HIIT exercise, hydrogel, and hydrogel/HIIT exercise groups on days 7, 14, and 21.

from margin to the center on day 7, the defect was covered by a very thin layer of connective tissue, and the wound healing was higher on day 14 compared to day 7. Wound healing from the margin to the center of the defect was detected with H&E and Masson's trichrome staining. On day 21, the rate of healing and infiltration of cells into the center of the defect as well as the thickness of the three layers was significant compared to day 14 (Figures 4(a) and 6(a)).

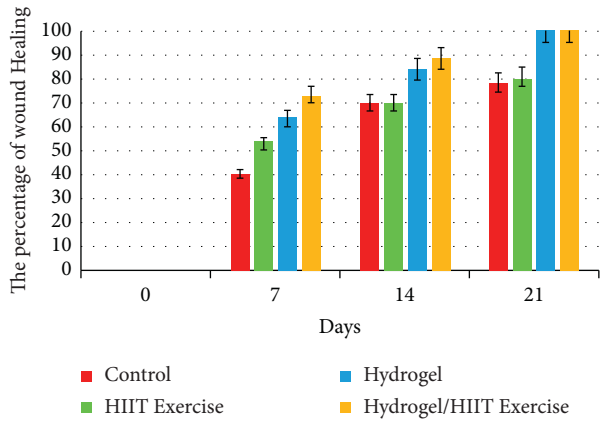

Figure 3: The rate of wound contraction in the control, HIIT exercise, hydrogel, and hydrogel/HIIT exercise groups on days 7, 14, and 21.

Table 3: The wound contraction rate (millimeter) in 0, 7, 14, and 21 days.

Groups	Day 0	Day 7	Day 14	Day 21
Control	8	4.77	2.44	1.7
HIIT exercise	8	3.76	2.4	1.55
Hydrogel	8	2.9	1.3	0
Hydrogel/HIIT exercise	8	2.11	0.9	0

All samples were tested three times in independent experiments ($p < 0.05$).

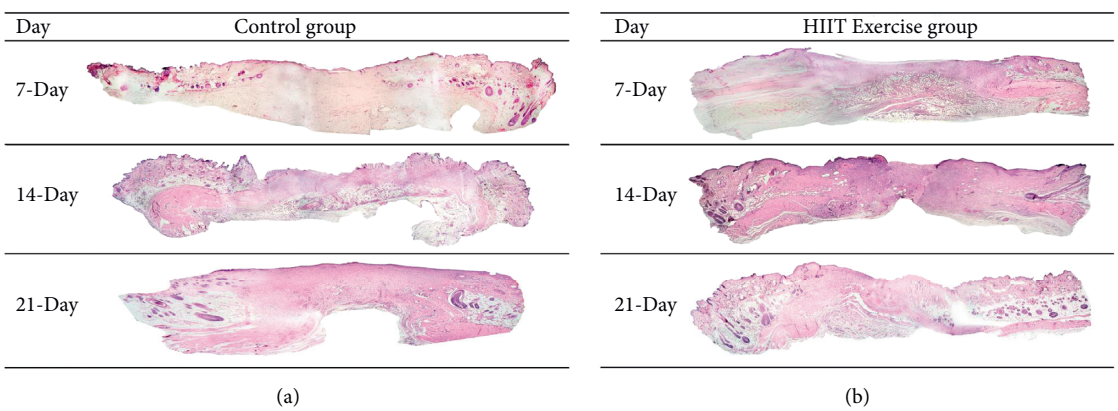

Figure 4: Histological analysis of control (a: ×40) and HIIT exercise (b: ×40) with H&E staining.

In the HIIT exercise group, cell infiltration was observed in the center of the defect on day 7, and a small amount of healing and high density of connective tissue layer was detected. On day 14, the formation of skin layers, the rate of healing, and infiltration of cells were observed, and wound healing was increased compared with day 7. The amount of healing and formation of three layers of skin was determined on day 21. The formation of a relatively regular layer of collagen and the presence of hair follicles were observed (Figures 4(b) and 6(b)).

In the hydrogel group, there was no healing from margin to center during 7 days, but infiltration of cells into the center area of defect and forming of connective tissue were detected. The amount of regeneration and infiltration of cells from to the center of the defect was observed on day 14, and the formation of an irregular layer of collagen and hair follicles was observed in the margin of the defect. The amount of healing and infiltration of cells from the margin to the center of the defect was observed on day 14, and the formation of an irregular layer of collagen and hair follicles was detected in the margin of the defect. On day 21, this amount of three-layer healing and the presence of hair follicles were remarkable in the defect site. In addition, regular collagen was observed in the margin and defect site, and this amount of healing from the margin to the center was significant compared to days 7 and 14 (Figures 5(a) and 7(a)).

In the hydrogel/HIIT exercise group, the rate of connective tissue formation was very high in the defect site, and the infiltration of cells and wound healing was relatively

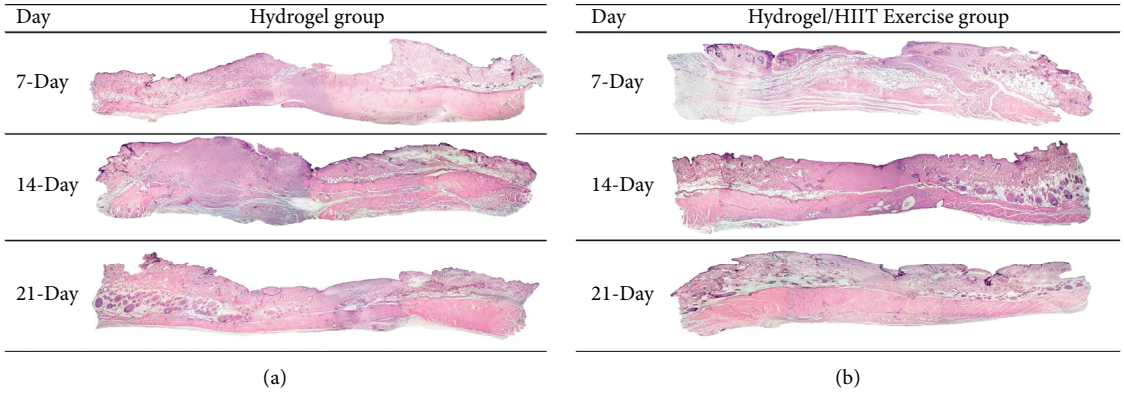

Figure 5: Histological analysis of hydrogel (a: ×40) and hydrogel/HIIT exercise (b: ×40) with H&E staining.

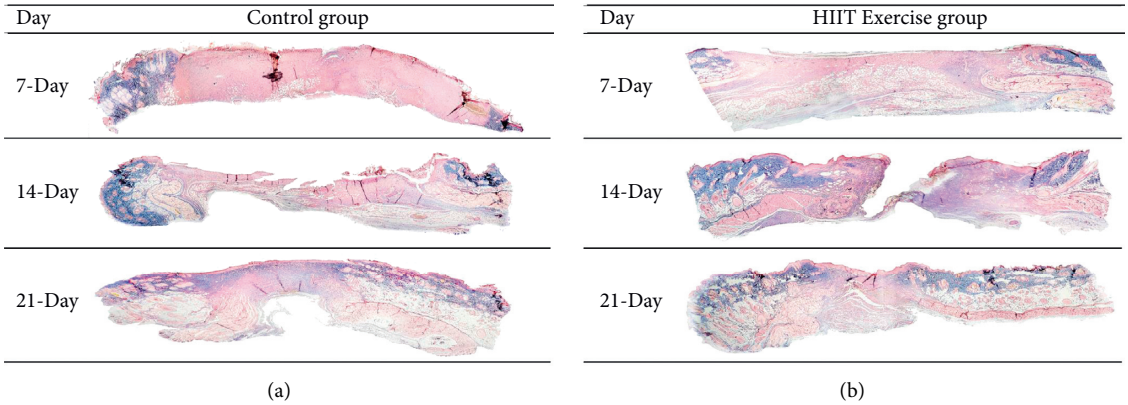

Figure 6: Histological analysis of control (a: ×40) and HIIT exercise (b: ×40) with Masson's trichrome staining.

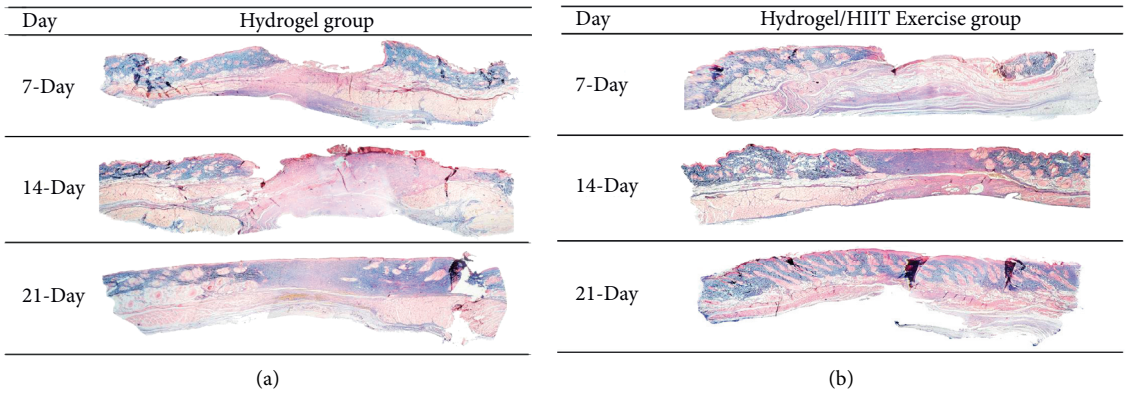

Figure 7: Histological analysis of hydrogel (a: ×40) and hydrogel/HIIT exercise (b: ×40) with Masson's trichrome staining.

considerable from margin to the center during 7 days. Furthermore, the formation of collagen substrate for wound healing was better than other treatment groups. On day 14, the rate of healing and formation of three layers were slightly suitable, and the infiltration of cells and the formation of the hypodermis were observed from the margin to the center. In addition, the formation of hair follicles and remarkable healing were detected in the margin and center of the defect, respectively. Irregular collagen substrate was considerable in the margin of the defect, and the cell infiltration and suitable healing were increased. On day 21, the rate of healing and formation of hair follicles was considerably increased in the defect site. The formation of regular collagen clusters was observed in Masson's trichrome staining, and the hydrogel/HIIT exercise group showed better results compared to other groups in diabetic wound healing (Figures 5(b) and 7(b)).

4. Discussion

Diabetes is one of the important factors for the dysfunction of epidermal cells, fibroblasts, tissue maturation, and failed angiogenesis, which causes delayed wound healing processes. Also, diabetes is responsible for reepithelialization and wound contraction during the process of wound healing. Hydrogel wound dressings are highly regarded due to their appropriate moisturization feature for supporting cellular activities in the wound zone during the healing process. Furthermore, they provide enough flexibility, facilitate the proliferation of cells and biodegradation, and accelerate wound contraction, attachment, reepithelialization, and neovascularization. Hydrogel dressings composed of the bioactive molecule would have a significant influence on expediting the healing of the diabetic wound [18]. Collagen is also used as a therapeutic component for correcting diabetic wounds irregularities. Collagen has been known as the most significant extracellular matrix component that is essential for wound closure. Synthesis of collagen fibers, deposition, restoration, and maturation are vital phases among regeneration and repairment of tissue. Collagen synthesis is principally based on proline availability. Actively, proline is synthesized from glutamic acid in the granulation tissues, and the amount of proline synthesized by lactate increases [18]. Goldsmith et al. showed that oral administration of tadalafil once daily can be effective in the acceleration of reepithelialization and decreasing scarring in a partial thickness of animal burns model [14]. García-Villén et al. demonstrated that hydrogel of nanoclays has improved biocompatibility. Also, the hydrogel can support the motility of fibroblasts and attenuate wound healing in an *in vitro* study and clarify new promising prospects in novel therapeutic formulations [21]. Moreover, Soufdoost et al. reported a novel tadalafil/polycaprolactone as a novel suture that ameliorated the wound healing process by releasing the tadalafil around the sutured wound [22]. Effect of HIIT exercise in combination with resistance training on health of vessels in a one-year follow-up study of Magalhaes et al. in patients with diabetes mellitus type II has demonstrated that HIIT might be a candidate as a key method in long-term improvement of vascular complications in type II of diabetes mellitus [23].

In this study, the developed hydrogel with collagen/nanoclay/tadalafil was prepared and investigated for wound healing in diabetic wounds with and without HIIT exercise. *In vitro* biocompatibility studies were performed by culturing HEK 293 cells on collagen/nanoclay/tadalafil hydrogel and the control (tissue culture plate) for 24, 48, and 72 h. Collagen/nanoclay/tadalafil hydrogel did not exhibit any significant cytotoxicity in comparison with control. Findings revealed that the cells cultured on the collagen/nanoclay/tadalafil hydrogel are viable and multiplying at a rate comparable to those on the control.

The antibacterial effects of skin dressing play a vital role in eliminating bacterial infections, which have been known as a major result of the wound healing postponement [24]. Mojtaba et al. used the nanoclay and chitosan to prepare an active nanocomposite according to their antimicrobial features to assess its influence on the microbial limitation. The chitosan and nanoclay nanocomposite had excellent executed and well antibacterial effects against microbial limitations (coliforms, *Salmonella* spp., coagulase-positive *Staphylococcus*, E. *coli*, yeast, and mold) [25]. Olivetti et al. showed that DDSA (dodecenylsuccinic anhydride)-collagen hydrogels, either unloaded or loaded with simvastatin, showed sustained antimicrobial activity against *Pseudomonas aeruginosa* and *Staphylococcus aureus* for 72 hours, maybe because of the hydrophobic DDSA chain interaction with cell wall bacteria. The antimicrobial activity was stronger against S. *aureus*. Also, collagen hydrogels provided a prolonged antibacterial activity when they involved simvastatin, and findings revealed that these materials could stimulate macrophages which is useful in wound healing processes [26]. The MTT assay of Chakrabarti et al. study showed that bFGF and collagen matrix hydrogel had minimal toxicity on the L929 mouse fibroblast cell line, did not inhibit cell proliferation, and could be further investigated in burn wounds [27]. In the present study, the antibacterial evaluations showed that the number reduction of E. coli was more than S. aureus. The collagen/nanoclay/tadalafil hydrogel displayed an inhibition zone in comparison with the standard antibiotic disc. Therefore, this result revealed that the hydrogel might conduct an antibacterial effect on the healing process of the wound.

Wound contraction has been known as a progressive process that appears in the matrix of tissue and accelerates healing by providing adequate granulation tissue to restore the tissue damage. The wound healing process is crucially correlated with reepithelialization due to regenerating and attenuating the surface of the wound [18]. Huang et al. have used a clay-reinforced composite film, polycaprolactone/chitosan/curcumin (PCL/CS/Clay/Cur) for wound dressing, and they displayed the inhibitory effect of this film of clay on bacteria (168 mg/ml). Moreover, they demonstrated that Cur-loading films with increasing clay could be high potential candidates for the caring wound [28]. Thangavel et al. developed hydrogels containing LG (L-glutamic acid) and CS (chitosan) to treat diabetic ulcers. They displayed that the LG + CS hydrogel facilitated vascularization for the acceleration of diabetic wound healing. These findings revealed that the combination of LG can ameliorate deposition of collagen, vascularization, and purposes in the acceleration of diabetic wounds regeneration [18]. Neovascularization or angiogenesis has a crucial role in the rebuilding of injured skin and avoiding subsequent complications such as non-healing diabetic wounds. Neovascularization deficiency, especially deficit information of microvascular network, refers to the interruption of tissue repair in diabetic circumstances [18]. In this study, it was detected that collagen/nanoclay/tadalafil hydrogel demonstrated fine adhesiveness when administered at the surface of the wound topically, and the macroscopic results demonstrated that the wound contraction was considerable in the hydrogel/HIIT exercise and hydrogel groups compared with the HIIT exercise and control groups during 21 days. The hydrogel-treated diabetic wounds displayed complete epithelialization in 21 days. The present results showed an increased rate of epithelialization

in diabetic rats. These results display that using collagen/nanoclay/tadalafil hydrogel with HIIT exercise helps in wound healing. The rate of wound healing in the control and treated groups showed that the rate of regeneration in the hydrogel/HIIT exercise group was higher than that in the hydrogel group in 7 days and the connective tissue formation and cell infiltration were observed. In addition, this rate was very considerable in the hydrogel/HIIT exercise and hydrogel compared to the HIIT exercise and control groups. The rate of wound healing, connective tissue formation, and cell infiltration was very significant in the HIIT exercise group compared with the control in 7 days. The rate of wound healing, infiltration of cell, and hair follicle formation in the hydrogel/HIIT exercise was significant compared to the hydrogel and HIIT exercise group in 14 days. Also, treated groups with HIIT exercise can play a crucial role in the amelioration of wounds compared to the control group. Thus, wound healing, the formation of a regular layer of collagen, hair follicles, and the formation of three layers of wounds were accelerated and better performed in the hydrogel/HIIT exercise and hydrogel groups than those in the control and HIIT exercise groups, but hydrogel/HIIT exercise was remarkably more successful than the hydrogel group in wound repairing, forming skin layers and classifying arranged collagen. Enhanced content of collagen is detected in the hydrogel/HIIT exercise and hydrogel groups. Therefore, increment of collagen content is considered in the granulation tissues. Assessment of Masson's trichrome staining revealed that collagen/nanoclay/tadalafil hydrogel treatment enhanced the content of the collagen.

Tan et al. investigated the properties of a novel composite biomaterial, a collagen scaffold loaded with CBD-VEGF, for healing of the wound in a diabetic rat model. They found that collagen scaffold loaded with CBD-VEGF facilitated healing in the diabetic wound of the rat model, which may have promising therapeutic approaches for diabetic wound treatment [29]. Long et al. provided a collagen membrane as a drug delivery scaffold to assess whether the combined use of VEGF and SDF-1α has a synergistic effect on the treatment of diabetic wound healing. Their long-term findings elucidate that the comodified scaffold can accelerate wound healing, facilitate regeneration of blood vessels, and promote proliferation of assist cells, accumulation of extracellular matrix, and reepithelialization. Altogether, the study demonstrated that the CBD-SDF-1α and CBD-VEGF comodified scaffold support rapid recovery from diabetic wounds through matching inflammation and angiogenesis [30].

In this study, the amount of collagen in the HIIT exercise group was increased after 21 days, while this amount was much higher in the hydrogel/HIIT exercise and hydrogel groups than that in the control and HIIT exercise groups. Also, the presence of fibroblasts in the hydrogel/HIIT exercise and hydrogel groups was higher than that in the HIIT exercise and control groups. Moreover, this amount of fibroblasts was significant in the hydrogel/HIIT exercise group compared to the hydrogel. Epidermis density was higher in the hydrogel/HIIT exercise group than that in the hydrogel group, and the hydrogel/HIIT exercise and hydrogel groups were significantly different from the control and HIIT exercise groups. The rate of vascularization was decreased in the HIIT exercise group during 21 days that it was significantly different from the control group, and it indicated that the HIIT exercise could accelerate the healing by increasing vascularization on days 7 and 14, while the rate of vascularization was increased in the control group on day 21. The increase of vascularization rate showed the acceleration of healing in the hydrogel/HIIT exercise and hydrogel groups on days 7 and 14. After 21 days, the number of vessels was decreased, which indicated a suitable process of regeneration. The number of hair follicles was visible only on day 21 in the control group, and the number of hair follicles in the two groups of hydrogel/HIIT exercise and hydrogel was higher than that in the control and HIIT exercise groups with a significant difference. The presence of inflammatory cells in the control and HIIT exercise groups showed a significant difference between days 7 and 14 compared to the hydrogel/HIIT exercise and hydrogel groups, and inflammatory cells were decreased after day 21. The hydrogel/HIIT exercise and hydrogel groups showed a significant reduction of inflammatory cell infiltration on days 7 and 14, and this amount was reduced on day 21. Generally, the amount of inflammatory in the hydrogel/HIIT exercise and hydrogel groups was remarkably different from the control and HIIT exercise groups.

5. Conclusion

In conclusion, collagen/nanoclay/tadalafil hydrogel facilitated movements of cells at the wound zone for improving scar formation and accelerating wound contraction. The HIIT exercise with hydrogels decreased the duration of epithelialization, increased wound contraction rate, and enhanced crosslinking and the content of collagen in diabetic animal models. These findings have also revealed that hydrogel-involved collagen/nanoclay/tadalafil can be conducted as a high potential therapeutic approach in the amelioration of diabetic wounds. Therefore, hydrogel/HIIT exercise hydrogel would be an appropriate candidate for wound healing due to the acceleration of wound healing, the formation of hair follicles, and the arrangement of collagen fibers.

Data Availability

All the data generated or analyzed during this study are included in this published article, and the datasets analyzed to support the findings of this study are available from the corresponding author upon request.

Ethical Approval

All of the *in vitro* and *in vivo* tests were approved by the Ethical Committee for Animal Research, Tehran, Iran.

Conflicts of Interest

The authors declare that there are no conflicts of interest regarding the publication of the present paper.

References

[1] S. Patel, S. Srivastava, M. R. Singh, and D. Singh, "Mechanistic insight into diabetic wounds: pathogenesis, molecular targets and treatment strategies to pace wound healing," *Biomedicine & Pharmacotherapy*, vol. 112, Article ID 108615, 2019.

[2] S. M. Ayuk, H. Abrahamse, and N. N. Houreld, "The role of matrix metalloproteinases in diabetic wound healing in relation to photobiomodulation," *Journal of Diabetes Research*, vol. 2016, Article ID 2897656, 2016.

[3] K. C. Broussard and J. G. Powers, "Wound dressings: selecting the most appropriate type," *American Journal of Clinical Dermatology*, vol. 14, no. 6, pp. 449–459, 2013.

[4] S. A. Hosseini, O. R. Slehi, F. Keikhosravi et al., "Mental health benefits of exercise and genistein in elderly rats," *Experimental Aging Research*, pp. 1–16, 2021.

[5] S. Ito, "High-intensity interval training for health benefits and care of cardiac diseases-the key to an efficient exercise protocol," *World Journal of Cardiology*, vol. 11, no. 7, pp. 171–188, 2019.

[6] F. Torma, Z. Gombos, M. Jokai, M. Takeda, T. Mimura, and Z. Radak, "High intensity interval training and molecular adaptive response of skeletal muscle," *Sports Medicine and Health Science*, vol. 1, no. 1, pp. 24–32, 2019.

[7] K. Norton, L. Norton, and D. Sadgrove, "Position statement on physical activity and exercise intensity terminology," *Journal of Science and Medicine in Sport*, vol. 13, no. 5, pp. 496–502, 2010.

[8] J. S. Ramos, L. C. Dalleck, A. E. Tjonna, K. S. Beetham, and J. S. Coombes, "The impact of high-intensity interval training versus moderate-intensity continuous training on vascular function: a systematic review and meta-analysis," *Sports Medicine*, vol. 45, no. 5, pp. 679–692, 2015.

[9] A. Mitropoulos, A. Gumber, H. Crank, M. Akil, and M. Klonizakis, "Exploring the feasibility of an exercise programme including aerobic and resistance training in people with limited cutaneous systemic sclerosis," *Clinical Rheumatology*, vol. 39, no. 6, pp. 1889–1898, 2020.

[10] D. Baltzis, I. Eleftheriadou, and A. Veves, "Pathogenesis and treatment of impaired wound healing in diabetes mellitus: new insights," *Advances in Therapy*, vol. 31, no. 8, pp. 817–836, 2014.

[11] G. M. Virador, L. de Marcos, and V. M. Virador, "Skin wound healing: refractory wounds and novel solutions," *Methods in Molecular Biology (Clifton, N.J.)*, vol. 1879, pp. 221–241, 2019.

[12] A. Jarad, A. Hamoody, M. Hasan et al., "Diabetic wound healing enhancement by tadalafil," *International Journal of Pharmaceutical Research*, vol. 12, pp. 841–847, 2020.

[13] C. Davenport and A. Dubin, "Tadalafil therapy and severe chronic foot wound resolution," *International Wound Journal*, vol. 12, no. 6, pp. 733–736, 2015.

[14] K. Goldsmith, E. Goradia, S. A. McClain, S. Sandoval, and A. J. Singer, "The effect of tadalafil on reepithelialization and scarring of partial thickness porcine burns," *Wound Repair and Regeneration*, vol. 28, no. 1, pp. 26–32, 2020.

[15] K. T. Huang, Y. L. Fang, P. S. Hsieh, C. C. Li, N. T. Dai, and C. J. Huang, "Non-sticky and antimicrobial zwitterionic nanocomposite dressings for infected chronic wounds," *Biomaterials Science*, vol. 5, no. 6, pp. 1072–1081, 2017.

[16] K. T. Huang, Y. L. Fang, P. S. Hsieh, C. C. Li, N. T. Dai, and C. J. Huang, "Zwitterionic nanocomposite hydrogels as effective wound dressings," *Journal of Materials Chemistry B*, vol. 4, no. 23, pp. 4206–4215, 2016.

[17] A. D. Metcalfe and M. W. J. Ferguson, "Tissue engineering of replacement skin: the crossroads of biomaterials, wound healing, embryonic development, stem cells and regeneration," *Journal of The Royal Society Interface*, vol. 4, no. 14, pp. 413–437, 2007.

[18] P. Thangavel, B. Ramachandran, S. Chakraborty, R. Kannan, S. Lonchin, and V. Muthuvijayan, "Accelerated healing of diabetic wounds treated with L-glutamic acid loaded hydrogels through enhanced collagen deposition and angiogenesis: an in vivo study," *Scientific Reports*, vol. 7, no. 1, Article ID 10701, 2017.

[19] E. Robinson, C. Durrer, S. Simtchouk et al., "Short-term high-intensity interval and moderate-intensity continuous training reduce leukocyte TLR4 in inactive adults at elevated risk of type 2 diabetes," *Journal of Applied Physiology (1985)*, vol. 119, no. 5, pp. 508–516, 2015.

[20] M. V. Machado, A. B. Vieira, F. G. da Conceição, A. R. Nascimento, A. C. L. da Nóbrega, and E. Tibirica, "Exercise training dose differentially alters muscle and heart capillary density and metabolic functions in an obese rat with metabolic syndrome," *Experimental Physiology*, vol. 102, no. 12, pp. 1716–1728, 2017.

[21] F. García-Villén, A. Faccendini, D. Miele et al., "Wound healing activity of nanoclay/spring water hydrogels," *Pharmaceutics*, vol. 12, no. 5, p. 467, 2020.

[22] R. S. Soufdoost, S. A. Mosaddad, Y. Salari et al., "Surgical suture assembled with tadalafil/polycaprolactone drug-delivery for vascular stimulation around wound: validated in a preclinical model," *Biointerface Res Appl Chem*, vol. 10, pp. 6317–6327, 2020.

[23] J. P. Magalhães, X. Melo, I. R. Correia et al., "Effects of combined training with different intensities on vascular health in patients with type 2 diabetes: a 1-year randomized controlled trial," *Cardiovascular Diabetology*, vol. 18, no. 1, p. 34, 2019.

[24] M. Bahadoran, A. Shamloo, and Y. D. Nokoorani, "Development of a polyvinyl alcohol/sodium alginate hydrogel-based scaffold incorporating bFGF-encapsulated microspheres for accelerated wound healing," *Scientific Reports*, vol. 10, no. 1, p. 7342, 2020.

[25] M. V. Mojtaba, H. Seyed Masoud, M. Ali, J. Mahdi, and M. Hadi, "Investigation of the antimicrobial properties of nanoclay and chitosan based nanocomposite on the microbial characteristics of Gouda cheese," *Iranian Journal of Microbiology*, vol. 12, no. 2, 2020.

[26] C. E. Olivetti, M. I. Alvarez Echazú, O. Perna et al., "Dodecenylsuccinic anhydride modified collagen hydrogels loaded with simvastatin as skin wound dressings," *Journal of Biomedical Materials Research Part A*, vol. 107, no. 9, pp. 1999–2012, 2019.

[27] S. Chakrabarti, B. Mazumder, J. Rajkonwar, M. P. Pathak, P. Patowary, and P. Chattopadhyay, "bFGF and collagen matrix hydrogel attenuates burn wound inflammation through activation of ERK and TRK pathway," *Scientific Reports*, vol. 11, no. 1, p. 3357, 2021.

[28] Y. Huang, N. Dan, W. Dan, and W. Zhao, "Reinforcement of polycaprolactone/chitosan with nanoclay and controlled release of curcumin for wound dressing," *ACS Omega*, vol. 4, no. 27, pp. 22292–22301, 2019.

[29] Q. Tan, B. Chen, X. Yan et al., "Promotion of diabetic wound healing by collagen scaffold with collagen-binding vascular endothelial growth factor in a diabetic rat model," *Journal of Tissue Engineering and Regenerative Medicine*, vol. 8, no. 3, pp. 195–201, 2014.

[30] G. Long, D. Liu, X. He et al., "A dual functional collagen scaffold coordinates angiogenesis and inflammation for diabetic wound healing," *Biomaterials Science*, vol. 8, no. 22, pp. 6337–6349, 2020.

Hindawi
Advances in Materials Science and Engineering
Volume 2021, Article ID 3499645, 9 pages
https://doi.org/10.1155/2021/3499645

Research Article

Comparative Study of the Mechanical and Water Absorption Behaviour of Basalt Fiber Reinforced Polymer Matrix Composites with Different Epoxies as Matrix for Biomedical Applications

R. Raghavendra Rao,[1] S. Pradeep,[1] Nasim Hasan,[2] B. S. Shivashankara,[1] Mohamed Abdelghany Elkotb,[3,4] C. Ahamed Saleel,[3] Asif Afzal,[5,6] and B. Saleh[7]

[1]*Department of Mechanical Engineering, Malnad College of Engineering, (Affiliated to Visvesvaraya Technological University, Belagavi), Hassan, Karnataka, India*
[2]*Mechanical Engineering Department, Mettu University, Mettu Oromia, P.O. Box 318, Ethiopia*
[3]*Department of Mechanical Engineering, College of Engineering, King Khalid University, PO Box 394, Abha 61421, Saudi Arabia*
[4]*Mechanical Engineering Dept., Faculty of Engineering, Kafrelsheikh University, Kafr el-Sheikh, Egypt*
[5]*Department of Mechanical Engineering, P. A. College of Engineering, Mangalore (Affiliated to Visvesvaraya Technological University, Belagavi 574153, Karnataka, India*
[6]*Department of Mechanical Engineering, School of Technology, Glocal University, Delhi-Yamunotri Marg, SH-57, Mirzapur Pole, Saharanpur District, Uttar Pradesh–247121, India*
[7]*Mechanical Engineering Department, College of Engineering, Taif University, P.O. Box 11099, Taif 21944, Saudi Arabia*

Correspondence should be addressed to Nasim Hasan; nasim.hasan@meu.edu.et

Received 9 August 2021; Accepted 17 November 2021; Published 22 December 2021

Academic Editor: Ravichandran M

In comparison to conventional materials, polymer matrix composite materials have witnessed a surge in applicability due to their higher specific strength-to-weight ratio, abundant availability, and ease of shaping. Due to technological, economic, environmental, and societal challenges, bio-based fibers began to emerge quickly for use in industrial components. Due to its unique chemistry-related characteristics, basalt fiber holds a prominent position among the many bio-based fibers. So, it could be thought of used as a replacement for some components used in the biomedical equipments. In the present investigation, plain-woven basalt fiber at a constant percentage of 55% is added as reinforcement to three different epoxy resin-hardener combinations such as Lapox L12-Lapox K6, Araldite LY1564-Aradur 22962, and Araldite LY556-Aradur HY951 as matrix, and comparative studies are carried out. Fabrication is carried out by hand lay-up technique. Test specimens are prepared as per the respective ASTM standards by subjecting the laminate to water jet machining. Mechanical characterization such as tensile, flexural, and density tests is conducted for the test specimen using BISS-50 kN Universal Testing Machine (UTM). Water absorption tests are also conducted for 24 and 48 hours duration. From the results obtained, it is concluded that the highest tensile, flexural strengths are obtained for laminate *L3* which used LY556 epoxy and HY951 hardener combination as matrix. Also, less rate of water absorption is seen for *L3* laminate for both 24 and 48 hrs which makes it suitable for biomedical applications.

1. Introduction

Polymer matrix composites offer a wide range of uses due to its superior strength-to-weight ratio, corrosion resistance, less weight, adaptability, shape ability, and suitability for a variety of technical applications. Although polymer matrix composites (PMCs) were first used in the early twentieth century, they were only widely used in the

second half of the century. Basalt is a clean and environmentally benign substance that originates from volcanic rocks and has a melting temperature of 1500°C to 1700°C [1, 2]. The density of basalt fibers ranges between 2.7 g/cc and 2.8 g/cc. It is extremely hard compared with some conventional materials and has higher abrasion resistance [3]. It is stated that the basalt fiber could be a possible alternative compared with natural plant fibers [4]. Czigany [5] proved that the basalt could be considered as natural fiber. It is chemically inert and could be a major breakthrough as bio material. Dhand et al. [6] have considered that despite their severe mechanical qualities, basalt fiber resources are widely available around the world. They could be manufactured using a low-energy process at a lower cost than glass and, more specifically, carbon strands. They are created by spinning liquid volcanic basalt rock through a spinning cycle. This cycle is similar to that of making glass strands. However, in case of the basalt, no additional substances are required. This reduces the risk of the piece being exposed to poisonous substances. As a result, the manufacturing process is more environmentally friendly [7, 8]. Basalt fibers are more chemically stable and have a very strong corrosion resistance [9]. The major constituent of basalt is SiO_2 (42–56% by weight), Al_2O_3 (14–18%), Fe_2O_3 (11–12%), CaO (7–9%), and other oxides (refer Figure 1) [10]. Raghavendra Rao et al. [11] have undergone a study of UHMWPE/basalt reinforced hybrid polymer matrix composite. They have concluded that the inclusion of UHMWPE fibers has increased the flexural strength considerably. Fiore et al. [12] investigated the effect of uniaxial basalt fiber on the mechanical properties of a glass fiber/epoxy composite (GFRP) intended for marine use. The presence of two outer layers of basalt in comparison to GFRP laminates has resulted in improved mechanical properties of the fabricated laminates. Lilli et al. [13] studied the effect of low temperature plasma polymerization on the interfacial behaviour of basalt fiber reinforced polymer matrix composites. A polymer coating based on pure tetra vinyl silane (TVS) or its combination with two different oxygen levels was deposited on the surface of an unsized basalt fiber using plasma-assisted chemical vapour deposition. The impact of the plasma procedure was initially investigated using a single fiber tensile test characterization, which revealed that the changed fibers had no loss of strength. Following that interfacial strength was investigated using single fiber pullout tests with an epoxy matrix. When compared with untreated basalt fibers, the addition of oxygen to the polymer film combination has shown increased interfacial shear strength (IFSS) by 79%. Many studies have previously concentrated on improving the interface for synthetic fibers, particularly glass and carbon fibers, while basalt fibers have received less attention. Goudar Santosh Gangappa and S. Sripad Kulkarni [14] have experimented and validated basalt and jute fiber reinforced hybrid polymer matrix composites. Polymer hybrid composites are created using compression moulding techniques, with polyester resin as the matrix and basalt and jute as

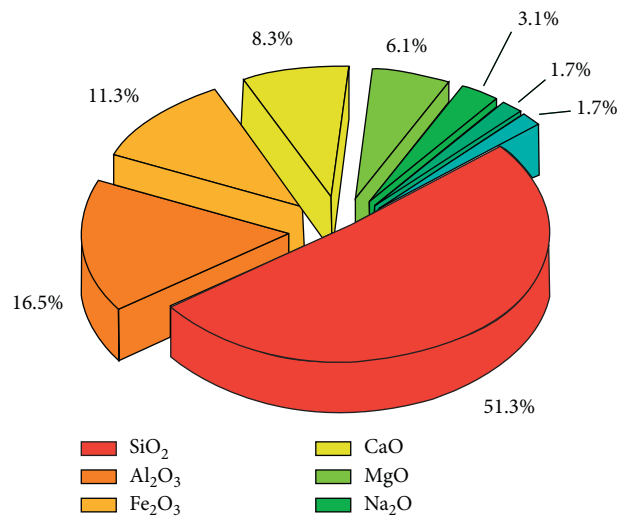

Figure 1: Chemical composition of basalt fiber [10].

reinforcement. The static and dynamic behaviours are studied. It is revealed that the hybrid laminates had better damping ratio and hence could be used as vibration absorbing materials. Xing Zhao et al. [15] investigated the effect of different resin matrices on static and fatigue loading conditions in basalt fiber reinforced polymer composites. Four different types of resins were used in their study. Normal and toughened vinyl ester resins, as well as room and elevated temperature curing epoxy systems, were used. The scanning electron microscopy (SEM) system embedded in the fatigue test equipment was used to perform fractography of failed surfaces in parallel with the static and fatigue tests. The static tensile strength of the BFRP with normal vinyl ester resin was comparable with that of the BFRP with elevated temperature cured epoxy, according to the results. However, due to more matrix cracking and fiber peeling on the surface of the vinyl ester resin-based BFRP, the former had a significantly shorter fatigue life than the latter. However, the former had a significantly shorter fatigue life than the latter due to more matrix cracking and fiber peeling on the surface of the vinyl ester resin-based BFRP. Siwon Yu et al. [16] have studied the effect of plasma polymerization to improve the interfacial bonding strength and hence its effect on the mechanical properties of the developed BFRP. The former had exhibited significantly shorter fatigue life than the latter due to more matrix cracking and fiber peeling on the surface of the vinyl ester resin-based BFRP. However, due to more matrix cracking and fiber peeling on the surface of the vinyl ester resin-based BFRP, the former had a significantly shorter fatigue life than the latter. The results showed that APTES plasma-polymerized BF produced a robust interface with a 50.3 percent increase in interfacial shear strength and a 32.5 percent increase in tensile strength when compared with untreated BF. On the BF surface, the APTES was plasma polymerized for 3, 5, 7, and 9 minutes. The mechanism of reaction during plasma polymerization was investigated and compared with a traditional solution dipping method.

According to the available literature, no research articles have reported the comparative evaluation of the effect of various epoxies on the mechanical and water absorption behaviours of BFRP composites. An effort is made in this direction from the point of view of biomedical applications.

2. Materials and Methods

2.1. Materials. Reinforcement used in the present investigation is basalt plain-woven fabric of 300 GSM. Details of fabrics are illustrated in Table 1. The epoxy resin and hardener combinations used are shown in Table 2.

2.2. Fabrication of Composites. Hand lay-up approach was used for the fabrication of laminates. First, the basalt fabrics were cut to the dimensions of $300 \times 300\ \text{mm}^2$. Then, laminates are prepared using 10 layers of fabric to maintain approximate thickness of 3 mm for different epoxy-hardener combinations as indicated in Table 2. The epoxy resin and hardener were mixed in the ratio of 100 : 10 by weight. First, wax was applied over the top of a mould, and then the fabric layers were laid one over another in the mould, simultaneously applying the measured quantity of epoxy on each layer of the fabrics. Then, the epoxy was uniformly spread using roller. As soon as the last layer of fiber was properly rolled, the toughened glass slab of required size was kept on top of the mould. On the top of the glass slab, dead weights are placed and sustained in that spot for 24 to 48 hours and then withdrawn. The laminates $L1$ and $L2$ are cured in oven for a temperature range of 60 to 80°C for 2 hours, but the laminate $L3$ is cured at the room temperature. Then, the test samples were prepared using water jet machining as per the ASTM standards.

2.3. Density Test. For a sample of $10\ \text{mm} \times 10\ \text{mm} \times 3\ \text{mm}$, the mass "$m$" is weighed on a precision weighing scale. The volume "V" of the sample is determined using the Archimedes principle. A 100 ml beaker is partially filled with distilled water. The initial water level "V_1" is noted at lower level of the meniscus. The samples are then dipped one by one to determine the ultimate or final water level "V_2." The sample volume "V" is calculated by subtracting the initial water level "V_1" from the final water level "V_2."

Therefore, $V = V_2 - V_1$. Then, the density of a material is calculated using the formula as follows:

$$\rho = \frac{m}{V}\ \text{grams/cm}^3, \tag{1}$$

where "m" is the mass of the sample in grams and "V" is the volume of the sample in cm^3.

2.4. Water Absorption Test. According to the ASTM D570 standard, water absorption tests are performed for 24 and 48 hours duration. The initial weight "W_1" of a sample size of $10 \times 10 \times 3\ \text{mm}^3$ is determined. Then, it is steeped for 24 hours in distilled water inside a beaker. It is extracted after 24 hours, and its final weight "W_2" is determined. The water absorption weight percentage is calculated using the formula as follows:

$$\text{water absorption weight}\ \% = \frac{W_2 - W_1}{W_1} \times 100\%. \tag{2}$$

By dipping the samples for 48 hours duration, the same procedure is repeated.

Table 1: The basic properties of basalt fabrics used.

Parameters	Value	ASTM
Density (g/cc)	2.77–2.80	ASTM D3800
Weight (GSM)	300	—
Thickness (mm)	0.25	—
Melting point	1500–1700°C	ASTM D276
Tensile strength (MPa)	1800–4100	ASTM D2256
Modulus of elasticity (GPa)	96–100	ASTM C169

2.5. Tensile Test. The tensile test was performed with data capture software on a BISS-50 kN capacity Universal Testing Machine (UTM). The sample ($115 \times 19 \times 3\ \text{mm}^3$) was chosen according to the ASTM: D638-IV standard, with a gauge length of 33 mm and a crosshead speed of 1.0 mm/min, and the test was carried out at room temperature. The results obtained are used to plot the respective graphs.

2.6. Flexural Test. 3-point bending test is conducted as per the ASTM: D790 standard using the same UTM. Testing was conducted at loading rate of 2.0 mm/min, at room temperature. The dimension of the specimen is $90 \times 12.5 \times 3\ \text{mm}^3$, and the flexural specimens were fixed between two jaws with a gauge length of 60 mm, and the load was applied at the center. Loading is applied to the specimen until it ruptures. The flexural strength and modulus are obtained with the help of data acquisition software.

2.7. Surface Morphology. Fractured tensile specimens were examined for microstructure using TESCAN-VEGA 3 LMU scanning electron microscope. SEM was carried out to visualize the dispersion of fibers within the matrix and the adhesion characteristics amongst fiber and matrix. In order to enhance the conductivity of the samples, the surface of the sample was coated with a thin gold film and the micrographs were captured from the fractured samples for different magnifications.

3. Results and Discussion

3.1. Density Test. Figure 2 depicts the experimental values of densities for the prepared composite laminates. Minute difference in experimental densities was observed amongst of the laminates since they are only with varied epoxy-hardener combinations but prepared for a constant fiber percentage of 55% as shown in Figure 2. The $L3$ laminate exhibited the maximum density of 1.78 g/cc, the $L2$ laminate exhibited the lowest density of 1.71 g/cc, and laminate $L1$ exhibited a density of 1.73 g/cc.

Table 2: Properties of different epoxy-hardener combinations.

Laminate	Epoxy-hardener combination	Epoxy density at 25°C in g/cc (ISO 1675)	Hardener density at 25°C in g/cc (ISO 1675)	Epoxy viscosity at 25°C in MPa s (ISO 12058-1)	Hardener viscosity at 25°C in MPa s (ISO 12058-1)	Curing conditions used
*L*1	Lapox L12-hardener K6	1.120	0.954	9000–12000	5000–8000	80^0 C for 1-2 hrs
*L*2	Araldite LY1564-Aradur 22962	1.1 to 1.2	0.89–0.90	1200–1400	5–20	80^0 C for 1 hr
*L*3	Araldite LY556-Aradur HY951	1.1 to 1.2	0.980	1350–2000	10–20	Room temperature (25°C for 24 to 48 hrs)

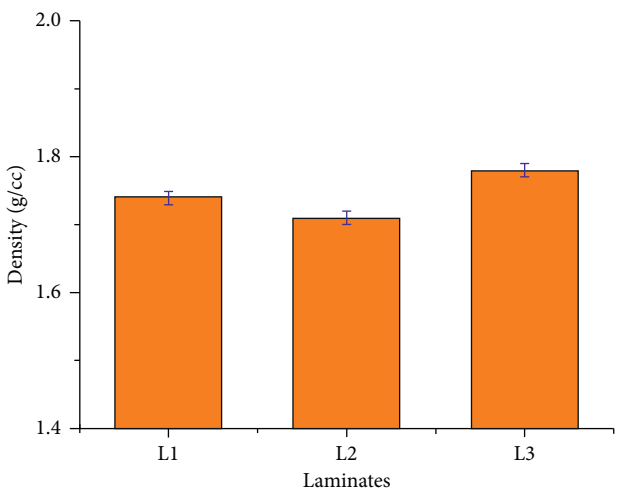

Figure 2: Representation of densities of different laminates.

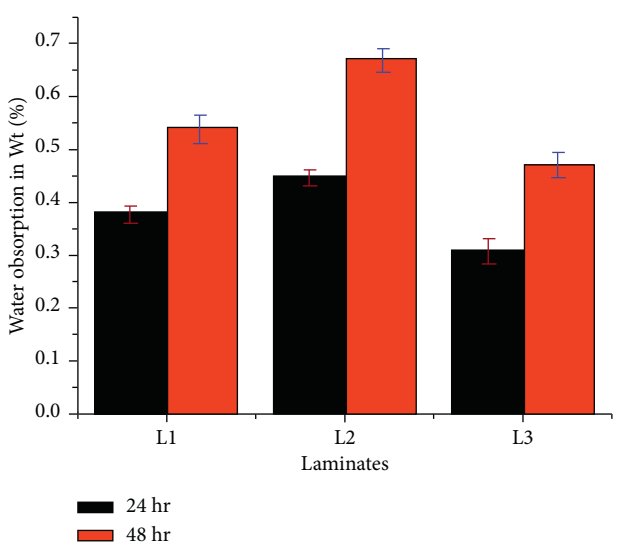

Figure 3: Representation of water absorption comparative plot.

3.2. Water Absorption Test. Figure 3 depicts the water absorption percentages of different laminates. For both 24 and 48 hours, laminate *L*3 exhibited the least water absorption percentage of 0.31% and 0.47%, respectively. The laminate *L*2 exhibited the highest water absorption percentage of 0.45% and 0.67%, respectively. Similarly, laminate *L*1 exhibited the moderate water absorption percentage of 0.37% and 0.54% for 24 hours and 48 hrs, respectively. In first 24 hours, all the laminates show a higher rate of water absorption, while in the next 24 hours they had shown a lesser rate of water absorption.

3.3. Tensile Property Evaluation. Figures 4 and 5 illustrate the tensile strength and modulus of different laminates, respectively. The laminate *L*3 had the maximum tensile strength and modulus, while the laminate *L*2 had the least tensile strength and modulus, as shown in the figure. The composite laminate *L*3 exhibited highest tensile strength and modulus of 304.36 MPa and 10.41 GPa, respectively, and *L*2 laminate exhibited the least tensile strength and modulus of 143.8 MPa and 5.1 GPa, respectively. The laminate *L*1 exhibited moderate tensile strength and modulus of 210.5 MPa and 9.1 GPa, respectively. Figure 6 demonstrates the mode of failure and fiber pullout happening during the tensile test. As seen from Figures 6(a) and 6(b) for laminates *L*1 and *L*2, respectively, the fiber pullout is occurring inappropriately. The fabric layers are peeled out during tensile testing, which indicates that the fiber-matrix adhesions are very low. Figure 6(c) depicts the tensile tested sample for laminate *L*3, which clearly shows the good fiber-matrix adhesion characteristics and appropriate fiber breakage and pullout.

3.4. Flexural Property Evaluation. Figures 7 and 8 illustrate the flexural strength and modulus, respectively. The laminate *L*3 exhibited the highest flexural strength and modulus, while the laminate *L*2 exhibited the lowest flexural strength and modulus [17–20]. The composite laminate *L*3 exhibited highest flexural strength and modulus of 318.8 MPa and 12.18 GPa, respectively, and laminate *L*2 exhibited lowest flexural strength of 151.1 MPa and modulus of 6.41 GPa, respectively. The laminate *L*1 exhibited moderate flexural strength and modulus of 220 MPa and 10.2 GPa, respectively. Figures 9(a)–9(c) show the flexural tested samples for *L*1, *L*2, and *L*3 laminates, respectively.

The present research revealed that the ultimate tensile strength, tensile modulus, flexural strength, and flexural modulus were seen maximum for *L*3 laminate [21–25]. Also, least water absorption percentage is seen for *L*3 laminate.

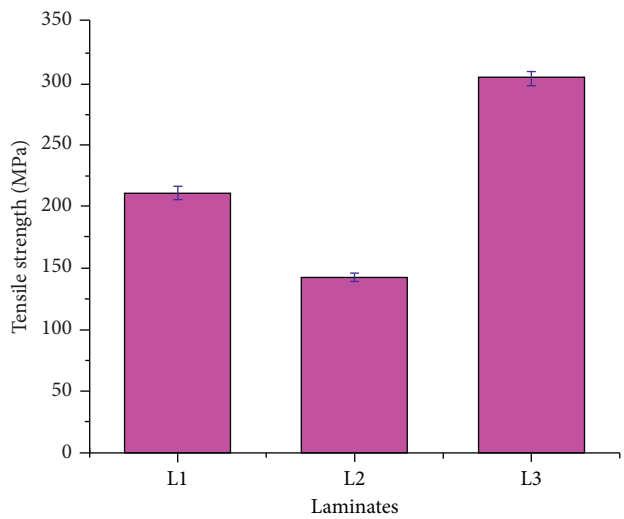

Figure 4: Representation of tensile strengths of different laminates.

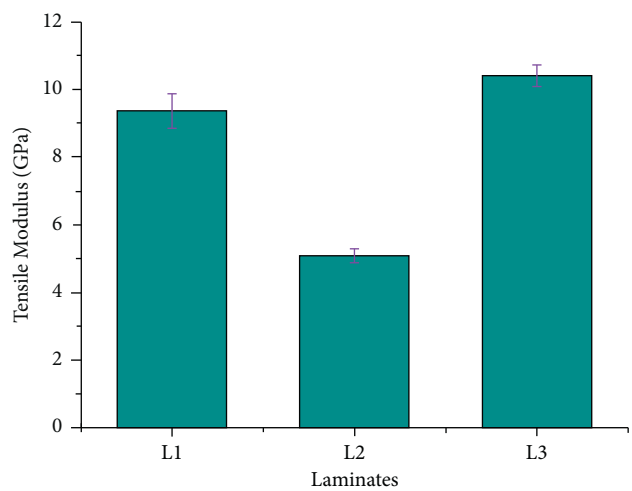

Figure 5: Representation of tensile modulus of different laminates.

3.5. Morphological Studies through SEM. Microstructural studies were conducted to visualize the failure surfaces of the fabricated laminates subjected to tensile loading. The fracture in the tested samples takes place due to the application of uniaxial tensile loading. The void content, fiber-matrix adhesion, and pullout properties are analyzed using the SEM images. All the composite specimens were coated with gold before observing them through SEM. The fractured micrographs of various laminate designations $L1$, $L2$, and $L3$ are shown in Figures 10(a)–10(c), respectively. It is seen that the fiber filaments are almost completely covered with an epoxy system. It showed (Figures 10(a)–10(c)) fewer amounts of voids in the fractured samples of laminates except $L3$ laminate. Not much interfacial deboning, matrix cracking and delamination were observed in the case of $L3$ laminate. It is evident from Figures 10(a) and 10(b) that the presence of voids, matrix cracking, fiber pullouts, and delamination is predominant in the case of laminates $L1$ and $L2$. Comparatively, $L3$ laminates had lesser amount of voids and cracks than other laminates, which helped to get better

Figure 6: Representations of tensile tested samples for (a) laminate $L1$; (b) laminate $L2$; (c) laminate $L3$.

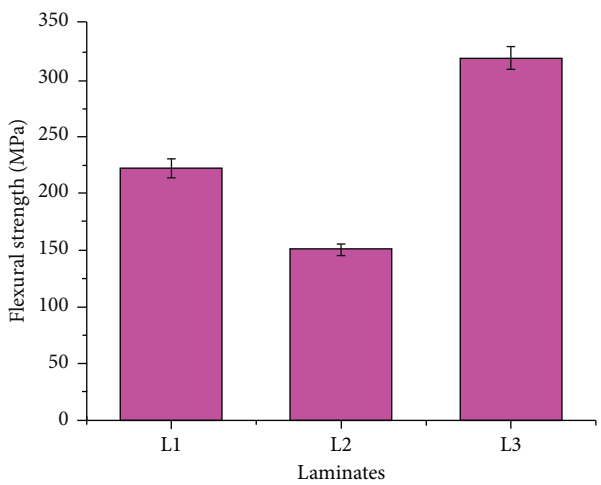

Figure 7: Representation of flexural strengths of different laminates.

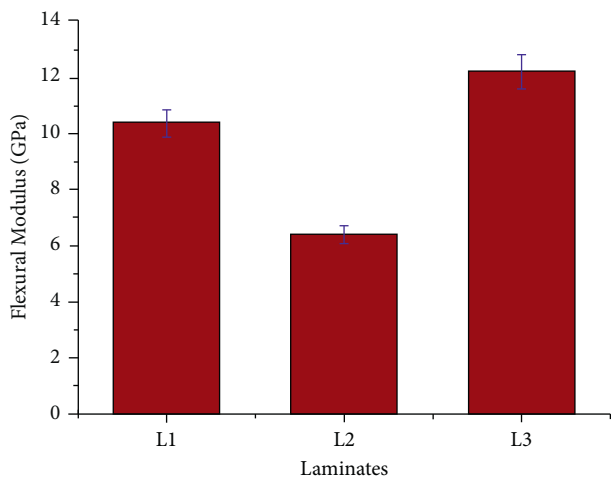

Figure 8: Representation of flexural modulus of different laminates.

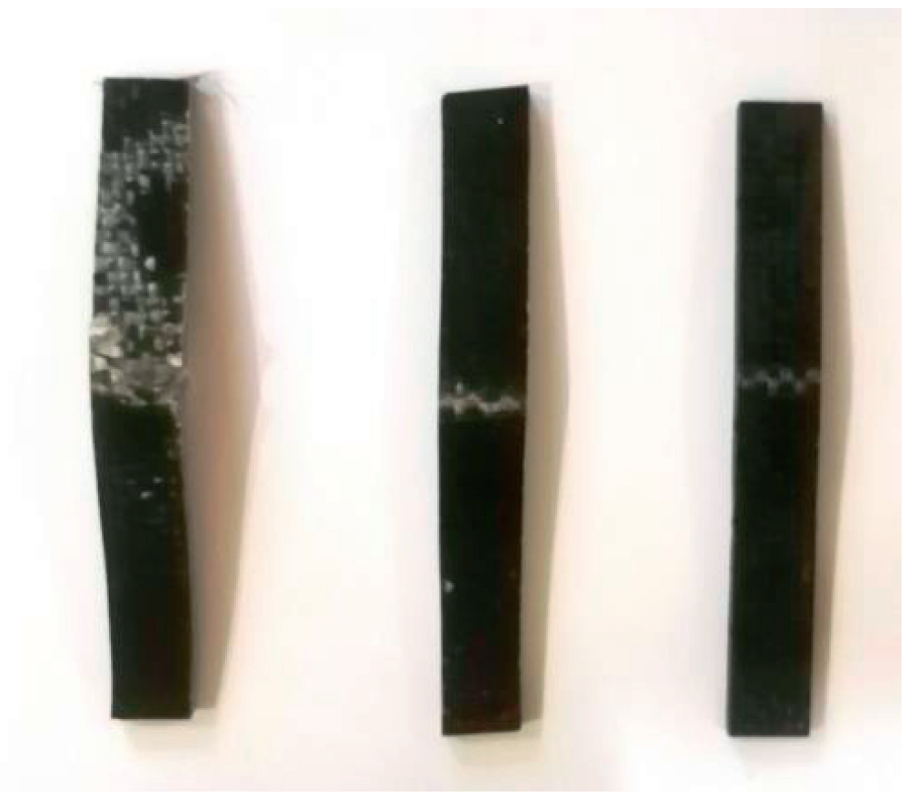

Figure 9: Representations of flexural tested samples for (a) $L1$ laminate; (b) $L2$ laminate; (c) $L3$ laminate.

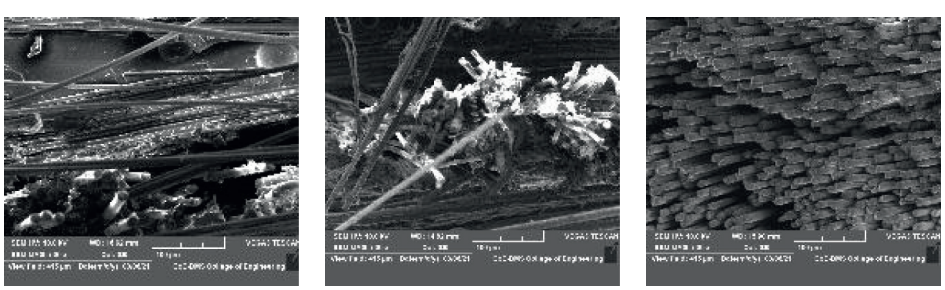

(a) (b) (c)

Figure 10: SEM images of tensile tested samples for (a) $L1$ laminate; (b) $L2$ laminate; (c) $L3$ laminate.

mechanical properties and improved adhesion amongst the fibers and matrix.

4. Conclusions

Effect of three different epoxy resins on the water absorption and mechanical properties of plain-woven basalt fiber reinforced polymer matrix composites was studied for 55 wt.%. The following conclusions were drawn based on the present experimental results:

(i) The composite laminate *L*3 shows highest tensile strength and modulus of 304.36 MPa and 10.41 GPa and *L*2 laminate shows the least tensile strength and modulus of 143.8 MPa and 5.1 GPa.

(ii) The composite laminate *L*3 indicated highest flexural strength and modulus of 318.8 MPa and 12.18 GPa and laminate *L*2 indicated lowest flexural strength of 151.1 MPa and modulus of 6.41 GPa.

(iii) The nonhybrid *L*3 laminate exhibited highest density of 1.78 g/cc and the *L*2 laminate exhibited the least density of 1.71 g/cc.

(iv) Laminate *L*2 exhibited highest water absorption percentage of 0.45% and 0.67% and the laminate *L*3 exhibited least water absorption percentage of 0.31% and 0.47% for 24 and 48 hours, respectively.

(v) Failure pattern confirmed that the *L*3 composite laminates showed better adhesion between fibers and matrix, appropriate fiber breakage, and pullout. Also, better mechanical properties and least water absorption are observed for laminate *L*3. So, it is suggested to go with the LY556-HY951 epoxy hardener combination as a matrix for the basalt fiber reinforced polymer composites.

(vi) SEM analysis confirmed that the *L*3 composite laminates showed lesser voids, better adhesion between fibers and matrix, appropriate fiber breakage, and pullout.

(vii) Good water absorption behaviour and mechanical strengths are seen which make the composite developed to be used for biomedical applications.

Data Availability

The data used to support this study are available upon request.

Conflicts of Interest

The authors declare that there are no conflicts of interest regarding the publication of this article.

Acknowledgments

The authors extend their appreciation to the Deanship of Scientific Research at King Khalid University, Saudi Arabia, for funding this work through the Research Group Program under Grant No. RGP 2/108/42. This study was supported by Taif University Researchers Supporting Project number (TURSP-2020/49), Taif University, Taif, Saudi Arabia. The authors would like to thank Taif University for financial support. This study was supported by TEQIP III, MCE, Hassan. The authors would like to thank Malnad College of Engineering, Hassan, for financial support.

References

[1] J. Militký, V. R. Kovačič, and J. Rubnerova, "Influence of thermal treatment on tensile failure of basaltfibers," *Engineering Fracture Mechanics-Journals*, vol. 69, pp. 1025–1033, 2002.

[2] J. Militky and V. Kovacic, "Ultimate mechanical properties of basalt filaments," *Textile Research Journal*, vol. 66, no. 4, pp. 225–229, 1996.

[3] M. Di Ludovico, A. Prota, and G. Manfredi, "Structural upgrade using basalt fibers for concrete confinement," *Journal of Composites for Construction*, vol. 14, no. 5, pp. 541–552, 2010.

[4] T. Tabi and J. Kovacs, "Examination of starch pre-process drying and water absorption on injection moulded poly (lactic acid)/starch blends," *Polymer Engineering & Science*, vol. 51, pp. 843–850, 2011.

[5] T. Czigány, "Basalt fiber reinforced hybrid polymer composites," *Materials Science Forum*, vol. 473-474, pp. 59–66, 2005.

[6] V. Dhand, G. Mittal, K. Y. Rhee, S.-J. Park, and D. Hui, "A short review on basalt fiber reinforced polymer composites," *Composites Part B: Engineering*, vol. 73, pp. 166–180, 2015.

[7] C. Colombo, L. Vergani, and M. Burman, "Static and fatigue characterisation of new basalt fibre reinforced composites," *Composite Structures*, vol. 94, no. 3, pp. 1165–1174, 2012.

[8] M. H. Lapena, G. Marinucci, M. H. Lapena, and G. Marinucci, "Mechanical characterization of basalt and GlassFiber epoxy composite tube," *Materials Research*, vol. 21, 2017.

[9] G. Wu, X. Wang, Z. Wu, Z. Dong, and G. Zhang, "Durability of basalt fibers and composites in corrosive environments," *Journal of Composite Materials*, vol. 49, no. 7, pp. 873–887, 2015.

[10] T. Deák and T. Czigány, "Chemical composition and mechanical properties of basalt and glass fibers: a comparison," *Textile Research Journal*, vol. 79, pp. 645–651, 2009.

[11] R. Raghavendra Rao, S. Pradeep, S. Karthik, K. R. Gopi, and B. S. Shivashankara, "Experimental investigation of effect of hybridization of UHMWPE fibers on the mechanical and physical properties of Basalt fiber reinforced polymer matrix composites," *IOP Conference Series: Materials Science and Engineering*, vol. 1189, no. 1, Article ID 012025, 2021.

[12] V. Fiore, G. Di Bella, and A. Valenza, "Glass-basalt/epoxy hybrid composites for marine applications," *Materials & Design*, vol. 32, no. 4, pp. 2091–2099, 2011.

[13] M. Lilli, M. Zvonek, V. Cech, C. Scheffler, J. Tirillò, and F. Sarasini, "Low temperature plasma polymerization: an effective process to enhance the basalt fibre/matrixinterfacial adhesion," *CompositesCxommunications*, vol. 27, Article ID 100769, 2021.

[14] G. S. Gangappa, S. S. Kulkarni, "Experimentation and validation of basalt & jute fiber reinforced in polymer matrix hybrid composites," *Materials Today: Proceedings*, vol. 38, no. 5, pp. 2372–2379, 2021.

[15] X. Zhao, X. Wang, Z. Wu, and J. Wu, "Experimental study on effect of resin matrix in basalt fiber reinforced polymer

composites under static and fatigue loading," *Construction and Building Materials*, vol. 242, Article ID 118121, 2020.

[16] S. Yu, K. H. Oh, and S. H. Hong, "Enhancement of the mechanical properties of basalt fiber-reinforced polyamide 6,6 composites by improving interfacial bonding strength through plasma-polymerization," *Composites Science and Technology*, vol. 182, Article ID 107756, 2019.

[17] S. S. Kumbar, D. A. Jadhav, C. S. Jarali et al., "Enhancement in cathodic redox reactions of single-chambered microbial fuel cells with Castor oil-emitted powder as cathode material," *Materials*, vol. 14, no. 16, p. 4454, 2021.

[18] T. H. M. Mysore, A. Y. Patil, G. U. Raju et al., "Investigation of mechanical and physical properties of big sheep horn as an alternative biomaterial for structural applications," *Materials*, vol. 14, no. 14, p. 4039, 2021.

[19] B. N. Sharath, C. V. Venkatesh, A. Afzal et al., "Multi ceramic particles inclusion in the aluminium matrix and wear characterization through experimental and response surface-artificial neural networks," *Materials*, vol. 14, no. 11, p. 2895, 2021.

[20] S. Nagaraja, K. U. Nagegowda, A. V. Kumar et al., "Influence of the fly ash material inoculants on the tensile and impact characteristics of the aluminum AA 5083/7.5SiC composites," *Materials*, vol. 14, no. 9, p. 2452, 2021.

[21] M. N. Akhtar, M. Khan, S. A. Khan et al., "Determination of non-recrystallization temperature for niobium microalloyed steel," *Materials*, vol. 14, no. 10, p. 2639, 2021.

[22] S. Nasri, B. Ebrahimi-Hosseinzadeh, M. Rahaie, A. Hatamian-Zarmi, and R. Sahraeian, "Thymoquinone-loaded ethosome with breast cancer potential: optimization, in vitro and biological assessment," *Journal of Nanostructure in Chemistry*, vol. 10, no. 1, pp. 19–31, 2020.

[23] P. Joshi, S. Mehtab, M. G. H. Zaidi, T. Tyagi, and A. Bisht, "Development of polyindole/tungsten carbide nanocomposite-modified electrodes for electrochemical quantification of chlorpyrifos," *Journal of Nanostructure in Chemistry*, vol. 10, no. 1, pp. 33–45, 2020.

[24] Z. Amirsardari, A. Dourani, M. A. Amirifar, N. Ghadiri Massoom, and R. Ehsani, "Development of novel supported iridium nanocatalysts for special catalytic beds," *Journal of Nanostructure in Chemistry*, vol. 10, no. 1, pp. 47–53, 2020.

[25] G. S. N. Rethnam, S. Manivel, V. K. Sharma et al., "Parameter study on friction surfacing of AISI316Ti stainless steel over EN8 carbon steel and its effect on coating dimensions and bond strength," *Materials*, vol. 14, no. 17, p. 4967, 2021.

Hindawi
Advances in Materials Science and Engineering
Volume 2021, Article ID 6078155, 13 pages
https://doi.org/10.1155/2021/6078155

Research Article

Fabrication and Experimental Analysis of Treated Snake Grass Fiber Reinforced with Polyester Composite

I. Jenish,[1] A. Felix Sahayaraj,[2] M. Appadurai,[3] E. Fantin Irudaya Raj,[4] P. Suresh,[5] T. Raja,[6] Saleh H. Salmen,[7] Saleh Alfarraj,[8] and Velu Manikandan[9]

[1]*Department of Applied Mechanics, Seenu Atoll School, Hulhu-medhoo, Addu City, Postal Code-19060, Maldives*
[2]*Department of Mechanical Engineering, Kalaignar Karunanidhi Institute of Technology, Coimbatore-641402, Tamilnadu, India*
[3]*Department of Mechanical Engineering, Dr. Sivanthi Aditanar College of Engineering, Tuticorin District-628215, Tamilnadu, India*
[4]*Department of Electrical and Electronics Engineering, Dr. Sivanthi Aditanar College of Engineering, Tuticorin District-628215, Tamilnadu, India*
[5]*Department of Mechanical Engineering, VV College of Engineering, Tisaiyanvilai, Tirunelveli–627657, Tamilnadu, India*
[6]*School of Mechanical Engineering, Vellore Institute of Technology, Chennai–600127, Tamilnadu, India*
[7]*Department of Botany and Microbiology, College of Science, King Saud University, P.O. Box -2455, Riyadh-11451, Saudi Arabia*
[8]*Zoology Department, College of Science, King Saud University, Riyadh 11451, Saudi Arabia*
[9]*College of Environmental & Bioresource Sciences, Chonbuk National University, Iksan 570752, Republic of Korea*

Correspondence should be addressed to I. Jenish; jenish@satollschool.edu.mv

Received 4 August 2021; Revised 24 September 2021; Accepted 19 November 2021; Published 22 December 2021

Academic Editor: Alicia E. Ares

The selection of fiber is predominant for natural fiber-reinforced polymer composite materials, which should have easy extraction and good bonding with considerable strength. In this paper, some chemical treatments were done on the fiber material to increase interfacial bonding between the snake grass fiber (*Sansevieria ehrenbergii*) and polyester matrix, such as alkali treatment (NaOH), potassium permanganate treatment, sodium carbonate treatment, hydrogen peroxide treatment, and calcium carbonate treatment. The chopped snake grass fiber-reinforced polymer composite material was prepared by keeping 25 wt.% of fiber and 30 mm fiber length reinforced with an unsaturated polyester resin that was cured with the help of the catalyst methyl ethyl ketone peroxide (MEPK). Cobalt naphthenate was used as an accelerator. Tribological properties were discussed for the highly potential sample with the help of a pin-on-disc wear tester, and the results were analysed by the Taguchi L9 orthogonal array. This paper exhibited the best mechanical and tribological properties among those chemical-treated fibers used in fiber-reinforced composite materials and untreated fibers used in fiber-reinforced composite materials. $CaCO_3$ treatment provided higher tensile strength (45 MPa), impact strength (3.35 J), and hardness (27 BHN). Finally, the mechanical and tribological characterization of the samples was done with the aid of SEM (scanning electron microscope).

1. Introduction

Natural fiber-reinforced polymer composite materials have comprehensive interaction over the polymer matrix composite materials due to biodegradability and lower density compared to metals. Fiber surface modification is an identical technique to improve mechanical and tribological properties. In [1], the manual process for preparing the *Sansevieria cylindrica*/polyester composite is explained, and the properties of the unsaturated polyester are also given. It is concluded that the treated fibers have improved mechanical behavior than untreated fibers and good wettability. Fiber treatment separates the fiber and reduces the lignin content in the fiber while treated with $NaOH/Na_2SO_3$ [2]. The alkaline treatment (NaOH) increases the bonding of alfa fiber with the matrix, and the brittleness of the fiber also increases when the fiber is dipped 48 hours in the NaOH solution [3]. Natural fibers have extensive applications in the future. Natural fibers such as flax, hemp, and ramie have a definite mechanical characterization for various applications

[4]. *Sansevieria ehrenbergii* fiber, 30 mm length, treated 30 minutes with $KMnO_4$, and reinforced 30 percent fiber with polyester resin, provided good bonding than the untreated fiber [5]. The coir fiber-reinforced polyester composite is unsuitable for structural applications due to low flexural strength for increasing fiber concentration [6]. Polymer composites' void content and hydrophilic behavior at various temperatures fabricated through resin transfer molding are lower than other processing techniques [7]. The SEM analysis shows that randomly oriented untreated fibers do not give good bonding [8]. Alkali and silane treatments of the hemp fiber-reinforced polylactic acid (PLA) composite improve interfacial adhesion and increase the flexural strength. Generally, compared with short fibers, treated long fibers have higher flexural strength [9]. The surface morphology of treated coconut fiber composite shows excellent matrix-fiber adhesion [10]. Fiber treatment increased the tribological properties of the polymer composites impregnated with natural fibers [11]. *Pandanus* fiber/polyester composite provided significant improvement on the developed composites for the fiber with an average length of 40 mm. Fiber treatment is necessary to improve the mechanical properties of fiber-reinforced composite materials [12]. Silane treatment increased the tribological properties of the polymer composite by increasing the bonding strength [13].

Natural fibers are the best alternative to synthetic fibers such as glass and Kevlar, fulfilling the current green manufacturing requirement [14]. Natural fibers offer exceptional characteristics such as low density, great tensile strength, and lightness. Natural fibers are derived from various sections of fiber-producing plants. Natural fiber properties are determined by plant type, age, extraction technique, and the environment in which the plant was raised [15]. Various chemical treatments may decrease the incompatibility between plant fibers and polymer matrices. Different surface treatments on biofibers, such as benzoyl peroxide, potassium permanganate, stearic acid, and alkali treatment, improved the chemical, physical, and morphological characteristics of the fibers. Alkali treatment is the first treatment that changes fiber's surface by eliminating amorphous materials and contaminants from the surface [16]. The electrical, thermal, and mechanical properties of *Phaseolus vulgaris* fiber/unsaturated polyester composites have shown encouraging results for end-use applications [17]. It is critical to adjust the alkali treatment soaking time and concentration in order to achieve the fiber's desirable characteristics [18]. Polyester is defined by the Federal Trade Commission as synthetic fibers that form a long chain containing at least 85% by weight of an ester of a substituted aromatic carboxylic acid [19]. Since its debut in 1941, polyester has been one of the most widely utilized materials in the industry. Polyester accounted for about 69 percent of total fiber usage in 2017 [20].

The reinforcement and treatment are the following factors in changing the mechanical properties, enclosing this aspect in this study to evaluate mechanical and tribological properties for defined treating time of fiber (*Sansevieria ehrenbergii*) with the polyester composite.

2. Experimental Details

2.1. Materials. The leaves of *Sansevieria ehrenbergii* were used to extract snake grass fibers (SGFs) gathered from farms around Kanyakumari district, Tamil Nadu, India, by manual process. The chemicals such as sodium hydroxide, sodium carbonate, calcium carbonate, potassium permanganate, and hydrogen peroxide are used for treating the fiber outer surface to increase fiber roughness. The matrix used to prepare the composite material is unsaturated polyester resin with catalyst MEKP. Meanwhile, cobalt naphthenate was also used as an accelerator for the reaction. The matrix (unsaturated polyester), accelerator, and catalyst were supplied from M/S Leo Enterprise, Nagercoil, Tamil Nadu, India.

2.2. Surface Treatments for Fibers. The SGFs extracted from the plant were exposed to various surface treatments such as alkaline (NaOH), potassium permanganate, calcium carbonate, sodium carbonate, and hydrogen peroxide. Before treatment, SGFs were cut into 30 mm (optimum fiber length).

2.3. Alkali Treatment. The SGFs were dipped with 10% of NaOH solution with water for 3 hours. Then, the fibers were rinsed with pure water to remove the lignin content as well as excess chemicals. The fibers were dried for 3 hours in the oven at 70°C [2, 3].

2.4. Potassium Permanganate Treatment. In this treatment, the SGFs were dipped in a vessel containing 0.5% potassium permanganate with water for 3 h. Then, the fibers were cleaned with water. Finally, the fibers were dried for 3 hours in the oven at 70°C [2].

2.5. Calcium Carbonate Treatment. In this treatment, SGFs were soaked with 10% Ca_2CO_3 solution for 3 h. Then, the treated SGFs were rinsed with pure water. The fibers were dried with the aid of the oven for 3 hours in the oven at 70°C.

2.6. Sodium Carbonate Treatment. In this treatment, the SGFs were dipped in the solution for 3 h, which contains 10% of Na_2CO_3. Then, treated SGFs were rinsed with fresh water. The fibers were dried using the oven for 3 hours in the oven at 70°C.

2.7. Hydrogen Peroxide Treatment. The SGFs were dipped in a vessel containing 10% hydrogen peroxide solution with water for 3 h. The final process was done by cleaning the fiber with water. Then, treated fibers were dried in the oven for 3 hours at 70°C to remove the moisture content.

3. Fabrication of Composite Materials

The hand lay-up followed by the compression molding method was used to develop the samples [21]. The

composites were developed separately with untreated as well as chemically treated SGFs. Untreated SGFs were cut into 30 mm (optimal fiber length) [1].

SGFs (chemically treated) are cut into 30 mm length as it is a critical fiber length. The fiber content of 25% by weight was taken for preparing the composite samples [1]. The fibers were filled in the mold cavity and prepressed after closing the mold with mild steel plates to prepare the chopped fiber mat. Polyester resin (97.5%) was blended with the catalyst (2% of MEKP) and accelerator (0.5% of cobalt naphthenate) which are used as binding materials.

Degassed binding material was poured on a chopped fiber mat and spread over the fibers by using a brush. After that, the mold was closed, and 40 kN load was applied on the mild steel plate until complete closure, and this load was kept for 24 h [2]. The SGF-reinforced composite materials were prepared according to mold size. Similarly, the sample for alkali (NaOH), potassium permanganate-, calcium carbonate-, sodium carbonate-, and hydrogen peroxide-treated SGFs was prepared separately. Figure 1 shows the fabricated composite materials.

4. Experimental Study

4.1. Mechanical and Tribological Tests for the Prepared Composite Materials. Tensile test and three-point flexural test were done in Computerized Universal Testing Machine (TUE C-1000) with 100 ton capacity. This tensile testing is carried out under ASTM D638-01 with a crosshead speed of 1 mm/min [2]. Impact test was performed with a machine XJJU-5.5, and the ASTM standard is ASTM D256. The Brinell hardness testing machine examined the hardness value of the samples. To analyse the wear behavior of the samples, a two-body dry sliding wear test was conducted in the machine pin-on-disc wear tester. All the experiments are conducted properly, as mentioned in the respective ASTM standard, to avoid errors.

4.2. Scanning Electron Microscope. The reason for failure due to tensile and impact tests would be analysed by imaging analysis using the SEM instrument. SEM analysis was done by the JEOL model 6390 machine. The specimen was cut into $3 \times 3 \times 3\ mm^3$ size in the fracture region to take the SEM image. The magnification range of this machine is 50x–500,000x. It is working under the voltage range of 80 to 200 kV. The surface of the sample was laminated with a mild layer of gold for better conductivity.

5. Results and Discussion

5.1. Mechanical Characterization. The fabricated SGF-reinforced polymer composites undergone various tests to measure the mechanical properties. A variety of mechanical testing was done on the prepared composite materials, and their properties are evaluated. In Figure 2, stress developed against the load is high for $CaCO_3$-treated fiber-reinforced polyester composite material. For the untreated fiber, it is comparatively low because of the presence of lignin content which decreases the bonding strength. The tensile strength of the $CaCO_3$-treated fiber/polyester composite is 45.33 MPa. Moreover, from the three-point flexural test result, $CaCO_3$ treatment is comparatively good. It has a reasonable deflection due to bending until fracture, which leads to higher bending strength, as shown in Figure 3. Figure 4 indicates that the $CaCO_3$-treated fiber-reinforced polymer composite material has good resistance against the sudden load compared with other types of treated fiber-reinforced polymer materials. It has an impact strength of 3.35 Joule. The hardness of the developed samples was done with the aid of the Brinell hardness testing machine. The hardness of 27 BHN was obtained in the $CaCO_3$-treated fiber-reinforced polyester composite material which is comparatively higher than other treatments, as shown in Figure 5. The hardness of the material is probably related to the wear resistance of the material.

The NaOH-treated fiber-reinforced polymer composite poorly resists the sudden load due to higher treatment time. The $CaCO_3$-treated fiber-reinforced composite material has good surface hardness compared to other treated snake grass fiber-reinforced polymer composites.

5.2. Tribological Characterization. The coefficient of friction (CoF) of the $CaCO_3$-treated SGF-reinforced polyester was investigated using a pin-on-disc wear tester under the dry sliding wear condition. This treatment produces better properties compared with other treatment methods. The mechanical properties are improved at a significant level by treating with $CaCO_3$. So, $CaCO_3$-treated samples have been subjected to a wear test. To predict the outcome of the results, Taguchi method (L9 orthogonal array) was used. Different levels of input parameters are shown in Table 1, and the design table is given in Table 2.

The optimum level of the input parameter for obtaining minimum wear loss was identified through the signal-to-noise ratio (S/N) figure as shown in Figures 6 and 7 for wear loss and CoF. Trial run 1 (load = 10 N, sliding velocity = 2 m/s, and sliding distance = 500 m) produces minimum wear loss. The "lower-the-best" condition was implemented to find the minimum wear loss. The optimum CoF was achieved with a load of 10 N, a sliding velocity of 4 m/s, and a sliding distance of 1500 m. The "higher-the-best" condition was implemented to find optimum CoF as the wear of the material is analysed for the maximum roughness to evaluate the material's wear behavior. The fabricated material can be used in high gripping applications.

The influence level of each input parameter is calculated from Tables 3 and 4 for wear loss and CoF based on the delta value. For wear loss, the load is ranked as one, sliding distance is ranked as two, and sliding velocity is ranked as three. It described that the load provided more influence on the wear loss. For CoF, the sliding velocity is ranked as one, load is ranked as two, and sliding distance is ranked as three. It described that the sliding velocity provided more influence on the wear loss.

Tables 5 and 6 show the analysis of variance tables for wear loss and CoF. Table 5 contains degrees of freedom (DOFs), adjusted sum of squares (ASS), adjusted mean

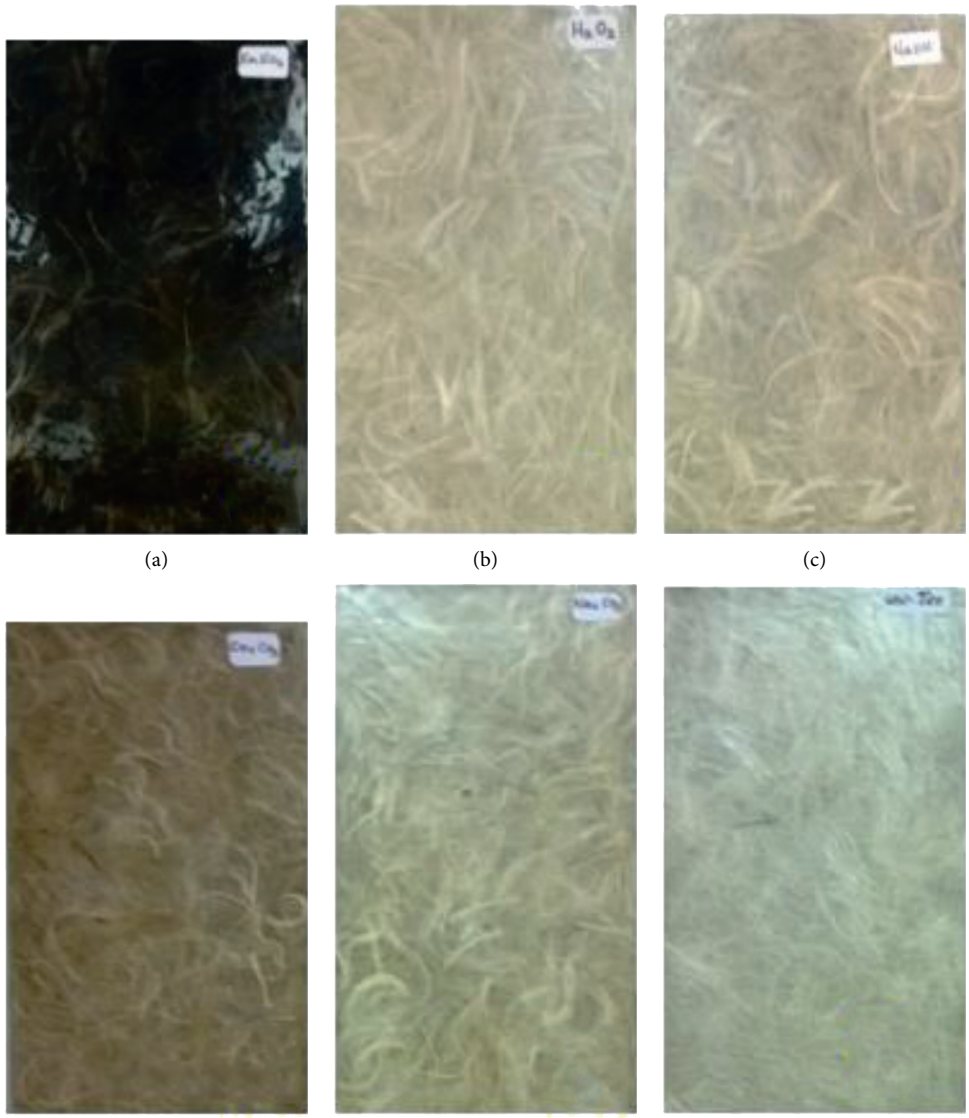

Figure 1: Fabricated composite materials: (a) potassium permanganate-treated composite, (b) hydrogen peroxide-treated composite, (c) alkali (NaOH) treated composite, (d) calcium carbonate-treated composite, (e) sodium carbonate composite, and (f) untreated composite.

square (AMS), F-value, and P value for analysis. The analysis described 95% confidence level and 5% significant level of the parameters. In the wear loss table, Adj SS and Adj MS values are below 0.05, emphasizing that the model is more significant. For wear loss, the P values of load, sliding velocity, and sliding distance are 0.38, 0.18, and 0.496, respectively. Hence, the impact of sliding distance is more on wear loss. The P value of load, sliding velocity, and sliding distance for CoF is 0.238, 0.159, and 0.185, respectively. The load has more P value, which emphasizes that the load has more influence on CoF.

The linear regression equation to identify the wear loss and CoF for any value within the domain was predicted using equations (1) and (2). All coefficient values of the wear loss equation are below 0.05, which means the model is more significant. The siding distance has a negative coefficient. It indicates that the sliding distance increases with the decrease in wear loss. In the wear loss equation, both load and sliding velocity values are positive, emphasizing that these values increase with an increase in wear loss. The coefficient of load in the CoF equation is negative, which describes that the CoF decreases while increasing the load. The coefficient values of sliding velocity and sliding distance are positive, showing that the CoF increases while increasing the sliding velocity and sliding distance.

$$\begin{aligned}\text{Wear loss} = {} & -0.00291 + 0.000153\,\text{load (N)} \\ & + 0.000833\,\text{sliding velocity (m/s)} \\ & - 0.000001\,\text{sliding distance (m)},\end{aligned} \tag{1}$$

$$\begin{aligned}\text{CoF} = {} & -0.114 - 0.0214\,\text{load (N)} \\ & + 0.265\,\text{sliding velocity (m/s)} \\ & + 0.000491\,\text{sliding distance (m)}.\end{aligned} \tag{2}$$

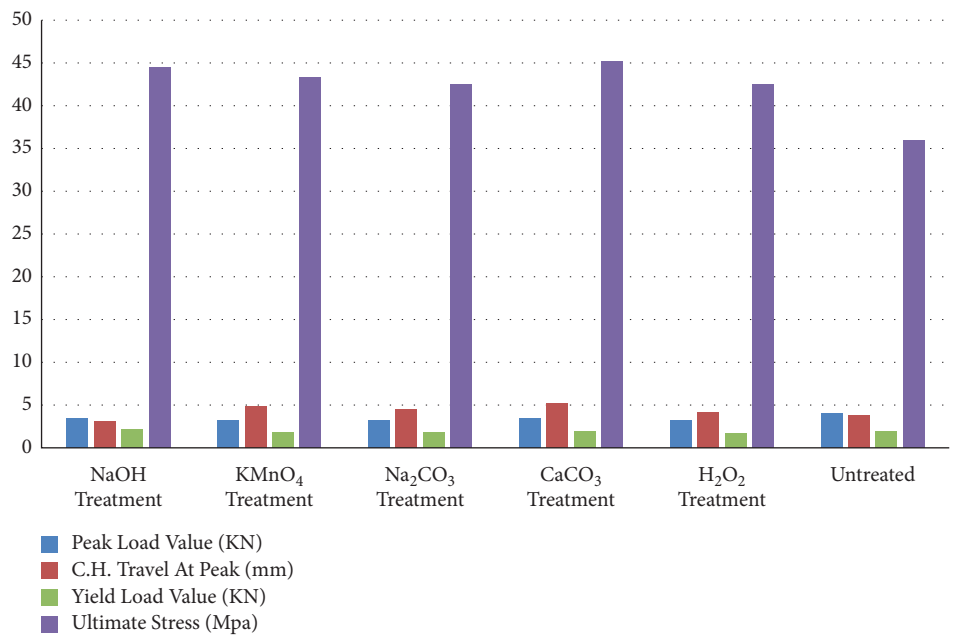

Figure 2: Ultimate tensile strength vs. treated and untreated fibers with polyester.

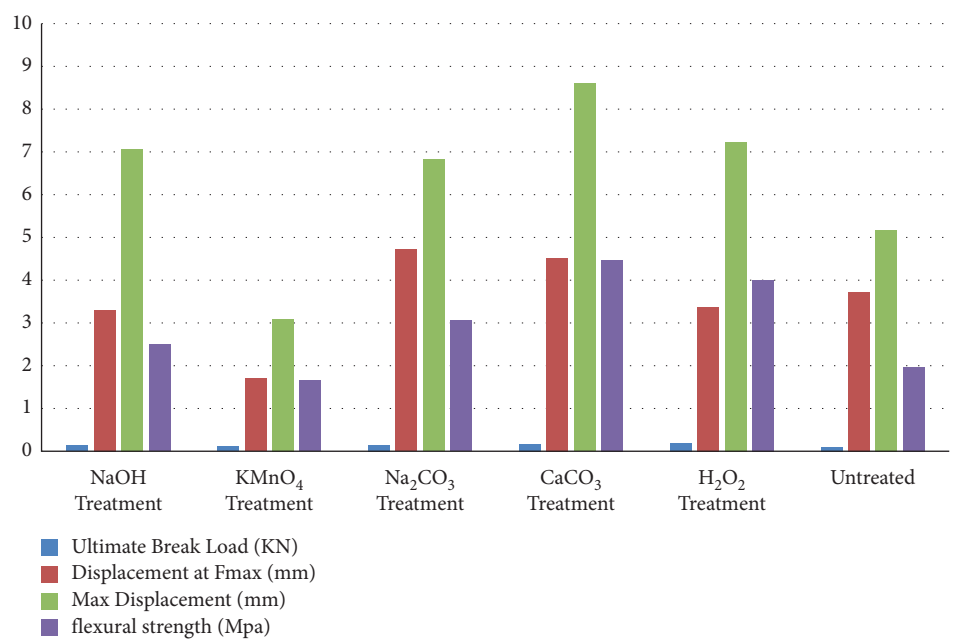

Figure 3: Ultimate flexural strength vs. treated and untreated fibers with polyester.

The interaction and independent effect of parameters on wear loss and CoF are identified in the contour plot of Figures 8 and 9. Different colours with their respective values are listed in the figure. Light colour represents the minimum value, and dark colour represents the maximum value. Figure 8(a) depicts the interaction and independent effect of load as well as sliding velocity on wear loss. The independent effect of load and sliding velocity increases with a slight increase in wear loss. Wear loss increases due to the interaction effect of load and sliding velocity. Trial run 9 (load = 30 N and sliding velocity = 4 m/s) produces the maximum outcome. The interaction and independent effects of load and sliding distance on wear loss are depicted in Figure 8(b). From the results, it was clear that the wear loss increases steeply while increasing the load. The sliding distance increases with a decrease in wear loss. The load-sliding distance interaction effect significantly increases the wear loss.

The interaction and independent effect of load and sliding velocity on CoF are depicted in Figure 9(a). Sliding

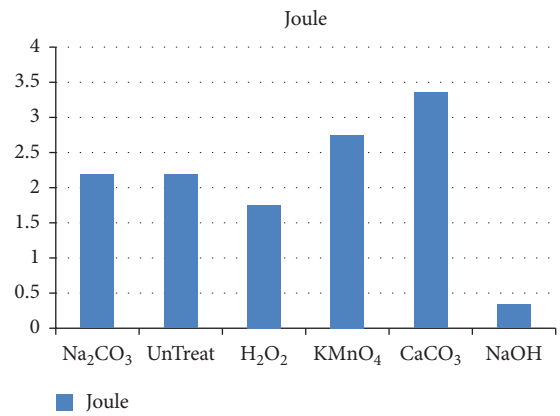

Figure 4: Impact strength (Joule) vs. treated and untreated SGFs with polyester.

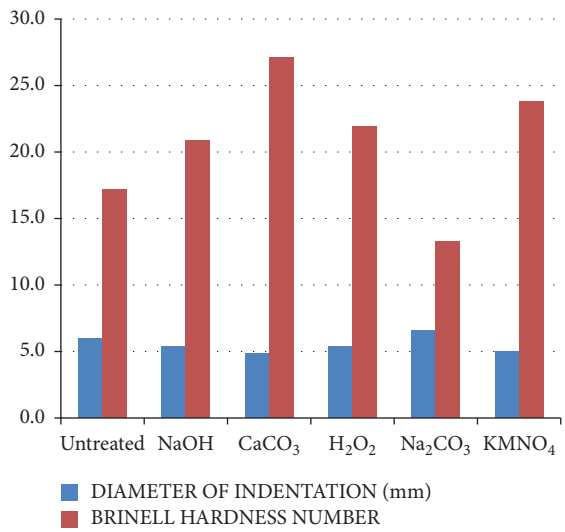

Figure 5: BHN vs. treated and untreated SGFs with polyester.

Table 1: Level of factors.

Name	Units	Levels		
		1	2	3
Load	N	10	20	30
Sliding velocity	m/s	2	3	4
Sliding distance	m	500	1000	1500

Table 2: Design table.

Run	Load (N)	Sliding velocity (m/s)	Sliding distance (M)	Wear loss	CoF
1	10	2	500	0.0006	0.526
2	10	3	1000	0.0007	0.644
3	10	4	1500	0.0004	0.609
4	20	2	1000	0.0012	0.487
5	20	3	1500	0.0018	0.582
6	20	4	500	0.0013	0.549
7	30	2	1500	0.0021	0.602
8	30	3	500	0.0037	0.644
9	30	4	1000	0.0061	0.647

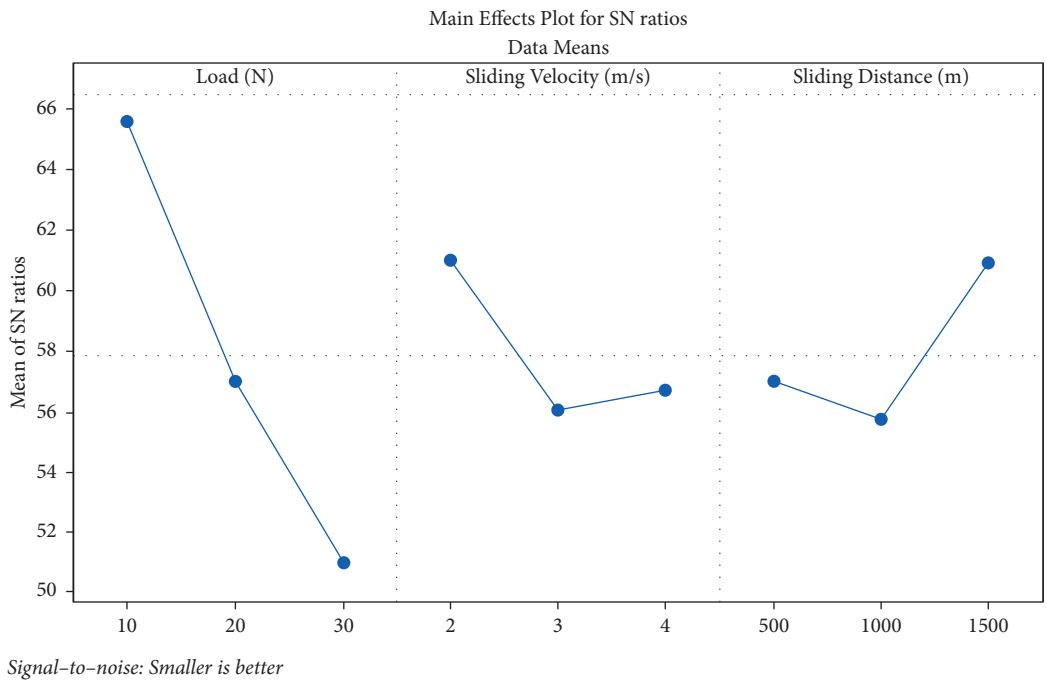

Figure 6: Main effects' plot for the S-N ratio of wear loss.

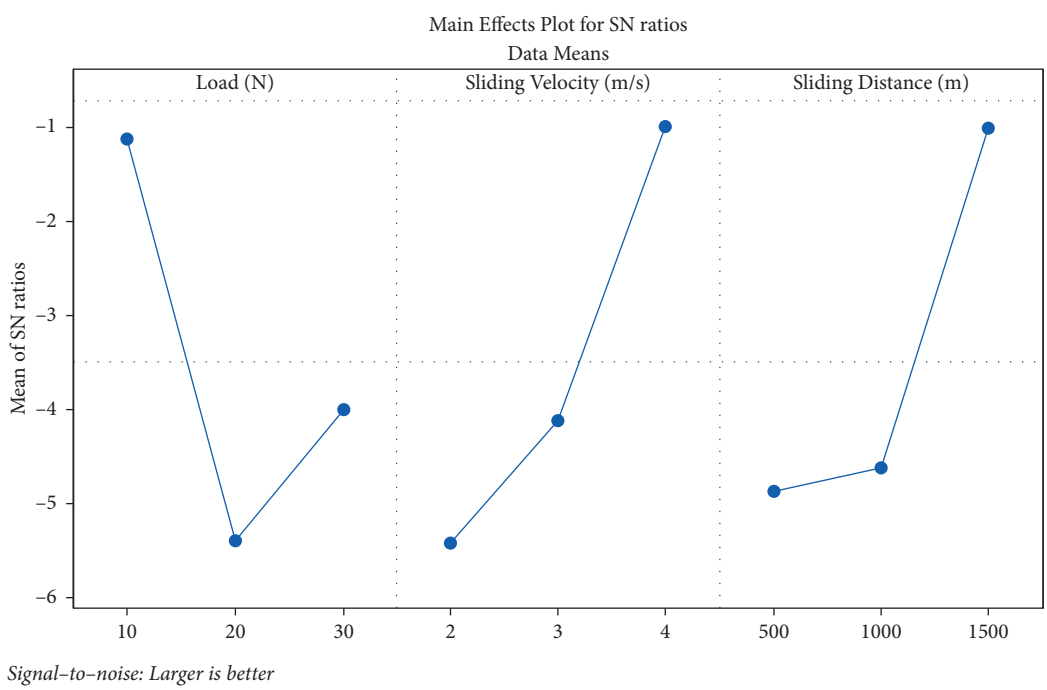

Figure 7: Main effects' plot for the S-N ratio of CoF.

Table 3: S/N ratio value of wear loss.

Level	Load (N)	Sliding velocity (m/s)	Sliding distance (m)
1	65.61	60.95	56.93
2	57.01	55.99	55.72
3	50.98	56.66	60.95
Delta	14.63	4.96	5.24
Rank	1	3	2

Table 4: Signal-to-noise ratio value of CoF.

Level	Load (N)	Sliding velocity (m/s)	Sliding distance (m)
1	−1.1143	−5.4126	−4.8704
2	−5.3865	−4.1154	−4.6179
3	−4.0041	−0.9770	−1.0167
Delta	4.2722	4.4356	3.8537
Rank	2	1	3

Table 5: ANOVA test for wear loss.

Source	DOF	ASS	AMS	*F*-value	*P* value
Regression	3	0.000019	0.000006	3.59	0.101
Load (N)	1	0.000014	0.000014	7.90	0.038
Sliding velocity (m/s)	1	0.000004	0.000004	2.33	0.187
Sliding distance (m)	1	0.000001	0.000001	0.54	0.496
Error	5	0.000009	0.000002		
Total	8	0.000028			

Table 6: ANOVA test for CoF.

Source	DOF	ASS	AMS	*F*-value	*P* value
Regression	3	1.0591	0.3530	2.30	0.195
Load (N)	1	0.2756	0.2756	1.79	0.238
Sliding velocity (m/s)	1	0.4213	0.4213	2.74	0.159
Sliding distance (m)	1	0.3621	0.3621	2.36	0.185
Error	5	0.7685	0.1537		
Total	8	1.8276			

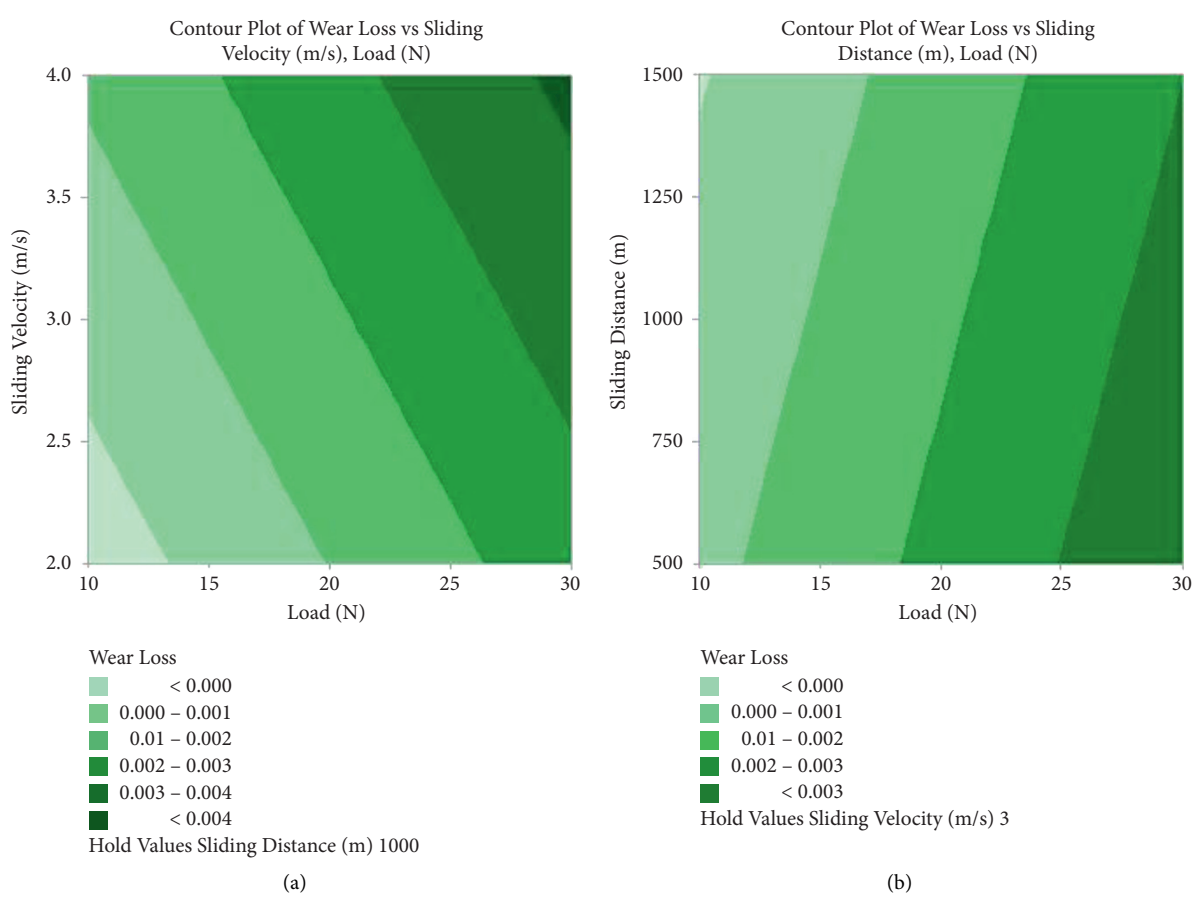

Figure 8: Wear loss (contour plot). (a) Load vs. sliding velocity. (b) Load vs. sliding distance.

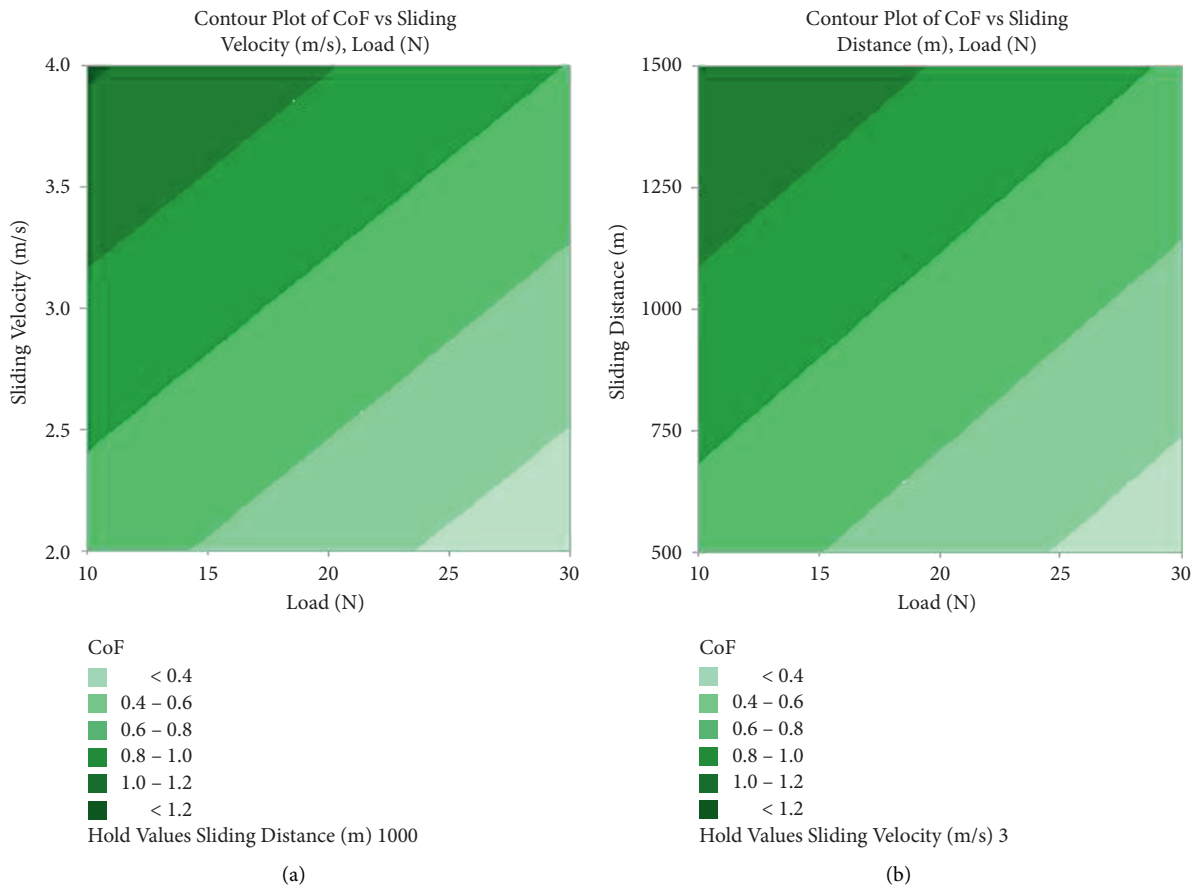

Figure 9: CoF (contour plot). (a) Load vs. sliding velocity. (b) Load vs. sliding distance.

velocity increases the outcome of CoF. However, the load increases with the decrease in CoF. CoF increases due to the interaction effect of load and sliding velocity. The optimum result was obtained at the load of 10 N and sliding velocity of 4 m/s. Figure 9(b) shows the interaction and independent effect of load and sliding distance on CoF. The sliding distance increases with an increase in CoF. The interaction effect is not significantly affecting the CoF.

5.3. Scanning Electron Microscope (SEM) Analysis. SEM images revealed the inadequate bonding of SGFs with polyester. Under tensile and impact loading, matrix-fiber debonding, fiber pullout, matrix fracture, and fiber fracture were seen in both the untreated snake fibers with polyester and the NaOH-treated snake grass fibers with polyester composites. From the tensile and impact fractography results, it was clear that $CaCO_3$-treated snake grass fiber with polyester was good. Under tensile and impact loading, matrix and fiber fracture was the most common failure mechanism in short $CaCO_3$-treated snake grass fiber with polyester composites. Figures 10(a)–10(c) show tensile test images of the untreated fiber with polyester and $CaCO_3$-treated fiber with polyester composite, respectively. Figures 11(a) and 11(b) show the impact test images of the NaOH-treated fiber with polyester and $CaCO_3$-treated fiber with polyester composite, respectively.

The SEM images of the $CaCO_3$ composite materials (worn surface) are given in Figure 12. Figure 12(a) shows the SEM images of the worn surface for the minimum input conditions (load = 10 N, sliding velocity = 2 m/s, and sliding distance = 500 m). It shows very minimum wear on the surface due to the strong matrix-fiber bonding. The contour plot emphasizes that both sliding distance and sliding velocity do not cause any effect on the wear loss. Similarly, minimum damages occurred at maximum sliding velocity and sliding distance, as shown in Figure 12(b). The main wear mechanisms are matrix pitting, microgrooves, and debris. More damages occurred at the maximum load condition, as shown in Figure 12(c). High wear loss occurred due to increased load (high pressure), which broke the interlaminar structure's cohesive and adhesive bonds. The main wear mechanisms are matrix cutting, fiber-matrix detachment, matrix pitting, and delamination.

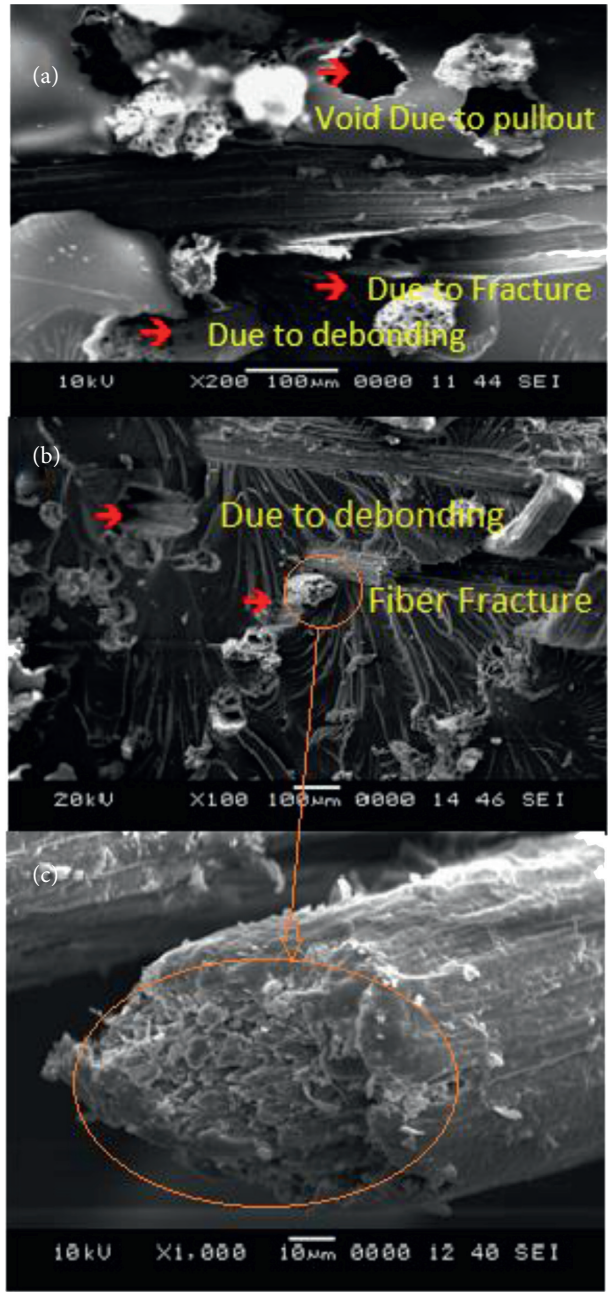

Figure 10: Tensile test: (a) untreated fiber with polyester; (b, c) $CaCO_3$-treated fiber with polyester.

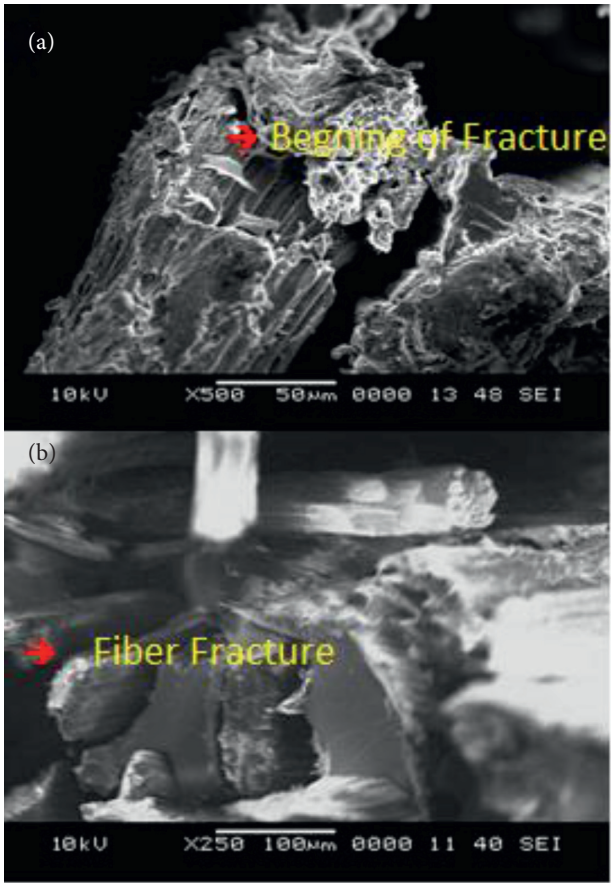

Figure 11: Impact test: (a) NaOH-treated fiber with polyester; (b) $CaCO_3$-treated fiber with polyester.

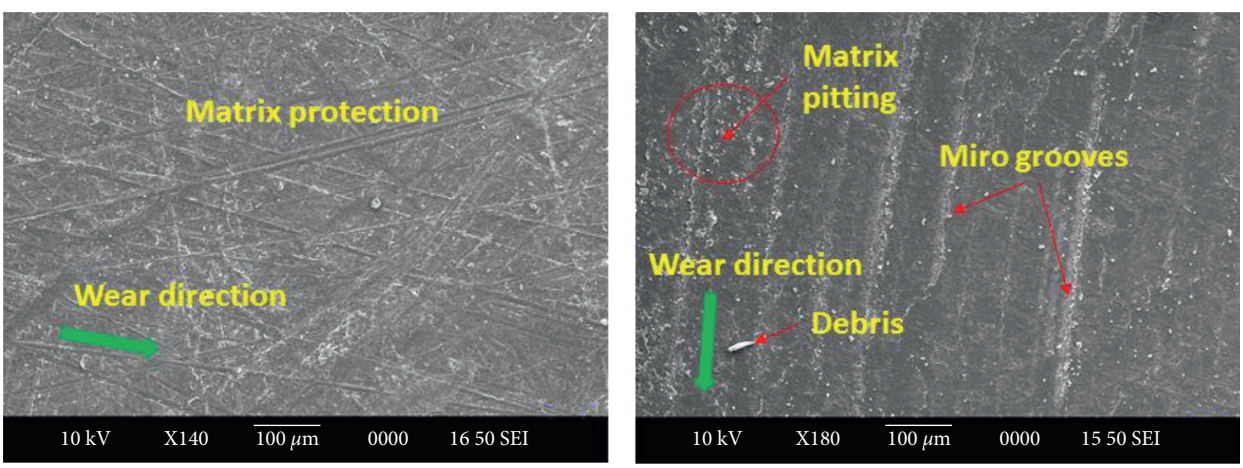

(a) (b)

Figure 12: Continued.

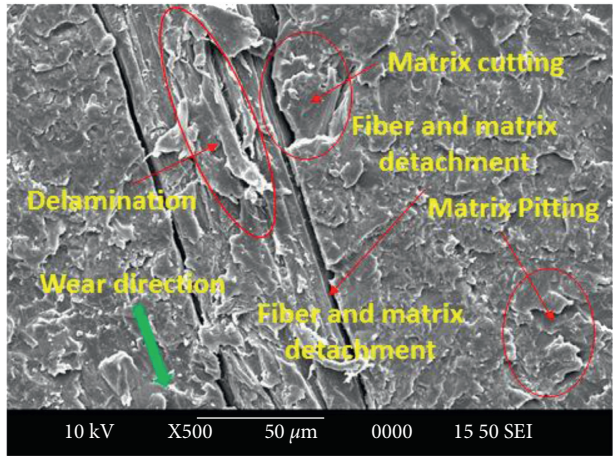

(c)

Figure 12: SEM images of worn surfaces using a variety of input parameters such as load, sliding velocity, and sliding distance. (a) 10 N, 2 m/s, and 500 m. (b) 10 N, 4 m/s, and 1500 m. (c) 30 N, 4 m/s, and 1000 m.

6. Conclusion

In this work, snake grass fiber (*Sansevieria ehrenbergii*) was treated with different chemicals such as NaOH, potassium permanganate, calcium carbonate, sodium carbonate, and hydrogen peroxide to eliminate lignin for getting better fiber-reinforced polyester composite materials. The experimental investigation of mechanical and tribological behavior of treated SGF-reinforced polyester composites derives the following conclusions:

(i) This research demonstrates that the successful manufacture of chemical-treated snake grass fiber-reinforced polyester composites with 25% fiber reinforcement was done by the hand lay-up method.

(ii) Calcium carbonate-treated fiber-reinforced polyester composite has the highest hardness value of 27 BHN in the hardness test, which is more than 50% compared to untreated snake grass fiber-reinforced polyester composite materials.

(iii) From the tensile test, the calcium carbonate-treated reinforced composite has high mean ultimate strength of 45.335 N/mm^2.

(iv) Calcium carbonate-treated fiber-reinforced composite has a high impact strength of 3.35 J. Ca_2CO_3-treated fiber-reinforced composite has a high ultimate flexural strength of 4.5 N/mm^2.

(v) In the overall view, the newly experimented calcium carbonate-treated fiber-reinforced composite has very good mechanical properties.

(vi) The SEM images of the fractured samples showed the reason for the poor adhesion and fiber fraction for untreated fiber-reinforced polymer composite materials. After the treatment, comparatively good adhesion, decrement in fiber pullout, and minimum debonding were identified. The maximum damages occurred at 30 N load, which is substantiated by SEM images. Sliding velocity and sliding distance increased with an increase in CoF. The identified main wear mechanisms are matrix cutting, matrix pitting, microgrooves, delamination, fiber-matrix detachment, and debris.

(vii) $CaCO_3$ treatment is inevitable to improve the wear resistance. Because of the strong fiber-matrix adhesion, sliding velocity and sliding distance have negligible wear loss. However, applied load increases with an increase in wear loss.

Data Availability

The data used to support the findings of this study are included within the article.

Conflicts of Interest

The authors declare that there are no conflicts of interest regarding the publication of this article.

Acknowledgments

The authors thank Seenu Atoll School, Hulhumeedhoo, Maldives, and Kalaignar Karunanidhi Institute of Technology, Coimbatore, for providing the facility support to complete this research work and this project was supported by Researchers Supporting Project number (RSP-2021/385) King Saud University, Riyadh, Saudi Arabia.

References

[1] V. S. Sreenivasan, D. Ravindran, V. Manikandan, and R. Narayanasamy, "Influence of fibre treatments on mechanical properties of short Sansevieria cylindrica/polyester composites," *Materials & Design*, vol. 37, pp. 111–121, 2012.

[2] G. W. Beckermann and K. L. Pickering, "Engineering and evaluation of hemp fibre reinforced polypropylene composites: fibre treatment and matrix modification," *Composites*

Part A: Applied Science and Manufacturing, vol. 39, no. 6, pp. 979–988, 2008, Jun. 2008.

[3] M. Rokbi, H. Osmani, A. Imad, and N. Benseddiq, "Effect of chemical treatment on flexure properties of natural fiber-reinforced polyester composite," *Procedia Engineering*, vol. 10, pp. 2092–2097, 2011, Jan. 2011.

[4] D. B. Dittenber and H. V. S. Gangarao, "Critical review of recent publications on use of natural composites in infrastructure," *Composites Part A: Applied Science and Manufacturing*, vol. 43, no. 8, pp. 1419–1429, 2012.

[5] T. Sathishkumar, P. Navaneethakrishnan, S. Shankar, R. Rajasekar, and N. Rajini, "Characterization of natural fiber and composites - a review," *Journal of Reinforced Plastics and Composites*, vol. 32, no. 19, pp. 1457–1476, 2013.

[6] J. Almeida, S. N. Monterio, and L. A. H. Terrones, "Mechanical properties of coir/polyester composites," *Elseveir Polym. Test.*vol. 27, pp. 591–595, 2008.

[7] P. A. Sreekumar, K. Joseph, G. Unnikrishnan, and S. Thomas, "A comparative study on mechanical properties of sisal-leaf fibre-reinforced polyester composites prepared by resin transfer and compression moulding techniques," *Composites Science and Technology*, vol. 67, no. 3-4, pp. 453–461, 2007, Mar. 2007.

[8] V. S. Sreenivasan, D. Ravindran, V. Manikandan, and R. Narayanasamy, "Mechanical properties of randomly oriented short Sansevieria cylindrica fibre/polyester composites," *Materials & Design*, vol. 32, no. 4, pp. 2444–2455, 2011, Apr. 2011.

[9] M. A. Sawpan, K. L. Pickering, and A. Fernyhough, "Flexural properties of hemp fibre reinforced polylactide and unsaturated polyester composites," *Composites Part A: Applied Science and Manufacturing*, vol. 43, no. 3, pp. 519–526, 2012, Mar. 2012.

[10] D. R. Mulinari, C. A. R. P. Baptista, J. V. C. Souza, and H. J. C. Voorwald, "Mechanical properties of coconut fibers reinforced polyester composites," *Procedia Engineering*, vol. 10, pp. 2074–2079, 2011, Jan. 2011.

[11] H. H. Parikh and P. P. Gohil, "Sliding wear experimental investigation and prediction using response surface method: fillers filled fiber reinforced composites," *Materials Today: Proceedings*, vol. 18, pp. 5388–5393, 2019.

[12] G. V. Vigneshwaran, I. Jenish, and R. Sivasubramanian, "Design, fabrication and experimental analysis of pandanus fibre reinforced polyester composite," *Advanced Materials Research*, vol. 984-985, no. 985, pp. 253–256, 2014.

[13] J. R. Prabhu Stalin, I. Jenish, and S. Indran, "Tribological charecterization of carbon epoxy composite materials with particulate silane treated SiC fillers," *Advanced Materials Research*, vol. 984-985, no. 985, pp. 331–335, 2014.

[14] V. K. Thakur, M. K. Thakur, and R. K. Gupta, "Review: raw natural fiber-based polymer composites," *International Journal of Polymer Analysis and Characterization*, vol. 19, no. 3, pp. 256–271, 2014.

[15] A. Saravana Kumaar, A. Senthilkumar, T. Sornakumar, S. S. Saravanakumar, and V. P. Arthanariesewaran, "Physicochemical properties of new cellulosic fiber extracted from carica papaya bark," *Journal of Natural Fibers*, vol. 16, no. 2, pp. 175–184, 2017.

[16] S. S. Saravanakumar, A. Kumaravel, T. Nagarajan, and I. G. Moorthy, "Investigation of p-chemical properties of alkali-TreatedProsopis julifloraFibers," *International Journal of Polymer Analysis and Characterization*, vol. 19, no. 4, pp. 309–317, 2014.

[17] B. Gurukarthik Babu, D. Prince Winston, P. V. Aravind Bhaskar, R. Baskaran, and P. Narayanasamy, "Exploration of electrical, thermal, and mechanical properties of Phaseolus vulgaris fiber/unsaturated polyester resin composite filled with nano-SiO2," *Journal of Natural Fibers*, vol. 18, no. 12, pp. 2156–2172, 2021.

[18] G. B. Balachandran, P. W. David, A. B. P. Vijayakumar, A. E. Kabeel, M. M. Athikesavan, and R. Sathyamurthy, "Enhancement of PV/T-Integrated single slope solar desalination still productivity using water film cooling and hybrid composite insulation," *Environmental Science and Pollution Research*, vol. 27, no. 26, pp. 32179–32190, 2019.

[19] T. Sabu, K. Joseph, S. K. Malhotra, K. Goda, and M. S. Sreekala, *Polymer Composites Macro- and Microcomposites*, Wiley VCH, Weinheim, Germany, 2014.

[20] C. Vigneswaran, M. Ananthasubramanian, and P. Kandhavadivu, *Bioprocessing of Textiles*, Woodhead Publishing India PVT LTD, New Delhi, 2014.

[21] R. Ganesamoorthy, R. Meenakshi Reddy, T. Raja et al., "Studies on mechanical properties of kevlar/napier grass fibers reinforced with polymer matrix hybrid composite," *Advances in Materials Science and Engineering*, vol. 2021, pp. 1–9, 2021.

Hindawi
Advances in Materials Science and Engineering
Volume 2021, Article ID 5835867, 11 pages
https://doi.org/10.1155/2021/5835867

Research Article

Comparative Study of Mechanical Properties and Thermal Stability on Banyan/Ramie Fiber-Reinforced Hybrid Polymer Composite

T. Raja,[1] S. Ravi,[2] Alagar Karthick,[3] Asif Afzal,[4,5] B. Saleh,[6] M. Arunkumar,[7] Ram Subbiah,[8] P. Ganeshan,[9] and S. Prasath[10]

[1]*Department of Mechanical Engineering, Vel Tech Rangarajan Dr. Sagunthala R&D Institute of Science and Technology, Chennai 600062, India*
[2]*Centre for Materials Research, Chennai Institute of Technology, Chennai 600069, India*
[3]*Renewable Energy Lab, Department of Electrical and Electronics Engineering, KPR Institute of Engineering and Technology, Coimbatore 641407, Tamil Nadu, India*
[4]*Department of Mechanical Engineering, P.A. College of Engineering (Affiliated to Visvesvaraya Technological University, Belagavi), Mangalore 574153, Tamil Nadu, India*
[5]*Department of Mechanical Engineering, School of Technology, Glocal University, Delhi-Yamunotri Marg, SH-57, Mirzapur Pole, Saharanpur, Uttar Pradesh 247121, India*
[6]*Mechanical Engineering Department, College of Engineering, Taif University, P.O. Box 11099, Taif 21944, Saudi Arabia*
[7]*Department of Agriculture Engineering, Sri Shakthi Institute of Engineering and Technology, Coimbatore 641062, Tamil Nadu, India*
[8]*Department of Mechanical Engineering, Gokaraju Rangaraju Institute of Engineering and Technology, Nizampet, Hyderabad 500090, India*
[9]*Department of Mechanical Engineering, Sethu Institute of Technology, Virudhunagar 626115, Tamil Nadu, India*
[10]*Department of Mechanical Engineering, College of Engineering and Technology, Mizan Tepi University, Tepi Campus, Tepi 121, Ethiopia*

Correspondence should be addressed to T. Raja; rajasd28@gmail.com

Received 8 July 2021; Accepted 13 November 2021; Published 17 December 2021

Academic Editor: Pawel Klosowski

The usage of natural fibers has increased recently. They are used to replace synthetic fiber products in aircraft and automobile industries. In this study, natural fibers of bidirectional banyan mat and ramie fabrics are used for reinforcement, and the matrix is an epoxy resin to fabricate composite laminates by traditional hand layup technique at atmospheric temperature mode. Five different sequences of reinforcements are as follows to quantify the effect of thermal stability and mechanical behavior of silane-treated and untreated hybrid composites. The results revealed that silane-treated fabric composite laminates were given enhanced mechanical properties of 7% tensile, 11% flexural, and 9% impact strength compared with untreated fabric composite, and at the same time when the increasing of ramie fabric was given the positive influence of 41% improved tensile strength of 40.7 MPa, 49% improved in flexural strength of 38.9 MPa and negative influence in 57% lower impact strength in sample E and positive value in sample A 21.12 J impact energy absorbed in the hybrid composite. Thermogravimetric analysis (TGA) revealed the thermal stability of the hybrid composite. In sample A, the thermal stability is more than in other samples, and 410°C is required to reduce the mass loss of 25%. The working mass condition of the hybrid composite is up to 3.25 g after it moves to degrade.

1. Introduction

The expanding interest in ecological cordial materials and the longing to diminish the expense of conventional fiber leads to the improvement of normal fiber composites. Normal fibers are described by indistinguishable parameters and properties from every single fiber and are relied upon to offer equivalent strengthening impacts in a network as their manufactured partners, even though the productivity and level of support might be unique [1]. It is essential to know the reaction of materials under effect stacking to accomplish dependable polymer composite structures. One of the powerless purposes of fiber-strengthened composites is their powerlessness to affect stacking contrasted with metallic structures. The effect prompting harm to structures by outside articles is a test for the creator because of the low effect opposition of the fiber-strengthened composites [2]. It is essential to know the reaction of materials under effect stacking to accomplish dependable polymer composite structures. One of the powerless purposes of fiber-strengthened composites is their powerlessness to affect stacking contrasted with metallic structures. The effect prompting harm to structures by outside articles is a test for the creator because of the low effect opposition of the fiber-strengthened composites [3]. Aramid composites are not as acceptable in compressive quality as glass or carbon composites. Dry aramid fibers are intense and have been utilized as links or ropes and habitually utilized in ballistic applications. Kevlar is maybe the most popular case of aramid fiber. Aramid is the prevalent natural fortifying fiber material for the replacement of steel belting in tires [4]. In a fiber-strengthened polymer, the fibers fill in as support while the assignments of the framework are to hold the strands together, to transmit the shear force, and to function as a covering [5]. The chemical composition also affects the properties of the composite with a percentage of cellulose, hemicellulose, lignin, and waxes. Numerous research work has evidenced the availability, demands, and properties of natural fibers used in polymeric matrices [6].

A successful strategy for improving the effect properties of graphite fiber strengthened composites is to add to them a little level of low modulus high-quality glass strands. Other than improving effect execution, the consolidation of glass strands diminishes the cost, which is confinement for the use of graphite fiber composites [7]. Mechanical testing or structure test is performed to decide the different mechanical properties of materials; there are a few sorts of tests to decide the different mechanical and physical properties of the material. The accuracy aftereffects of these tests are used to decide the practicality of materials for the field application [8]. The capacity to oppose breaking under tractable pressure is one of the most significant and broadly estimated properties of materials utilized in basic applications [9]. The PALF composite revealed that it has low tensile, flexural strength, and high impact strength, and flexural modulus. The hybrid composite offered good tensile and flexural strength by adding KF to 70% by weight. The PALF raised the impact strength and percentage of energy absorption and flexural modulus of the 3P7K hybrid composite [10]. The advancement on regular fiber hybrid composites was observed for cutting edge applications. Natural fiber, as a substitution of designed fiber, has been one of the most inquired about subjects over the previous years. This is because of its inalienable properties, for example, biodegradability, inexhaustibility, and plentiful accessibility when contrasted with manufactured fibers. Manufactured fibers are obtained from limited assets (nonrenewable energy sources) and are in this way influenced chiefly by instability of oil costs and their gathering in the earth or potential landfill destinations which are their primary disadvantages. Their mechanical properties and thermal properties outperform those of regular strands. A mix of these strands/fillers, as fortification of different polymeric materials, offers new chances to create multifunctional materials and structures for cutting edge applications [11]. This article expects to cover late advancements from 2013-forward-thinking on hybrid composites, because of regular fibers with different fillers. Crossover composites planning and portrayal towards their relevance in cutting edge applications and the present difficulties are likewise displayed. The thermal conduct and dynamic mechanical examination of *Pennisetum purpureum*/glass-strengthened hybrid composites were explored. Hybrid composite insulation was manufactured utilizing untreated, 5%, or 10% alkali-treated *Pennisetum purpureum* filaments with woven E-glass fibers and epoxy resin [12]. Thermogravimetric (TG) investigation showed that the measure of a build-up of the hybrid composites diminished as the grouping of the alkali used to treat the *Pennisetum purpureum* filaments expanded. The cracked surface morphology of the examples showed that improved fiber network interfacial holding was accomplished for the 5% antacid treated *Pennisetum purpureum*/glass hybrid composites [13].

In this present research, from the above-stated work, natural fibers selected from banyan and ramie fibers are treated with silane solution and without treatment used as reinforcement for the adhesion of epoxy matrix to fabricate five different sequences and analyze the mechanical properties of the treated and untreated hybrid composite, based on the significant results from treated composite laminates to study the thermal stability of mass loss and time taken to degrade the material in silane-treated hybrid composite.

2. Materials and Methods

2.1. Materials Overview. Banyan and ramie fiber are the prime materials to fabricate the hybrid composite. Bidirectional banyan mat is supplied by Natural Fabrics, Mumbai, India, and a ramie fabric mat is supplied by Gogreen Products, Chennai, India. The matrix materials of LY556, epoxy resin, hardening HY951, and mold releasing agent of liquid wax were supplied by Javanthi enterprisers, Chennai, India. The physical and chemical properties of the materials used are given in Table 1 [14, 15].

2.2. Fabrication Process of the Hybrid Composite. The research initiates with the collection of natural fibers of banyan and ramie mat. Sequential to the fiber preparation, it is chemically treated with the silane solution of triethoxy-(ethyl) silane solution (pH = 4) for 2 hrs, and it can be dried 3 hrs at 90°C in a hot furnace which is used to improve the mechanical properties of the hybrid composite [16]. The

Table 1: General properties of banyan and ramie fibers.

Sl. no.	Details	Banyan fiber	Ramie fiber
1	Density	1.92 g/cm^3	1.50 g/cm^3
2	Tensile strength	51 MPa	47.7 MPa
3	Young's modulus	1.5 GPa	1.3 GPa
4	Cellulose	16%	68.6%
5	Lignin	14%	0.6%

fabrication process of the hybrid composites was done with the hand layup method. The matrix phase combining Bisphenol-F LY556 epoxy polymer and Araldite HY 951 hardener is used for the better bonding properties of the natural fibers [17]. The comparative study between the samples fabricated with two sets shows that they are treated with silane solution and without fiber treatment to check the mechanical properties, and based on this, thermogravimetric analysis was carried out with an effective set of treated samples of hybrid composite. The motive of the testing of these samples is to verify which weight fraction of the hybrid composition obtained a better result in terms of mechanical and thermal behavior [18]. The weight concentration of banyan/ramie hybrid composite was given in Table 2.

2.3. Testing of the Hybrid Composite. After the successful fabrication, the material is subjected to mechanical testing and followed by thermal analysis. The strength of the fabricated natural fiber-reinforced composite is tested by tensile, flexural, and impact strength and hardness under loading conditions [19]. The experiments are conducted as per the ASTM standard, as follows: ASTM D638 dimension is 3.2 mm × 13 mm × 165 mm for tensile strength, ASTM D790 dimension is 3.2 mm × 12.7 mm × 125 mm for flexural strength, ASTM D 370 dimension is 3.2 mm × 12.7 mm × 64 mm for impact strength, and their deflections of samples were recorded and categorized for finding the better combination of fiber fraction [20]. Moreover, the thermal stability can be obtained from thermogravimetric analysis with ASTM E1131, and the testing standard was followed for this hybrid composite. Figure 1 shows the testing samples of silane-treated and untreated samples, and Figure 2 shows the experimental setup of tensile testing and SEM analysis equipment. The schematic flow of thermogravimetric analysis is shown in Figure 3.

3. Results and Discussion

3.1. Mechanical Properties of the Hybrid Composite

3.1.1. Tensile Strength. The tensile strength of ramie/banyan hybrid composite is graphically shown in Figure 4. It is observed that increasing the banyan fiber layer was given higher tensile strength compared to increasing ramie fiber loading. In sample E was given a maximum tensile strength of 40.7 MPa and 38.06 MPa, respectively. The standard deviation was calculated using

$$s = \sqrt{\frac{1}{N-1}\sum_{i=1}^{N}\left(x_i - \overline{x}\right)^2}. \quad (1)$$

In each sample, five different specimens were taken for calculating the better results. The error bar indicates the average value of all the tested samples of hybrid composite. The standard deviation was calculated for five samples in all the experiments: tensile, flexural, and impact strength of the hybrid composite. The standard deviation between five samples for tensile strength is 7.23 for silane-treated samples, and for untreated samples, the standard deviation is 7.69. Similar work was done with natural fibers of kenaf/grass fibers composite showing the 8.65 standard deviations [20]. Therefore, in silane treatment, the standard deviation was 5% smaller, with improved tensile strength of the hybrid composite. The maximum tensile strength was obtained for sample E, and the standard deviation calculated with five specimens of sample E is 0.502 for silane-treated samples and 0.364 for untreated samples. A similar way was followed for other samples of hybrid composite; the tensile test results of epoxy composite laminates are given in Table 3. Therefore, the standard deviation for the silane-treated sample A is 24 ± 0.23 and for the untreated sample is 19 ± 0.13.

The major objective of this study is focused on the difference between the chemically treated and untreated reinforcements that can reveal the mechanical properties of ramie/banyan hybrid composite. Therefore, the tensile strength of the hybrid composite clearly shows that the silane-treated fiber mats significantly improved the tensile strength of the hybrid composite [21]. In sample A, the maximum difference of 20% more tensile strength was given due to silane treatment for this hybrid composite, and a minimum of 7% was achieved in sample E. Therefore, the average difference between treated and untreated fibers in tensile capacity is 13% more due to silane treatment of fibers before fabrication can give the positive influence between the five different weight fractions of hybrid composite. In another work, banana and neem fibers are reinforced with polymer matrix showing the enhanced tensile strength of 70 MPa due to silane treatment when compared with alkali treatment with 54 MPa and untreated fiber showing 45 MPa of hybrid composite [22]. Therefore, when preparing the hybrid composite, the silane treatment of natural fibers improved the tensile behavior of the hybrid polymer composite.

3.1.2. Flexural Strength. Flexural strengths of treated and untreated ramie/banyan fiber-reinforced hybrid polymer composites with different weight fractions are shown in Figure 5. The flexural strength of the hybrid composite is a major test needed to identify the bending capacity due to this flexural load. In this study, 2% of the bending capacity can be identified for this hybrid composite by this flexural experiment, and the results revealed that silane-treated samples had improved flexural strength when compared to untreated

Table 2: The weight concentrations of banyan/ramie fiber hybrid epoxy composite.

Sample	Epoxy matrix (g)	Ramie fiber mat wt. (g)	Banyan fiber mat wt. (g)	Ramie/banyan weight fraction	Total composite wt. (g)	No. of layers present in composite (banyan/ramie)
A	100	80	20	4 : 1	200	8 B/2 R
B	100	60	40	3 : 2	200	6 B/4 R
C	100	50	50	1 : 1	200	5 B/5 R
D	100	40	60	2 : 3	200	4 B/6 R
E	100	20	80	1 : 4	200	2 B/8 R

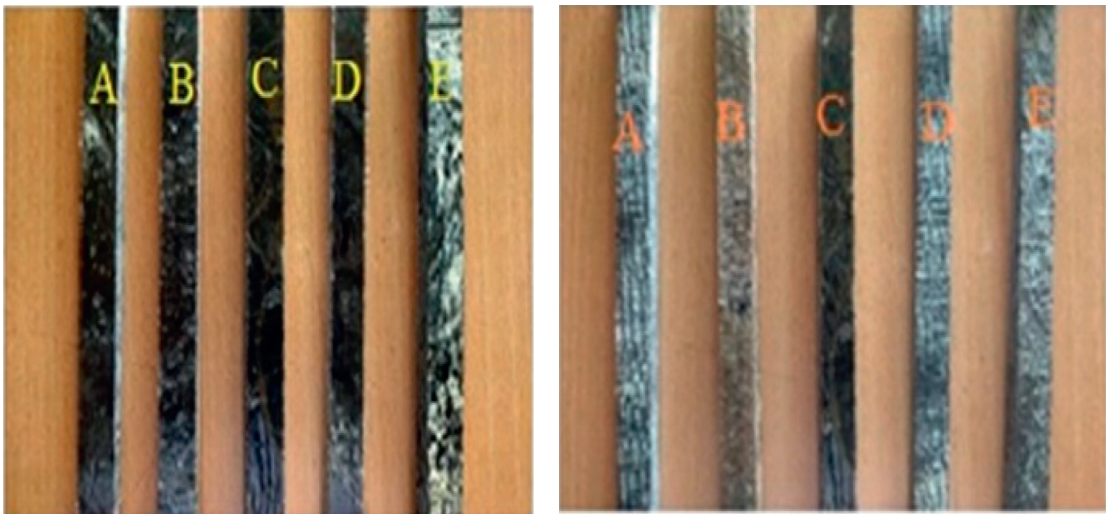

(a) (b)

Figure 1: Tested samples for the flexural test of hybrid composite. (a) Silane-treated samples. (b) Untreated samples.

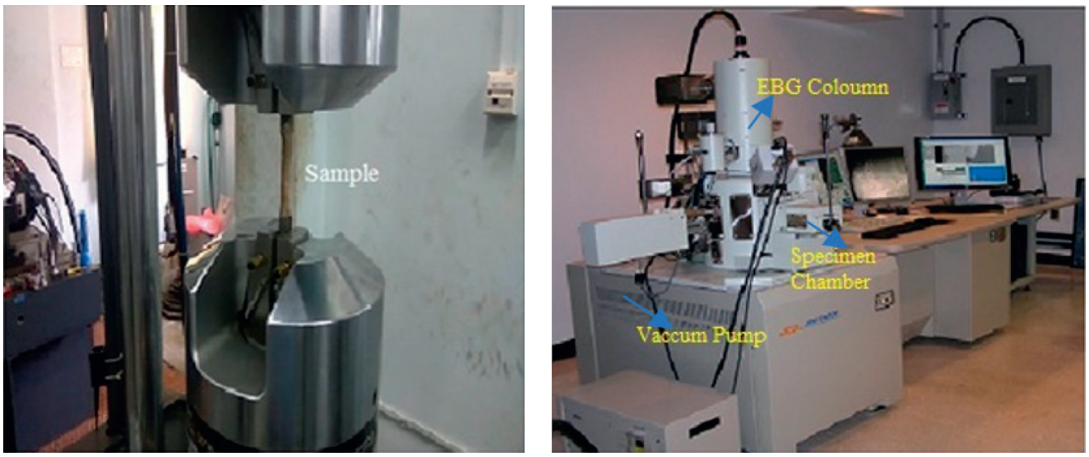

(a) (b)

Figure 2: Experimental setup of (a) tensile test and (b) scanning electron microscopy analysis.

fiber samples [23]. Banyan fiber loading composite sample showed enhanced results when compared to ramie fiber loading composite laminates. The standard deviation of maximum flexural strength for the sample E with the values of five different specimens was 0.376 for the silane-treated sample and 0.412 for the untreated sample, and the same five different specimens were taken in all the five samples of hybrid composite. Flexural test results of epoxy composite are given in Table 4. Therefore, the standard deviation for silane-treated sample A is 20 ± 0.14 and for untreated sample A is 19 ± 0.11.

In sample E, the superior flexural strength of hybrid composite was given among all other samples. It clearly shows that increasing banyan fiber loading can withstand

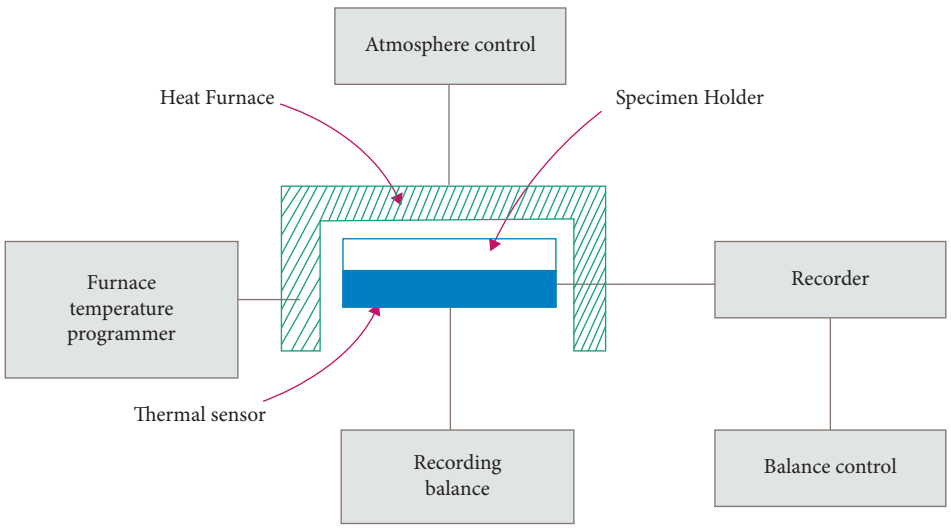

Figure 3: Schematic flow of thermogravimetric analysis.

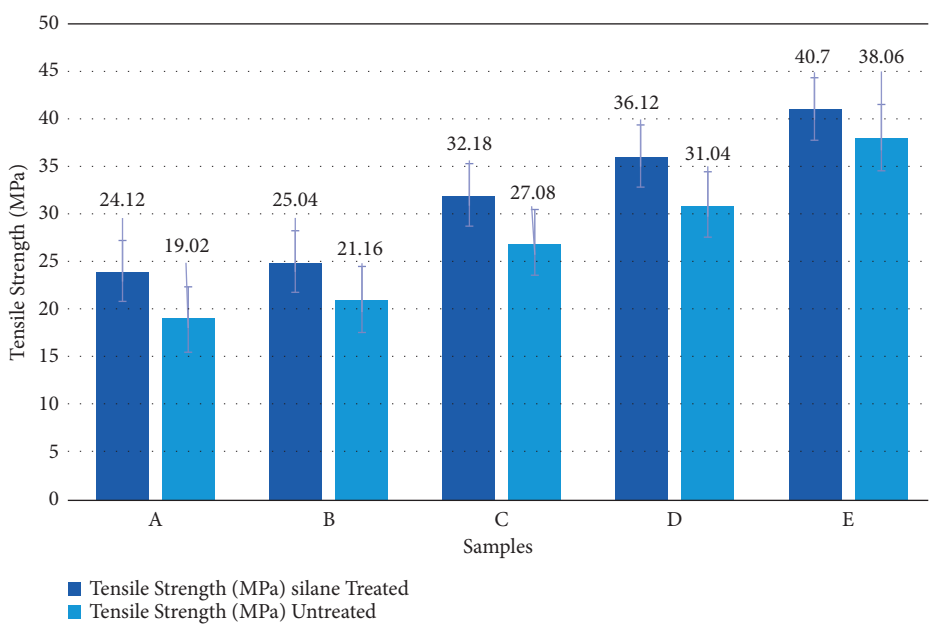

Figure 4: Tensile strength of the hybrid epoxy composite.

Table 3: Tensile test results of an epoxy composite.

Trials	Silane-treated samples					Untreated samples				
	A	B	C	D	E	A	B	C	D	E
1	24.0	24.9	32.2	36.4	40.5	19.2	20.9	27.6	31.2	38.5
2	24.1	24.8	32.2	36.1	41.0	19.1	21.2	27.1	31.0	38
3	24.3	25.1	32.8	35.9	41.5	18.9	21.4	27.0	31.1	37.5
4	23.8	25.3	31.9	36.0	40.2	18.9	21.1	26.9	31.1	38.2
5	24.4	25.1	31.8	36.2	40.6	19.0	21.2	26.8	30.8	38.1
Mean	24.12	25.04	32.18	36.12	40.7	19.02	21.16	27.08	31.04	38.06
Standard deviation	0.238	0.194	0.389	0.192	0.502	0.130	0.212	0.311	0.151	0.364

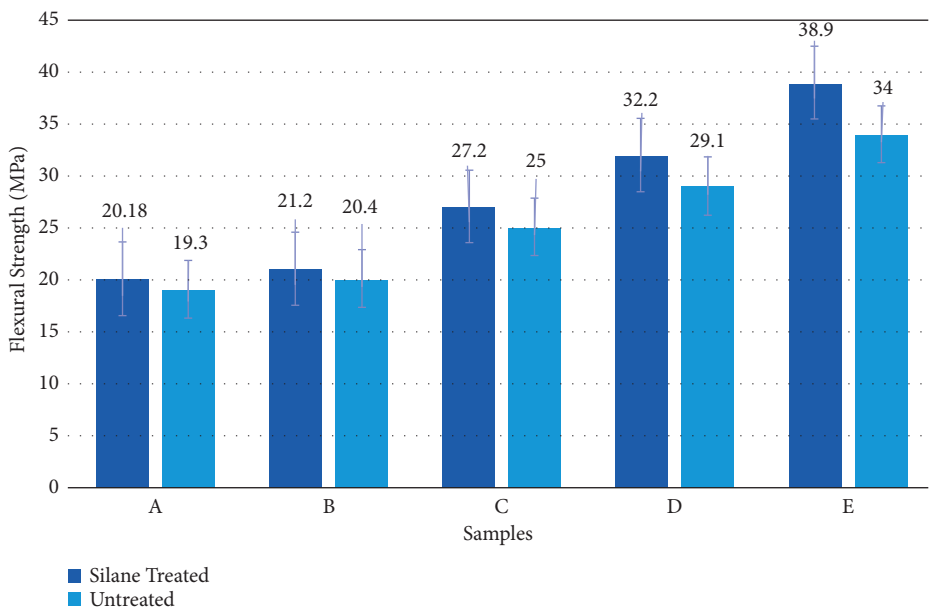

Figure 5: Flexural strength of the hybrid epoxy composite.

Table 4: Flexural test results of an epoxy composite.

Trials	Silane-treated samples					Untreated samples				
	A	B	C	D	E	A	B	C	D	E
1	20.1	20.9	27.3	32.1	39	19.2	20.1	25.1	29.4	34
2	20.4	20.8	271	32.4	38.5	19	20.1	25.2	28.9	34.5
3	20.2	21.4	27.1	32.0	39.5	19.1	20.0	25.3	28.8	34.3
4	20.0	21.1	27.0	32.2	38.7	19.1	20.0	25.0	29.0	33.5
5	20.2	21.2	27.2	32.2	38.9	19.3	20.4	25.0	29.1	33.7
Mean	20.18	21.08	27.16	32.18	38.9	19.14	20.12	25.12	29.04	34.0
Standard deviation	0.148	0.238	0.114	0.148	0.376	0.114	0.164	0.130	0.230	0.412

more vibration during this bending analysis compared to ramie fiber loading. At the same time, a comparison between treated and untreated fibers can show 4.9 MPa of more flexural strength of the hybrid composite. Similar work was done with different natural fibers of banana and neem also showing that silane treatment of natural fibers can improve the average of 10% flexural strength of hybrid composite when compared with alkali-treated and untreated fiber composite laminates [24]. Therefore, 12% superior flexural strength is obtained due to the silane treatment of these natural fibers. In sample A, flexural strengths are 20.18 and 19.3 MPa revealing 49% worse results due to the ramie fiber loading with untreated natural fibers. The standard deviation between the silane-treated samples is 7.79 and between the untreated samples is 6.26. Therefore, the difference between the silane-treated and untreated fibers composite is 1.53 MPa.

3.1.3. Impact Strength. Impact strength of ramie/banyan fiber-reinforced composite laminates is shown in Figure 6. The results show that ramie fiber loading has given superior results compared with banyan fiber loading. It is indicated that the physical properties of ramie can give higher impact energy absorption, and silane-treated fiber laminate has given 9% enhanced impact energy to untreated fibers of hybrid composite laminates. The standard deviation in impact strength analysis for silane-treated hybrid composite is 5.09 and for the untreated fibers composite laminates is 4.82. The standard deviation between the samples is 0.27 J. The better coordination between the fibers and matrix of hybrid composite is revealed. For maximum impact energy, five different specimens were taken for calculating the standard deviation in each sample. For sample A, it is 0.494 in silane-treated mode and 0.439 in the untreated sample of hybrid composite. Impact test results of epoxy composite are given in Table 5. Therefore, the standard deviation of silane-treated sample A is 21 ± 0.4.

The comparative study between the silane-treated and untreated results shows the average of 2 J varies with untreated fiber-reinforced composites from 7.1 J to 19.16 J and with silane-treated fiber composites from 9.04 J to 21.12 J. It can be identified that the superior results from silane-treated laminates are bonded between the fibers and the matrix which are properly blended. However, all samples are having the unique impact energy absorption capacity, but the major

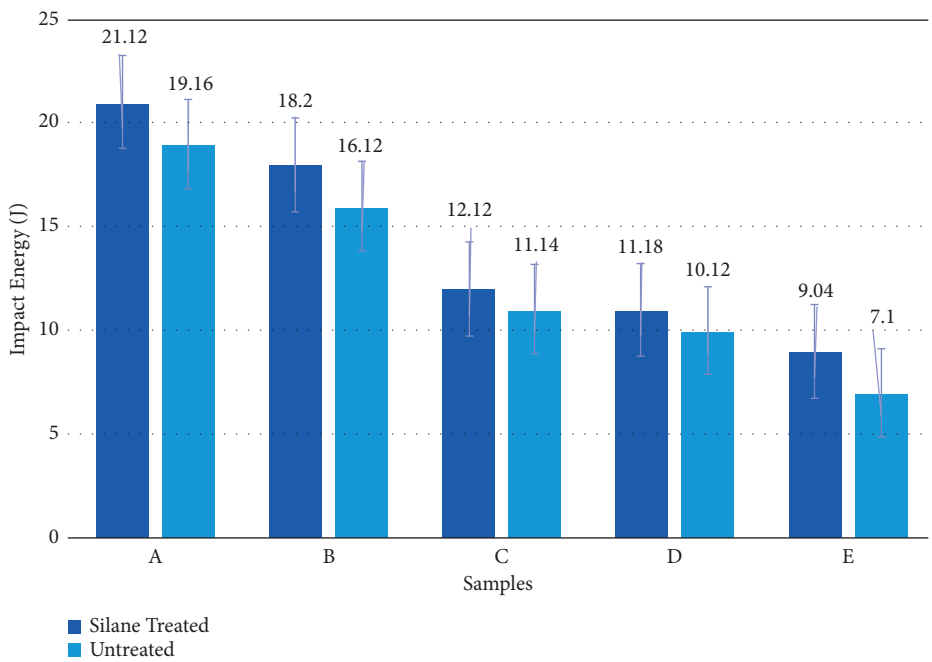

Figure 6: Impact strength of the hybrid epoxy composite.

Table 5: Impact test results of epoxy composite.

Trials	Silane-treated samples					Untreated samples				
	A	B	C	D	E	A	B	C	D	E
1	21	18.0	12.1	11.1	9.2	19	16.2	11.0	10.4	7.1
2	20.5	18.0	12.4	11.3	9.1	19.5	16.1	11.0	9.8	7.3
3	21.5	18.1	12.0	11.2	8.9	19.2	16.0	11.2	9.9	7.1
4	21.7	18.3	12.0	11.1	9.0	18.5	16.0	11.4	10.2	7.0
5	20.8	18.6	12.1	11.2	9.0	19.6	16.3	11.1	10.3	7.0
Mean	21.1	18.2	12.12	11.18	9.04	19.16	16.12	11.14	10.12	7.1
Standard deviation	0.494	0.254	0.164	0.083	0.114	0.439	0.130	0.167	0.258	0.122

variation between the banyan fiber loading and ramie loading in sample A is 57% improved impact strength compared with sample E in silane-treated mode and 63% worse impact energy absorption in sample E compared with sample A. Similarly, a hybrid composite of hemp/kenaf fibers reinforced with epoxy matrix in untreated and alkali-treated fibers can show an average of 12% improved impact strength with chemical treatment [25]. Therefore, the positive influence of this hybrid composite is indicated due to increasing banyan fiber loading compared to ramie fiber loading.

3.2. Morphological Analysis of Treated Hybrid Composites. The fiber pullouts are negligible in the greater weight fraction of ramie fiber-reinforced hybrid composites, as seen in the SEM micrograph of the fractured surface of the hybrid composites. However, as the weight fraction of banyan fibers increases, the fiber pullouts rise as well, owing to the poor adhesion between the banyan fiber and matrix. The SEM image of silane-treated hybrid composite laminates is shown in Figure 7.

3.3. Thermal Stability of the Hybrid Epoxy Composite. Thermal analysis is mandatory for all natural fiber composites [26]. In this research, identifying the thermal stability of silane-treated hybrid composite laminates was selected due to their enhanced mechanical properties when compared to untreated fiber-reinforced composite laminates, and the test was carried out by using thermogravimetric analysis. As per ASTM standard, 13 g of mass is selected for conducting this thermogravimetric analysis. The mass reduction due to temperature change and time taken for changing the phase of this hybrid composite can be collected from this TGA analysis [27], and the graph is plotted between the percentage of mass reduction and temperature change and the time taken for materials to degrade from its original phase of the hybrid composite, with nitrogen inert gas used as a medium in the furnace of thermogravimetric analysis [28]. The rate of degradation concerning the rate of temperature distribution is at 20°C/min of this hybrid composite [15], and the mass loss percentage selected is 99%, 90%, 75%, 50%, and 25% of the mass, and then it will move to decompose [21]. Therefore, up to 25% mass of this hybrid composite can be utilized with good efficiency. The graph is

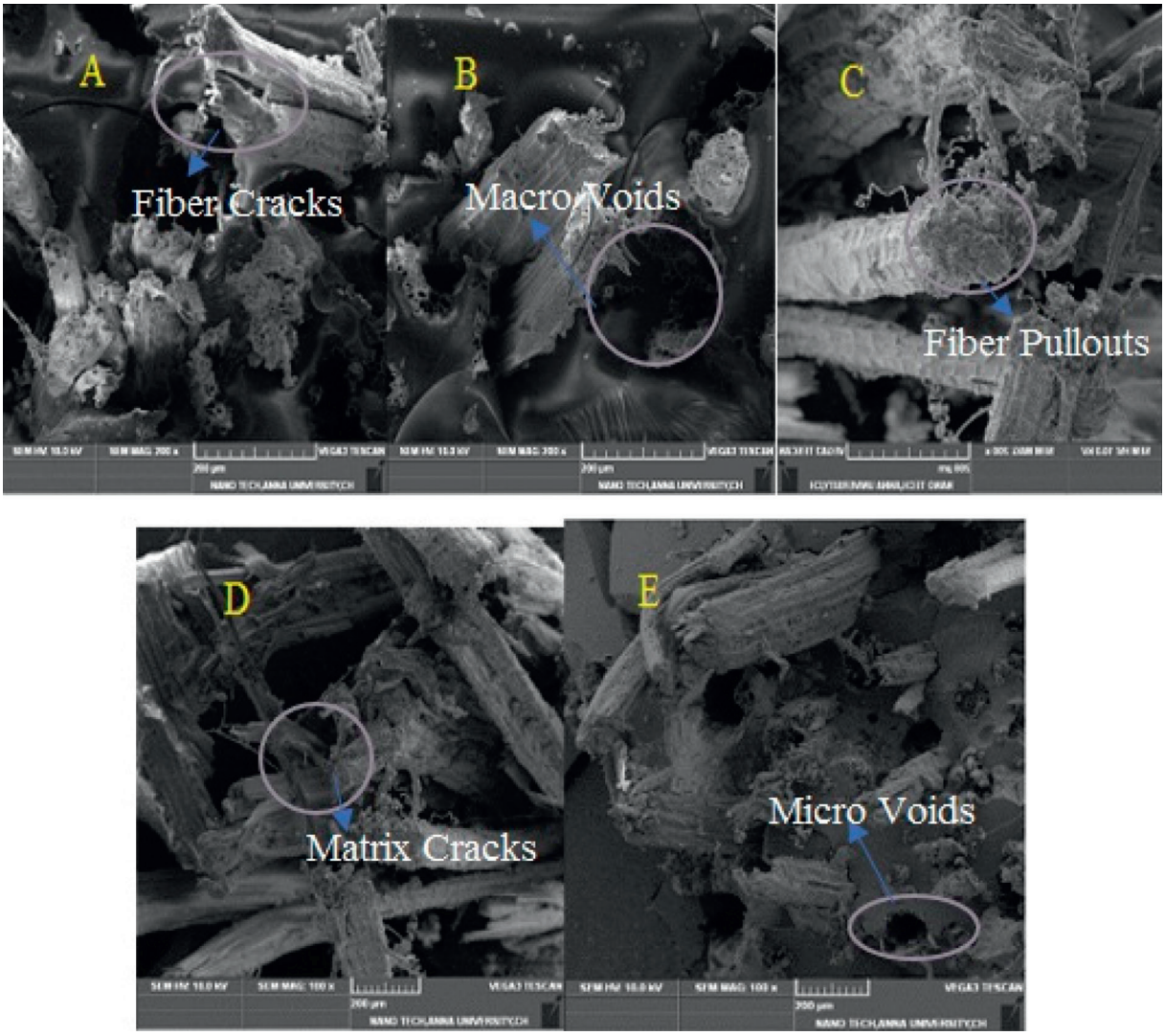

Figure 7: SEM micrographs of treated fiber composite laminates.

plotted between the mass loss in terms of percentage and temperature rise as shown in Figure 8.

Thermal stability graphs are revealed when the increasing temperature mass of the hybrid composite is reduced and the thermal stability is more in ramie fiber loading compared to the banyan fiber loading of this hybrid composite. Sample A contains a 4 : 1 ratio of ramie/banyan fibers which was withstanding a maximum temperature of 410°C at 25% of the mass, and the initial yield temperature of this sample is at 320°C at 99% of the mass. Sample E contains the same ratio with different fibers of banyan/ramie (4 : 1) which was withstanding 329°C at 25% of the mass, and the yield temperature is 251°C of this hybrid composite. Therefore, the ramie fiber loading can improve the thermal stability by 21% higher compared with banyan fiber loading during the initial mass reduction from 13 g to 12.9 g, and the final mass is 3.25 g. In another similar work carried out for natural fibers of neem and banyan, the 25% mass is taken as final, and then the material will go to decompose, and the thermal stability can maintain to 350°C of the hybrid composite [10]. This analysis can identify from the graph that sample A is having higher thermal stability compared with other samples, and it indicates that the ramie fiber has more thermal capacity compared with banyan fiber due to the higher hemicellulose present in this fiber.

Figure 9 shows the graph between the times taken for the composite to degrade concerning mass loss due to temperature rise. The time taken for the decomposition of this hybrid composite can be calculated in all samples, compared with all samples in sample A is taking 16 min to attain the initial mass

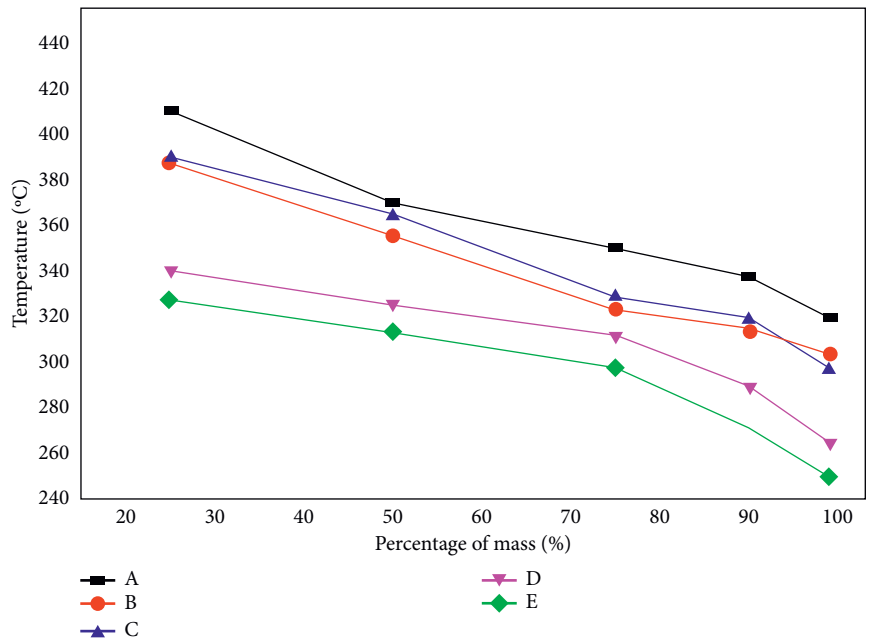

Figure 8: The graph between mass loss and temperature of the hybrid composite.

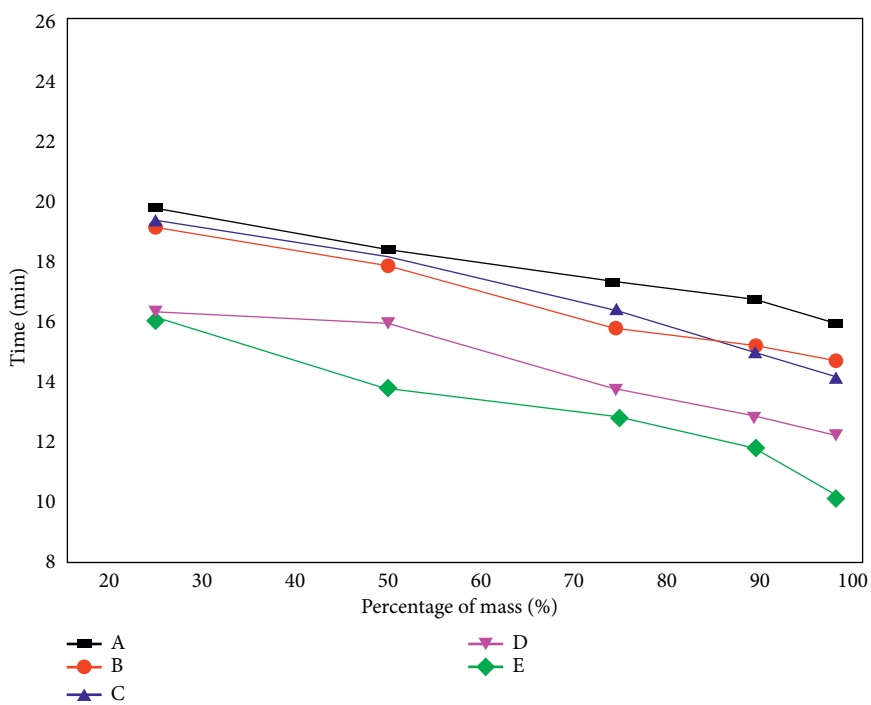

Figure 9: The graph between mass loss and time of the hybrid composite.

loss of 12.9 g and then increasing the temperature that can reflect and reduce the mass up to the working condition of 3.25 g is taken 20 min and in other samples are not attain this life of the hybrid composite. Compared with samples A and E, sample A has 36% more lifetime, and similarly, compared to the sample between B and D, ramie fiber loading can overcome the banyan fiber loading because the bonding between the fibers with the matrix is high, and sample B has 16% more lifetime with the fiber ratio of 3 : 2 (ramie/banyan). Therefore, the lifetime of hybrid composite by thermal analysis is more in ramie fiber loading compared with banyan.

4. Conclusion

This work revealed the comparative study of the mechanical behavior of silane-treated composites with untreated ramie/banyan fiber hybrid epoxy composite, and

thermal stability was also carried out to identify the different properties of hybrid composites. The following major observation was carried out in this research:

(i) The major study of this work is a comparison between the treated and untreated natural fiber composite properties, and the result shows clearly that the silane-treated natural fibers can obtain enhanced mechanical properties of tensile, flexural, and impact strength of the hybrid epoxy composite. Based on these superior results present in silane-treated fibers, the composite was selected for conducting thermal analysis by TGA experiments.

(ii) However, the silane treatment can improve the mechanical strength, but the reinforcement of banyan fiber mat is increasing and can give the superior tensile strength of 40.7 MPa and flexural strength of 38.9 MPa. At the same time when the ramie fiber increases, the higher impact strength of 21.12 J of the hybrid epoxy composite was given.

(iii) Therefore, an average of 12% improved mechanical properties was obtained due to the initial fiber treatment by silane treatment mode and the reinforcement of both ramie and banyan fibers having good mechanical properties and the bonding of *t* natural fibers with epoxy polymer matrix that can be suitable for making hybrid composites.

(iv) Thermal stability is more in sample A due to the higher amount of ramie fiber content. Having more cellulose can resist the mass loss during the increasing of temperature and can withstand the maximum of working temperature at 410°C in 20 min and the average of 20% more lifetime compared with other samples from the thermogravimetric analysis results.

Data Availability

The data used to support the findings of this study are included within the article.

Disclosure

The current research work can provide a wide resource of future research extensions to investigate the broad area in hybrid composites. Some of the recommendations towards the future research extension include the following: some of the other properties such as tribological behavior and moisture absorption can be investigated using extensive experiments. The manufacturing of the hybrid fiber composite can be further experimented with extending the addition of other conventional natural fibers and filler materials with various levels of fiber orientation and characteristics.

Conflicts of Interest

The authors declare that they have no conflicts of interest.

References

[1] R. Balaji, M. Sasikumar, and A. Elayaperumal, "Thermal, Thermo oxidative and Ablative behavior of cenosphere filled ceramic/phenolic composites," *Polymer Degradation and Stability*, vol. 114, pp. 125–132, 2015.

[2] E. Chandana and i . Syed Altaf Hussian, "Thermal conductivity characterization of bamboo fiber reinforced in epoxy resin," *IOSR Journal of Mechanical and Civil Engineering*, vol. 9, no. 6, pp. 07–14, 2013.

[3] P. G. García, R. Ramírez-Aguilar, M. Torres, E. A. Franco-Urquiza, J. May-Crespo, and N. Camacho, "Mechanical and thermal behavior dependence on graphite and oxidized graphite content in polyester composites," *Polymer*, vol. 153, no. 06, pp. 9–16, 2018.

[4] A. Qadeer Dayo, B.-chang Gao, J. Wang et al., "Natural hemp fiber reinforced polybenzoxazine composites: curing behavior, mechanical and thermal properties," *Composites Science and Technology*, vol. 144, no. 03, pp. 114–124, 2017.

[5] S. D. Kumar, M. Ravichandran, A. Jeevika, B. Stalin, C. Kailasanathan, and A. Karthick, "Effect of ZrB2 on microstructural, mechanical and corrosion behaviour of aluminium (AA7178) alloy matrix composite prepared by the stir casting route," *Ceramics International*, vol. 47, no. 9, pp. 12951–12962, 2021.

[6] U. Achutha Kini, M. Shettar, S. Sharma, M. C. G. Pavan Hiremath, H. Anand, and D. Siddhartha, "Effect of hydrothermal aging on the mechanical properties of nanoclay glass fiber epoxy composite and optimization using full factorial design," *Materials Research Express*, vol. 6, pp. 510–523, 2019.

[7] B. Stalin, M. Ravichandran, G. T. Sudha et al., "Effect of titanium diboride ceramic particles on mechanical and wear behaviour of Cu-10 wt% W alloy composites processed by P/M route," *Vacuum*, vol. 184, Article ID 109895, 2021.

[8] B. Ravichandran and M. Sasikumar, "Mechanical, ablative, and thermal properties of cenosphere-filled ceramic/phenolic composites," *Polymer Composites*, vol. 37, no. 6, pp. 1906–1913, 2016.

[9] M. Ramesh, K. Palanikumar, and K. H. Reddy, "Plant fibre based bio-composites: s," *Renewable and Sustainable Energy Reviews*, vol. 79, no. 5, pp. 558–584, 2017.

[10] V. Kavimani, B. Stalin, P. M. Gopal, M. Ravichandran, A. Karthick, and M. Bharani, "Application of r-GO-MMT hybrid nanofillers for improving strength and flame retardancy of epoxy/glass fibre composites," *Advances in Polymer Technology*, vol. 2021, Article ID 6627743, 9 pages, 2021.

[11] T. G. Yashas Gowda, M. R. Sanjay, K. Subrahmanya Bhat et al., "Polymer matrix-natural fiber composites: an overview," *Cogent Engineering*, vol. 5, no. 1, 2018.

[12] K. Yorseng, M. R. Sanjay, J. Tengsuthiwat et al., "Information in United States patents on works related to 'natural fibers': 2000-2018," *Current Materials Science*, vol. 12, no. 1, pp. 4–76, 2019.

[13] S. Mr, S. Siengchin, J. Parameswaranpillai, M. Jawaid, C. I. Pruncu, and A. Khan, "A comprehensive review of techniques for natural fibers as reinforcement in composites: preparation, processing and characterization," *Carbohydrate Polymers*, vol. 83, no. 11, pp. 108–121, 2018.

[14] K. Bharath, M. Sanjay, M. Jawaid, S. B. Harisha, S. Basavarajappa, and S. Siengchin, "Effect of stacking sequence on properties of coconut leaf sheath/jute/E-glass reinforced phenol formaldehyde hybrid composites," *Journal of Industrial Textiles*, vol. 49, no. 1, pp. 3–32, 2019.

[15] S. Abhishek, M. R. Sanjay, G. Raji, S. Siengchin, J. Parameswaranpillai, and C. I. Pruncu, "Development of new hybrid Phoenix, pusilla/carbon/fish bone filler reinforced polymer composites," *Journal of the Chinese Advanced Materials Society*, vol. 6, no. 5, 2018.

[16] K. Ganesan, C. Kailasanathan, M. R. Sanjay, P. Senthamaraikannan, and S. S. Saravanakumar, "A new assessment on mechanical properties of jute fiber mat with egg shell powder/nanoclay-reinforced polyester matrix composites," *Journal of Natural Fibers*, vol. 17, no. 4, pp. 480–490, 2018.

[17] P. Kumaran, S. Mohanamurugan, S. Madhu et al., "Investigation on thermo-mechanical characteristics of treated/untreated Portunus sanguinolentus shell powder-based jute fabrics reinforced epoxy composites," *Journal of Industrial Textiles*, vol. 50, no. 4, pp. 427–459, 2019.

[18] P. Madhu, M. R. Sanjay, P. Senthamaraikannan, S. Pradeep, S. S. Saravanakumar, and B. Yogesha, "A review on synthesis and characterization of commercially available natural fibers: Part-I," *Journal of Natural Fibers*, vol. 16, no. 8, pp. 1132–1144, 2018.

[19] T. Raja and P. Anand, "Evaluation of thermal stability and thermal properties of neem/banyan reinforced hybrid polymer composite," *Materials Performance and Characterisation*, vol. 8, pp. 1 481–490, 2019.

[20] K. Mehar, S. K. Panda, and T. R. Mahapatra, "Thermoelastic deflection responses of CNT reinforced sandwich shell structure using finite element method," *Scientia Iranica*, vol. 25, pp. 2722–2737, 2017.

[21] S. D. Salman, Z. Leman, M. T. H. Sultan, M. R. Ishak, and F. Cardona, "The effects of orientation on the mechanical and morphological properties of woven kenaf-reinforced poly vinyl butyral film," *Bio Resources*, vol. 11, no. 1, pp. 1176–1188, 2015.

[22] R. Thandavamoorthy and A. Palanivel, "Testing and evaluation of tensile and impact strength of neem/banyan fiber-reinforced hybrid composite," *Journal of Testing and Evaluation*, vol. 48, no. 1, pp. 647–655, 2020.

[23] M. Jawaid, H. P. S. Abdul Khalil, and O. S. Alattas, "Woven hybrid bio-composites: dynamic mechanical and thermal properties," *Compos Part A Appl Sci Manuf*, vol. 43, no. 2, pp. 288–293, 2012.

[24] V. J. Binu Kumar, J. Bensam Raj, R. Karuppasamy, and R. Thanigaivelan, "Influence of chemical treatment and moisture absorption on tensile behavior of neem/banana fibers reinforced hybrid composites: an experimental investigation," *Journal of Natural Fibers*, Article ID 1838995, 12 pages, 2020.

[25] S. Huo, A. Thapa, and C. A. Ulven, "Effect of surface treatments on interfacial properties of flax fiber-reinforced composites," *Advanced Composite Materials*, vol. 22, no. 2, pp. 109–121, 2013.

[26] D. Hristozov, L. Wroblewski, and P. Sadeghian, "Long-term tensile properties of natural fibre-reinforced polymer composites: comparison of flax and glass fibres," *Composites Part B: Engineering*, vol. 95, pp. 82–95, 2016.

[27] A. V. Kiruthika, "A review on physico-mechanical properties of bast fibre reinforced polymer composites," *Journal of Building Engineering*, vol. 9, pp. 91–99, 2017.

[28] L. Yan, N. Chouw, L. Huang, and B. Kasal, "Effect of alkali treatment on microstructure and mechanical properties of coir fibres, coir fibre reinforced-polymer composites and reinforced-cementitious composites," *Construction and Building Materials*, vol. 112, no. 1, pp. 168–182, 2016.

Hindawi
Advances in Materials Science and Engineering
Volume 2021, Article ID 2905150, 14 pages
https://doi.org/10.1155/2021/2905150

Research Article

Natural Jute Fibre-Reinforced Polymer Composite System for Posttensioned Beam Strengthening in Flexure

D. P. Archana,[1] **H. N. Jagannatha Reddy**,[1] **N. Jeevan**,[1] **R. Prabhakara**,[2] **M. U. Aswath**,[1] **and Basavaraju Paruti**[3]

[1]*Department of Civil Engineering, Bangalore Institute of Technology, Bengaluru 560004, India*
[2]*Structural Engineering, VTU, Belagavi 590018, India*
[3]*Department of Hydraulics and Water Resource Engineering, HHIOT Campus, Ambo University, Ambo, Ethiopia*

Correspondence should be addressed to D. P. Archana; archanadpbit@gmail.com and Basavaraju Paruti; basavaraj.paruti@ambou.edu.et

Received 9 September 2021; Accepted 10 November 2021; Published 27 November 2021

Academic Editor: Ravichandran M

Existing structures require repair and strengthening owing to degradation caused by incorrect design and construction, environmental impacts, or structural upgradation to meet new seismic design standards or to correct execution problems that occurred during construction. These strengthening requirements can be satisfied by a variety of strengthening techniques. The creation of a fibre-reinforced polymer (FRP) composite system offers a new design method for the strengthening of existing structures. In this study, posttensioned beams are strengthened by using sustainable materials such as natural jute fibre-reinforced polymer (FRP) composites. The performance of these composite systems in the flexural strengthening of posttensioned beams was used to assess their effectiveness. Consequential result for longitudinal reinforcement throughout the length of the beam for flexural strengthening was evaluated. Flexural performance, crack width, ductility, and load-deflection relationship study of control beams (Scheme A) and retrofitted beams (Schemes B and C) under different wrappings were considered in the investigation. An experimental study depicts that using the full wrapping (FW) technique increases the flexural strength of PSC beams wrapped in JFRP by 23% and, by using the strip wrapping (SW) technique, the flexural strength is increased by 10%. The JFRP composite system of strengthening has shown the highest deformability index and showed that the JFRP material has enormous potential as a structural strengthening material.

1. Introduction

Structural strengthening and rehabilitation have grown in popularity over the last decade because of their obvious benefits and applications. A lot of research has looked into the flexural and shear behaviour of artificial fibre-reinforced concrete structures in the literature. Badawi and Soudki [1] conducted extensive research on the flexural behaviour of reinforced and plain concrete beams with glass and carbon fibre-reinforced polymer (GFRP and CFRP) confinement, which demonstrated enhanced structure performance by minimizing the cracks. A report by Toutanji et al. [2] demonstrated that the load carrying capacity is drastically improved by the number of layers in the composite system. In detail, Esfahani et al. [3] showed how the reinforcement ratio affects the properties of the beam strengthened by CFRP composites. Syed Ibrahim et al. [4] studied the behaviour of steel fibre-reinforced concrete beams strengthened with GFRP laminates. When compared to reference RC beams, these beams performed well in tests. Al-Deen Bsisu et al. [5] investigated the flexural behaviour of steel- and CFRP-strengthened reinforced concrete beams. Esfahani et al. [3], Ashour et al. [6], Garden and Hollaway [7], and Smith and Teng [8] conducted experimental studies that revealed three major failure categories in concrete structures retrofitted with FRP. Mahalingam et al. [9] experimentally conducted the strength and ductility study of externally bonded steel fibre-reinforced concrete beams. GFRP laminates were used as an externally bonded material. Beams were evaluated for their static responses in terms of strength,

ductility, and stiffness. The results reveal that externally bonded laminates were more effective than internal fibre reinforcements. Khalifa et al. [10] observed shear deficiencies in artificial carbon fibre composite-retrofitted beams. There is potential for developing new materials with improved properties for the strengthening of structures and their improvement [11]. Diverse materials have been used for structural upgrades in order to meet some criteria for the sake of sustainability and improved quality with functional efficiency [12]. Alam et al. [13] used chemically treated kenaf fibre, jute rope, and jute fibres to prepare composites that were used in the application for strengthening RC structures. Bhutta et al. [14] tested the structural performance of concrete beams strengthened with natural Kenaf FRP. Chin et al. [15] considered pineapple leaf fibre-epoxy composite plates for strengthening reinforced concrete beams. Fibres were alkali-treated to improve their efficiency. Fibre loading was varied between 0.1 and 0.4 v/v and was used for external RC beam strengthening. Strengthened beams were tested under four-point bending. The beam strengthened with composite plates has a larger beam capacity (approximately 7%) than the reference beam, according to the test results. At a fibre volume ratio of 40%, the maximum flexural strength of 301.94 MPa was achieved. Di Luccio et al. [16] demonstrated the feasibility of retrofitting RC walls using flax fibre-reinforced polymers, and results were compared with reference wall and carbon fibre-reinforced polymer-strengthened wall. Flax fibre-reinforced polymer-strengthened RC wall specimens showed better strength and ductility gains, and also, the tests show that walls strengthened with flax FRP generally dissipate more energy than those strengthened with CFRP. Sen and Reddy [17] compared the natural to artificial fibre-reinforced polymer composite-retrofitted RC beams for their flexure strength, strengthening significantly improved ductility, flexural strength, and load-deflection behaviour. Alam and Al Riyami [18] investigated the use of natural FRP (sisal, jute, and kenaf) laminates for the strengthening of concrete beams under shear. Sen and Reddy [19] worked on the strengthening of RCC beams with bamboo FRP. Ghalieh et al. [20] investigated the efficacy of hemp fibre-reinforced composites, and Sen and Reddy [21] studied the strengthening of beams with coir FRP for load carrying capacity. Computational techniques have become an important tool to model, analyze, and optimize the parameters/characteristics that affect the properties of natural FRP composites. Mulenga et al. [22] reviewed various computational tools including support vector machines, decision trees, K-means, K-nearest neighbor, Naive Bayes, and artificial neural networks (ANNs). Kumar et al. [23] studied the machining characteristics of natural abaca, hemp, and Mudar fibre particle-reinforced polymer composite using the ANN. Pujari et al. [24] predicted the water absorption capacity of natural fibre-reinforced epoxy composites using artificial neural network and regression analysis. Predicted physical property of natural fibre composites was compared among two methodologies. The ANN shows better results than the regression analysis.

A review of the literature revealed the behaviour and effect of fibre-reinforced polymer composites (both artificial and natural) strengthening on RC beams under flexural loading systems. There has been little research on retrofitting structures, which has been limited to the use of naturally occurring fibres. Very few researchers attempted to evaluate the flexural behaviour of artificial fibre-reinforced composite system-strengthened posttensioned beams. But, it has been clear from the literature that none of the work was reported on the strengthening of posttensioned beams using natural fibre-reinforced polymer composite system. So, in this research study, the purpose is to determine the influence of natural JFRP on the posttensioned concrete beams, structurally retrofitted, and to improve the flexural behaviour of the concrete beams.

1.1. Research Significance. The following issues are intended to be addressed in the current research investigation: (a) the first step is to investigate the feasibility/applicability of using a natural fibre system to strengthen beams and improve their performance and (b) the second objective is to comprehend the flexural capacity of the posttensioned beams wrapped with jute fibre-reinforced polymer (JFRP) composites. The authors investigated JFRP composites for their mechanical properties to confirm their suitability [25].

2. Materials and Procedure

OPC 53 grade (Ultratech Cement grade 53) conforming to IS 12269-1987 and locally available river sand were used. A coarse aggregate of 12 mm was crushed (angularly) in accordance with IS 383:1970. Calculated proportions of water, cement, coarse aggregate, and fine aggregate were mixed in the ratio of 0.4:1:2.13:1.27 to prepare concrete, according to IS 10262-2009 standards and design strength of 40 N/mm^2. The ratio of water and cement allowed was max. 0.55 as per IS: 456-2000, and workability was found to be 100 mm, measured from the slump cone. Cubes were casted according to the designed mix proportion. Average compression strength was measured at different intervals and was found to be 22.7 N/mm^2 for 7 days, 38.95 N/mm^2 for 14 days, and 43.34 N/mm^2 for 28 days of curing. An epoxy resin (MBrace® Saturant) was used. In addition, as reinforcement, 8 mm diameter Fe 500 HYSD bars with a tensile strength of 500 N/mm^2 were used.

2.1. Specimens for Testing. A total of nine beams under three configurations were fabricated as per calculated mix proportions in a single stage. The configurations are (i) control beams (CB) (3 no's), (ii) beams with full wrapping (FW) configuration (3 no's), and (iii) beams with strip wrapping (SW) configuration (3 no's). Table 1 represents all three test beam configurations.

Wood molds having dimensions of 3400 mm (length) × 300 mm (width) × 260 mm (breadth) were used. Lubricant oil was sprayed on the inner walls to facilitate removal after 1 day of curing. The steel reinforcement, along with the sheathing pipe assembly, was placed inside the mold with a 25 mm clear cover shown in Figure 1. The concrete was then poured into the mold, left for one complete day for solidifying, and cured

Table 1: Beam details.

Configuration	Strengthening element	Beam designation	Strengthening scheme	FRP layers
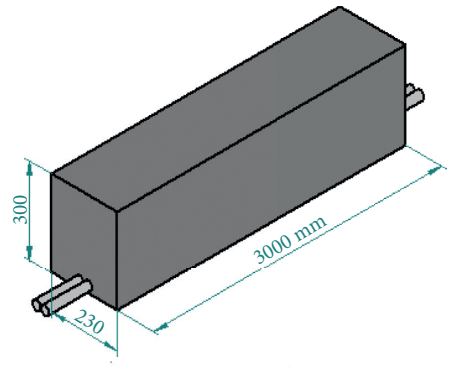	—	CB1, CB2, CB3 Scheme "A"	—	—
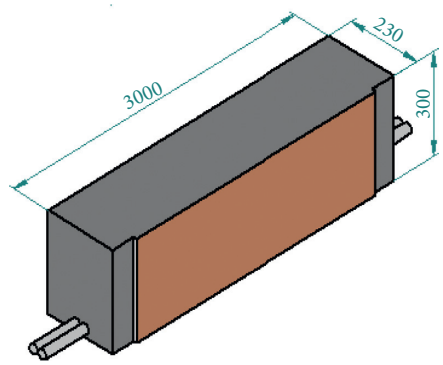	Jute FRP	Full wrapping (JFB4, JFB5, and JFB6) Scheme "B"	3-sided full U-wrap	One layer
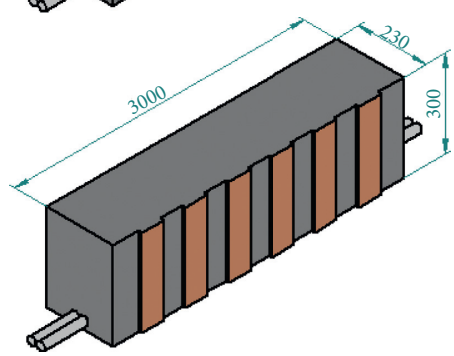	Jute FRP	Strip wrapping (JFB7, JFB8, and JFB9) Scheme "C"	3-sided strip U-wrap	One layer

CB: control beam; JFB: jute fibre-retrofitted beam.

for 28 days. Proper compaction was accomplished with 20 mm needle vibrator. Figures 2(a)–2(h) show the complete procedure followed during the casting of beams.

The beam was stressed with the help of a hydraulic Jack. Three surfaces of the beam (except the top surface) were grounded and cleaned to ensure proper bonding between the laminate and the beam. Then, a thin coat of primer is applied on all three sides in Schemes "B" and "C" beams. The resin and hardener were mixed according to the manufacturer's recommendations, which is 3 : 1. The resin and hardener proportions were calculated, and resin and hardener were thoroughly mixed and applied to the beam surfaces. Hand layup technique was used for retrofitting, whereas U-wrapping configuration of pretreated mats was used to bond the beams to form natural FRP composites. The laminates were then pressed with light pressure to ensure the removal of trapped air. Curing of beams was permitted. For the retrofitting, all of the manufacturer's guidelines were followed.

2.2. Configurations. Scheme "A" beams were designed as control beams without JFRP, with three PSC beam specimens' models labelled CB1, CB2, and CB3. In Scheme B, the beams were designed with FW technique 90°, U-wrap (three sided), and single-layer laminate bonded to the three sides of the beams, which included three PSC beam models designated as JFB4, JFB5, and JFB6. Scheme "C" beams were designed with the SW technique 90°, U-wrap (three sided), and single-layer laminate is bonded to the beam comprising three RC beam models designated as JFB7, JFB8, and JFB9. Flexural strengthening was evaluated using all beams. The

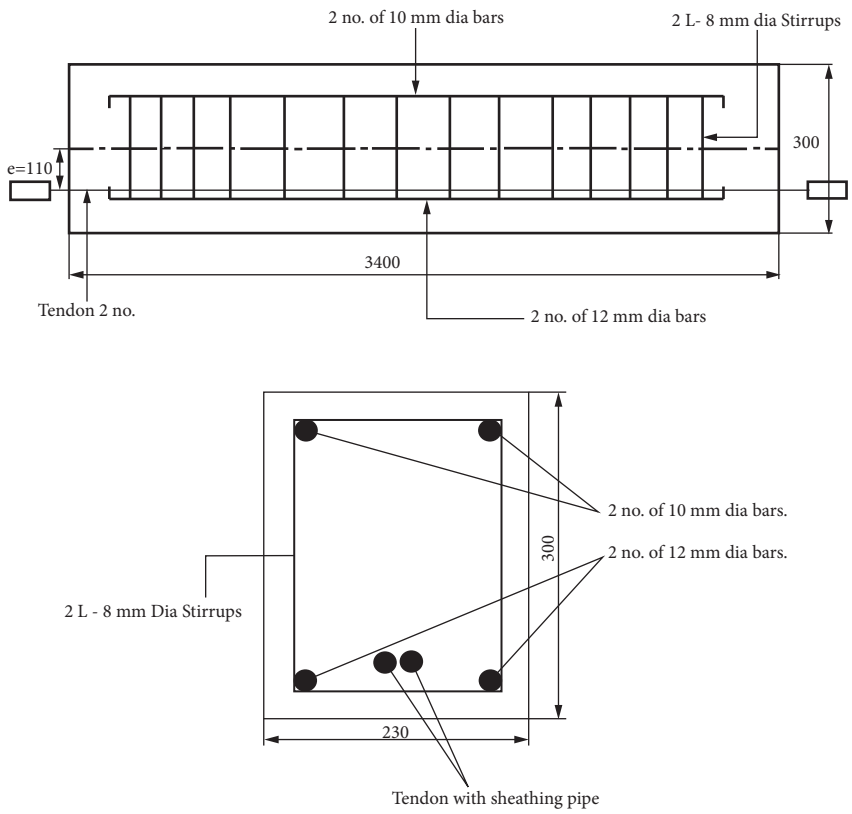

Figure 1: Beam reinforcement structure.

beam configurations and strengths are summarized (Table 2). Uniform reinforcement was used in all beams in order to measure the strengthening effectiveness with and without JFRP wrappings.

3. Experimental Study

Figure 3 depicts the results of the experiments. Three experimental schemes (detailed in Table 1) were used to evaluate the strengthening effect under flexure. The beam behaviour under flexure was studied experimentally using a loading frame of 50-tonne capacity. Load applied using a hydraulic jack. To measure the loading increments, a loading cell is attached to the jack and intern to a digital indicator. A four-point bending system was used to test all beams over a 2100 mm simply supported span with a shear span of 700 mm. The spreader beam was used to apply two-point load, which transfers the load from the loading jack to the specimen. Under the beam, three digital deflection gauges were installed: two beneath the loads and one in centre were used to measure deflection. The manual load was applied in 2 kN span with a hand-held lever until failure. Figure 4 depicts experiments on control, fully wrapped, and strip-wrapped beams.

3.1. Failure Mode Study, Load-Deflection Relationship, and Ultimate Strength. Flexural performance assessment study of control beams (Scheme A) and retrofitted beams (Schemes B and C) was conducted, and the beams were designed to undergo flexural failure. They were all tested using a two-point loading arrangement in accordance with the standard procedure. The following were noted and addressed: (i) load-deflection relationship, (ii) ultimate failure load, and (iii) fracture mode study.

3.2. Crack Width Study under Working Loads. During the experiment, strengthened and unstrengthened beams were subjected to different working loads, for which the crack width was measured (Figure 4(c)), and these are compared with the codal requirement. The measured values are found to be within the codal requirement. Experimental observations confirmed that the cracking behaviour of the beams was significantly altered by the use of FRP wraps.

4. Experimental Results

The ultimate strength of three sets of beams was tested: Scheme "A," Scheme "B," and Scheme "C." During the experiment, the deflection behaviour and the ultimate load of the beams were observed. The load carrying capacity of the beams in Scheme "A," CB1, CB2, and CB3, was lower than those of Scheme "B" (fully strengthened) and Scheme "C" (partially strengthened) beams. In a single-layer 90° fully wrapped JFRP, the value of ultimate strength was found to be the highest in Scheme "B": JFB4, JFB5, and JFB6. In order to achieve 50% of total area strengthening, in Scheme "C," the beams were strengthened by single-layer 90° strip wrapping with JFRP and have shown ultimate

Figure 2: Procedure adopted. (a) Steel reinforcement. (b) Anchorage. (c) Sheathing pipe installation. (d) Pouring concrete and compacting with vibrator. (e) Beams to solidify in the mold for 24 hrs. (f) Beams after burr removal. (g) Stressing with hydraulic jack. (h) Jute mat wrap.

Table 2: Experimental findings.

Scheme	Beam designation	Failure of FRP	First crack load (Avg.) kN	Ultimate load (Avg.) kN	Increase in load carrying capacity over control beam-strengthening effect (%)
"A"	CB1, CB2, and CB3	—	82	140	—
"B"	JFB4, JFB5, and JFB6	Yes	130	172	23
"C"	JFB7, JFB8, and JFB9	No	114	154	10

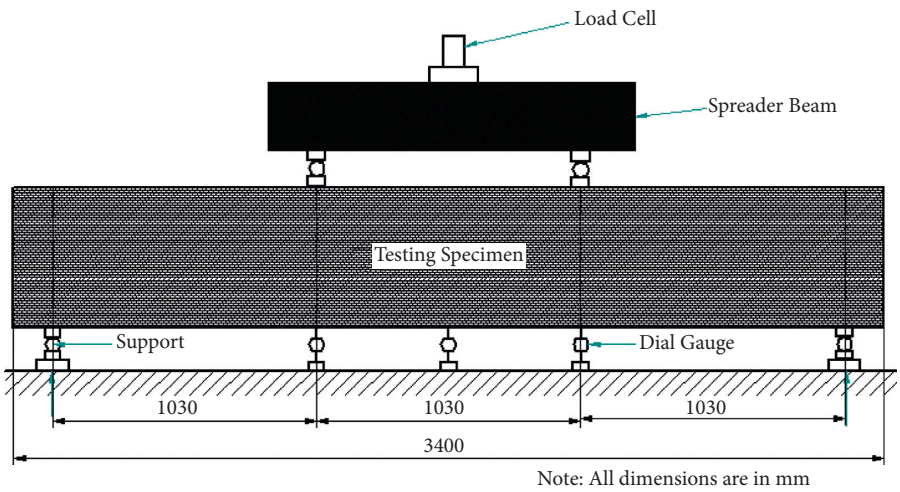

Figure 3: Details of experimentation.

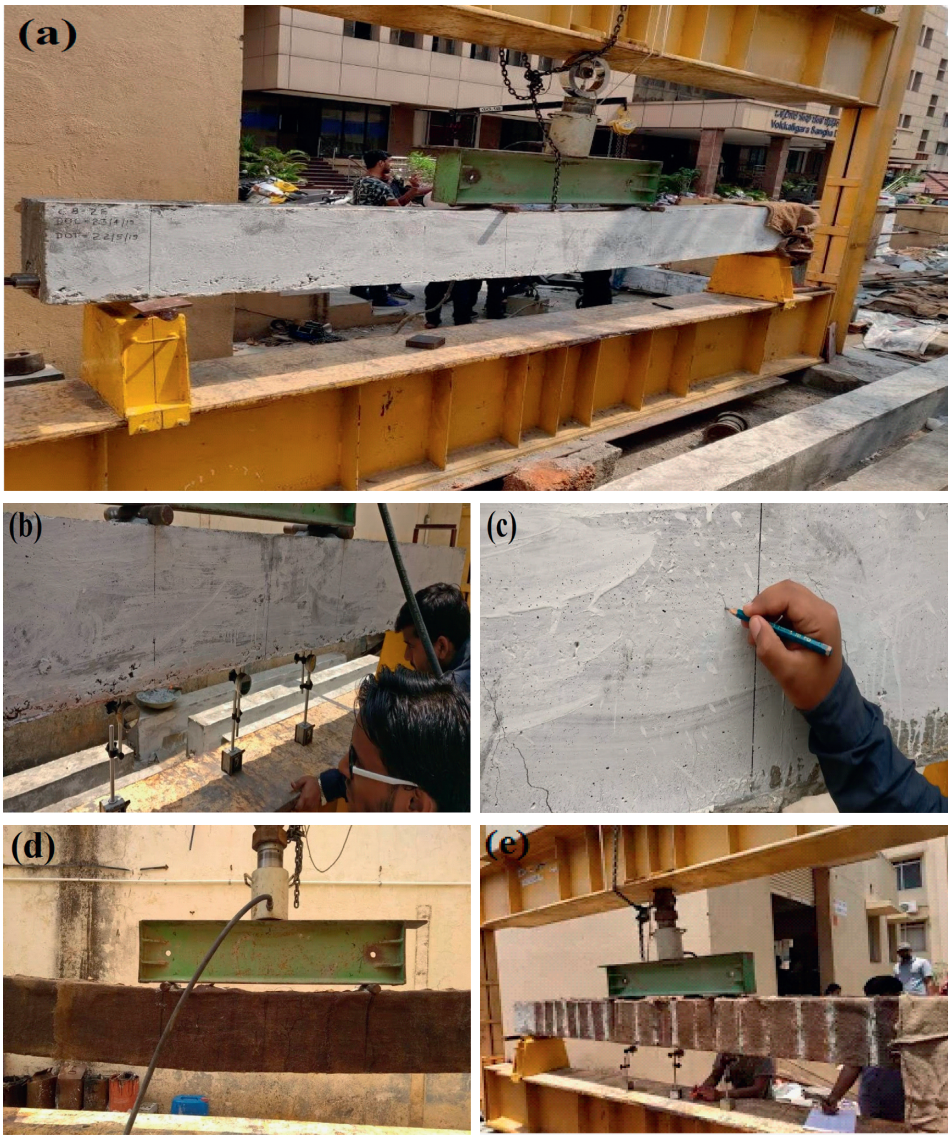

Figure 4: (a) Control beam placed on the loading frame. (b) Dial gauge measurements. (c) Crack on CB. (d) Jute fibre FW. (e) Jute fibre SW.

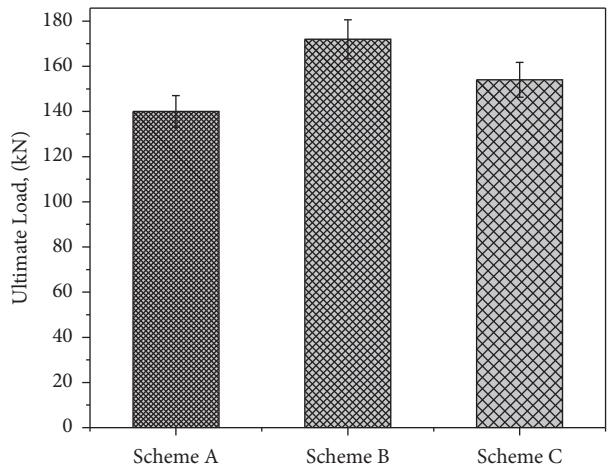

Figure 5: All scheme beams with maximum load carrying capacity.

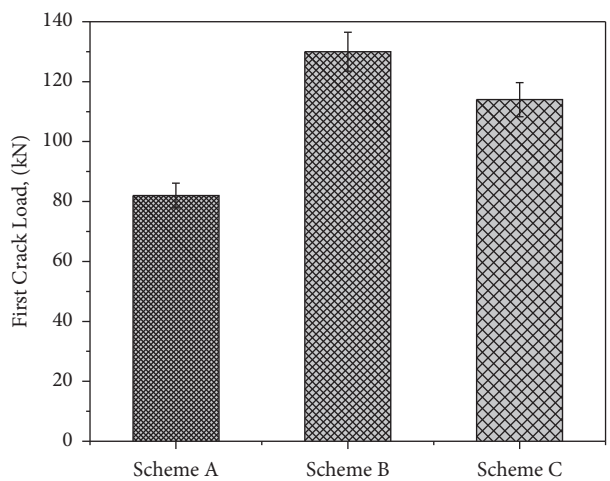

Figure 6: First crack load of beams under three schemes.

strength greater than the control beams. These bonded strips have the width of 80 mm and are at 160 mm C/C (at a clear gap of 80 mm). Table 2 summarizes the experimental findings of all beam schemes.

4.1. Failure Mode Study and Ultimate Failure Load. During experimentation, various failure modes were observed. The first set of beams, Scheme "A," failed in flexure, demonstrating that the beams were lacking in flexure. Cracks were observed in the pure flexure zone, which is located in the middle of the span length. These cracks began on the lower face of the beam and progressed to the top face. Scheme "A" beams' ultimate strength was 140 kN on average. It was seen that Scheme "B" beams failed in flexure and had a much higher ultimate load carrying capacity than beams of Scheme "A." When initial loading was applied to beams, the matrix began to crack. When the load was increased further, JFRP began to crack, and the cracks in the JFRP began to widen, resulting in a vertical crack in the flexure zone in the beam. At a later stage, this crack began to move slowly from the bottom to the top face of the beam. The ultimate strength of Scheme "B" beams JFB4, JFB5, and JFB6 was 172 kN on average. JFB4, JFB5, and JFB6 all failed in a same trend. The ultimate load carrying capacity of Scheme "C" beams JFB7, JFB8, and JFB9, which were strip-wrapped with JFRP, is determined experimentally. From the experimental results, it is found that the ultimate load carrying capacity for these beams was found to be greater than that for the unstrengthened beams (Scheme A) and less than that for fully wrapped beams (Scheme B). It is observed that, in Scheme C beams, the cracks were appeared first in the unwrapped portion of the beam and then in the JFRP wrapped portion, which shows that the bonding of JFRP added extra strength to the beams, which increases the ultimate load carrying capacity. When load was applied to JFB7, JFB8, and JFB9, majority of vertical cracks were observed in the mid portion of the span, which is the pure flexure zone. The JFRP did not develop even a single flexural crack, nor did it rupture. These cracks were initiated on the lower surface and propagated to the upper surface of the beam. The ultimate load carrying capacity of the JFRP strip wrapping technique has increased up to a

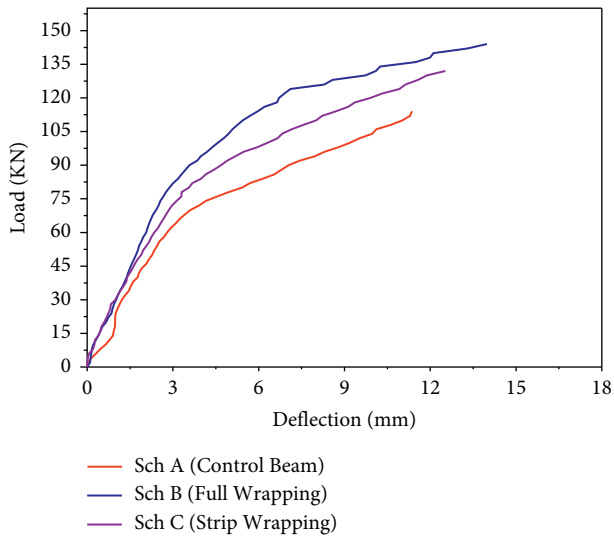

Figure 7: Load-deflection (average mid span) for all schemes.

Table 3: Deformability indices for beams designed to fail under flexure.

Designation	First crack load (kN)	Avg. mid span deflection at first crack (mm)	Avg. mid span deflection at failure (mm)	Deformability index
Scheme A	CB1, CB2, and CB3	3.687	6.522	1.77
Scheme B	JFB4, JFB5, and JFB6	The first crack deflection was not observed in fully U-wrapped beams		—
Scheme C	JFB7, JFB8, and JFB9	4.531	10.727	2.36

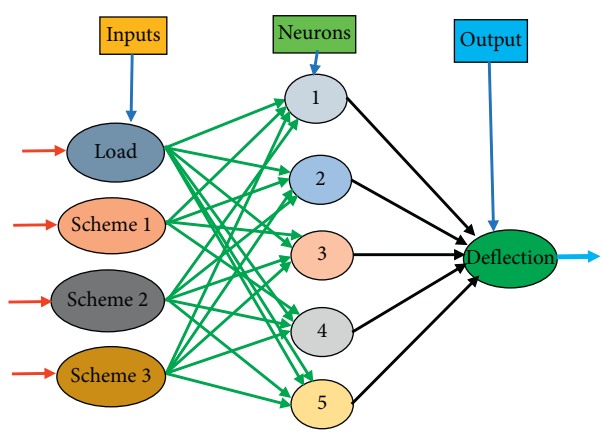

Figure 8: General ANN structure.

certain point, which is in between the increase in the load carrying capacities of full wrapped and control beams. The ultimate strength of 154 kN on average was observed in Scheme "C" beams. The graphs in Figure 5 show a comparison of the ultimate failure load of different beam schemes. The use of JFRP, whether in continuous form or in strips, has the effect of delaying the formation of cracks. The study revealed that the initial cracks were caused by load. The graphs in Figure 6 show a comparison of the first crack load of different beam schemes. When the load-deflection behaviour of retrofitted beams with continuous U-wrap JFRP was compared to strip wrapping, it was confirmed that the continuous U-wrap JFRP-retrofitted beams had a better load-deflection behaviour. Here, brittle failure of the beams was drastically managed by continuous JFRP because the beams carried large deflections before failure and thus provided adequate warnings before collapsing. The presence of strips slowed the formation of the first cracks where JFRP was bonded to the beams.

4.2. Load-Deflection Relationship Study. All of the beams' load-deflection behaviour was observed and compared among them with the same reinforcement. In addition, mid span deflections of each beam were compared to those of control beams. For Scheme A, B, and C beams, a

Table 4: Determination coefficient R^2 for different learning algorithms to predict deflection for Scheme A.

Number of hidden layers	Neurons in hidden layer	Coefficient of determination R^2			
		Training data	Validating data	Testing data	All data
1	8	0.99987	0.99978	0.99964	0.99976
1	10	0.99989	0.99981	0.99968	0.99980
1	20	0.99992	0.99983	0.99972	0.99982
1	25	0.99995	0.99985	0.99974	0.99984
1	**30**	**0.99999**	**0.99989**	**0.99978**	**0.99987**
1	40	0.99997	0.99984	0.99975	0.99983

The bold values indicate the optimum value.

Table 5: Determination coefficient R^2 for different learning algorithms to predict deflection for Scheme B.

Number of hidden layers	Neurons in hidden layer	Coefficient of determination R^2			
		Training data	Validating data	Testing data	All data
1	10	0.99974	0.99976	0.99250	0.99801
1	20	0.99979	0.99979	0.99254	0.99805
1	25	0.99984	0.99986	0.99260	0.99810
1	30	0.99988	0.99990	0.99265	0.99815
1	**35**	**0.99992**	**0.99996**	**0.99271**	**0.99821**
1	40	0.99990	0.99992	0.99267	0.99812

The bold values indicate the optimum value.

Table 6: Determination coefficient R^2 for different learning algorithms to predict deflection for Scheme C.

Number of hidden layers	Neurons in hidden layer	Coefficient of determination R^2			
		Training data	Validating data	Testing data	All data
1	8	0.99957	0.99778	0.99954	0.99913
1	10	0.99966	0.99780	0.99958	0.99918
1	20	0.99970	0.99784	0.99960	0.99925
1	30	0.99973	0.99787	0.99962	0.99930
1	**40**	**0.99977**	**0.99789**	**0.99964**	**0.99933**
1	50	0.99972	0.99786	0.99961	0.99931

The bold values indicate the optimum value.

comparative study of average load and mid span deflection behaviour is depicted in Figure 7. When Scheme B beams is bonded with fully wrapped JFRP, the behaviour was found to be superior compared to that of control beams of Scheme A. The ultimate load at failure was found to be much higher when the mid span deflection was externally bonded with JFRP. The FRP bonded to the beam, resulted in a delay in the formation of cracks. Continuous/fully wrapped FRP-retrofitted beams outperformed strip wrapping retrofitted beams in terms of load-deflection. The brittle failure can be avoided in the beams by using this configuration, which was found to be more effective, since beams have deflected and given enough warnings prior to failure.

4.3. Effect on Ductility. The ability of a reinforced structure to withstand inelastic deformation without losing its load carrying capacity prior to failure is a desirable structural property. Deformation can take the form of deflection, strain, or curvature [26]. The results demonstrated in Table 3 indicate that the wrapped JFRP beams have greater ductility than the control beam.

5. Artificial Neural Network (ANN) Modeling

It is recommended that a three-layer feed-forward ANN method be used, with 1 input, 1 hidden, and 1 yield layers. Figure 8 depicts the general ANN structure of the defined problem. For the deflection, the input layer had 4 neurons, whereas the yield layer only had 1. The findings were sent into the ANN model, with each piece of data representing a complex aggregation of process variables. The training, validation, and testing data were separated into three groups, with 60, 20, and 20% of all training, validation, and testing data, respectively. The model was trained using the Levenberg–Marquardt approach. Learning networks have made use of it. The artificial neural network (ANN) was repeatedly trained to lessen the MSE score metric among the ANN outputs and the target data. The outcomes of ANN computations for the preceding network are shown in Tables 4–6 for Schemes A, B, and C, respectively. With the partial data, ANN modeling using less neurons inside a hidden layer correctly predicts the deflection in all circumstances. Despite this, because to the optimal point of the modeling coefficient, 30 neurons in a solitary hidden layer architecture were regarded to reflect

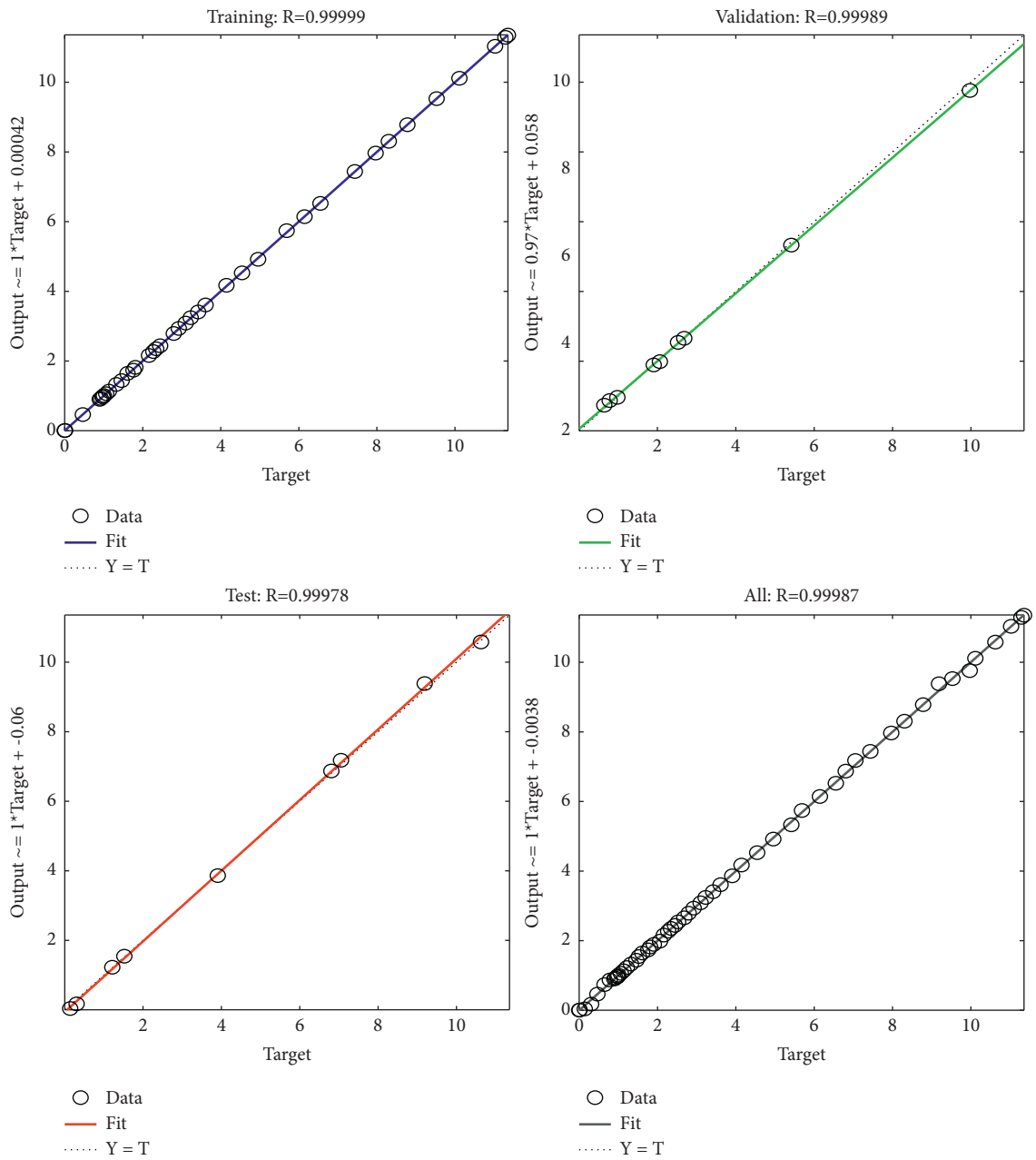

Figure 9: Neural network training regression analysis (optimal performance at 30 neurons in the hidden layer for Scheme A).

the ANN modeling outcome (for Scheme A). The deflection produced from ANN modeling for hidden neurons inside the hidden layer network is shown in Figure 9 (Scheme A), Figure 10 (Scheme B), and Figure 11 (Scheme C). For all retrofitting strategies, experimental data are compared to ANN's estimated deflection data. Figure 12 (Scheme A), Figure 13 (Scheme B), and Figure 14 (Scheme C) show the correlations between actual and expected outcomes. Scheme A, B, and C samples' observed responses (deflection) are compared to the model's projected responses, and the relative correlation charts are shown. The "R^2" values for the above schemes are found to be in the region of 0.99, suggesting that the test values and anticipated values are highly correlated.

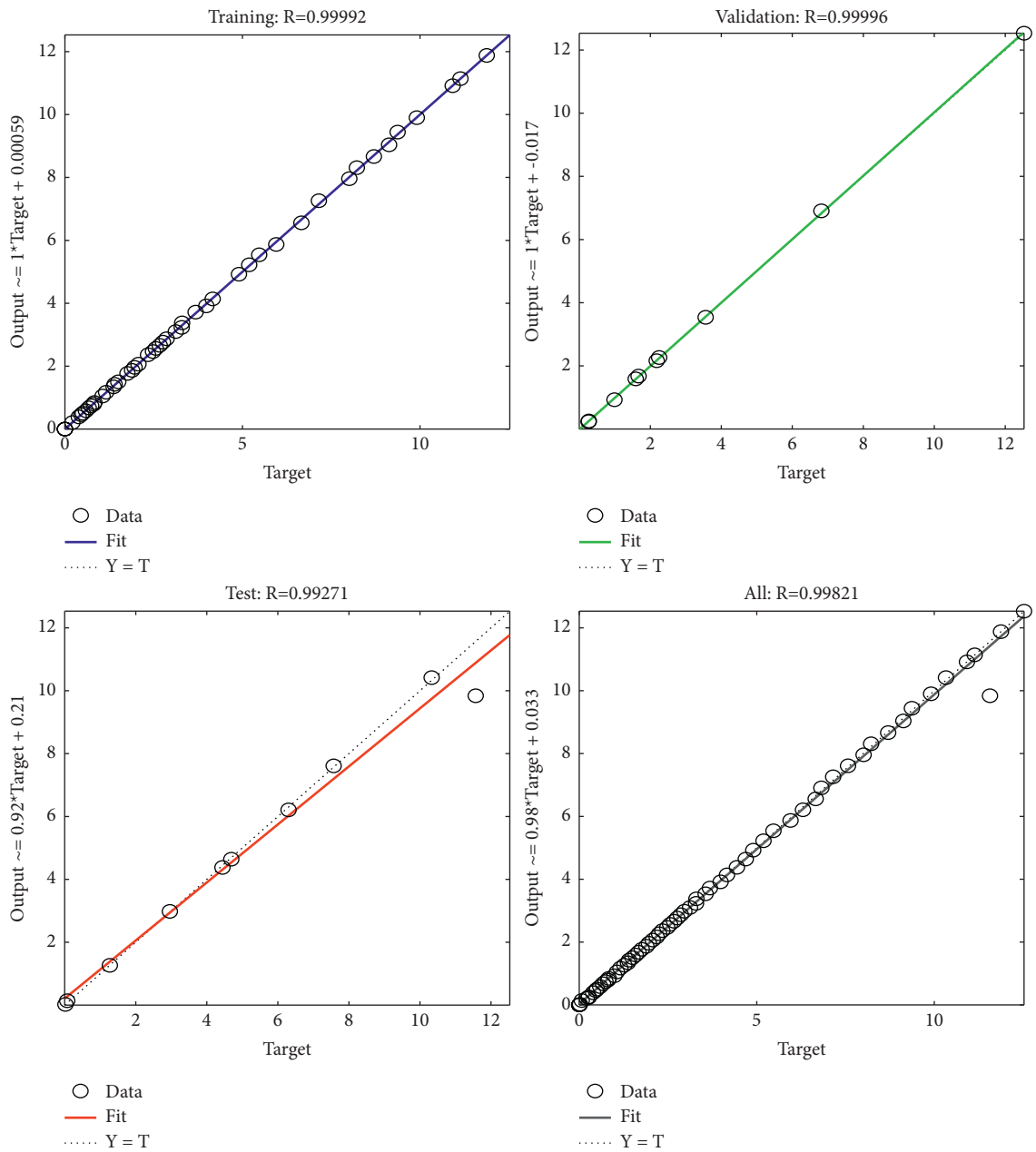

Figure 10: Neural network training regression analysis (optimal performance at 40 neurons in the hidden layer for Scheme B).

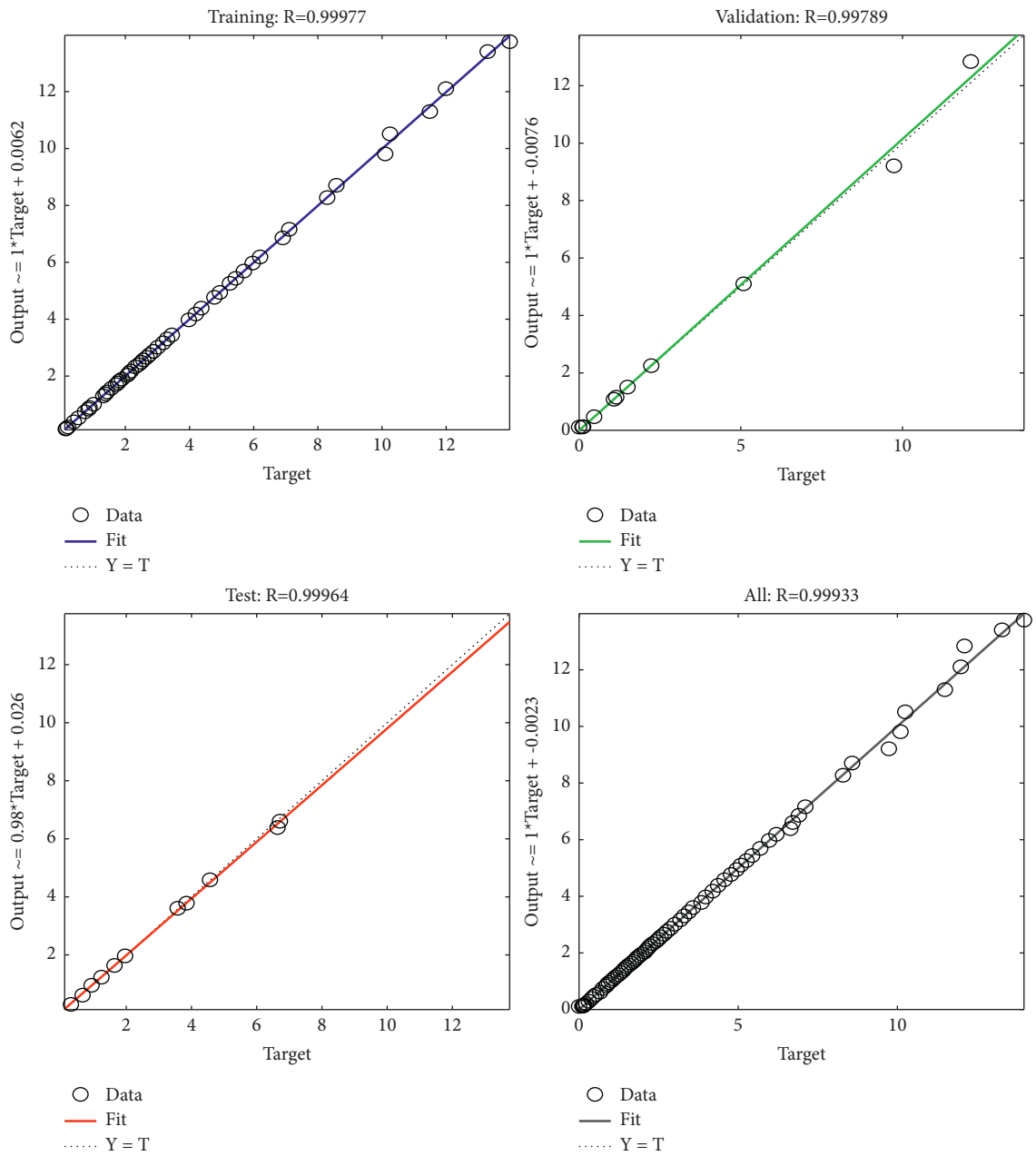

Figure 11: Neural network training regression analysis (optimal performance at 50 neurons in the hidden layer for Scheme C).

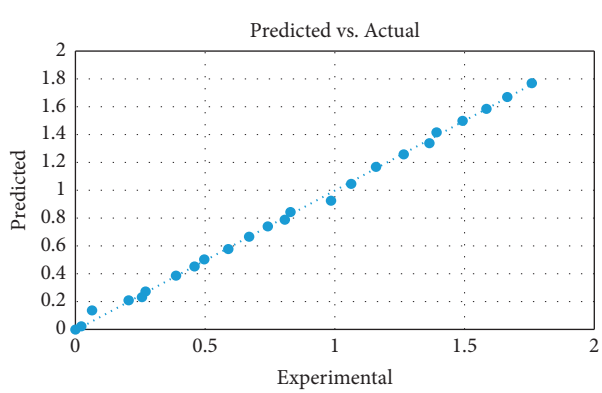

Figure 12: Correlation graph for Scheme A specimen.

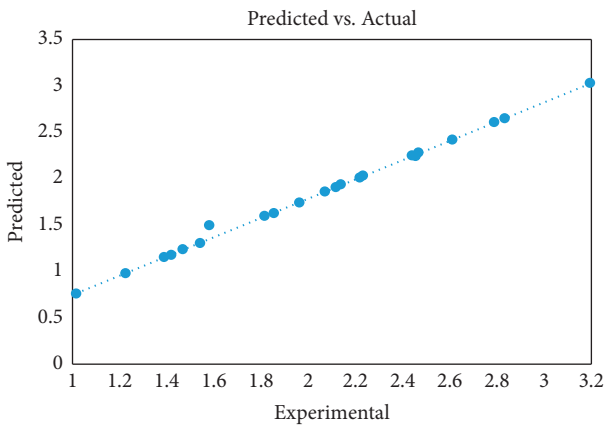

Figure 13: Correlation graph for Scheme B specimen.

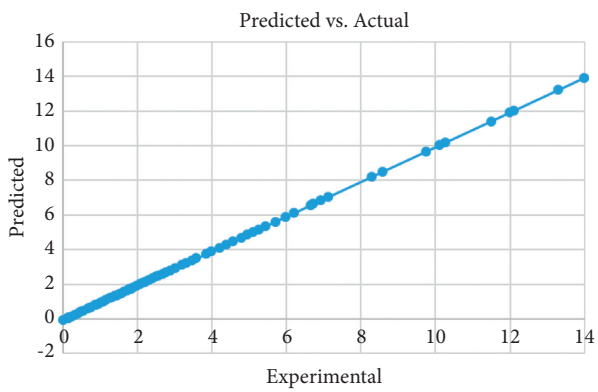

Figure 14: Correlation graph for Scheme C specimen.

6. Conclusions

The applicability and efficiency of JFRP as a strengthening material, as well as the effect of various wrapping techniques on the strengthening of beams, were experimentally investigated in this study.

(i) Load carrying capacity of the single layer of fully wrapped and strip-wrapped beams is improved by 23% and 10%, respectively, in comparison with the control beams. The JFRP bonded to the beam, which inhibited the development of cracks and delayed their formation. When the JFRP was used in the flexure deficient beams, initial cracks formed at higher loads than their respective control beams.

(ii) It showed that the use of polymer composites was effective for the flexural strengthening of structures. In all the strengthened beams, ultimate strength was found to be increased with the increase in laminate width, and strip wrapping exhibits lower load carrying capacity than full wrapping. The load-deflection behaviour of JFRP-enhanced beams was superior to that of controlled beams. The failure pattern of a JFRP-strengthened beam showed a significant difference. In JFB4, JFB5, and JFB6, a single crack has been developed in the flexural region and two cracks were developed away from it.

(iii) Widening of the cracks within the flexure zone was noticed as the load increased, but fortunately, there was no brittle failure maybe because of the good amount of confinement provided by the JFRP in the strengthened beam. The ductile behaviour obtained with JFRP provided sufficient warning prior to ultimate failure.

(iv) In Scheme C beams (JFB7, JFB8, and JFB9), favorable observation was made that flexural cracks were formed only in the beam area and not on the JFRP, as well as failure, which supports the experimental outcomes.

(v) The predicted values agree well with the experimental values, as evidenced by the good agreement of R^2 values of deflection.

(vi) The results of the study, experiments, and data analysis have confirmed that the efficiency of the beams and also the load carrying capacity can be increased by using JFRP, which has high potential for enhancing these characteristics. The study reveals the use of natural fibres such as jute in FRP for increasing the flexural strength of concrete structures is found to be a good alternative method.

Data Availability

The data used to support the findings of this study are included within the article.

Conflicts of Interest

The authors declare that there are no conflicts of interest regarding the publication of this article.

Acknowledgments

The authors acknowledge BBR India Pvt. Ltd., and Miki Steels Pvt. Ltd., Bengaluru, for assistance during this study.

References

[1] M. Badawi and K. Soudki, "Effect of FRP wraps on the tensile strength of plain and reinforced concrete beams," in *Proceedings of the 4th Structural Specialty Conference*, pp. 1–10, Canada, June 2002.

[2] H. Toutanji, L. Zhao, and Y. Zhang, "Flexural behavior of reinforced concrete beams externally strengthened with CFRP sheets bonded with an inorganic matrix," *Engineering Structures*, vol. 28, no. 4, pp. 557–566, 2006.

[3] M. R. Esfahani, M. R. Kianoush, and A. R. Tajari, "Flexural behaviour of reinforced concrete beams strengthened by CFRP sheets," *Engineering Structures*, vol. 29, no. 10, pp. 2428–2444, 2007.

[4] S. Syed Ibrahim, S. Eswari, and T. Sundararajan, "Experimental investigation on FRC beams strengthened with GFRP laminates," *Electronic Journal of Structural Engineering*, vol. 15, no. 1, pp. 55–59, 2015.

[5] K. Al-Deen Bsisu, Y. Hunaiti, and Y. Raja, "Flexural ductility behavior of strengthened reinforced concrete beams using steel and CFRP plates," *Jordan Journal of Civil Engineering*, vol. 6, no. 3, pp. 304–312, 2012.

[6] A. F. Ashour, S. A. El-Refaie, and S. W. Garrity, "Flexural strengthening of RC continuous beams using CFRP laminates," *Cement and Concrete Composites*, vol. 26, no. 7, pp. 765–775, 2004.

[7] H. N. Garden and L. C. Hollaway, "An experimental study of the influence of plate end anchorage of carbon fibre composite plates used to strengthen reinforced concrete beams," *Composite Structures*, vol. 42, no. 2, pp. 175–188, 1998.

[8] S. T. Smith and J. G. Teng, "FRP-strengthened RC beams. I: review of debonding strength models," *Engineering Structures*, vol. 24, no. 4, pp. 385–395, 2002.

[9] M. Mahalingam, R. P. N. Rao, and S. Kannan, "Ductility behavior fibres reinforced concrete beams strengthened with externally bonded Glass fibres reinforced polymer laminates," *American Journal of Applied Sciences*, vol. 10, no. 1, pp. 107–111, 2013.

[10] A. Khalifa, G. Tumialan, A. Nanni, and A. Belarbi, "Shear strengthening of continuous RC Beams using externally bonded CFRP sheets," in *Proceedings of the 4th International Symposium on FRP for Reinforcement of Concrete Structures*, pp. 995–1008, Baltimore, MD, USA, October 1999.

[11] D. P. Archana and H. N. Jagannatha Reddy, "Potential of natural fibres for strengthening existing structures–a review," *International Journal of Structural Engineering and Analysis*, vol. 4, no. 2, pp. 38–46, 2018.

[12] T. Sen and H. N. Jagannatha Reddy, "Strengthening of RC beams in Flexure using natural jute fibre textile reinforced composite system and its comparative study with CFRP and GFRP strengthening systems," *International Journal of Sustainable Built Environment*, vol. 2, no. 1, pp. 41–55, 2013.

[13] A. Alam, K. Alriyami, M. Z. Jumaat, and Z. C. Muda, "Development of high strength natural fibre based composite plates for potential application in retrofitting of RC structure," *Indian Journal of Science and Technology*, vol. 8, no. 15, 2015.

[14] M. A. R. Bhutta, A. K. Nur Hafizah, M. Y. Jamaludin, M. H. Warid, M. Ismail, and M. Azman, "Strengthening reinforced concrete beams using kenaf fiber reinforced polymer composite laminates," in *Proceedings of the 3rd International Conference on Sustainable Construction Materials and Technologies*, Kyoto, Japan, August 2013.

[15] S. C. Chin, F. S. Tong, D. S. Ing, J. Gimbun, H. R. Ong, and J. P. Serigar, Strengthening performance of PALF-epoxy composite plate on reinforced concrete beams," *IOP Conference Series: Materials Science and Engineering*, vol. 318, Article ID 012026, 2018.

[16] G. Di Luccio, L. Michel, E. Ferrier, and E. Martinelli, "Seismic retrofitting of RC walls externally strengthened by flax-FRP strips," *Composites Part B: Engineering*, vol. 127, pp. 133–149, 2017.

[17] T. Sen and H. N. J. Reddy, "Flexural Strengthening of RC beams using natural sisal and artificial carbon and glass fabric reinforced composite system," *Sustainable Cities and Society*, vol. 10, pp. 195–206, 2014.

[18] M. A. Alam and K. Al Riyami, "Shear strengthening of reinforced concrete beam using natural fibre reinforced polymer laminates," *Construction and Building Materials*, vol. 162, pp. 683–696, 2018.

[19] T. Sen and H. N. J. Reddy, "A Numerical study of Strengthening of RCC beam using natural Bamboo fibre," *International Journal of Computer Theory and Engineering*, vol. 3, no. 5, 2011.

[20] L. Ghalieh, E. Awwad, G. Saad, H. Khatib, and M. Mabsout, "Concrete columns wrapped with hemp fiber reinforced polymer - an experimental study," *Procedia Engineering*, vol. 200, pp. 440–447, 2017.

[21] T. Sen and H. N. J. Reddy, "Finite element simulation of Retrofitting of RCC beam using coir fibre composite," *International Journal of Innovation, Management and Technology*, vol. 2, no. 2, 2011.

[22] T. K. Mulenga, A. U. Ude, and C. Vivekanandhan, "Techniques for modelling and optimizing the mechanical properties of natural fiber composites: a review," *Fibers*, vol. 9, no. 1, 2021.

[23] T. Naresh Kumar, B. Murali, and J. Arulmani, "Machining characteristics of natural fiber particle reinforced polymer composite material using artificial neural network," *International Journal of Innovative Technology and Exploring Engineering*, vol. 8, no. 9, pp. 3350–3354, 2019.

[24] S. Pujari, A. Ramakrishna, and K. T. Balaram Padal, "Comparison of ANN and regression analysis for predicting the water absorption behaviour of jute and banana fiber reinforced epoxy composites," *Materials Today proceedings*, vol. 4, no. 2, pp. 1626–1633, 2017.

[25] D. P. Archana, H. N. Jagannatha Reddy, R. Prabhakara, M. U. Aswath, and A. Chandrashekar, "Processing and properties of biodegradable composites to strengthen structures," *The Institution of Engineers: Series C*, 2021.

[26] E. Natarajan, "Ductility response of hybrid fibre reinforced concrete beams," *Journal of Urban and Environmental Engineering*, vol. 11, no. 2, pp. 174–179, 2017.

Hindawi
Advances in Materials Science and Engineering
Volume 2021, Article ID 6907631, 9 pages
https://doi.org/10.1155/2021/6907631

Research Article

Studies on Mechanical Properties of Kevlar/Napier Grass Fibers Reinforced with Polymer Matrix Hybrid Composite

R. Ganesamoorthy,[1] R. Meenakshi Reddy,[2] T. Raja,[3] Pradeep Kumar Panda,[4] Sneha H. Dhoria,[5] Omaima Nasif,[6] Saleh Alfarraj,[7] Velu Manikandan,[8] and I. Jenish[9]

[1]*Centre for Materials Research, Chennai Institute of Technology, Chennai 600059, Tamil Nadu, India*
[2]*Department of Mechanical Engineering, G. Pulla Reddy Engineering College, Kurnool 518007, Andhra Pradesh, India*
[3]*Department of Mechanical Engineering, Vel Tech Rangarajan Dr. Sagunthala R&D Institute of Science and Technology, 400 Feet Outer Ring Road, Avadi, Chennai 600062, India*
[4]*Department of Chemical and Materials Engineering, Chang Gung University, Taoyuan 33302, Taiwan*
[5]*Department of Mechanical Engineering, R.V.R & J.C College of Engineering, Guntur, Andhra Pradesh, India*
[6]*Department of Physiology, College of Medicine and King Khalid University Hospital, King Saud University, Medical City, P.O. Box-2925, Riyadh 11461, Saudi Arabia*
[7]*Zoology Department, College of Science, King Saud University, Riyadh 11451, Saudi Arabia*
[8]*College of Environmental & Bioresource Sciences, Jeonbuk National University, Iksan 570752, Republic of Korea*
[9]*Department of Applied Mechanics, Seenu Atoll School, Hulhumeedhoo, Addu City 19060, Maldives*

Correspondence should be addressed to I. Jenish; jenish@satollschool.edu.mv

Received 4 August 2021; Accepted 18 September 2021; Published 11 October 2021

Academic Editor: Jinyang Xu

A percentage of natural fibers is used for developing a composite, the materials are quite increasing in recent trends, and they can be a potential replacement of synthetic fibers in the reinforcement phase of hybrid composite. In this research, the combination of natural fibers and synthetic fibers can be used as reinforcement, and epoxy polymer can be used as matrix material. The fibers of Kevlar and Napier grass are reinforced with epoxy matrix to develop a new composite by using conventional hand layup fabrication process and to quantify the effect of this hybrid composite laminate, with five different sequences following. To identify the mechanical properties of this hybrid composite through tensile, flexural, compression strength, impact strength, and hardness tests, among all five samples, sample A was given the maximum mechanical strength, such that the tensile strength is 210 MPa, flexural strength is 165 MPa, the impact energy absorption is 23 J, the average is 40% over the other samples, and, at the same time, the compression strength of sample E is 19 MPa, revealing the negative influence of hybrid composite. The SEM morphology was carried out to identify the failure mode of the hybrid composites.

1. Introduction

The combination of natural fibers and synthetic fibers can give unique properties in physical and chemical categories in a developed composite material [1]. These unique properties are quite increasing the product efficiency and can reduce the environment impact. Composites can be developed either naturally or synthetically. Wood, a characteristic composite, is a mix of cellulose or wood fibers and a substance called lignin [2]. The fiber strengthens wood; lignin is the lattice or normal paste that ties and balances them out. Different composites are engineered (man-made). Compressed wood is a man-made composite that consolidates common and manufactured materials; a composite made of neem and banyan fibers reinforced with epoxy polymer was given a maximum tensile strength of 25 MPa; therefore, the utilization of natural fibers with synthetic fibers can improve the mechanical properties of the hybrid composite [3]. Designed

structures are probably going to be presented to affect loading by outside courses, and this could be relied upon to occur during the maintenance, assembling, and administration tasks. Impact resistance is one of the significant uncertainties in matrix polymer composites [4]. Composites are exceptionally delicate to loading; in this way, after this sort of stacking, they are genuinely harmed, and their mechanical properties are decreased. The term hybrid is defined as combining one or two matrix elements, which resulted as hybrid composites [5]. Hybrid composites are made to join the upside of one fiber with the other. For instance, high modulus fiber like graphite has outstandingly high solidarity to weight proportion, yet their effect quality has commonly been seen as moderately low contrasted and traditional steel and aluminum alloys, and, furthermore, with glass fiber strengthened composites [6]. Henceforth, the utilization of natural fibers alone in the polymer matrix is lacking in sufficiently handling all specialized needs of a fiber-strengthened composite. With an end goal to build up an unrivalled, yet sensible composite, a characteristic fiber can be combined with a manufactured fiber in a similar network material to exploit the properties of both filaments. This results in a characteristic manufactured hybrid fiber composite [7]. The most well-known engineered fiber utilized in these hybrid composites is the glass fiber as a result of ease and simplicity of accessibility contrasting other synthetic strands [8]. The measure of the power required to break material and the sum it reaches out before breaking are significant properties. For most materials, the underlying protection from power or modulus and the purpose of changeless distortion are got from plots of power against elongation [9]. Examination of elongation force or stress-strain curvatures can pass on much about the material being tried, and it can help in anticipating its manner. It is usually estimated in units of force per cross-sectional zone. This is a significant idea in design, particularly in the fields of material science, mechanical structure, and basic design [10]. Hardness test strategies utilize an indenter test that is dislodged from a surface under a particular burden. Space was regularly characterized as stand time. Large scale hardness covers testing with an applied burden more than 1 kg or around 10 Newtons (N). Microhardness testing with applied loads under 10 N is commonly utilized for small sample sizes, plated surfaces, or thin films [11]. Microstructure examination is finished by utilizing the optical magnifying instrument; however, these days, there is improvement finished with a computerized investigation utilizing image processing techniques. By utilizing this examination, we can discover that the yield quality and extreme flexible or compressive quality are not also settled predominantly, because of the high hardness and low malleability that make the declaration of solid data of the material a difficult task. Fibers have been delivered utilizing various materials, for example, steel, polypropylene, and glass, among others, slowly across the board in various applications, specifically in the creation of fiber-strengthened cement, [12]. Composites reinforced with plant fibers are especially intriguing, particularly flax fiber strengthened polymers (FFRP). Build up a vacuum packing technique to investigate the mechanical properties of covers arranged on various pieces of banana and E-Glass fabrics. The mechanical properties assessed are elasticity, flexural quality, sway quality, and hardness. Portrayed mechanical property assessment of glass–jute fiber reinforced polymer composites. Glass–jute fiber strengthened polymer composite is created, and the mechanical properties are examined, the reinforcement (60%) and matrix (40%) of the composite laminates are different weight fractions of reinforcement, and the natural fibers utilized to assess the effect of the hybrid composites are chopped bamboo fibers and kenaf fiber in the matrix and type of woven fabric, conducting a dynamic mechanical analysis to determine the storage modulus (DMA) and the results of the chopped bamboo laminates [13, 14]. The materials chosen for the investigations were jute fiber and glass fiber as the support and epoxy sap as the matrix. The hand layout strategy was utilized to manufacture these composites. Cracked surfaces were exhaustively analyzed using SEM to decide the microscopic crack mode [15]. Results indicated that, by fusing the ideal measure of jute filaments, the general quality of the glass fiber strengthened composites can be expanded, and cost sparing of beyond 30% can be accomplished. It would, thus, be able to be surmised that jute fiber can be an exceptionally potential up-and-comer in the manufacture of composites, particularly for the incomplete substitution of significantly expense glass fibers for low load bearing capacities [16]. In comparison with other hybrid composite samples, the hardness and water absorption values of the hybrid composite increased with 83 hardness numbers and 1.2 percent water absorption capacity when equal weight fractions of neem and banyan fibers were used. When the applied loading is applied to the hybrid composite, the matrix failure rate and fracture are predominant, as indicated by the micrographs [17]. Portrayed hybrid composites of glass/bamboo fiber were fortified to assess the impact of stacking arrangement on ductile, flexural, and erosive wear properties of mixture polymer composites. The outcomes demonstrated that the properties of bamboo composite can be altogether improved by consolidation of glass fiber in polymer composite. The layer succession has a more prominent impact on the mechanical and tribological properties of the hybrid composite in the developed composite made of neem fiber and banyan fibers are analyzed with dynamic mechanical behavior, and it shows that the solidness of the material with high temperature ratio and the glass transition temperature of 89°C can withstand the material with the storage modulus of 1150 MPa; therefore, reinforcement of natural fibers can give good dynamic properties, and, at the same time, the addition of synthetic fiber can improve the materials behavior in static and dynamic loading conditions of hybrid composite. [18].

From the above details about the hybrid composite, the research gap was identified; in the present work, the combination of natural and synthetic fibers is Napier grass and Kevlar fibers selected for reinforcement, using epoxy polymer as matrix material to identify the effect of this hybrid composite with varying layers of fiber sequence to conduct the mechanical behavior and analyze the surface morphology of hybrid composite.

2. Materials and Methods

2.1. Materials Used. The hybrid materials are selected on the base of material properties such as mechanical strength and dynamic strength [19]. The common materials are selected over layup with various arrangements. Kevlar is a synthetic fiber, and Napier grass is a natural fiber, which is collected as woven fabric from go Green Pvt. Limited, Chennai, India, and the epoxy resin araldite LY 556 type and hardener HY 951 type were selected as matrix materials, and they were collected from Javanthi enterprises Chennai India. The general properties of reinforcement materials, Kevlar fiber and Napier grass fiber, are given in Table 1 and the epoxy matrix material properties are given in Table 2.

2.2. Experimental Methods. In this work, the reinforcement of Kevlar and Napier grass fibers is selected with epoxy matrix to fabricate the hybrid composite by traditional hand layup technique. Steel mould box 30 cm × 30 cm is selected for the fabrication process; initially, the steel mould box is cleaned thoroughly, and it keeps the thin layer of polythene sheet and applies the wax to this thin sheet for releasing agent [20]. As per the fiber volume fraction 40% of reinforcement and 60% of matrix material is selected. A thin nonreactive laminate is used to cover the steel board to attain a decent superficial finish. After the process, the mould releasing mediator is applied for sticking the polymer resin to the surface [21]. The resin material is functional as layered by a brush, and the Kevlar fiber mat and Napier grass mat were placed accordingly on the steel board. The stacking sequences of these fibers are varied and develop five different laminates of the hybrid composite. The completely wetted fiber laminated composite is then allowed to cure for 4 hours at a temperature of around 75°C in a hot air furnace at a very slow rate of heating (10°C per minute), followed by 2 hours of postcuring at a temperature of 120°C [22]. Schematic image of the hand layup fabrication process is shown in Figure 1 and the production of Kevlar/Napier grass fiber hybrid composite is shown in Figure 2.

2.3. Mechanical Properties of Hybrid Composite. Weight concentration and stacking sequence of K/N hybrid composite laminates are given in Table 3. The most widely recognized and thoroughly utilized testing is tensile testing. Different tests are kept away from for a homogeneous material, and there is an immediate connection between the tensile and compression. The testing samples of Kevlar/Napier grass fiber hybrid polymer composite are shown in Figure 3.

Tensile Testing: The tensile test is performed as per ASTM 638 standard on the hybrid composite at ambient temperature with a slow rate of loading (1 mm/min), and the compressive test is performed as per ASTM 3410 standard on the hybrid composite using the same UTM as the tensile test [23].

Izod Impact Test: As per ASTM D256, the Izod impact test is used to evaluate the impact resistance of hybrid composites. The impact test is done on hybrid composites to assess the impact energy absorption capacity of the hybrid composite based on the fiber weight fraction and stacking sequences of the constituent fibers [24].

Table 1: General properties of Kevlar fiber and Napier grass fiber.

Properties	Kevlar fiber	Napier grass fiber
Category	Synthetic fiber	Natural fiber
Type	Bidirectional woven fabric	Bidirectional woven fabric
GSM	200	200
Fiber diameter	50 micron (avg)	40 micron (avg)
Density	1.44 g/cc	1.25 g/cc

Table 2: Properties of epoxy polymer resin.

Matrix material: epoxy polymer resin	
Aspect (visual)	Clear liquid
Density at 30°C	1.23 g/cc
Viscosity at 30°C	10–12 Pa s
Curing temperature	75°C
Glass transition temperature (Tg)	120°C

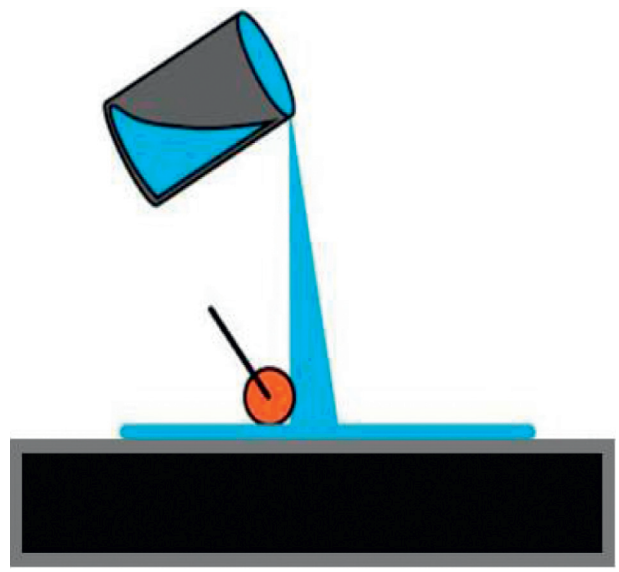

Figure 1: Schematic image of hand layup process.

Figure 2: Fabrication of K/N fiber hybrid polymer composite.

Table 3: Stacking sequence of hybrid composite laminates

Sample	Weight of Kevlar fiber in g	Weight of Napier grass fiber in g	Weight fraction of Kevlar/Napier grass fiber	Weight of epoxy matrix in g	Weight of composite laminate	Stacking sequence of Kevlar/Napier grass mat
A	150	0	4:0	220	370	K-K-K-K
B	112	38	3:1	220	370	K-K-K-N
C	75	75	1:1	220	370	K-K-N-N
D	38	112	1:3	220	370	N-N-N-K
E	0	150	0:4	220	370	N-N-N-N

K, Kevlar fiber mat, N, Napier grass fiber mat.

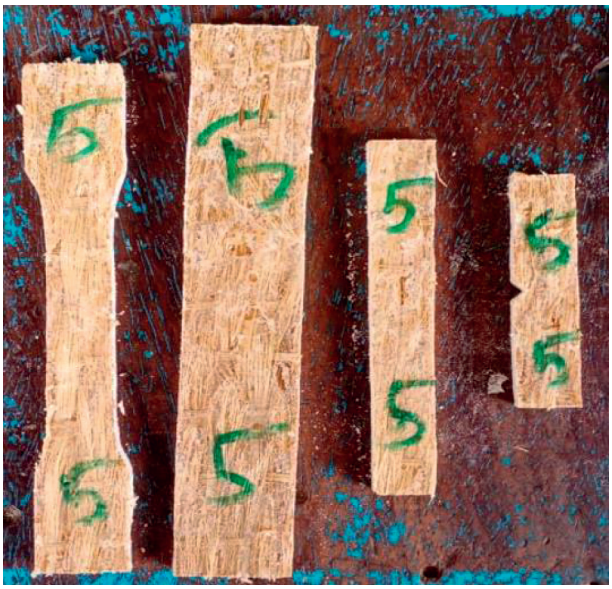

Figure 3: Testing samples of K/N hybrid composite.

Flexural Testing: The ASTM Standard D790-03 was used to create the flexural test specimens, which were fabricated from a composite plate. The specimen was 127 mm × 12.7 mm × 5 mm in dimension. The flexural test was performed at 28°C with a relative humidity of 50 2% using the Lloyd instrument LR 100 kN. The crosshead moved at a rate of 2 mm/min. The sample was loaded until the core cracked, as shown in Figure 3, 64.1, and the flexural strength and flexural loads were recorded. The values of the flexural modulus were determined [25]. For each composition, three samples were evaluated, and the mean value was reported.

Hardness Testing: The Rockwell hardness test is used to determine the hardness of the hybrid composite in this study. The specimens were prepared in accordance with ASTM E 18-07. The load range for the Rockwell hardness testing equipment is 60 kgf–150 kgf, using a 1/16 inch steel ball indenter. The load value of 60 kgf is used in this study, and the impression is detected in the hybrid composite. The hardness value of the hybrid composite is measured using the dial gauge in the testing equipment based on the impression [26]. The same method is repeated three times for each sample of natural fiber hybrid composite and the average hardness values of hybrid composite, and three trial list samples are taken. Scanning Electron Microscope is used to examine the surface interaction and morphology of the hybrid composite. The hybrid composites are sputter coated with gold particles prior to surface microanalysis to improve visibility.

3. Results and Discussion

3.1. Tensile Strength of Epoxy Composite. Tensile strength of epoxy composites with different weight fraction is shown in Figure 4. The hybrid composite is made of synthetic fibers of Kevlar mat, and natural fibers of Napier grass mat are selected for reinforcement with 40%, and epoxy resin with harden used as matrix is 60% for the samples. Weight fractions of Kevlar/Napier grass fibers varying in the samples are as follows: 150/0, 112/38, 75/75, 38/112, and 0/150. Based on this tensile experiment, increasing the weight ratio of Kevlar fiber has given significant values of tensile strength compared to the increasing Napier grass fibers; however, the variations in the results are higher in amount. Therefore, the comparison between synthetic fibers with natural fibers can give unique properties for lower tensile applications. Regarding the output from this tensile analysis, sample A has given higher tensile strength of 210 MPa, and this value shows 89% higher than sample E. Sample E contains a total composite laminate, which is made with the reinforcement of Napier grass fibers. For the comparison between samples B and D, sample B has 69% higher tensile strength compared with sample D due to the higher weight ratio of Kevlar fibers present in sample B containing 112 g Kevlar fiber and 38 g Napier grass fiber. The results can also depend on the stacking sequence of these fibers, the bonding of the Kevlar mat with epoxy matrix is a high covalent bond, and it can resist more during tensile loading, and the stress distribution also is high when increasing with Kevlar fiber mat.

In the above graph, it is revealed that the variation between samples A to E is decreasing the tensile strength when the equal weight ratio of K/N indicates that the 61 MPa of tensile strength is 71% lower than sample A and 51% lower than sample B. The major reason for the lower tensile strength in sample E is that all layers contained Napier grass fibers with epoxy matrix and are bonded thoroughly; however, the composite laminates can release the bonding when applying of tensile load, and this indicates that the fiber properties can play an important role during the tensile experiment [27]. Therefore, Kevlar fibers can be suitable for higher tensile applications compared to Napier grass fibers,

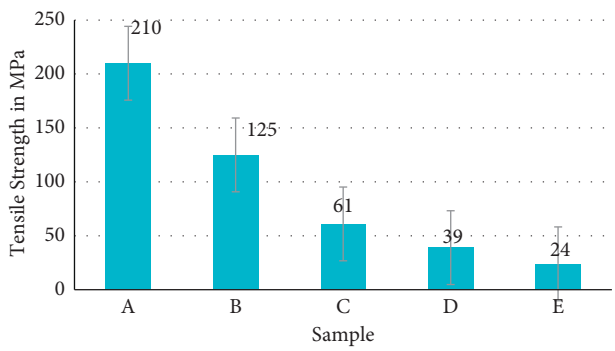

Figure 4: Tensile Strength of K/N hybrid composite laminates.

because they withstand higher tensile loading. The failure mode of the hybrid composite can be identified during the morphological analysis.

3.2. Compressive Strength of Hybrid Composite. Similar to tensile strength, the compressive strength of hybrid composite can be identified from five different samples of Kevlar/Napier grass fiber composite laminates. In this result, to quantify the effect of hybrid composite during compression test, the compressive strength of the hybrid composite is shown in Figure 5. The graph revealed that when the increase of Kevlar fiber mat has been given, a positive influence of hybrid composite in sample A shows higher compressive strength of 150 MPa, compared to other higher samples, and it contains four layers of Kevlar fiber; in sample B, it shows 81 MPa of compressive strength, and it contains three layers of Kevlar and one layer of Napier grass fiber mat giving 46% reduced compressive strength compared with sample A.

Adding equal amount of Kevlar/Napier grass fibers can give 42 MPa of compressive strength, and it is 72% lesser than sample A, and, at the same time, sample D containing equal ratio with different sequences of fibers compared with sample B can give 23 MPa. It shows 71% lesser than sample B. In sample E, all layers of natural fibers of Napier grass fiber show the least value of compressive strength of 19 MPa, and it shows 87% lesser than sample A. Therefore, it can be determined that the decrease of Kevlar fiber mat and the increase of Napier grass fiber mat gave the negative influence of hybrid composite laminates. In another work, the neem and banyan fibers are used to calculate the compressive strength of hybrid composite showing the better result of 23 MPa [28]. The present study reveals that the addition of 3-layer Napier grass with one layer of Kevlar fiber mat can compensate for the same results.

3.3. Flexural Strength of Hybrid Composite Laminates. Flexural strength of this hybrid composite can be identified from the different stacking sequence effect, and it is the gradual load applied on the direct contact of materials; it was performed under three-point bending test. In this work, the flexural strength was calculated for 2 mm deflection of the hybrid composite during this experiment.

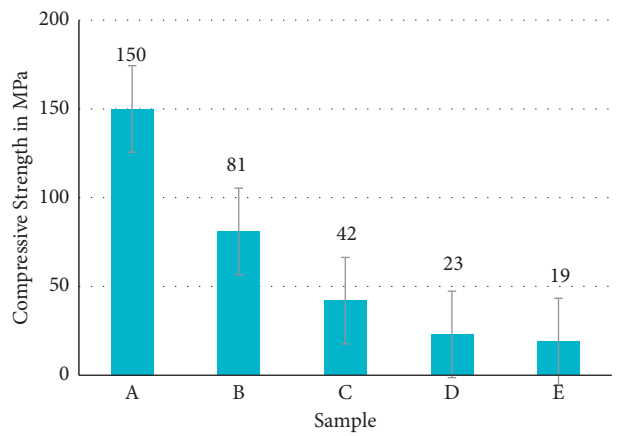

Figure 5: Compressive strength of K/N hybrid polymer composite.

The result showed that sample A was given a significant result over other samples, and it shows 42% more flexural capacity when compared with sample B, and it is contained in three layers of Kevlar and one layer of Napier grass fiber mat with epoxy matrix. It can withstand 70% more flexural load compared with sample D, in this category, samples B and D are sample weight fraction with different fibers of K/N; however, Kevlar fiber mat can improve the flexural load capacity compared with Napier grass fiber mat. The flexural strengths of the hybrid composite of K/N laminates are shown in Figure 6.

When applied, the equal amount of natural and synthetic fibers of K/N composite laminates has been given 51 MPa flexural strength; this value is 69% lesser than that of sample A. The impact of adding two layers of Napier grass fiber mat shows a negative influence of hybrid composite compared with four layers of Kevlar fiber composite laminate. In another work, banyan/ramie fibers are used as reinforcement in equal amount, with epoxy matrix polymer composite being developed and giving the good flexural behavior of 35 MPa [29]. This result can be compared with that of the present study, where the equal amount of Kevlar/Napier grass fibers gave 51 MPa flexural strength, and it shows 31% higher flexural strength, and it can be developed for an alternate material for gradual loading applications of hybrid composite.

3.4. Impact Energy of Hybrid Composite. Impact strength was calculated from the Izod impact test for this hybrid composite, the material can withstand gradual load normally, and it can be an important analysis to check the impact energy absorption for a new material [30]. In this study, two fibers are selected to quantify the effect of impact energy of this hybrid composite, the results are the same like other mechanical properties of the sample, and A is a higher impact energy of 23 J and can absorb during the sudden force applied on the K/N composite specimen. When the addition of one-layer Napier grass fiber mat was given 19 J, it shows 25% weight fraction impact of 17% lesser impact energy compared with all four layers of Kevlar fiber mat; however, it can be an improved result because of 8%

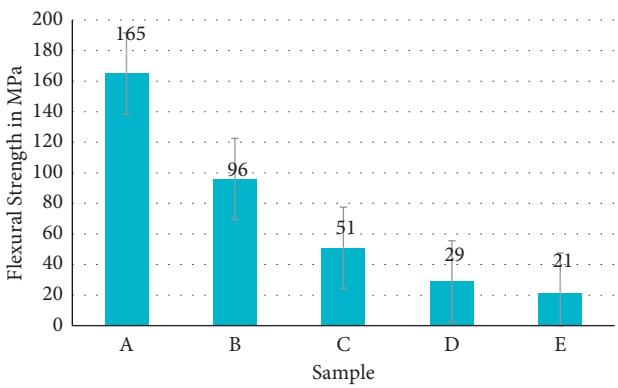

Figure 6: Flexural strength of K/N hybrid composite laminates.

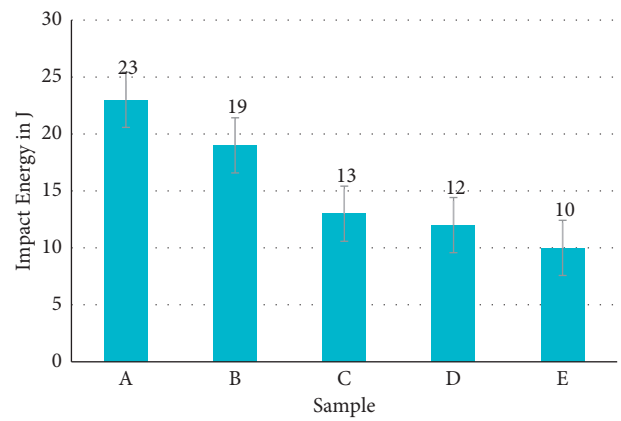

Figure 7: Impact energy of K/N fiber hybrid composite.

deviation in the results of material weight fraction. When adding two layers of Napier grass fiber with two layers of Kevlar fiber was given 13 J impact energy absorption, it shows 32% negative influence over sample B. The impact energy of K/N fiber hybrid composite laminates is shown in Figure 7.

Impact energy results can be compared with other mechanical properties of tensile, flexural, and compressive strength, and it shows good response to gradual deviation between the samples of hybrid composite. Sample D contains 3 layers of Napier grass fibers and one layer of Kevlar fiber, and the mat was given 12 J, and this can be compared with the same sequence with more Kevlar weight fraction in sample B that is 37% more impact energy and in sample E also 57% lesser impact energy compared with sample A. It can be calculated when increasing Napier grass and decreasing Kevlar fiber weight fraction show the negative influence of hybrid composite laminates.

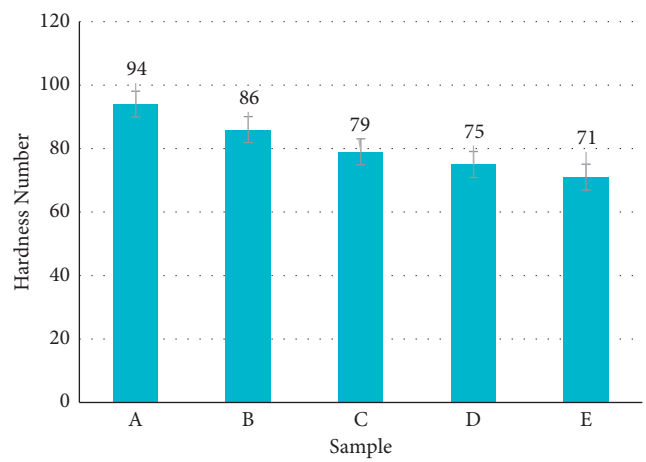

Figure 8: Hardness number of K/N hybrid polymer composite.

3.5. Hardness Value of Hybrid Composite Laminates. Hardness values of hybrid composite laminates are calculated from Rockwell hardness experiment; in this study, to quantify the hardness capacity of Kevlar and Napier grass fibers, the composite was identified, and the results are shown in Figure 8. Among the five different samples, sample A was given higher hardness number of the hybrid composite. The output of this experiment is majorly depending upon the top layer of the hybrid composite material and in samples A, B, and C having Kevlar fiber mat, the top layer of composite laminates can reflect the results of hardness values. In sample B, we got 86 of RHN, and it is 8% lesser than sample A, so the hardness values are depending on not only the top layer, but also the impact of the top layer that is more on the hardness value output of this hybrid composite. When the equal amounts of both fibers of Kevlar and Napier grass fibers are the same, 8% lesser than sample B, however, sample B of three layers of synthetic fiber and one layer of natural fiber.

In another work, a developed composite with jute fiber was given, 87 RHN with the addition of fillers can impact on this material [31], and, at the same time, this work reveals that, without any filler, the materials can reach higher values. The deviations between the samples are also less with other properties, sample D has 12% lesser RHN compared with sample B with the same sequence and different weight fractions, and the top layer of Napier grass can resist the gradual loading in hardness capacity. Sample E shows the least value of 71 RHN compared to sample A, 24% lesser hardness value of hybrid composite laminates.

3.6. Morphological Analysis. The conclusion from the Scanning Electron Microscopy (SEM) micrographs is obvious from the pictures that the fiber pull-outs, cracks, and failure are the major causes of hybrid fiber failure when subjected to tensile loading [32]. These failures are usually produced owing to the weak contact between the matrix orientations, which leads to the stress concentration producing catastrophic failure in the hybrid composite. Because of the increased level of stress concentration in the material, increasing the weight fraction of Napier grass fiber in hybrid composites results in a more complex level of cracks. The SEM micrographs of the hybrid composite are shown in Figure 9.

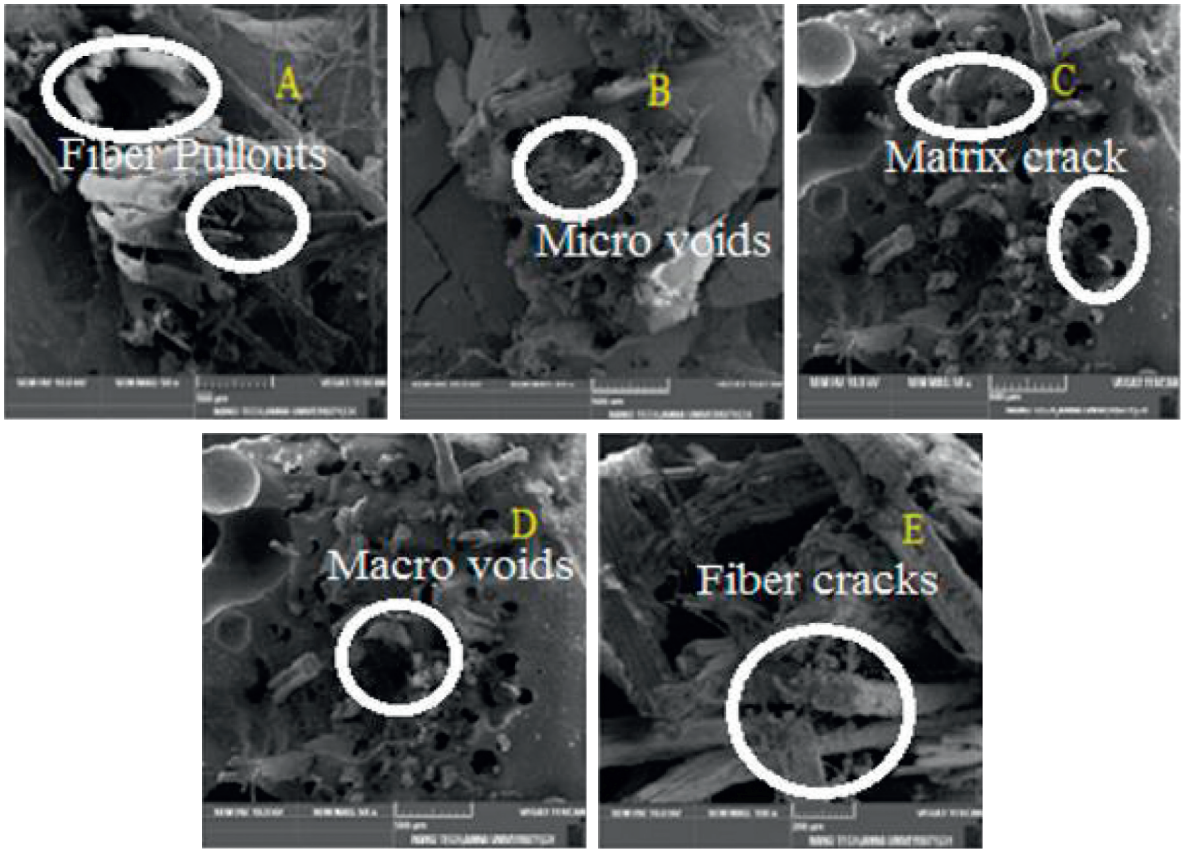

Figure 9: SEM micrographs of K/N hybrid composites.

4. Conclusion

Towards the improvement of natural fibers with synthetic fiber reinforcement, we can give the unique properties of hybrid composite for light weight applications. The followings are the main findings from the above works:

(i) The utilization of Kevlar fiber weight fraction in the sample A gave higher tensile strength of 210 Mpa, compressive strength of 150 MPa, flexural strength of 165 MPa, and impact energy of 23 J. The average of 40% improved the mechanical properties in sample A and 89% higher than sample E of the hybrid composite.

(ii) In sample B, three layers of Kevlar fiber mat and one layer of Napier grass fiber mat gave significant results over sample D in different weight fractions. Equal numbers of fibers also can give significant results for light weight applications.

(iii) Therefore, synthetic fiber layers can give the positive influence of these mechanical properties of the hybrid composite. Natural fiber layers increased the failure rate compared to synthetic fiber composite.

(iv) Surface morphology reveals the failure rate and failure mode of hybrid composites, and the increase of Napier grass fiber composite laminates occurred with more stress concentration leading to material failure during the gradual loading.

(v) It can be determined that the amount of Napier grass fibers can utilize the light weight application with the addition of synthetic fibers, can improve the results, and can be used in aerospace applications of hybrid composite.

Data Availability

The data used to support the findings of this study are included within the article.

Disclosure

This study was performed as a part of employment in Seenu Atoll School, Maldives.

Conflicts of Interest

The authors declare that there are no conflicts of interest regarding the publication of this article.

Acknowledgments

The authors appreciate the supports from Seenu Atoll School, Maldives. The authors thank Chennai Institute of Technology, Chennai, and Vel Tech Rangarajan Dr. Sagunthala R&D Institute of Science and Technology, Chennai, for providing technical assistance to complete this experimental work. This project was supported by researchers supporting project

number RSP-2021/257, King Saud University, Riyadh, Saudi Arabia.

References

[1] T. G. Yashas Gowda, M. R. Sanjay, K. Subrahmanya Bhat, P. Madhu, P. Senthamaraikannan, and B. Yogesha, "Duc Pham Polymer matrix-natural fiber composites: an overview," *Cogent Engineering*, vol. 5, no. 1, Article ID 1446667, 2018.

[2] K. Yorseng, M. R. Sanjay, J. Tengsuthiwat et al., "Information in United States patents on works related to 'natural fibers': 2000-2018," *Current Materials Science*, vol. 12, no. 1, pp. 4–76, 2019.

[3] R. Thandavamoorthy and A. Palanivel, "Testing and evaluation of tensile and impact strength of neem/banyan fiber-reinforced hybrid composite," *Journal of Testing and Evaluation*, vol. 48, no. 1, pp. 647–655, 2020.

[4] S. Mr, S. Siengchin, J. Parameswaranpillai, M. Jawaid, C. Pruncu, and A. Khan, "A comprehensive review of techniques for natural fibers as reinforcement in composites: preparation, processing and characterization," *Carbohydrate Polymers*, vol. 83, no. 11, pp. 108–121, 2018.

[5] K. Bharath, M. Sanjay, M. Jawaid, S. Basavarajappa, and S. Siengchin, "Effect of stacking sequence on properties of coconut leaf sheath/jute/E-glass reinforced phenol formaldehyde hybrid composites," *Journal of Industrial Textiles*, vol. 49, no. 1, pp. 3–32, 2019.

[6] S. Abhishek, M. R. Sanjay, G. Raji, S. Suchart, J. Parameswaranpillai, and C. I. Pruncu, "Jyotishkumar Parameswaranpillai & Catalin Iulian Pruncu Development of new hybrid Phoenix, pusilla/carbon/fish bone filler reinforced polymer composites," *Journal of the Chinese Advanced Materials Society*, vol. 6, no. 5, pp. 553–560, 2018.

[7] K. Ganesan, C. Kailasanathan, M. R. Sanjay, P. Senthamaraikannan, and S. S. Saravanakumar, "A new assessment on mechanical properties of jute fiber mat with egg shell powder/nanoclay-reinforced polyester matrix composites," *Journal of Natural Fibers*, vol. 17, no. 4, pp. 480–490, 2018.

[8] P. Kumaran, S. Mohanamurugan, S. Madhu et al., "Investigation on thermo-mechanical characteristics of treated/untreated Portunus sanguinolentus shell powder-based jute fabrics reinforced epoxy composites," *Journal of Industrial Textiles*, vol. 50, no. 4, pp. 427–459, 2019.

[9] P. Madhu, M. R. Sanjay, P. Senthamaraikannan, S. Pradeep, S. S. Saravanakumar, and B. Yogesha, "A review on synthesis and characterization of commercially available natural fibers: Part-I," *Journal of Natural Fibers*, vol. 16, no. 8, pp. 1132–1144, 2018.

[10] T. Raja and P. Anand, "Evaluation of thermal stability and thermal properties of neem/banyan reinforced hybrid polymer composite," *Materials Performance and Characterisation*, vol. 8, no. 1, pp. 481–490, 2019.

[11] K. Mehar, S. K. Panda, and T. R. Mahapatra, "Thermoelastic deflection responses of CNT reinforced sandwich shell structure using finite element method," *Scientia Iranica*, vol. 25, pp. 2722–2737, 2017.

[12] S. D. Salman, Z. Leman, M. T. H. Sultan, M. R. Ishak, and F. Cardona, "The effects of orientation on the mechanical and morphological properties of woven kenaf-reinforced poly vinyl butyral film," *Bio Resources*, vol. 11, no. 1, pp. 1176–1188, 2015.

[13] T. Raja, P. Anand, K. Karthik, and J. Udaya Prakash, "Mechanical properties and moisture behaviour of neem/banyan fibres reinforced with polymer matrix hybrid composite," *Advances in Materials and Processing Technologies*, pp. 1–12, 2021.

[14] M. Jawaid, H. P. S. Abdul Khalil, and O. S. Alattas, "Woven hybrid bio-composites: dynamic mechanical and thermal properties," *Composer Part A Appl Sci Manuf*, vol. 43, no. 2, pp. 288–293, 2011.

[15] V. J. Binu Kumar, J. Bensam Raj, R. Karuppasamy, and R. Thanigaivelan, "Influence of chemical treatment and moisture absorption on tensile behavior of neem/banana fibers reinforced hybrid composites: an experimental investigation," *Journal of Natural Fibers*, pp. 1–12, Article ID 1838995, 2020.

[16] R. Balaji, M. Sasikumar, and A. Elayaperumal, "Thermal, Thermo oxidative and Ablative behavior of cenosphere filled ceramic/phenolic composites," *Polymer Degradation and Stability*, vol. 114, pp. 125–132, 2015.

[17] E. Chandana and I. Syed Altaf Hussian, "Thermal conductivity characterization of bamboo fiber reinforced in epoxy resin," *IOSR Journal of Mechanical and Civil Engineering*, vol. 9, no. 6, pp. 7–14, 2013.

[18] T. Raja and P. Anand, "Investigations on dynamic mechanical analysis and crystalline effect of neem/banyan fiber–reinforced hybrid polymer composite," *Journal of Testing and Evaluation*, vol. 50, no. 1, Article ID 20200580, 2022.

[19] P. G. García, R. Ramírez-Aguilar, M. Torres, E. A. Franco-Urquiza, J. May-Crespo, and N. Camacho, "Mechanical and thermal behavior dependence on graphite and oxidized graphite content in polyester composites," *Polymer*, vol. 153, no. 6, pp. 9–16, 2018.

[20] V. Mohanavel, S. Suresh Kumar, J. Vairamuthu, P. Ganeshan, and B. NagarajaGanesh, "Influence of stacking sequence and fiber content on the mechanical properties of natural and synthetic fibers reinforced penta-layered hybrid composites," *Journal of Natural Fibers*, pp. 1–13, 2021.

[21] H. Alamri, I. M. Low, and Z. Alothman, "Mechanical, thermal and microstructural characteristics of cellulose fibre reinforced epoxy/organoclay nanocomposites," *Composites Part B: Engineering*, vol. 43, no. 7, pp. 2762–2771, 2012.

[22] U. Achutha Kini, M. Shettar, S. Sharma et al., "Effect of hydrothermal aging on the mechanical properties of nanoclay-glass fiber-epoxy composite and optimization," *Using Full Factorial Design Materials Research Express*, vol. 6, pp. 510–523, 2019.

[23] M. Atagur, A. Orhan, K. Sever et al., "Investigation of thermal and mechanical properties of synthetic graphite and recycled carbon fiber filled polypropylene composites Materials," *Research Express*, vol. 6, pp. 524–536, 2019.

[24] T. Raja and P. Anand, "Mechanical investigations on Neem/Banyan fibers reinforced with ceramic powder particulates hybrid polymer composite helmet," *IOP Conference Series: Materials Science and Engineering*, vol. 988, Article ID 012090, 2020.

[25] B. Ravichandran and M. Sasikumar, "Mechanical, ablative, and thermal properties of cenosphere-filled ceramic/phenolic composites," *Polymer Composites*, vol. 37, no. 6, pp. 1906–1913, 2016.

[26] A. Vasudevan, B. Navin kumar, M. V. Depoures, T. Maridurai, and V. Mohanavel, "Tensile and flexural behaviour of glass fibre reinforced plastic -Aluminium hybrid laminate manufactured by vacuum resin transfer moulding technique (VARTM)," *Materials Today Proceedings*, vol. 33, no. 7, pp. 3072–3079, 2020.

[27] M. Ramesh, K. Palanikumar, and K. H. Reddy, "Plant fibre based bio-composites: sustainable and renewable green materials," *Renewable and Sustainable Energy Reviews*, vol. 79, no. 5, pp. 558–584, 2017.

[28] D. Hristozov, L. Wroblewski, and P. Sadeghian, "Long-term tensile properties of natural fibre-reinforced polymer composites: comparison of flax and glass fibres," *Composites Part B: Engineering*, vol. 95, pp. 82–95, 2016.

[29] A. V. Kiruthika, "A review on physico-mechanical properties of bast fibre reinforced polymer composites," *Journal of Building Engineering*, vol. 9, pp. 91–99, 2017.

[30] L. Yan, N. Chouw, L. Huang, and B. Kasal, "Effect of alkali treatment on microstructure and mechanical properties of coir fibres, coir fibre reinforced-polymer composites and reinforced-cementitious composites," *Construction and Building Materials*, vol. 112, no. 1, pp. 168–182, 2016.

[31] A. Q. Dayo, B.-C. Gao, J. Wang et al., "Natural hemp fiber reinforced polybenzoxazine composites: curing behavior, mechanical and thermal properties," *Composites Science and Technology*, vol. 144, no. 3, pp. 114–124, 2017.

[32] M. Ramesh, C. Deepa, and U. S. Aswin, "Effect of alkalization on mechanical and moisture absorption properties of Azadirachta indica (neem tree) fiber reinforced green composites," *Transactions of the Indian Institute of Metals*, vol. 70, no. 6, pp. Pp187–199, 2017.

Hindawi
Advances in Materials Science and Engineering
Volume 2021, Article ID 6030096, 7 pages
https://doi.org/10.1155/2021/6030096

Research Article

Thermal and Mechanical Properties of Vinyl Ester Hybrid Composites with Carbon Black and Glass Reinforcement

Geetanjali S. Guggari,[1] S. Shivakumar,[1] G. A. Manjunath,[1] R. Nikhil,[1] Alagar Karthick,[2] Abhilash Edacherian,[3] C. Ahamed Saleel,[3] Asif Afzal,[4,5] S. Prasath,[6] and B. Saleh[7]

[1]*Department of Mechanical Engineering, KLS Gogte Institute of Technology, Belagavi 590008, Karnataka, India*
[2]*Department of Electrical and Electronics Engineering, KPR Institute of Engineering and Technology, Coimbatore 641407, Tamilnadu, India*
[3]*Department of Mechanical Engineering, College of Engineering King Khalid University, Asir Abha 61421, Saudi Arabia*
[4]*Department of Mechanical Engineering, P. A. College of Engineering (Affiliated to Visvesvaraya Technological University, Belagavi), Mangalore 574153, India*
[5]*Department of Mechanical Engineering, School of Technology, Glocal University, Delhi-Yamunotri Marg, SH-57, Mirzapur Pole, Saharanpur, Uttar Pradesh 247121, India*
[6]*Department of Mechanical Engineering, College of Engineering and Technology Mizan Tepi University Tepi Campus, Teppi 121, Ethiopia*
[7]*Mechanical Engineering Department, College of Engineering Taif University, P.O. Box 11099, Taif 21944, Saudi Arabia*

Correspondence should be addressed to S. Prasath; prasath@mtu.edu.et

Received 14 July 2021; Accepted 2 September 2021; Published 21 September 2021

Academic Editor: Mohanavel V

The objective of the work is to investigate both thermal and mechanical properties of vinyl ester/glass composites incorporated with different percentages of carbon black reinforcements through experimental approaches. Analysis of glass transition temperature, thermogravimetric analysis (TGA), degradation temperature, hardness, flexural strength, etc. is performed using differential scanning calorimeter, X-ray diffraction, tensile machine, and flexural machine, respectively. The scanning electron microscope was used for surface fracture studies. The degradation temperature reduces initially with the percentage of carbon black and then increases. Glass transition temperature increases with the percentage of carbon black while above 500°C temperature, the weight percentage of composite drops. The results also reveal that 4% of carbon with vinyl ester improved the tensile strength by 30%, hardness by 35%, flexural strength by 45%, flexural modulus by 66%, and interlaminate shear strength by 44% when compared with the other percentage of carbon black.

1. Introduction

Recent studies reported improved performance of carbon black dispersed polymer nanocomposites by exfoliating carbon black in polymeric resin. Several researchers [1–4] studied the effect of processing techniques on the dispersion of polymeric resin and reported that a high shear force mixing enabled better exfoliation, higher basal spacings, greater surface area, and increased interaction of carbon black platelets in polymeric resin. Dispersion of carbon black in thermoset resins such as epoxy and vinyl ester resin [5, 6] also showed better exfoliation and improved mechanical properties in case of high shear mixing and low volume fraction of carbon black.

Microhardness of polymer nanocomposites indicates surface hardness and is enhanced by nanofiller addition due to the addition of harder phase in soft polymer matrix. Ho et al. [7] reported increase in microhardness by 17.34% with the addition of 8 wt.% of garamite carbon black in epoxy. Lam and Lau [8] studied 0 to 4 wt.% of SiO2/epoxy using a

mechanical stirrer and ultrasonicator and reported that microhardness increased by 16.96% with the addition of 4 wt.% SiO2 to epoxy. Review of the open literature on the study of microhardness of carbon black/polymer revealed that microhardness of carbon black/polymer depends on the amount of carbon black added to the polymer.

Sundaram et al. [9] reported that adding 5 wt.% UTS can increase UTS by 50%, increase yield strength by 7.24 N/mm^2, and increase Poisson's ratio by 50%. % ceramic is higher than polyester/glass. Add 10% by weight. For the same sample, % carbon black increased the elongation by 3.9%. Haque et al. [10] reported that for every addition of 1 wt.%, the interlaminar shear strength, flexural strength, and fracture toughness increased by 8%, 17%, and 23%, respectively. Kornmann et al. [11] reported that after adding carbon black to epoxy/glass, the flexural strength increased by 27% and Young's modulus increased by 6%. The increase in flexural modulus is attributed to the presence of layered silicate, which increases the flexural strength of the fiber and improves the interface properties between the matrix and the fiber. There are many studies on mechanical properties [12], but there are few or no studies on the thermodynamic properties of nanohydride composite materials. The purpose of this project is to study the effect of carbon black on the thermal and mechanical properties of vinyl ester hybrid composites Nikhil et al. [13] discussed delaminations which occur due to improper binding, nonuniform distribution of resin, presence of foreign particles, absorption of moisture, nonuniform compaction during pressing of laminate, and curing of resin along the layers.

2. Experimental Studies

Polymer nanocomposite specimens were prepared using carbon blacks as a reinforcement which significantly influence the dispersion efficiency and mechanical and barrier properties of the nanocomposites. Carbon black was dispersed in vinyl ester using ultrasonication followed by twin screw extrusion, and carbon black/vinyl ester specimens were prepared. Carbon black/vinyl ester (VE)/glass (GF) nanocomposite laminates were prepared using carbon black-dispersed vinyl ester and 360 gsm woven glass fiber mat by wet hand layup technique and the fabrication technique. Specimens were prepared by moulding the mixture of CB and vinyl ester in a sun mica mould of $100 \times 100 \times 1$ mm^3. X-ray diffraction (XRD) and differential scanning calorimetry (DSC) were used to characterize the phases present in specimens and glass transition temperature (Tg) of CB/vinyl ester specimens. Vickers microhardness is used to measure the microhardness of CB/vinyl ester nanocomposites. A universal testing machine (UTM) is used to determine ultimate tensile strength (UTS), Young's modulus, flexural strength, flexural modulus, and interlaminar shear strength (ILSS). Scanning electron microscopy (SEM) was used to characterize surface geomorphology of CB/vinyl ester specimens as well as tensile fractured surface of CB/vinyl ester/glass composites. The specimens were characterized by XRD, DSC, SEM, and TEM according to the ASTM procedure.

3. Experimental Results

3.1. X-Ray Deflection of Carbon Black/Vinyl Ester. Figure 1 shows XRD of vinyl ester, carbon black, and 2 to 5 wt.% carbon black/vinyl ester composites, the amorphous structure without any sharp peak as a general characterisation of noncrystalline polymeric material. XRD of carbon blacks in characteristic peaks at 7.70, 2.870, and 3.320 of 2θ indicated basal spacing of 11.38 Å, 31.5 Å, and 26.53 Å for carbon black.

3.2. Differential Scanning Calorimetry of Carbon Black/Vinyl Ester. Figure 2 presents the sway of carbon black on the glass conversion temperature (Tg) of vinyl ester obtained from DSC. The highest increase in Tg was achieved with the addition of 5 wt.% CB. Increase in Tg of vinyl ester was achieved for carbon black due to complete exfoliation of carbon black in vinyl ester as indicated by XRD and TEM studies. Amount of carbon black and type of carbon black influenced Tg of vinyl ester.

3.3. Thermogravimetric Analysis. Figure 3(a) shows TGA pattern for 0 to 5 wt.% CB/vinyl ester, and degradation temperature is presented in Figure 3(b). The weight reduction is due to the volatile nature of the molecules which release the functional ions. Degradation temperature for neat vinyl ester was 349°C, and the same was lower for 2 and 4 wt.% of CB and slightly higher for 3 and 5 wt. CB addition to vinyl ester. Degradation of vinyl ester and CB/vinyl ester occurred in a single step which indicates that only resin phases volatilized during this period.

The degradation rate for CB/vinyl ester was comparatively lower than that of neat vinyl ester. Such a behavior can be explained by the presence of stacked carbon layers in vinyl ester which can act as thermal barrier to the vinyl ester system and decelerated the degradation process. Carbon is used as a thermal insulation layer to enhance the overall thermal stability of the system and help form carbon after complete thermal degradation. The mass loss of the completely decomposed CB/vinyl ester is 4 wt.% less than pure vinyl ester. By adding CB to vinyl ester, a marginal improvement in thermal stability and clay yield can be observed.

3.4. Microhardness of CB/Vinyl Ester. Figure 4 shows microhardness of 0 to 5 wt. CB/vinyl ester composite specimens. The setup for microhardness testing used is microindentation hardness testing machine. Microhardness increased with the addition of CB, and the improvement was 20.96%, 36.81%, and 21.95% with the addition of CB. Microhardness improved due to the addition of harder CB in soft vinyl ester matrix. Amount and type of CB influenced the microhardness of vinyl ester.

While testing materials such as metals, the microhardness linearly correlates with the tensile strength.

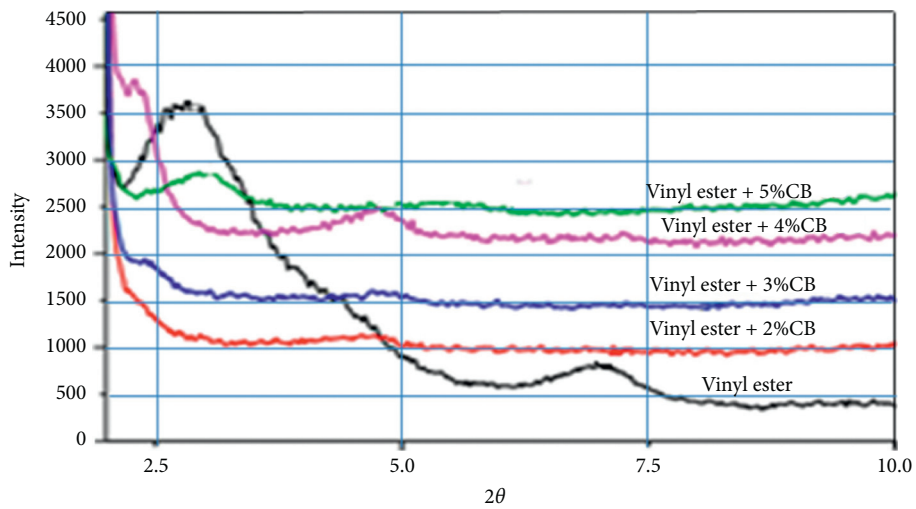

Figure 1: XRD pattern for vinyl ester and its composites.

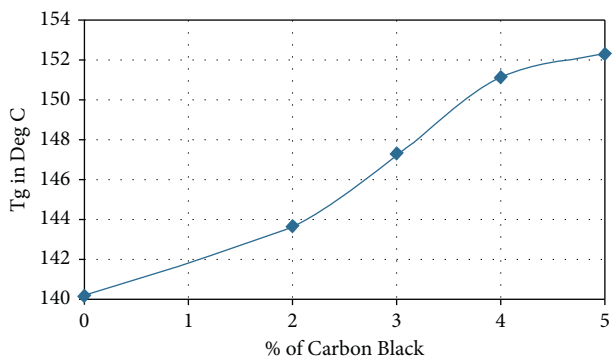

Figure 2: Effect of carbon black on Tg of the vinyl ester composites.

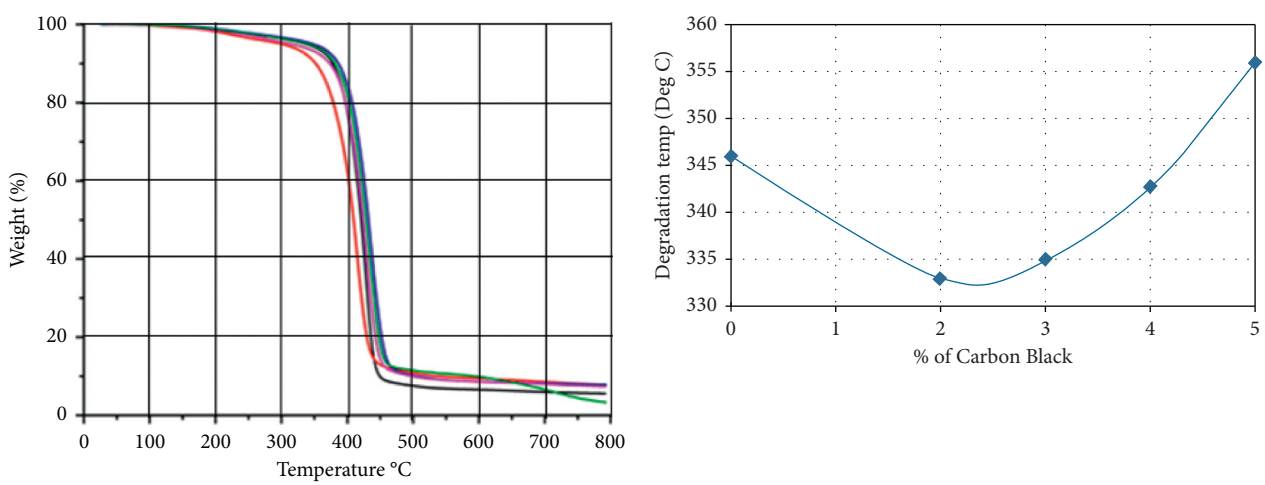

Figure 3: (a) Effect of carbon black on thermal stability (% of degradation) of the vinyl ester composites. (b) Effect of carbon black on degradation temperature of the vinyl ester composites.

3.5. Ultimate Tensile Strength and Young's Modulus of Carbon Black/Vinyl Ester/Glass Composites. Figures 5(a) and 5(b) show ultimate tensile strength (UTS) and Young's modulus of various percentages of carbon black reinforced glass reinforced vinyl ester nanocomposites. UTS and Young's modulus increased with the addition of carbon black. Improvements in UTS are 31.35%, 34.64%, and 20.62% and in Young's modulus 21.61%, 32.12%, and 16.55% with the

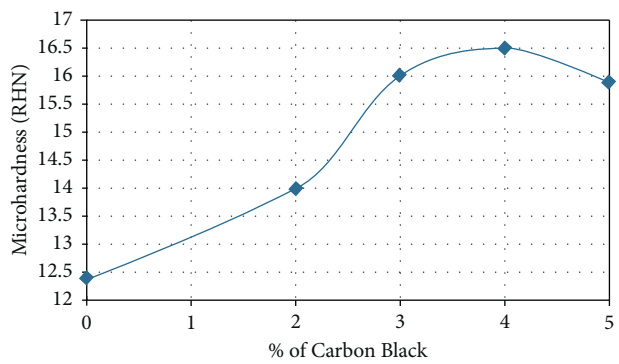

Figure 4: Effect of carbon black on microhardness of the vinyl ester composites.

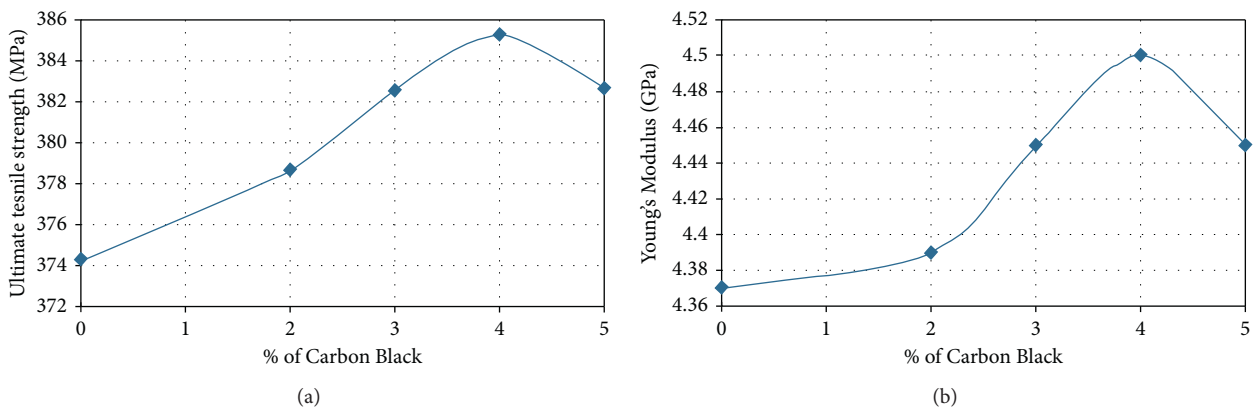

Figure 5: (a) Effect of carbon black on ultimate tensile strength of the vinyl ester composites. (b) Effect of carbon black on Young's modulus of the vinyl ester composites.

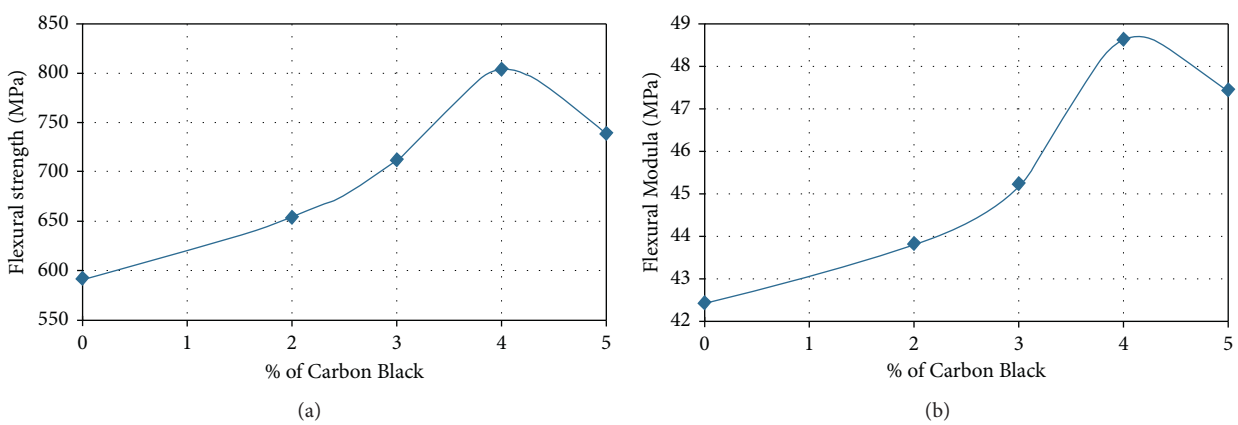

Figure 6: (a) Effect of carbon black on flexural strength of the vinyl ester composites. (b) Effect of carbon black on flexural modulus of the vinyl ester composites.

addition of 4 wt.% each of carbon black reinforced vinyl ester/glass composites. Both UTS and Young's modulus show highest for 4 wt.% addition to vinyl ester/glass composites.

3.6. Flexural Strength and Flexural Modulus of Carbon Black/Vinyl Ester/Glass. Figures 6(a) and 6(b) show flexural strength and flexural modulus of 0 to 5 wt. carbon black reinforced vinyl ester/glass fiber composites. Flexural strength and modulus increased with the addition of carbon black. Increases in flexural strength were 36%, 45%, and 8% and in flexural modulus were 34%, 66%, and 34% with the addition of carbon black reinforced vinyl ester/glass. The highest increase in flexural strength and modulus was observed for 4 wt.% carbon blacks and vinyl ester/glass composites.

3.7. Interlaminar Shear Strength (ILSS) of Carbon Black/Vinyl Ester/Glass. Figure 7 shows interlaminar shear strength (ILSS) of 0 to 5 wt.% carbon black/vinyl ester/glass

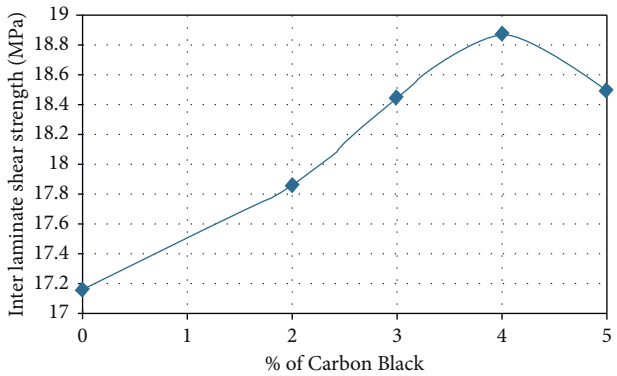

Figure 7: Effect of carbon black on interlaminar shear strength of the vinyl ester composites.

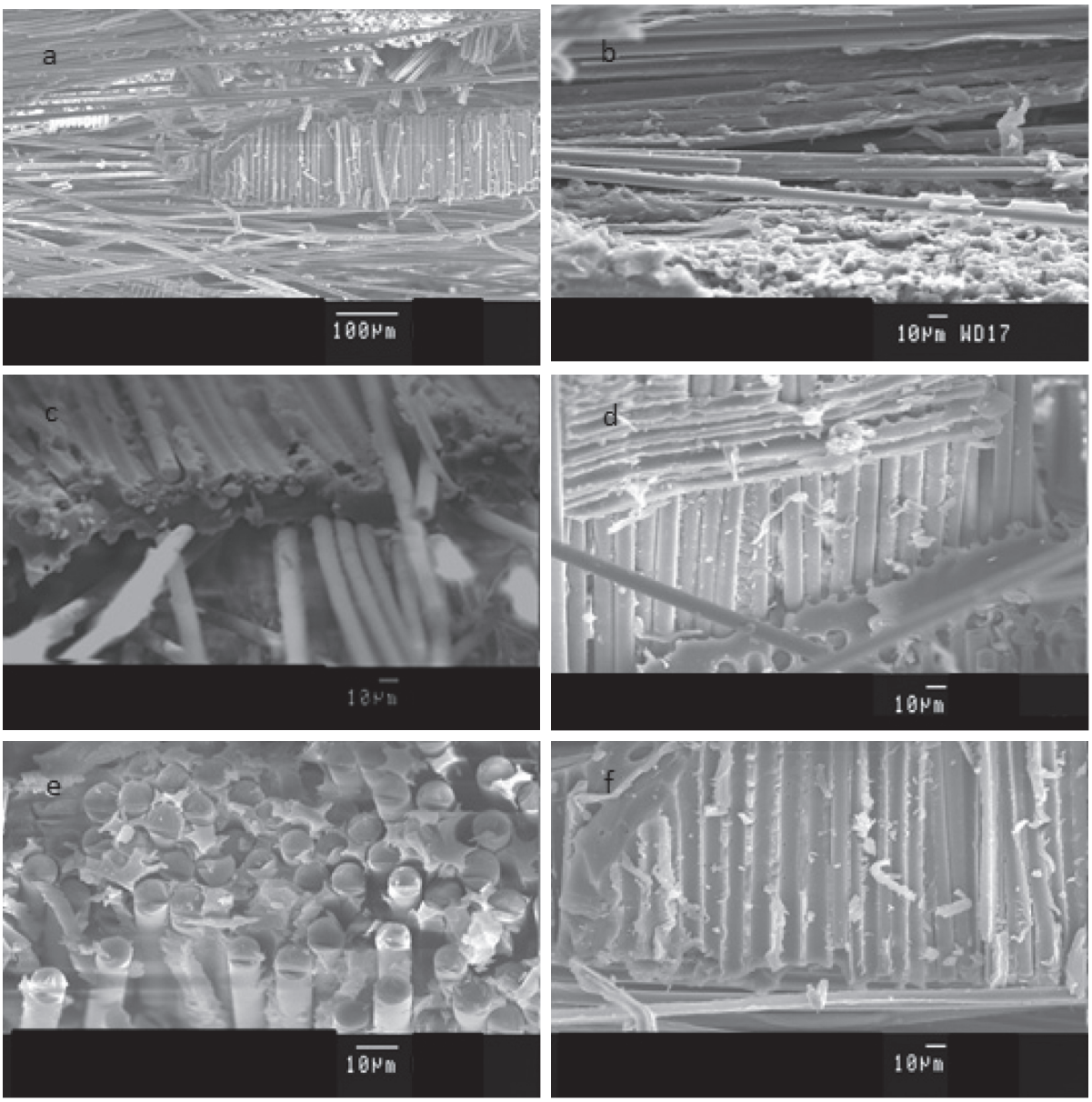

Figure 8: Fracture surface of the (a) glass/vinyl ester composite, (b) 2% CB reinforced, (c) 3% CB reinforced, (d) 4% CB reinforced, and (e) and (f) 5% CB reinforced glass/vinyl ester composites.

specimens. ILSS increased with the addition of carbon black. Increases in ILSS were 26%, 44%, and 16% with the addition of carbon black. The highest increment was observed for 4 wt.% addition of carbon black to vinyl ester.

The present research showed that UTS, Young's modulus, flexural strength, flexural modulus, and ILSS increased with the addition of carbon black to vinyl ester/glass. The highest improvement in mechanical properties was observed for 4 wt.% of carbon addition to vinyl ester/glass. The improvement in mechanical properties can be attributed to higher basal spacings and the modifier in carbon black, which helped in better exfoliation and stronger interfacial bond between glass fiber and vinyl ester [14–20].

4. Fracture Studies

Figure 8 shows SEM of tensile fractured specimen of vinyl ester/glass composites. Fractured fibers in the micrograph are cut straight, and the surfaces are smooth and clean. Clean fiber surface implies failure at the fiber matrix interface, indicating a weak interface bond.

Figure 8(b) shows SEM of tensile fractured specimen of 2 wt.% carbon black/vinyl ester/glass. The straight cut fibers exhibit better tensile strength, whereas the trace amount of debris attached indicates improper bonding of fibers and resin. Figures 8(c) and 8(d) show fractured specimens of 3 and 4% CB reinforced vinyl ester/glass composites. Fibers are cut straight and surfaces are adhered with debris of vinyl ester, and the amount of adhered vinyl ester is greater than those of 3% of CB-based composites. Figure 8(e) shows 5% CB reinforced vinyl ester glass composites. Addition of carbon black showed greater amount of vinyl ester adhered to glass fiber surface. This is due to stronger interfacial bond between the CB and fiber surface.

5. Conclusion

Effect of carbon black on the thermal and mechanical properties of vinyl ester and vinyl ester/glass was studied for 0 to 5 wt.% carbon black/vinyl ester. The following conclusions were drawn based on the present experimental results:

(i) XRD analysis of carbon black/vinyl ester showed exfoliation without any evidence of agglomeration.

(ii) Glass transition temperature of vinyl ester increased with addition of carbon black.

(iii) TGA showed slower rate single stage degradation of the nanocomposites.

(iv) Microhardness of vinyl ester increased addition of carbon black.

(v) Tensile strength, Young's modulus, flexural strength, flexural modulus, and ILSS of vinyl ester/glass addition carbon black.

(vi) Addition of carbon black improved mechanical properties of vinyl ester/glass which can be explained in complete exfoliation of carbon black in vinyl ester evidenced by XRD studies due to the dispersion of carbon black using ultrasonication and extrusion.

Data Availability

The data used to support the findings of this study are included within the article.

Conflicts of Interest

The authors declare that there are no conflicts of interest regarding the publication of this article.

Acknowledgments

The authors extend their appreciation to the Deanship of Scientific Research at King Khalid University, Saudi Arabia, for funding this work through the Research Group Program under grant no. RGP 1/238/41. This study was supported by Taif University Researchers Supporting Project number (TURSP-2020/49), Taif University, Taif, Saudi Arabia. The authors would like to thank Taif University for financial support.

References

[1] I. Balberg, "A comprehensive picture of the electrical phenomena in carbon black–polymer composites," *Carbon*, vol. 40, no. 2, pp. 139–143, 2002.

[2] J. P. Adohi, A. Mdarhri, C. Prunier, B. Haidar, and C. Brosseau, "A comparison between physical properties of carbon black-polymer and carbon nanotubes-polymer composites," *Journal of Applied Physics*, vol. 108, Article ID 074108, 2010.

[3] A. Kausar, "Contemporary applications of carbon black-filled polymer composites: an overview of essential aspects," *Journal of Plastic Film and Sheeting*, vol. 34, no. 3, pp. 256–299, 2018.

[4] N. Ahmed, A. Kausar, and B. Muhammad, "Shape memory properties of electrically conductive multi-walled carbon nanotube-filled polyurethane/modified polystyrene blends," *Journal of Plastic Film and Sheeting*, vol. 32, no. 3, pp. 272–292, 2016.

[5] B. L. Xing, J. L. Cao, and Y. Wang, "Preparation of lignite-based activated carbon with high specific capacitance for electrochemical capacitors," *Funct Mater Lett*, vol. 8, Article ID 1550031, 1 page, 2015.

[6] Y. V. Surovikin, A. G. Shaitanov, V. A. Drozdov, I. V. Rezanov, and A. D. Morozov, "Effect of thermal oxidative treatment on the structure and electrical conductivity of nanodispersed carbon black particles," *Solid Fuel Chemistry*, vol. 48, no. 6, pp. 392–403, 2014.

[7] M.-W. Ho, C.-K. Lam, K.-t. Lau, D. H. L. Ng, D. Hui, and D. Hui, "Mechanical properties of epoxy-based composites using nanoclays," *Composite Structures*, vol. 75, no. 1-4, pp. 415–421, 2006.

[8] C. Lam and K. Lau, "Theoretical modeling of tribological behavior of nanoclay/epoxy composites," in *Proceedings of the 16th International Conference on Composite Materials*, Kyoto, Japan, July 2007.

[9] S. Sundaram, R. Nagalingam, and R. Satheesh Raja, "Experimental analysis on tensile properties of FRP with nano clay," *International Journal of Advanced Manufacturing Technology*, vol. 39, no. 9, pp. 1–5, 2008.

[10] A. Haque, M. Shamsuzzoha, F. Hussain, and D. Dean, "S2-glass/epoxy polymer nanocomposites: manufacturing, structures, thermal and mechanical properties," *Journal of Composite Materials*, vol. 37, no. 20, pp. 1821–1837, 2003.

[11] X. Kornmann, M. Rees, Y. Thomann, A. Necola, M. Barbezat, and R. Thomann, "Epoxy-layered silicate nanocomposites as matrix in glass fibre-reinforced composites," *Composites Science and Technology*, vol. 65, no. 14, pp. 2259–2268, 2005.

[12] D. Pantea, H. Darmstadt, S. Kaliaguine, and C. Roy, "Electrical conductivity of conductive carbon blacks: influence of surface chemistry and topology," *Applied Surface Science*, vol. 217, no. 1-4, pp. 181–193, 2003.

[13] R. Nikhil, S. S. kumar, K. Anupama, and S. Manjunath, "Experimental and numerical investigation of mode II failure behavior evaluation using three point bend, end notched flexure test," *MATEC Web of Conferences*, vol. 144, Article ID 02009, 2018.

[14] M. Meignanamoorthy, M. Ravichandran, V. Mohanavel et al., "Microstructure, mechanical properties, and corrosion behavior of Boron Carbide Reinforced Aluminum Alloy (Al-Fe-Si-Zn-Cu) matrix composites produced via powder metallurgy route," *Materials*, vol. 14, no. 15, Article ID 4315, 2021.

[15] T. H. M. Mysore, A. Y. Patil, G. U. Raju et al., "Investigation of mechanical and physical properties of big sheep horn as an alternative biomaterial for structural applications," *Materials*, vol. 14, no. 14, Article ID 4039, 2021.

[16] T. Sathish, V. Mohanavel, K. Ansari et al., "Synthesis and characterization of mechanical properties and wire cut edm process parameters analysis in AZ61 magnesium Alloy + B4C + SiC," *Materials*, vol. 14, no. 13, Article ID 3689, 2021.

[17] B. N. Sharath, C. V. Venkatesh, A. Afzal et al., "Multi ceramic particles inclusion in the aluminium matrix and wear characterization through experimental and response surface-artificial neural networks," *Materials*, vol. 14, no. 11, Article ID 2895, 2021.

[18] T. Sathish, A. R. R. Kaladgi, V. Mohanavel et al., "Experimental investigation of the friction stir weldability of aa8006 with zirconia particle reinforcement and optimized process parameters," *Materials*, vol. 14, no. 11, Article ID 2782, 2021.

[19] M. N. Akhtar, M. Khan, S. A. Khan et al., "Determination of non-recrystallization temperature for niobium microalloyed steel," *Materials*, vol. 14, no. 10, Article ID 2639, 2021.

[20] S. Nagaraja, K. U. Nagegowda, A. Kumar V et al., "Influence of the fly ash material inoculants on the tensile and impact characteristics of the Aluminum AA 5083/7.5SiC composites," *Materials*, vol. 14, no. 9, Article ID 2452, 2021.

Hindawi
Advances in Materials Science and Engineering
Volume 2021, Article ID 9720297, 10 pages
https://doi.org/10.1155/2021/9720297

Research Article

Simulation Process of Injection Molding and Optimization for Automobile Instrument Parameter in Embedded System

S. Ramesh,[1] **P. Nirmala**,[2] **G. Ramkumar**,[2] **Satyajeet Sahoo**,[3] **G. Anitha**,[2] **A. K. Gnanasekar**,[4] **and J. Isaac JoshuaRamesh Lalvani**[5]

[1]*Department of Electronics and Communication Engineering, Sri Shakthi Institute of Engineering and Technology, Coimbatore-641062, Tamilnadu, India*
[2]*Department of Electronics and Communication Engineering, Saveetha School of Engineering, SIMATS, Chennai 602 105, Tamil Nadu, India*
[3]*Department of Electronics and Communication Engineering, Vignan's Foundation for Science,Technology and Research (Deemed to be University), Vadlamudi, Guntur, Andra Pradesh 522213, India*
[4]*Department of Electronics and Communication Engineering, Rajalakshmi Institute of Technology, Chennai, Tamilnadu, India*
[5]*Department of Mechanical Engineering, Faculty of Mechanical and Production Engineering, AMIT, Arbaminch University, Arba Minch, Ethiopia*

Correspondence should be addressed to S. Ramesh; srameshece@siet.ac.in and J. Isaac JoshuaRamesh Lalvani; isaac.jrl@amu.edu.et

Received 23 July 2021; Accepted 7 August 2021; Published 30 August 2021

Academic Editor: Mohanavel V

The automobile instrument is the indispensable item that is essential to keep the driver conversant of the process of the engineer and the other system. There are different parameters involved in the automobile instrument, which requires a different process involved in creating the automobile parameter. This research is designed to show the simulation development of injection molding and optimization of automobile instrument parameters using different optimization techniques. In this paper, Taguchi Orthogonal parameter design and particle swarm optimization (PSO) are used to measure the shrinkage volume rate and warpage amount rate. Most of the studies are designed to calculate the reduction and warpage for the gate location and glass material. The Taguchi orthogonal design contains five different parameters which are inversely proportional to each other. Hence, by optimizing those parameters, the injection molding procedure is passed out. In this research, the paper is designed to process the injection molding for the automobile instrument parameter using optimization techniques.

1. Introduction

Injection molding is one of the rapid methods commonly used in the plastic industry and then widely used to create automobile parts. Automobiles are the important item used to keep the driver updated with the process happening in the engine and on another system [1]. The injection molding process is used to design the automobile instrument in different shapes and weights. Due to their inimitable properties like insubstantial, low cost, increase padding, and reasonable deterioration, confrontation injection molding is used in the manufacturing of automobile instruments. Based on the current situation, to reduce the manufacturing cost and weight of the vehicles like cars and buses, plastic parts were used in the large share. Numerous faults occur due to the short setting of ending flexible items. Therefore, it is important for the stimulation and analyses of every element in the inoculation procedure [2]. This has to be done before manufacturing the elastic portions to attain the enhanced injection molding procedure parameter, control defects, checking of artefact value, and advance efficiency manufacturing.

Most of the injection molding techniques use Minitab software to simulate plastic. At present, to design the whole

injection molding process, Minitab Insight is applied, and this also includes the drift, padding compression, warpage, reduction, cavitation, and strength alignment [3]. The software helps in finding the faults in the elastic parts that could be predicted, and this could also develop different plastic parts through the molding process. The parameter manufacturing using injection molding can be optimized. This could further reduce the manufacturing cost and the manufacturing productivity could be improved. This mainly avoids the defects like bulb welding marks, reduction holes, and distortion in the plastic parts due to excessive warping [4].

To obtain better process parameters for individual products, the engineer must be able to rely on his overall expertise to apply a test-error method or a Taguchi approach. Numerous experiments were done to achieve the suitable parameter combination; hence, both methods are considered time-consuming methods. To seek out the initial process in parameter setting Taguchi method requires the signal to noise ratio (S/N), and a relatively great effort is needed [5]. Mostly Taguchi orthogonal array table is used for the injection molding, and to investigate the optimal process, parameter injection extrusion molding is used. Important factors such as melting temperature, injection speed, mold temperature, and filling pressure are also studied. Grey level correlation analysis and response data were carried out in the Taguchi orthogonal test in the optimization process. To conduct the injection molding experiment in the Taguchi orthogonal method, four factors and three levels through the statistical design method are used. During the setting of final optimal process parameters, the optimization problem occurs, and this is mainly created in the production industry. The important step involved in the optimization procedure parameter during injection molding is the quality improvement of molded items or parameters [6]. This process is often handled by the experienced engineer, and reference handbook was given to them and parameter was improved, and trails were made to check the fine-tuning, and then the error is checked using the Taguchi design method. The experienced molding operator is needed for better operation, and this method is cost-efficient, and it takes a lot of time to operate specifically with a new application or new resins [7]. It is stated that by using trial and end process, the optimal process parameter actual value can be verified correctly. By using the Taguchi parameter design method, the specified process parameter can only be found, and the discrete setting value is included in the process parameter.

The quality of the molded plastic product could be affected by the injection molding and then by defining the parameter setting procedure. Production problem is caused due to the unsuitable process parameter, and competitive price advantage is reduced, and this could further decrease the profit of the company [8]. The four stages are included in the plastic injection molding process. They are filling, padding, cooling, and remolding. Different control process parameter has been used in the previous research and those parameters were used for injection-molded plastic and they are determined by the optimal initial process [9]. This includes the butter flask lid and single quality considerations. To determine the preliminary process parameter settings for the injection-molded plastic parts, four control process parameters were used and this is maintained with a thin shell feature and with the influence of the tractable control process parameter. Hence, different research deals with the optimization of a parameter using different research techniques, and they failed to optimize the problems caused during the injection molding process.

In this search, the volume removal and amount of warpage are calculated by optimizing the issue created during injection molding. By combining the Multiple-Input Multiple-Output (MIMO) with the Taguchi design parameter method, the problems during the various factors and the process parameter are reduced; along with it, particle swarm optimization is used to observe and determine the shrinkage and the warpage amount of correct accuracy. Thus, the problem in the optimization of the automobile instrument could be reduced. From the survey, it is observed that the previous methods lack testing methods and consume more time during implementation in molding process.

1.1. Literature Survey. With the problem of ecological trash and power exhaustion in recent years, an innovative control tech that recovers the routine of the motor car has been sought. The method for constructing a reactive surface is proposed by [2]. It expresses the method for optimizing control parameters for the car engine. This document defines a method to construct the response area model and a method to optimize the control parameters for the automotive diesel engine. It progresses a model-based monitoring system and a design-based early expansion technique. The projected technique for constructing the response surface model is capable of efficiently defining the numerous regulator limitations against the typical value, like petroleum ingesting and emissions. The optimization method of control parameters can be fast and efficient and can compute the ideal control restrictions to optimize assessment elements such as petroleum ingestion and emissions based on the model.

Kaveh and Rad [9] proposed a method to describe analysis and design called a hybrid genetic algorithm and optimization of the particle swarm for the force method. The computer inconveniences of existing numerical methods have forced researchers to rely on heuristic algorithms. Heuristic methodologies are powerful in resolving optimization problems. While these methods are approximate, they do not need to be derived from objective function and limitations. Here, we have a scalable algorithm based on hybrid genetic algorithm (AG) and particle swarm optimization (PSO), denoted by HGAPSO [4]. It is an evolutionary algorithm based on a hybrid genetic algorithm (GA) and particle swarm optimization (PSO), referred to as HGAPSO. The appropriateness of the algorithm is compared with both the genetic algorithm and the PSO in the overall strategy, an example of effectiveness and superiority, especially for executives who are more redundant.

The well-formed and tested Artificial Neural Network matrix has been attached with the enhanced PSO algorithm as an ANN-PSO fusion to optimize the parameters of the

inoculation molding process. The work in [10] proposed the injection molding process for the optimization of Bi-Aspheric lens and used the hybrid Artificial Neural Network (ANN) and particle swarm optimization (PSO) to optimize the problems created during the molding process. The PSA network (7-13-6) was developed and tested using tentative data derived from arithmetic methodologies. The formed and tested ANN network was coupled with the improved PSO system as an ANN-PSO hybrid to optimize the parameters of the injection molding process. The injection system optimizes the molding process parameters achieved with the ANN-PSO hybrid algorithm legalized with researches that please the J. S. W. injection molding machine.

The design of injection mold and the automotive panel optimization research paper is proposed by [3]. In this document, an automotive panel for analyzing injection molding processes and matrix design is presented. Injection molding parts on the instrument panel performs investigation to regulate the area for system synchronization. The injection molding components carry out a flow analysis of the mold to determine the probability, and the matrix timing system and the gas injection molding process are optimized. Thus, high quality spraying products are obtained. In practice, CAE technology for plastic mold design and plastic molding has been shown to play a major role.

Injection molding parts on the dashboard through mechanical examination and process to regulate the separation zone, synchronization systems. Injection molding optimization design is designed by (Ren and Zhang) based on particle swarm optimization and a genetic algorithm for a cooling system. In this article, a hybrid approach combining PSO with gene algorithms (GA) is developed to achieve the optimal design of the cooling system. Using the finite element method (FEM) and the finite difference method (FDM), the numerical simulation of the cooling process is conducted for part of the injection mold. On the basis of the limited element method and the limited difference method, a numerical simulation of the cooling process is carried out for a portion of the injection mold. An example of an injection cooling system illustrates how effective this approach is.

The process of filling the elastic melts into the shell of the injection mold for the loop in the interior embellishment of the automobile has been simulated based on Minitab software [11]. The best door slot has been reached in this work, which ensures that the product can be refilled. In addition, the optimal design of the door location and the number of plastic products were reviewed. Based on the qualified analysis of the door, the on its own door is greater than the double door in the function of the spreading of the air concise and the welding line. In short, the rational number of doors and the location guarantee the correct operation of the injection mold, thereby reducing the manufacturing cost.

2. Materials and Method

To determine the automotive instrument parameter, 3D model parts must be drawn up for the parameter to be designed. This is the major step for injection molding. In this method, optimal gate position and the simulation of the gating system are determined along with the cooling system. To design the 3D model of automobile instrument care, a drawing instrument is used [5]. Let us consider the certain dimension, length, and weight of an automobile instrument to be molded into a parameter. The instrument designed for the automobile must be compatible with the bottom circuit board and top plate. Subsequently, during the casting process, the volume withdrawal rate and the warping of the part must be minimized. The following factors come into play in the injection molding procedure. Figure 1 shows the flow diagram for the injection molding process.

Through the Hooper, the plastic pellets are passed to the high-temperature injection barrel during the molding process. The pellets are intense, liquefied, and recreated into plastic and again turned into the tacky liquid stream, which is then injected into lower temperature. At high speed and pressure, the melted pellets are passed through the injection nozzle and then wielded by the plunger or the screw. The molten plastic enters the cavity at high pressure and is also compressed. At this stage, it is possible to flow out of the cavity into the well and channel system. The artefact is released from the mold hollow after the cooling and forming are done.

(i) Feeding: The hopper is fed by the pellets or powder

(ii) Melting: In the barre, the plastic is heated, and it turns from solid pellets into the liquid stream, and this requires great plasticity

(iii) Injection: By piston or by screw, the flux of molten plastic is pushed into the barrel and fills the cavity of the mold by means of the injection nozzle and the core and the passageway. This is known as an injection.

(iv) Maintaining pressure: In the replenishment process, the molten material is pushed continuously by the diver or screw in the meantime due to the cooling of the molten material that shrinks inside. During this process, the complete structure is formed, and the texture of the product is created. This process is known as pressurization.

(v) Cooling: The cooling process inside the mold generally refers to the entire process from the moment it occurs. In this process, the melted material at the door, which is completely solidified to the plastic patch is ejected from the mold cavity. But in fact, the cooling phase begins the moment the molten plastic enters the cavity. This covers the period from the end of the injection, from the pressure retention to the moment prior to the beginning of the mold release.

(vi) Unmolding: Unmolding is allowed when cooled at a certain temperature, through which the plastic part is expelled from the mold by the ejectors.

2.1. Process of Making Automobile Instrument by Reaction Injection Molding. One of the most common techniques used in the design of automobiles instruments is Reaction Injection Molding (RIM). In this method, liquid reagents are

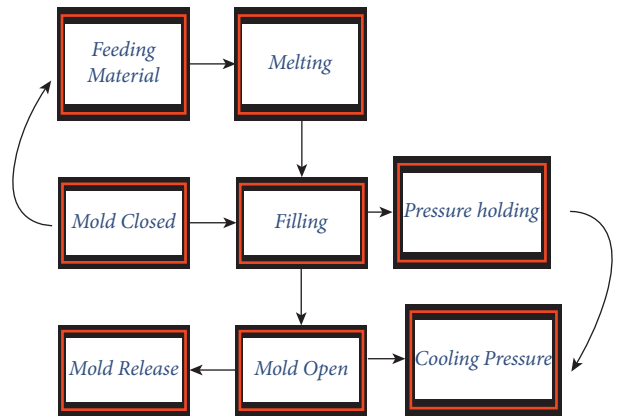

Figure 1: Injection molding process includes feeding and melting.

fed to the mold just before injection. This is followed by polymerization, which forms the plastic along with the molding. The polymerization process produces the material with the desired property and enhances the material property for reinforcement. Reinforcement loads are incorporated in any of the reagents and this is called enhanced reaction injection molding. Figure 2 represents the basic process of Reaction Injection Molding. In this process, to make a rapid polymerization reaction, a certain type of plastic is required, and they may be polyesters, epoxy, nylons, and vinyl monomers. Nonetheless, polyurethane is the most frequently used material. In this research to mold an automobile instrument parameter, the polyurethane and polystyrene are taken as the plastic resin and kept circulating in their separate system.

They are kept separate until they are ready to shed to the injection shot. Polyurethane and polystyrene were then added to the blend head and injected into the mold. Both the reactants in the separate system have low stickiness. The pressure injection is relatively low in the Reaction Injection Molding process. Comparing the conventional injection molding with reaction injection molding, the tightening force is the same for both molding processes. Even though the RIM process is mainly used to make the automobile instruments like a car bumper and body panels, in the RIM process, different materials can be used for the molding process due to the consequence of low injection pressure; they include aluminum and low copper metals [12]. Based on the research, aluminum is one of the best products for making automobile instruments due to its corrosion resistance, and the weight of the large mold parts is saved. Compared to injection molds, molds are less expensive. As the materials used in the RIM process are expensive, they need careful handling, and the particular product or the parameter must have the perfect finishing, and the surface finishing must be perfect and fine due to the expansion of the material. In the polymerization process, the surface of every detail must be reproduced during molding.

Filling Time: It is well-defined as the time needed to fill the whole cavity with the molten plastic and to analyze the configuration of the software of the molten part like Minitab can be used.

Flow Front Temperature: The temperature of the intermediate material flow is defined as the flow front temperature; the certain node is filled with molten plastic. The temperature is also termed the intermediate temperature.

Clamping Force: Clamping force is defined as the maximum clamping force needed to exert the node.

Welding Line: The molded plastic parts must be ensured based on perfection, good surface, and appearance, so to ensure those appearances, the welding line length and number should be minimized. In the places of visible areas and stress concentration areas, the welding wires are not permitted.

Based on the above factors like Filling period, flow front temperature, clamping power, and welding stripe, a tabulation is made based on a certain assumption of a part as mentioned in Table 1.

2.2. Design Using Taguchi Orthogonal Design. For optimizing the process parameter for simple and robust technique, Taguchi method has been applied, and it is successfully used among the optimization technique [13]. According to Taguchi's design objectives, there are three different average square deviations calculated for the signal-to-noise ratio and which include better-the-nominal, better-the-large, and better-the-small. The research aims to optimize the warpage and shrinkage amount. The shrinkage and warpage value must be minimum rate, and thus, the S/N ratio of the smaller-the-better formula has to be chosen for optimizing the parameter rate, and hence the combination is obtained.

2.3. Simulation of Automobile Instrument Part. For the simulation process of automobile instrument, assume a cluster instrument and as said before, polypropylene (PP), is used as the resin material. The properties of the materials were taken from the database of Mold Flow software: the properties include melt density, mold temperature, melt point, material flowrate, and Poisson rate, and the value is presented in Table 2.

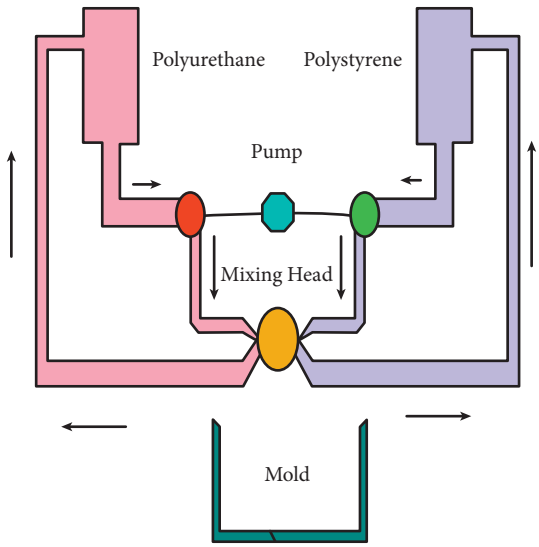

Figure 2: Basic process of reaction injection molding.

Table 1: Assumption for the automobile instrument based on four configurations includes filling period, temperature, power, and stripe characteristics

Filling period	Flow front temperature	Clamping power	Welding stripe characteristics
1.333	3.5	1060	The length is large and a greater number of pieces
1.381	12	807	
1.205	21.2	721.2	The distribution is reasonable and the smaller number of pieces
1.066	8.4	1070	

2.4. Experimental Design. At the first step, by using Taguchi orthogonal design, the analyses of finite element is carried out by implementing four constraints like material flow rate (FR_M), mold point(T_M), melt point (M_T), and the injection pressure (P_I) [14]. From the database of Minitab, the material properties are determined for the material flow rate, mold temperature, melting point, and based on the industry experiences, the injection pressure is calculated. Based on the analysis, the injection time is calculated, the maximum injection time is 4.557 (Sec), and the minimum time is 2.489 (sec). To determine the optimal level of parameters, the orthogonal design is used along with the four constrain such as injection time (T_I), packing pressure (P_P), packing pressure time (T_p), and the cooling point (T_C). In this, the injection time is the first step and followed by this, the packing pressure is done. After completing the packing pressure, the time is given for it, which is known as packing pressure time, and then finally a cooling point is given and the process gets completed.

According to the outcome of the analysis, the extreme warpage value of this part is 2.633 mm, stirring in the remote area of the doors. Figure 3 is created based on the 3D design of the Creo drawing tool and then by molding them, a dashboard of the automobile is designed. Automobile vehicles have faced a large problem in traffic management, so certain sensors were insulated in the automobile parameter to manage the traffic system [15]. In the above dashboard, the vehicle owner could communicate with the other vehicle owners. Certain settings include communication between the server and third parties such as perambulation police, ambulance, and fire department. In communication between the vehicle and the vehicle, the owner involves certain factors like vehicle speed, fuel, and kilometer between the starting point to the destination which are directly reported to the vehicle owner either by voice or by screening the message [1]. It is necessary to update the active data of the vehicle even when they are not in use and when the automobile is far away from the user and involved workstation is used. In order to reduce the accident happening around high traffic area, the automobile parameter is embedded with a certain microcontroller that tracks the movement of the vehicle, spots the high traffic zone, and then gives direct information to the vehicle owners to avoid accidents. The embedded system works on the basic of BX-24 microcontroller and it also combines with exterior strategies. To store the basic information of the X operating system, a fast core processor with Read-Only Memory is used in the BX-24 system. This basic process consists of Read-Only Memory and Random-Access Memory about 400 bytes and electronically erasable programmable read-only memory of 32 Kilobytes and a timer with an I/O device. Digital pins were also present in the basic BX-24 system. Thus, this embedded unit helps to receive information about the vehicle moving around the traffic zone. These exterior devices like input and output ports could be used in the car door along with a sensor device to open, close, and lock the car door even away from the vehicle. To offer a complete monitoring of the system, the embedded system uses the user interface such as LCD and

Table 2: Assets of particle.

Properties	Value
Melt density (g/cm^3)	0.87723
Mold point (°C)	66
Melt point (°C)	215
Material flowrate (g/5 min)	9
Poisson rate	0.3851

LED display and the interactive mode of work. This could help to evaluate the signal between traffic zone. The LCD and LED display could help to receive the data sent by the microcontroller. Some sensor sends beep sound to give an important message like alerts, break, begin, and emergency purpose. The interface element is used to control the sequence of the strings. The user database could be easily generated by the computer interface. To configure the final interface system, the user could use it after the completion of the final step sequence. Thus, the whole embedded processor works on the automobile instrument, specifically in locking and traffic management.

2.5. Particle Swarm Optimization. Particle Swarm Optimization (PSO) is a computational method that optimizes the problems in an iterative manner, which is used to improve the solution to the given measure of quality. To determine the importance of the constraints and influences, Particle Swarm Optimization is performed. By dividing the total variability into contributions based on each design parameter, the PSO result is carried out. This could also verify whether the altered level adjustment or experimental error causes any change in the observed variation in response. The sum of the square, degree of freedom, mean square, and F-test of significance is calculated using the PSO.

The improved form of PSO of fitness function states the error sum of square required, and it is defined by the following:

$$S = \sum_{m=1}^{n} \left(Z_{rm} - Z_{pm}\right)^2. \quad (1)$$

Fitness function is stated as S and the required and the predicted value are represented as Z_{rm} and Z_{pm}, where m is the output parameter individually. There is n number of the output parameter. To optimize the injection molding process parameter, the Genetic Algorithm (GA) optimization technique is used along with the PSO. These optimized process parameters were compared to the best process parameters in the PSO. GA is used to generate high quality solutions to optimization and search problems. PSO is a computational method that optimizes the problems in an iterative manner.

2.6. Design of Optimization. However, many calculations and high costs will be incurred due to many factors if the whole aspect method has been employed. Nevertheless, numerous calculations and high costs will be incurred due to many factors if the full factor methodology has been used. In this research, the Taguchi method was used to solve this problem. Firstly, an orthogonal network (OA) that provided sufficient information to form the inverse model using the minimum number of researches for the design of the condenser was built.

Finally, the information sets and MIMO were used to generate a model recitation the inverse affiliation between mechanized factors and a point-of-sale high point in specific locations. Figure 4 illustrates how the optimal plan is executed.

3. Results and Discussion

To run the experiment, the L27 Orthogonal array method is used. The wear characteristics response was measured. By retaining the Taguchi method, the optimized parameter is defined. To find the analysis variance and other necessary factors, L27 orthogonal Taguchi method is used. Using the orthogonal series, the analysis was systematized and the self-determined variables like temperature and distance sliding were noted.

3.1. Variance of Analysis. The variance of analysis is a decision-making tool and this is used to analyze the performance difference of the test conducted. By the squaring and estimation process, the variance of analysis is calculated, and error specific levels are measured. By using the following expression, the average test for the variance analysis is measured.

$$S_T = \sum_{n=1}^{m} \left(\beta_n - m_i\right)^2. \quad (2)$$

The influence of the processing parameter is influenced by the unique ratio of the sum of a square and the sum of deviation, and then they are processed by the parameter indices, where the total sum of squared deviation is represented as S_T, the total mean S/N ratio is defined as m_i, and the total number of experiments done in orthogonal array are defined as m, and the β_n is defined as the S/N experiment ratio. SNR for shrinkage volume and warping amount is shown in Table 3.

The important feature of the warpage amount is cooling time and warpage amount is proportional to each other as the time of cooling increases, the warpage amount increase, and then it starts to decrease. The melt temperature is considered as the second effective feature, and it is about 25.30% of the warpage amount [16]. The warpage amount decreases rapidly as the melt temperature decreases. It is noted that a similar interpretation is found for the pressure

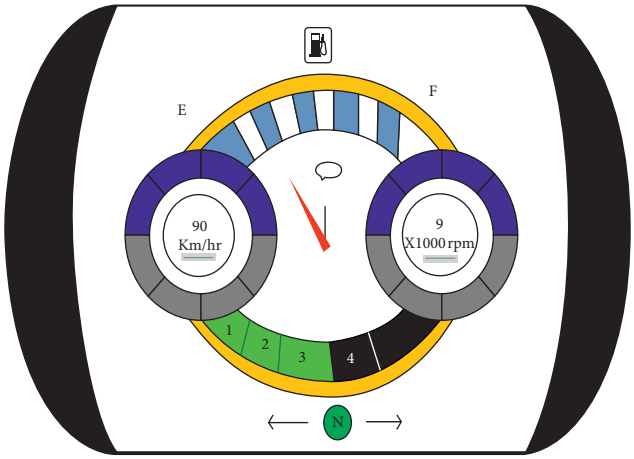

Figure 3: Automobile dashboard.

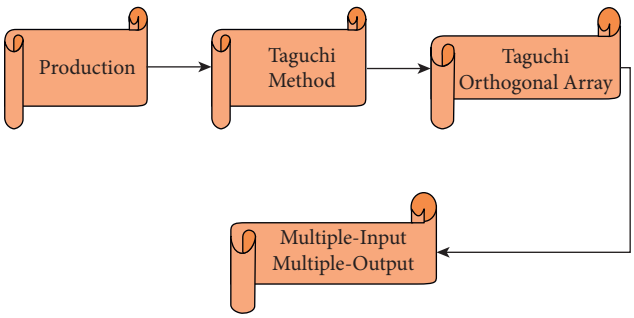

Figure 4: Optimization plan.

Table 3: Signal-to-noise ratio of shrinkage volume and warping amount.

Number of test	Signal-to-nose ratio of volume shrinkage rate and warping amount	
	Shrinkage rate	Warping amount
1	−20.688	−6.370
2	−19.255	−5.990
3	−18.607	−5.632
4	−17.775	−4.598
5	−22.100	−5.148
6	−17.450	−6.029
7	−16.584	−5.711
8	−17.741	−5.982
9	−21.591	−5.805
10	−21.980	−5.343
11	−16.845	−5.347
12	−17.690	−5.926
13	−21.600	−5.820
14	−16.970	−5.497
15	−17.350	−6.130
16	−19.390	−5.987
17	−21.970	−4.670
18	−16.880	−6.098
19	−21.970	−5.029
20	−16.880	−5.550
21	−16.910	−5.845
22	−21.580	−5.705
23	−21.900	−5.856
24	−18.024	−5.754
25	−18.351	−5.889
26	−20.590	−5.798
27	−18.438	−5.746

Table 4: Mean of SNR of shrinkage and warpage.

Objective optimization	Mean value	A^*	B^*	C^*	D^*	E^*
Shrinkage rate	I_1^*	−18.671	−18.045	−19.360	−19.480	−21.340
	I_2^*	−18.952	−18.630	−18.720	−18.781	−19.750
	I_3^*	−19.260	−19.500	−18.990	−19.185	−17.774
	I_4^*	−19.300	−20.030	−19.055	−18.730	−17.335
	Y^*			−19.005		
Warping amount	J_1^*	−5.343	−6.048	−5.856	−5.550	−5.497
	J_2^*	−5.347	5.850	−5.754	−5.830	−6.130
	J_3^*	−5.92	−5.640	−5.889	−5.748	−5.987
	J_4^*	−5.820	−5.550	−5.798	−5.531	−4.670
	Y^*			−5.746		

Table 5: Variance result.

Objective optimization	Variance of source	Mean square of deviation	Degree of freedom	Mean square value	Degree of influence
Shrinkage rate	A^*	0.355	3	0.075	
	B^*	2.555	3	0.880	
	C^*	0.215	3	0.075	
	D^*	0.375	3	0.130	
	E^*	10.400	3	3.468	
	SO	13.825	15		
Warping amount	A^*	0.0065	3	0.0025	1.06
	B^*	0.1550	3	0.0516	24.28
	C^*	0.4044	3	0.1016	47.65
	D^*	0.0915	3	0.0305	14.44
	E^*	0.0816	3	0.0275	12.77
	SO	0.6365	15		

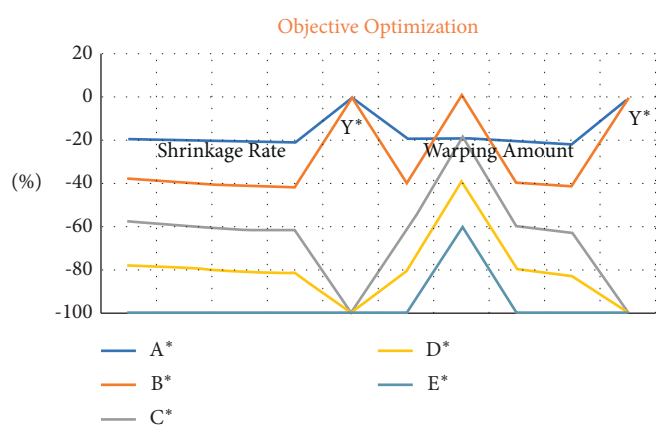

Figure 5: Objective optimization based on mean value.

Table 6: Final result of warpage and shrinkage amount based on Taguchi orthogonal array.

Index	Factor influence	Parameter combination	Shrinkage volume	Warping amount
Taguchi based warpage amount	$C^* > B^* > D^* > E^* > A^*$	$A^*1B^*1C^*2D^*4E^*4$	6.821	2.010
Taguchi based shrinkage rate	$E^* > B^* > D^* > A^* > C^*$	$A^*4B^*4C^*1D^*4E^*1$	12.70	1.780

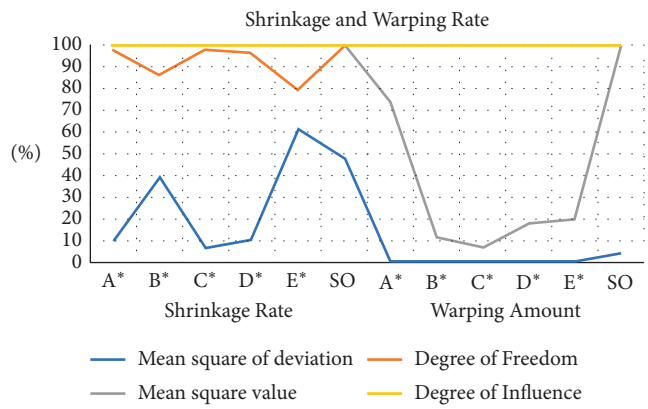

Figure 6: Result of variance.

of packing and packing time and this is about 15.33% and 12.66%.

Based on the Taguchi orthogonal test design, the influence degree of various molding parameters on volume shrinkage rate and warpage amount can be obtained. Accordingly, the optimal combination of molding parameters can be obtained to minimize the volume shrinkage rate and the warpage amount which is shown in Table 4.

Using the Taguchi orthogonal array method, the warpage and shrinkage volume is calculated from the above-mentioned analysis of finite elements and S/N ratio. Table 5 shows the variance result. Figure 5 is determined by using signal-to-noise ratio equation; warpage and shrinkage capacity are calculated [17].

Finally, the warpage and shrinkage volume amount of the automobile dashboard is calculated and the optimization of the automobile parameter is done using the Taguchi orthogonal array method. The signal-to-noise ratio is calculated using the above-mentioned expression and followed by the expression, the warpage and shrinkage volume is analyzed and represented in the graphical form [18, 19].

In Table 6, final result of warpage and whrinkage amount based on Taguchi orthogonal array is presented in which A^* denotes the mold temperature, B^* denotes the melt temperature, C^* denotes the cooling temperature, D^* denotes the packing pressure, and E^* denotes the packing time. The warpage and the shrinkage result depend on the following four-parameter: injection time, packing pressure, packing time, and cooling point. For three series of data, the following parameter is calculated and presented in Figure 6.

4. Conclusion

In the present study, the four configurations are primarily proposed for injection molding and for the optimization of automobile parameters using the Taguchi Orthogonal Array method. By using the Minitab software, the numerical analysis is made. The analysis of filling time, flow front temperature, clamping force, and welding line is compared. From the result, it is shown that the filling time is about 1.055 seconds and the different flow front temperature is about 7.4°C and the clamping force is 1060 kN, the welding line number is low, and distribution is low for welding. The paper mainly deals with the Taguchi Orthogonal Design as they help in reducing the factors of the injection molding system. As said before, the parameter like packing time, packing pressure, melt point, mold points are inversely proportional to each other, and when this optimization technique is used, they reduce the maximum temperature used in designing the mold. Specifically, the automobile parameter requires high temperature for melting and molding them, but by using the Orthogonal Array method, half the temperature and time are reduced and the defects in the parameter are found and changed by the particle swarm optimization. Hence, the paper clearly defines the simulation process of injection molding along with the optimization of automobile instrument parameters using the Taguchi Orthogonal Array design and Particle Swarm Optimization.

Data Availability

The data used to support the findings of this study are included within the article.

Conflicts of Interest

The authors declare that there are no conflicts of interest regarding the publication of this article.

References

[1] A. W. Judge, "Automobile electrical instruments," in *Modern Electrical Equipment For Automobiles*, pp. 292–315, Springer, Berlin, Germany, 1970.

[2] M. Ogawa, Y. Suzuki, H. Ogai, and J. Kusaka, "Development of method for construction of a response surface model and control parameter optimization method for automobile engine," *Transactions of the Society of Instrument and Control Engineers*, vol. 47, no. 10, pp. 501–510, 2011.

[3] Z. Zhao, X. He, M. Liu, and B. Liu, "Injection mold design and optimization of automotive panel," in *Proceedings of the 2010 Third International Conference on Information and Computing*, pp. 119–122, Wuxi, China, June 2010.

[4] M. Vishnuvarthanan, R. Panda, and S. Ilangovan, "Optimization of injection molding cycle time using moldflow analysis," *Middle-East Journal of Scientific Research*, vol. 13, no. 7, pp. 944–946, 2013.

[5] L. Ren and W. Zhang, "Optimization Design of Injection Mold Cooling System Based on Particle Swarm Optimization and Genetic Algorithms," in *Proceedings of the 2011 2nd International Conference on Artificial Intelligence, Management Science and Electronic Commerce (AIMSEC)*, p. 5, Deng Feng, China, August 2011.

[6] W.-C. Chen, M.-H. Nguyen, W.-H. Chiu, T.-N. Chen, and P.-H. Tai, "Optimization of the plastic injection molding process using the Taguchi method, RSM, and hybrid GA-PSO," *International Journal of Advanced Manufacturing Technology*, vol. 83, no. 9–12, pp. 1873–1886, 2016.

[7] K. Shelesh-Nezhad and E. Siores, "An intelligent system for plastic injection molding process design," *Journal of Materials Processing Technology*, vol. 63, no. 1–3, pp. 458–462, 1997.

[8] G. Ghosh, P. Mandal, and S. C. Mondal, "Modeling and optimization of surface roughness in keyway milling using ANN, genetic algorithm, and particle swarm optimization," *International Journal of Advanced Manufacturing Technology*, vol. 100, no. 5, pp. 1223–1242, 2019.

[9] A. Kaveh and S. M. Rad, "Hybrid genetic algorithm and particle swarm optimization for the force method-based simultaneous analysis and design," *Iranian Journal of Science and Technology Transaction B: Engineering*, vol. 34, p. 22, 2010.

[10] R. J. Bensingh, R. Machavaram, S. R. Boopathy, and C. Jebaraj, "Injection molding process optimization of a bi-aspheric lens using hybrid artificial neural networks (ANNs) and particle swarm optimization (PSO)," *Measurement*, vol. 134, pp. 359–374, 2019.

[11] G. Anitha, M. Ayyadurai, and G. Ramkumar, "Design of miniaturized single bit MEMS phase shifter using MEMS switches," in *Proceedings of the 2021 5th International Conference on Trends in Electronics and Informatics (ICOEI)*, pp. 235–239, IEEE, Tirunelveli, India, June 2021.

[12] M. S. Meiabadi, A. Vafaeesefat, and F. Sharifi, "Optimization of Plastic Injection Molding Process by Combination of Artificial Neural Network and Genetic Algorithm," *Journal of Optimization in Industrial Engineering*, vol. 6, 2013.

[13] V. Singh, G. Anitha, and K. Usha Kiran, "Conventional DMTL phase shifter is designed without meta-material and with meta-material," in *Optical and Microwave Technologies*, pp. 21–32, Springer, Berlin, Germany, 2018, Lecture Notes in Electrical Engineering.

[14] W.-C. Chen and D. Kurniawan, "Process parameters optimization for multiple quality characteristics in plastic injection molding using Taguchi method, BPNN, GA, and hybrid PSO-GA," *International Journal of Precision Engineering and Manufacturing*, vol. 15, no. 8, pp. 1583–1593, 2014.

[15] G. Ramkumar, R. Thandaiah Prabu, N. Phalguni Singh, and U. Maheswaran, "Experimental analysis of brain tumor detection system using Machine learning approach," *Materials Today: Proceedings*, 2021, In press.

[16] B. Ozcelik and T. Erzurumlu, "Comparison of the warpage optimization in the plastic injection molding using ANOVA, neural network model and genetic algorithm," *Journal of Materials Processing Technology*, vol. 171, no. 3, pp. 437–445, 2006.

[17] P. J. Ross, *Taguchi Techniques for Quality Engineering: Loss Function, Orthogonal Experiments, Parameter and Tolerance Design*, MCGRAW-Hill, New York, NY, USA, 1996.

[18] R. Sreenivasulu, "Optimization of surface roughness and delamination damage of GFRP composite material in end milling using Taguchi design method and artificial neural network," *Procedia Engineering*, vol. 64, pp. 785–794, 2013.

[19] R. Govindaraj and E. Logashanmugam, "Multimodal verge for scale and pose variant real time face tracking and recognition," *Indonesian Journal of Electrical Engineering and Computer Science*, vol. 13, no. 2, p. 665, 2019.

Hindawi
Advances in Materials Science and Engineering
Volume 2021, Article ID 2909033, 12 pages
https://doi.org/10.1155/2021/2909033

Research Article

Experimental Investigation on the Ecofriendly External Wrapping of Glass Fiber Reinforced Polymer in Concrete Columns

D. S. Vijayan,[1] **A. Mohan**,[2] **J. Jebasingh Daniel**,[3] **V. Gokulnath**,[4] **B. Saravanan**,[5] **and P. Dinesh Kumar**[6]

[1]*Department of Civil Engineering, Aarupadai Veedu Institute of Technology, Vinayaka Missions Research Foundation, Paiyanoor, Chennai, India*
[2]*Easwari Engineering College, Department of Civil Engineering, Ramapuram, Chennai, India*
[3]*Department of Civil Engineering, Hawassa University, Hawassa, Ethiopia*
[4]*Department of Civil Engineering, Saveetha School of Engineering, Saveetha Institute of Medical & Technical Sciences, Chennai, TN, India*
[5]*Department of Civil Engineering, Aarupadai Veedu Institute of Technology, Vinayaka Missions Research Foundation, Paiyanoor, Chennai, India*
[6]*Head of the Department, Department of Civil Engineering, Krishnasamy College of Engineering and Technology, TN, India*

Correspondence should be addressed to J. Jebasingh Daniel; jdaniel@hu.edu.et

Received 22 July 2021; Revised 16 August 2021; Accepted 19 August 2021; Published 29 August 2021

Academic Editor: Ravichandran M

An ecofriendly fiber reinforced polymer (FRP) had been used in the last decade to enhance the short concrete column's strength and deformation capacity. This study involves the wrapping of FRP sheets with a thickness of 3 mm and 5 mm on a short column, and then the compressive strength is determined. The rectangular columns of size 150 mm × 300 mm are used for this study, and cast under the grades of M20 and M40 are wrapped with GFRP sheets at the thickness of 3 mm and 5 mm. These results are clarified at a specific thickness of the FRP-wrapped columns. It provides a maximum axial compressive strength, and Young's modulus gets enhanced rigorously when it is to be compared to the normal concrete. This thesis deals with experimental studies of different parameters associated with wrapped glass fiber reinforced polymer (GFRP). In M20 grade, when the 3 mm wrapped specimen and the 5 mm wrapped specimen are compared, the specimen wrapped with 5 mm increases 5.182% more than the specimen wrapped with 3 mm. In M40 grade, when the 0 mm, 3 mm, and 5 mm wrapped specimens are compared, the specimen wrapped with 5 mm increases 2.47% more than the specimen wrapped with 0 mm. The 5 mm wrapping attains the maximum strength.

1. Introduction

Fiber reinforced polymer (FRP) is a composite material made up of a matrix reinforced with polymers. A vast amount of experimental work was conducted on FRP columns in the last decade. Natural disasters such as hurricanes, tornadoes, tsunamis, earthquakes, and unintended effects can destroy or damage the secondary structures in a matter of seconds. On the other hand, the salt water, chemical, and freeze-thaw cycles can induce structural degradation for a longer time [1]. Many old buildings and bridges were designed according to the old construction codes. FRP materials are a new technique that has gained popularity in recent years. As a result, these kinds of materials have been used for decades in other industries such as shipbuilding and defense, which provide novel solutions for rehabilitating decaying civil infrastructure. The continual deterioration of infrastructure has heightened awareness of the need for effective structure rehabilitation procedures. A peculiar challenging problem confronting engineers in the revival of the infrastructure is the rehabilitation of concrete structures. The use of externally bound FRP sheets and strips was

developed recently as effective tools for rehabilitating and reinforcing concrete structures [2]. In the case of strength application, the external bonding FRP plates with column member were found to provide vast advantages: they are easy to handle, have resistance against electrochemical corrosion and fatigue resistance, have maintained good weight to strength ratio, are easy to use in curved casting with any shape and length, and provide maximum compressive strength at lesser density. [3] So, glass fiber enhanced polymer sheets are being used gradually to rehabilitate and upgrade the concrete structures when compared with other types of FRP fibers. The resistance to corrosion and fatigue is typically high in strength-to-weight [4].

Simple concrete has low voltage and little ductility and no cracking resistance. Because of the low tensile strength, microcracks are present in concrete. Cracks spread with load application leading to fragile concrete fractures. Over the last two decades, the use of GFRP as external wrapping has gained significant popularity for the reinforcement and repair of concrete structures. The GFRP wrapping was effectively used to improve and enhance existing structures and weak reinforced concrete components [5]. The external wrapping of reinforced concrete columns is a common technique for GFRP strengthening to increase the axial strength, sheer power, stiffness, and deflection. The GFRP sheet was mainly wrapped in the fiber direction around the columns in this application. The fiber limits the concrete cover and increases the strength and rigidity. Columns of reinforced concrete must be confined laterally to ensure a broad deformation under the applied loads before failure and to provide ample bearing capacity. As an axial compressive load is applied to the GFRP-wrapped concrete column, the concrete core extends laterally. The GFRP avoids this expansion, and the concrete core is transformed into a three-dimensional compressive stress state. There have been numerous investigations into the actions of the uniaxial compressive loaded GFRP-wrapped concrete column, which shows that fibers should be aligned along with the cement core.

In reality, however, almost all the columns suffer from an eccentric axial load that can be solved in a uniaxial time [6]. FRP is ideal for any design program that requires saving weight, precise engineering, finite tolerances, and simplifying components both in production and service. Molded polymer devices are cheaper, quicker, and easier to produce than cast aluminum or steel devices and retain tolerances and material strengths equally and often better [4]. Further, the strength, stress-strain ratios, elasticity, and failure under compression of externally reinforced concrete were studied. The test results indicated that FRP confinement increases the compressive and flexural strengths of concrete by approximately 22% and 1-2 MPa, respectively. Natural jute fibers (bark or straw) may be used as reinforcements for external concrete cylinders and prisms equally as polypropylene fibers. For external concrete confinement, natural jute FRP is recommended [7]. It was also suggested that a modified compression field formulation approximates the shear in stir-welded reinforced concrete due to piers that proved to be reliable. Steel stirrup yield was taken into account by including an empirical decay law. Because both FRP stress debonding and tensile stress were considered, the strain's influence on FRP reinforcement was sufficiently explored. It successfully matched experimental data, showing that it can accurately predict the shear strength. Numerical analysis was also calculated to show the significance of the key factors in predicting ultimate shear strength [8].

A new analytical model was designed to predict the compressive strength of FRP-filled concrete columns concerning the precontainment axial load level. To do so, several small concrete cylinders were loaded, subjected to a series of destructive tests of pure axial compression. It was confined with plastic reinforced carbon fiber. Four different levels of existing loads had been simulated, including the unloaded condition. The analytical predictions indicate that the FRP jacket's mechanical action is effective, but the presence of extensive damage precludes exploiting the confinement in the same way that unloaded columns would. The comparison of analytical predictions and experimental results appeared to be consistent, even though an additional investigation is required to validate the proposed theory [9]. Further, tests on both the control and strengthened beams were conducted. The control beams failed in shears, whereas the strengthened beam ductility failed, with most cracks protruding in a flexural length, indicating the successful shift of the failure mode from scissors to flexures by the integrated steel bars. In addition, the reinforced beam (Beam-B) has increased its strength by around 31% as compared to the beam control (Beam-A) [10].

Usually, the beams were tests with two axial loads. Results indicated that a maximum load of 9.78% and 9.92% increased respectively when compared to an acoustic beam with a single layer or two-layer abaca-fiber composite as NFRP material for the shear-foster beam. Abaca fiber composite NFRP material contributed 11% and 18.57% of the maximum total shear load for one-layer and two-layer laminates, respectively. Additionally, shear-strengthened beams that were externally bonded affected the crack pattern and deflection value. However, in two-layer NFRP shear strengthened beams, debonding failure of NFRP laminates occurred. As a result, the beam did not perform optimally [11]. The effect of high temperatures on the behavior of low solid cement following its consolidation in a polymer carbon fiber layer (CFRP) was further investigated. Among 84 specimens that have been examined, 42 have been wrapped in CFRP fibers and 42 have not been wrapped. Cylinder specimens (150×300 mm) were used as a heat exposure period for one or two hours exposed to temperatures between 100°C and 600°C. The practical part of the study focuses on compressive strength, ultrasonic pulse rate, dynamic elasticity modulus, and low strength concrete weight loss properties. The results indicated that when wrapped specimens were exposed to a temperature of (200°C) for one and two hours, respectively, their compressive strength increased by 35% and 49%, respectively, compared at the same level with unwrapped specimens. Furthermore, the external CFRP sheet strengthening acted as a protection for the concrete, improving the behavior of the low-strength concrete [12].

The current investigation considered reinforced concrete columns reflecting a real-world position in which reinforcement of the FRP is taken on reinforced concrete columns instead of plain concrete. The use of externally bonded FRP composites to reinforce and restore the existing concrete columns can be an economical option for restoring or enhancing their performance. While a great deal of research has focused on circular columns, there has been comparatively less work on square and rectangular columns to study the effects of FRP containment on structural efficiency. However, the majority of all columns are square or rectangular in houses. Therefore, the strength and restoration of building facilities must be maintained. This article is aimed at this endeavor. Efficient wrapping can increase the strength of both the confined cement and the carrying capacity of the column. This research aims to measure the effects of upgrading the carriage capability of GFP flexible wraps compressed concrete columns. For the different grades of concrete columns, the GFRP sheets of different thicknesses are wrapped, and the results are to be analyzed. The comparison was made regarding thickness of GFRP sheets, the maximum strength attained, and the wrapped columns and unwrapped columns.

2. Material and Methods

2.1. Fiber Reinforced Polymer. FRP is a composite material composed of a matrix reinforced with polymers. The different types of FRP are organized as organic FRP and inorganic structure. The various types of organic and inorganic fiber laminates structures are shown in Figures 1 and 2.

Roving is a group of strands, which are more of a uniform product. Woven roving provides an inexpensive way of laminating large, flat areas, for quick construction and reinforcement of high strength. It is incompatible with applications that require conformance. The material of woven roving laminated sheet is shown in Figure 3.

These are two-dimensional random arrays of chopped strands. The use of woven roving with chopped strand mat (CSM) is common in reinforcing other materials, and it is especially useful for making repairs. The CSM is incompatible with epoxy and should only be used with polyester or vinyl ester resin. The material of the CHM laminated sheet is shown in Figure 4.

Several forms are bonded with each other based on the type of output fiber needed. Combi mat, which is made by stitching woven fabric together with a layer of the chopped strand, is commonly known as "woven roving Combi mat." It is also compatible with polyesters with a degree of unsaturation, vinyl ester resins, and epoxy resins as well as polyphenols [13]. The woven roving Combi mat sheet is shown in Figure 5.

2.1.1. Cement and Aggregates. The most critical form of cement is Portland pozzolana. In compliance with IS 4031-1988, the PPC was graded in three grades based on its intensity in 28 days. If the strength for 28 days is not less than 33 N/mm^2, it is referred to as a 33-grade cement, equivalent to the wise one. If its strength is not less than 43 N/mm2, it is called a 43 grade of cement. For future experiments, the Portland pozzolana cement of 53 grades was considered [14].

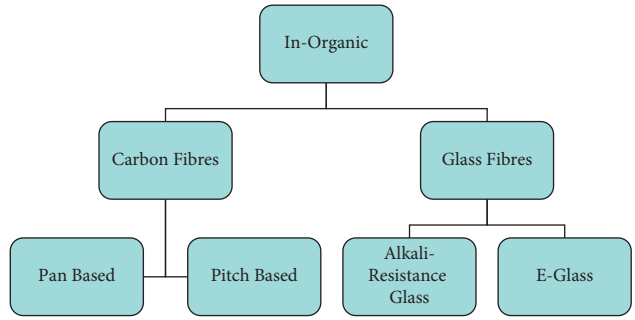

Figure 1: Inorganic structure of different types of fiber laminates.

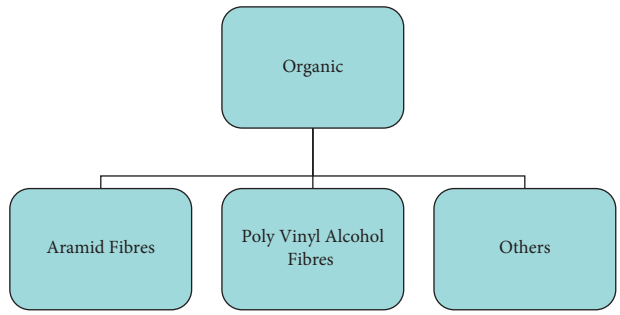

Figure 2: Organic structure of different types of fiber laminates.

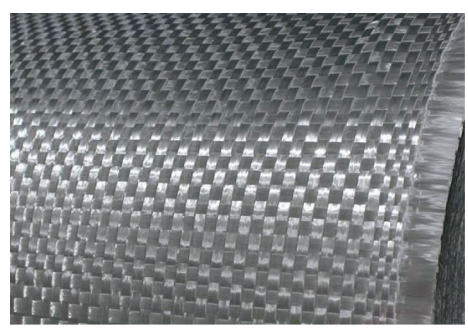

Figure 3: Woven roving laminated sheet.

Figure 4: CHM laminated sheet.

Figure 5: Woven roving Combi mat laminated sheet.

For this study, the 43 grade of cement was utilized based on the recommendation of previous researchers.

2.2. Testing of Cement. Testing of cement can be brought under two categories.

2.3. Field Testing

(i) The testing is done on the field itself, and it is sufficient for minor works.

(ii) Open the bag and take a good look at the cement.

(iii) There should not be any visible lumps, and the color should be greenish-grey.

(iv) When the hand is put into the cement bag, the feeling is incredible. After taking one pinch of cement and keeping it between the fingers, if it is a smooth and nongritty cement, then place it in a bucket full of water.

2.4. Laboratory Test. The following is usually done in the laboratory:

(i) The fine net should be smooth, and it should be applied with the concrete sample using resin. Let the sample to cure under room temperature for 28 days. After curing, the samples were tested and the results have to be analyzed based on the thickness of fine net.

(ii) A standard consistency test should be made.

(iii) The specific gravity of cement should be checked.

2.5. Fineness Test. The fine cement influences the hydration rate and the rate of increase in strength, as well as the rate of growth in heat. A cement sample should have a maximum particle count of fewer than 100 microns. Parts under 3 microns have a predominant impact on power, whereas 3–25 microns significantly affect 28 days of strength. The test is conducted under the standard guidelines of fineness of cement by dry sieving (IS: 4031-Part 1–1996).

2.6. Standard Consistency Test. The standard consistency test is designed to allow a 10 mm and 50 mm diameter VICAT PLUNGER to penetrate a depth of 33. The mold top is 35 mm in diameter. The VICAT system detects the percentage of water necessary to reach a standard consistency of cement. The test is conducted under the standard guidelines as Per IS Code 4031.

2.7. Procedure for Consistency Test

(i) Take some 500 grams of cement and plan for the first trial of the paste with a weighted quantity of water (24 percent cement weight).

(ii) The paste must be prepared regularly, and the Vic at mold must be filed within 3 to 5 minutes. After filling the mold fully, shake the mold to remove the air.

(iii) A 10 mm diameter, 50 mm standard long plunger is mounted, positioned to the surface if it is in the test block and released quickly so that it can fall into the paste due to its weight. Take the depth of penetration of the plunger by zero.

(iv) Conduct the second (25% water) test to determine the extent of penetration of the plunger. Similarly, conductivity is done daily, cement production for higher percentages of water and cement until the plunger penetrates the specified percentages of water from the top for a depth of 33–35 mm. Table 1 shows the cement test values.

2.8. Testing of Coarse Aggregate. The size of aggregate more significant than 4.75 mm is considered coarse aggregate and the primary source of aggregate. It increases the surface area, promotes workability, and calculates the amount of water absorbed by the coarse aggregates, while this experiment is conducted. The testing results are shown in Table 1. The test is conducted under the standard guidelines as per code 383 for aggregates.

2.9. Testing for Fine Aggregate. The overall size of less than 4.75 mm is considered to be perfect [15]. The primary source of fine aggregates is pit sand from the river or the seaside. The type of river or shore bed sand is round, and pit sand is irregular or partly circular. The satisfactory aggregate test results are shown in Table 1. The test is conducted under the standard specification as per Is code 383 [1970] for aggregates.

2.10. Water. Water is the primary ingredient of concrete since it participates strongly in cement chemical reactions. Quantity and consistency participate with cement in the chemical reaction [16]. Water quantity and consistency must be studied very carefully. Optimization of portable water with pH values is between 6 and 8 and water is free of organic matter. The pH value of water was estimated as 12.3 with the comparison of standard buffer solutions.

2.11. GFRP Sheets. GFRP Sheets are a common name like carbon fiber or steel and are commercially available in different chemical compositions. The glass fibers are made

Table 1: Test results for materials used in concrete.

S.NO	Properties	Cement	Coarse aggregate	Fine aggregate
1	Consistency	33%	—	—
2	Fineness	90 microns	3.8	3.2
3	Initial setting time	64 min	—	—
4	Final setting time	350 min	—	—
5	Specific gravity	3.15	20.7	2.67
6	Water absorption	—	2.68	—
7	Crushing strength	—	4.31	—
8	Zone	—	—	II

Table 2: Properties of glass fiber.

Properties of glass fiber	Values
The density of the fiber	2.5 g/cm^3
The thickness of the fiber sheet	0.363 mm
Orientation of the fiber sheet	Bi-directional
Nominal thickness	1mm
Tensile strength of the fiber	1.9–3.4 GPa
The elasticity modulus of the fiber	70 GPa

Table 3: Chemical composition of E-glass fiber.

Component	E-glass (%weight)
SiO_2	55.2
K_2O	0.2
MgO	4.6
CaO	18.7
Na_2O	0.3
Al_2O_3	8.0

up of 3 groups E, S, and C. E-glass is used for electrical use, and S-glass is specified for a higher power. C-glass is highly resistant to corrosion and is not famous for civil engineering. Of the three fibers, E-glass is the reinforcement element most common in civil applications [2]. It was suggested that many of the features of the glass fiber need to be investigated throughly before application with different types of concrete.

Popular fibers are silica based and contain an array of other calcium, boron, sodium, aluminum, and iron oxides (50–60% SiO_2). Glass fibers have high tensile strength and elasticity modulus. The choice of materials for various enhancement systems is an essential process [17].

The fibers and resins are intended for collaboration. This resin for one reinforcement system will not work correctly for another reinforcement system. Thus, it is inferred that the qualitatively evaluated systems are used to improve intensity. The goal of adhesives is to create a continuous connection between the concrete surface and the material to ensure the complete composite action [18]. This was created by passing shear stress over the thickness of the adhesive sheet. The GFRP physical and chemical features of Tables 2 and 3.

3. Method and Preparation for GFRP Wrapping

3.1. Grinding of Columns. The possibilities for sharp angles, except junctions, are negligible and the smooth surface needs to be ground and prepared; otherwise, air bubbles may occur when wrapping fiber. Grinding activity is necessary to remove the dust and cement loose layer [11]. Figure 6 depicts column grinding using gridding machine.

Figure 6: Grinding of columns.

3.2. Selection of GFRP Sheets. Varieties of techniques are involved in the wrapping of GFRP. The unidirectional wrapping is selected because of the orientation of fibers. These fibers are usually arranged uniformly. So, the suitable sheets are to be selected for the strengthening effect. Figure 7 represents GFRP sheets used in concrete.

Figure 7: Selection of GFRP sheets.

3.3. Mixing of Resin. Resins played an essential role in the GFRP wrapping. The resin mixture is applied to every layer of columns to seal the GFRP sheets [19]. Adding few drops of resin was considered as most challenging while mixing with the concrete [20]. The primary purpose of the epoxy resin is to harden the surface, as shown in Figure 8.

3.4. GFRP-Wrapped Columns. After applying the mixture of resins, the next step in the wrapping work is placing the GFRP sheets with a suitable thickness, and the setting of sheets

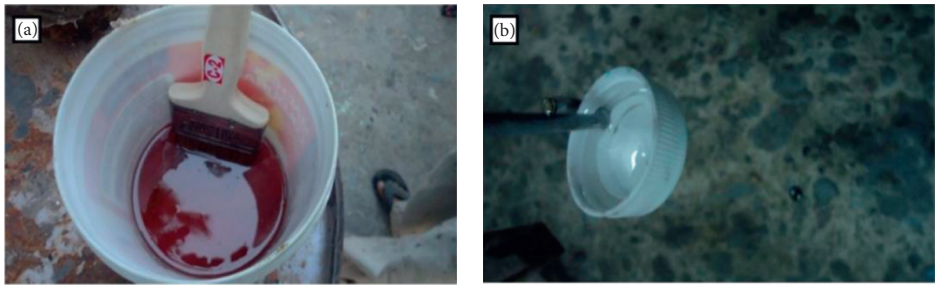

(a) (b)

Figure 8: (a) Epoxy resin. (b) Mixing agent.

usually takes 3 hours. After setting the activity of wrapped columns, the unnecessary wastages at the top are to be cut, and the GFRP-wrapped columns are shown in Figure 6.

The casted specimen was wrapped with Glass FRP which is shown in Figure 9. The castings of the columns are made for two grades, i.e., M20 and M40. The size of the columns is 150 mm × 300 mm. The thickness of the wrapping is about 3 mm and 5 mm. Now the compressive strength of the columns is to be tested, and then the results are to be analyzed: if thickness of wrapping can attain the maximum strength [8]. The comparison is made between the wrapped column and the unwrapped column [21]. The testing of the concrete beams is done for 28 days.

4. Result and Discussion

The experimental results are of M20 grade of columns and M40 grade of columns. First, the M20 grade of beams is taken. The specimens consist of the three columns in which two beams are wrapped with the GFRP of thickness 3 mm and 5 mm; one beam remains unwrapped with any sheets. Now the compressive strength of the beam is tested [9]. Here the wrapped beams will attain the maximum compressive strength when it is compared to the unwrapped beam. The test results are compared with the two thicknesses of the columns, and the maximum compressive strength is evaluated. A similar experiment is repeated for the M40 grade of concrete.

4.1. Testing of GFRP-Wrapped Columns. The wrapping of GFRP sheets is kept as it is for 48 hours. The specimens are ready for testing, the extensometer is fixed along with the columns, and the specimen is placed in the compressive testing machine [22]. The load is gradually applied and the deflection is to be noted. Figure 10(a) shows the arrangement of experimental setup and (b) depicts the experimental set up to test the specimens.

4.2. Testing of GFRP-Wrapped M20 Grade Concrete Columns with 0 mm Wrapping. When the column was cast under the grade of M20 and then the testing is made after 28 days, the compressive strength of the cube is about 236 kN. The column was cast under the grade of M40, and then the testing is made after 28 days. The compressive strength of the cube is about 387 kN. The quantity is a ratio of stress along an axis to the stress of the hook law [23]. Table 4 displays Young's M20 module with 0 mm stroke, and Figure 11 represents stress-strain analysis for M20 concrete with 0 mm wrapping.

Testing of GFRP-wrapped M40 grade concrete columns with 0 mm wrapping.

The Young's modulus for the grade of M40 with 0 mm wrapping is shown in Table 5, and the stress-strain analysis curve is shown in Figure 12.

4.3. Testing of GFRP-Wrapped M20 Grade Concrete Columns with 3 mm Wrapping. The Young's modulus for grade M20 with 3 mm wrapping is shown in Table 6, and the stress-strain analysis curve is shown in Figure 13. The column was cast and, after the curing, wrapping of the GFRP sheet is done with a thickness of 3 mm under the grade of M20. After that the specimen is tested in the compressive testing machine, and it attains the load of 1184 kN.

Testing of GFRP-wrapped M20 grade concrete columns with 5 mm wrapping.

The Young's modulus for grade M20 with 5 mm wrapping is shown in Table 7, and the stress-strain analysis curve is shown in Figure 14. The column was cast and after the curing, wrapping of the GFRP sheet is done with a thickness of 5 mm under grade M20. Now that the specimen is tested in the compressive testing machine, it attains a load of 1073 kN.

Testing of GFRP-wrapped M40 grade concrete columns with 3 mm wrapping.

The Young's modulus for grade M40 with 3 mm wrapping is shown in Table 8, and the stress-strain analysis curve is shown in Figure 15. The column was cast, and after the curing, wrapping of the GFRP sheet is done with a thickness of 3 mm under grade M40. Now that the specimen is tested in the compressive testing machine, it attains a load of 1171 kN.

4.4. Testing of GFRP-Wrapped M40 Grade Concrete Columns with 5 mm Wrapping. The Young's modulus for grade M40 with 5 mm wrapping is shown in Table 9, and the stress-strain analysis curve is shown in Figure 16. The column was cast, and after the curing, wrapping of the GFRP sheet is done to the thickness of 5 mm under the grade of M40. Now that the specimen is tested in the compressive testing machine, it attains a load of 1235 kN.

Figure 9: GFRP-wrapped columns.

(a) (b)

Figure 10: (a) Arrangement of experimental set. (b) Testing of GFRP-wrapped columns in compression testing machine.

Table 4: Young's modulus for M20 grade of the column with 0 mm wrapping.

S.No	Load (kN)	Deflection (mm)	Stress (N/mm^2)	Strain $\times 10^{-5}$	Young's modulus E
1	20	0.036	1.13	1.2	0.94
2	40	0.076	2.26	2.5	0.9
3	60	0.109	3.39	36.3	0.09
4	80	0.132	4.52	44	0.102
5	100	0.156	5.65	52	0.108
6	120	0.179	6.79	59.6	0.113
7	140	0.209	7.92	69.6	0.113
8	160	0.226	9.05	75.3	0.120
9	180	0.234	10.18	78.0	0.130
10	200	0.247	11.32	82.3	0.137
11	220	0.258	12.44	86.2	0.144

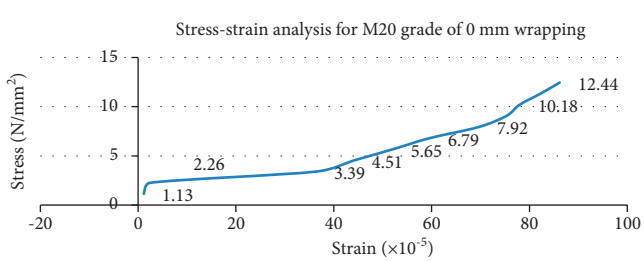

Figure 11: Stress-strain analysis for grade M20 with 0 mm wrapping.

Table 5: Young's modulus for M40 grade of the column with 0 mm wrapping.

S. No	Load (kN)	Deflection (mm)	Stress (N/mm^2)	Strain $\times 10^{-5}$	Young's modulus E
1	20	0.002	1.13	0.67	1.68
2	40	0.009	2.26	3	0.75
3	60	0.02	3.39	6.66	0.5
4	80	0.030	4.52	10	0.45
5	100	0.036	5.65	12	0.47
6	120	0.054	6.79	18	0.37
7	140	0.072	7.92	24	0.33
8	160	0.088	9.05	29	0.3
9	180	0.111	10.18	37.4	0.27
10	200	0.142	11.31	47.3	0.23
11	220	0.174	12.44	58	0.21
12	240	0.207	13.58	69	0.19
13	260	0.242	14.71	80.6	0.18
14	280	0.730	15.84	243	0.06
15	300	0.697	16.97	232	0.07
16	320	0.648	18.10	216	0.08
17	340	0.613	19.24	204	0.09
18	360	0.578	20.3	192	0.10
19	380	0.538	21.50	179	0.12

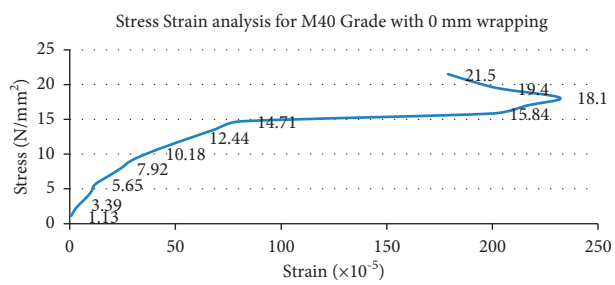

Figure 12: Stress-strain analysis for grade M40 with 0 mm wrapping.

Table 6: Young's modulus for M20 grade of column with 3 mm wrapping.

S.No	Load (kN)	Deflection (mm)	Stress (N/mm^2)	Strain ($\times 10^{-5}$)	Young's modulus E
1	50	0.550	2.829	1.83	0.15
2	100	0.236	5.658	7.86	0.70
3	150	0.758	8.488	2.52	0.33
4	200	1.363	11.317	4.54	0.24
5	250	2.872	14.145	9.57	0.14
6	300	2.418	16.972	8.06	0.21
7	350	2.760	19.805	9.20	0.23
8	400	4.026	22.635	13.42	0.16
9	450	4.355	25.464	14.51	0.17
10	500	4.692	28.294	15.42	0.18
11	550	4.927	31.123	16.42	0.18
12	600	5.274	33.953	17.58	0.19
13	650	5.515	36.782	18.38	0.20
14	700	7.879	39.611	26.26	0.15
15	750	8.143	42.441	27.14	0.15
16	800	10.476	45.270	34.93	0.12
17	850	11.721	48.100	39.07	0.12
18	900	15.972	50.929	53.24	0.09
19	950	15.402	53.759	51.34	0.01
20	1000	17.134	56.588	57.11	0.09
21	1050	18.920	59.417	63.06	0.09
22	1100	20.825	62.247	69.41	0.08
23	1150	22.568	65.076	75.22	0.08

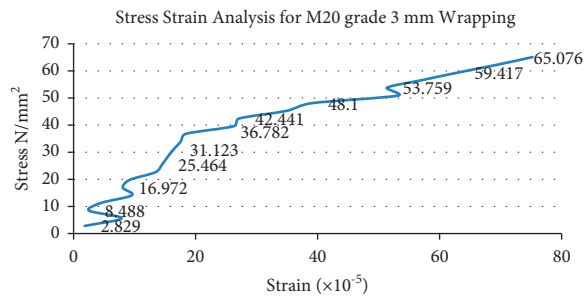

Figure 13: Stress-strain analysis for grade M20 with 3 mm wrapping.

Table 7: Young's modulus for M20 grade of column with 5 mm wrapping.

S.No	Load (kN)	Deflection (mm)	Stress (N/mm^2)	Strain ($\times 10^{-5}$)	Young's modulus E
1	50	0.160	2.830	5.333	0.5300
2	100	0.335	5.658	1.116	0.5069
3	150	0.524	8.488	1.746	0.4861
4	200	0.681	11.317	2.273	0.4978
5	250	0.804	14.147	2.684	0.5270
6	300	1.028	16.976	3.426	0.4955
7	350	1.324	19.805	4.413	0.4487
8	400	1.670	22.635	5.566	0.4066
9	450	2.135	25.464	7.116	0.3578
10	500	2.525	28.294	8.416	0.3361
11	550	2.894	31.123	9.646	0.3288
12	600	4.385	33.953	14.616	0.2323
13	650	3.784	36.782	12.613	0.2916
14	700	5.195	39.611	17.316	0.2287
15	750	4.578	42.441	15.260	0.2781
16	800	6.135	45.270	20.450	0.2213
17	850	7.578	48.100	25.260	0.1904
18	900	9.082	50.930	30.273	0.1682
19	950	17.764	53.760	59.213	0.0097
20	1000	20.478	56.588	68.260	0.0082

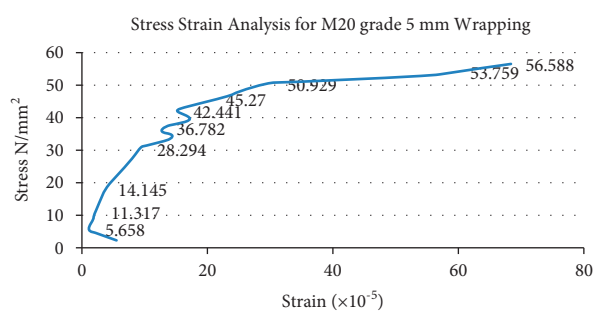

Figure 14: Stress-strain analysis for grade M20 with 5 mm wrapping.

In the grade of M20, the thickness of 3 mm attains the maximum load, and in the grade of M40, the thickness of 5 mm attains the maximum load. In case of M20 grade, when we compare the unwrapped specimen with the 3 mm wrapped specimen column, there is an increase of 80.06% more than the unwrapped column. In the case of M20 grade, when we compare the unwrapped specimen with the 5 mm wrapped specimen, the wrapped column increases 78.00% more than the unwrapped column. In M20 grade, when we compare the 3 mm wrapped specimen with the 5 mm wrapped specimen, the specimen wrapped with 3 mm increases 9.375% more than the specimen wrapped with 5 mm. In case of M40 grade, when we compare the unwrapped specimen with the 3 mm wrapped specimen, the wrapped column increases 66.96% more than the unwrapped column. In M40 grade, when we compared the unwrapped specimen

Table 8: Young's modulus for M40 grade of column with 3 mm wrapping.

S.No	Load (kN)	Deflection (mm)	Stress (N/mm^2)	Strain (×10^{-5})	Young's modulus E
1	50	0.030	2.830	1.000	0.283
2	100	0.070	5.658	2.333	0.242
3	150	0.119	8.488	3.970	0.213
4	200	0.161	11.317	5.370	0.210
5	250	0.202	14.147	6.733	0.210
6	300	0.245	16.976	8.170	0.207
7	350	0.286	19.805	9.533	0.207
8	400	0.338	22.635	1.126	0.201
9	450	0.401	25.464	1.336	0.190
10	500	0.468	28.294	1.560	0.181
11	550	0.545	31.123	1.816	0.171
12	600	0.607	33.953	2.023	0.167
13	650	0.670	36.782	2.233	0.164
14	700	0.736	39.611	2.453	0.161
15	750	0.803	42.441	2.676	0.158
16	800	0.879	45.270	2.930	0.154
17	850	0.962	48.100	3.206	0.150
18	900	1.067	50.930	3.556	0.143
19	950	1.216	53.760	4.053	0.132
20	1000	1.428	56.588	4.760	0.118
21	1050	1.750	59.417	5.833	0.101

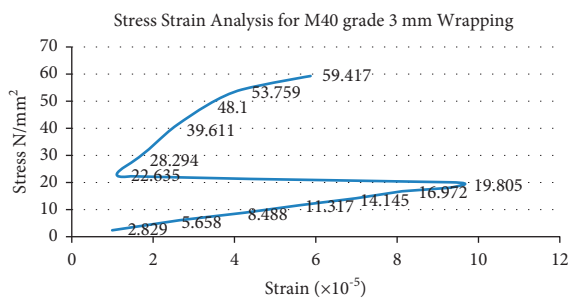

Figure 15: Stress-strain analysis for grade M40 with 3 mm wrapping.

Table 9: Young's modulus for M40 grade of column with 5 mm wrapping.

S.No	Load (kN)	Deflection (mm)	Stress (N/mm^2)	Strain (x10^{-5})	Young's modulus E
1	50	0.0720	2.830	2.400	0.117
2	100	0.120	5.658	4.000	0.141
3	150	0.183	8.488	6.100	0.139
4	200	0.262	11.317	8.733	0.129
5	250	0.321	14.147	1.070	0.132
6	300	0.380	16.976	1.270	0.133
7	350	0.437	19.805	1.455	0.136
8	400	0.501	22.635	1.670	0.135
9	450	0.564	25.464	1.880	0.135
10	500	0.633	28.294	2.110	0.134
11	550	0.693	31.123	2.310	0.134
12	600	0.770	33.953	2.570	0.132
13	650	0.881	36.782	2.930	0.125
14	700	0.040	39.611	1.333	0.297
15	750	0.131	42.441	4.370	0.097
16	800	0.263	45.270	8.770	0.051
17	850	0.409	48.100	1.363	0.352
18	900	0.532	50.930	1.773	0.287
19	950	0.780	53.760	2.600	0.206

Table 9: Continued.

S.No	Load (kN)	Deflection (mm)	Stress (N/mm^2)	Strain (x10^{-5})	Young's modulus E
20	1000	0.923	56.588	3.076	0.183
21	1050	1.014	59.417	3.380	0.175
22	1100	1.195	62.244	3.988	0.156
23	1150	1.351	65.076	4.503	0.144
24	1200	1.581	67.906	5.270	0.128
25	1250	1.794	70.735	5.980	0.118

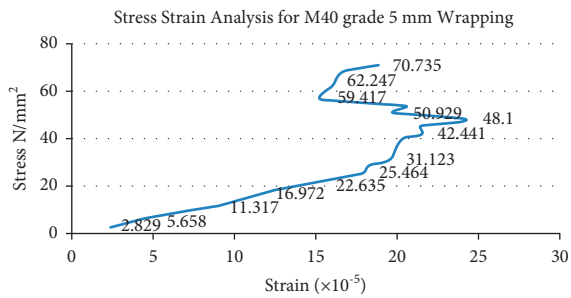

Figure 16: Stress-strain analysis for grade M40 with 5 mm wrapping.

with the 5 mm wrapped specimen, the wrapped column increases 68.66% more than the unwrapped column.

5. Conclusion

The experimental work carried out in this study concentrated primarily on determining the efficacy of concrete columns filled with reinforced polymer glass fiber. The experimental findings from experiments on concrete columns were reinforced by external E-glass fiber composite in load capacity and strains. In case of M40 grade, when the 3 mm wrapped specimen and the 5 mm wrapped specimen are compared, the specimen wrapped with 5 mm increases 5.182% more than the specimen wrapped with 3 mm. In M40 grade, when the 0 mm, 3 mm, and 5 mm wrapped specimen are compared, the specimen wrapped with 5 mm increases 2.47% more than the specimen wrapped with 0 mm. The 5 mm wrapping attains the maximum strength.

5.1. Future Work

(i) The GFRP materials are not providing satisfactory outcomes for creep and heavy sustained loads, hence increasing thickness or adding adequate materials as a support to resist the creep.

(ii) Impact loading causes more damage to GFRP concrete structural elements. So, providing ductile detailing could be the best solution for future research.

(iii) GFRP design should be improved to adapt to different environmental changes since it shows poor results in high temperature.

(iv) The elastic modulus of GFRP is significantly less compared to steel and concrete. It would be better if research has been carried out in this area to enhance elastic modulus.

(v) Adequate code provisions should be developed to fix the proportion of fiber used in concrete since it makes changes in concrete strength.

Data Availability

The data used to support the findings of this study are available upon request.

Conflicts of Interest

The authors declare that there are no conflicts of interest regarding the publication of this article.

Acknowledgments

Research outcomes of the manuscript were supported by the Department of Civil Engineering, Krishnasamy College of Engineering and Technology, Chennai. The authors would also like to extend their thanks to the authors and non-technical staff of Aarupadai Veedu Institute of Technology, Chennai, SRM Easwari Engineering College, and Saveetha School of Engineering for providing the needed technical support.

References

[1] S. Robert Ravi and G. Prince Arulraj, "Experimental investigation on the behavior of R.C.C. Beams-column joints retrofitted with GFRP-CFRP hybrid wrapping subjected to load reversal," *International Journal of Mechanics and Solids.ISSN*, vol. 5, no. 1, pp. 973–1881, 2010.

[2] C. E. Chalioris, "Tests and analysis of reinforced concrete beams under torsion retrofitted with FRP strips," in *Proceedings of the 13th Computational Methods and Experimental Measurements (CMEM 2007)*, vol. 11, Prague, Czech Republic, 2007.

[3] B. Ramesh, S. Eswari, and T. Sundararajan, "Flexural behaviour of glass fiber reinforced polymer (GFRP) laminated hybrid-fiber reinforced concrete beams," *SN Applied Sciences*, vol. 2, no. 2, p. 204, 2020.

[4] D. Parthiban, D. S. Vijayan, R. Sanjay Kumar, A. P. Santhu, G. Abraham Cherian, and M. Ashiq, "Performance evaluation of Fly ash based GPC with partial replacement of RHA as a cementitious material," *Materials Today: Proceedings*, vol. 33, pp. 550–558, 2020.

[5] M. N. Mahmood and A. Sh. Mahmood, "Torsional behavior of prestressed concrete beam strengthened with CFRP sheets," in *Proceedings of the 16th International Conference on Composite Structures, ICCS*, vol. 16, p. 14, Porto, Portugal, June 2011.

[6] D. S. Vijayan and J. Revathy, "Flexural response of fibre reinforced polymer laminated pre-stressed concrete beams," *Indian Journal of Science and Technology*, vol. 9, no. 42, 2016.

[7] K. Madhavi, V. V. Harshith, M. Gangadhar, V. Chethan Kumar, and T. Raghavendra, "External strengthening of concrete with natural and synthetic fiber compositesfiber Composites," *Materials Today: Proceedings*, vol. 38, pp. 2803–2809, 2021.

[8] N. Spinella, P. Colajanni, A. Recupero, and F. Tondolo, "Ultimate shear of RC beams with corroded stirrups and strengthened with FRP," *Buildings*, vol. 9, no. 2, p. 34, 2019.

[9] F. Micelli, A. Cascardi, and M. A. Aiello, "Pre-load effect on CFRP-confinement of concrete columns: experimental and theoretical studyfinement of concrete columns: experimental and theoretical study," *Crystals*, vol. 11, no. 2, p. 177, 2021.

[10] Ridwan, S. Dirar, Y. Jemaa, A. Kamaldi, and A. Kurniawandy, "Strengthening of reinforced concrete beam subjected to shear loading using deep embedment method," *Journal of Physics: Conference Series*, vol. 1655, Article ID 012089, 2020.

[11] T. Saidi, Z. Amalia, M. Hasan, I. Hasanuddin, and K. Setiawan, "Number of layer effect of abaca fiber as natural FRP material for shear-strengthened reinforced concrete beam," *IOP Conference Series: Materials Science and Engineering*, vol. 1087, no. 1, Article ID 012006, 2021.

[12] R. D. Shlla and K. I. Mohammad, "Experimental investigation on CFRP-confined low strength concrete after high-temperatures exposure," *IOP Conference Series: Materials Science and Engineering*, vol. 1094, no. 1, Article ID 012086, 2021.

[13] M. Dong, W. Lokuge, M. Elchalakani, and A. Karrech, "Modelling glass fiber-reinforced polymer reinforced geopolymer concrete columns," *Structure*, vol. 20, pp. 813–821, 2019.

[14] A. Acharya, S. Reddy, and K. Savaliya, "Effect of glass fibre reinforced polymer wrapping on strength of confined concrete," *International Journal of Technical Innovation in Modern Engineering & Science (IJTIMES)*, vol. 3, no. 5, 2017.

[15] V. Sreevidya and M. Ponkishan, "Strength evaluation of retrofitted geopolymer concrete using natural fibre," *International Research Journal of Engineering and Technology (IRJET)*, vol. 7, no. 9, Sep 2020.

[16] R. Nandhini, Dr. M. M. Saravanan, and A. Karunya Grace, "Retrofitting of concrete structures using fibre reinforced polymer (FRP): a review," *International Journal of Scientific & Technology Research*, vol. 9, no. 2, 2020.

[17] D. S. Vijayan and D. Parthiban, "Effect of Solid waste based stabilizing material for strengthening of Expansive soil- A review," *Environmental Technology & Innovation*, vol. 20, Article ID 101108, 2020.

[18] Ajidevi, "Experimental investigation on Properties of concrete using glass fibre," *International Journal of Engineering Research & Technology (IJERT)*, vol. 4, no. 8.

[19] A. Fitria, A. Saloma, S. A. Nurjannah, and A. P. Usman, "Numerical analysis of the behavior of light concrete panels with variations of thickness and door opening position in resisting static monotonic loads," *International Journal of Advanced Technology and Engineering Exploration*, vol. 7, no. 73, 2021.

[20] R. Raval and U. Dave, "Behavior of GFRP wrapped RC columns of different shapes," *Procedia Engineering*, vol. 51, pp. 240–249, 2013.

[21] B. Saravanan and D. S. Vijayan, "Status review on the experimental investigation on replacement of red-mud in cementitious concrete," *Materials Today: Proceedings*, vol. 33, pp. 593–598, 2020.

[22] A. Zhou, C. L. Chow, and D. Lau, "Structural behavior of GFRP reinforced concrete columns under the influence of chloride at casting and service stages," *Composites Part B: Engineering*, vol. 136, pp. 1–9, 2018.

[23] D. Parthiban and D. S. Vijayan, "Study on Stress-Strain effect of reinforced Metakaolin based GPC under compression," *Materials Today: Proceedings*, vol. 22, pp. 822–828, 2020.

Hindawi
Advances in Materials Science and Engineering
Volume 2021, Article ID 5450935, 15 pages
https://doi.org/10.1155/2021/5450935

Research Article

An Unconventional Approach for Analyzing the Mechanical Properties of Natural Fiber Composite Using Convolutional Neural Network

Govindaraj Ramkumar,[1] **Satyajeet Sahoo**,[2] **G. Anitha**,[1] **S. Ramesh**,[3] **P. Nirmala**,[1] **M. Tamilselvi**,[4] **Ram Subbiah**,[5] **and S. Rajkumar**[6]

[1]*Department of Electronics and Communication Engineering, Saveetha School of Engineering,SIMATS, Chennai 602105, Tamil Nadu, India*
[2]*Department of Electronics and Communication Engineering,Vignan's Foundation for Science, Technology and Research (Deemed to be University), Vadlamudi, Guntur, Andhra Pradesh 522213, India*
[3]*Department of Electronics and Communication Engineering, Sri Shakthi Institute of Engineering and Technology, Coimbatore-641062, Tamil Nadu, India*
[4]*Department of Mechatronics Engineering, T.S. Srinivasan Centre For Polytechnic College and Advanced Training, Chennai, Tamil Nadu, India*
[5]*Department of Mechanical Engineering, Gokaraju Rangaraju Institute of Engineering and Technology, Nizampet, Hyderabad, India*
[6]*Department of Mechanical Engineering, Faculty of Manufacturing, Institute of Technology, Hawassa University, Awasa, Ethiopia*

Correspondence should be addressed to Govindaraj Ramkumar; pgrvlsi@gmail.com and S. Rajkumar; rajkumar@hu.edu.et

Received 19 July 2021; Revised 4 August 2021; Accepted 16 August 2021; Published 24 August 2021

Academic Editor: Ravichandran M

Over the past few years, natural fiber composites have been a strategy of rapid growth. The computational methods have become a significant tool for many researchers to design and analyze the mechanical properties of these composites. The mechanical properties such as rigidity, effects, bending, and tensile testing are carried out on natural fiber composites. The natural fiber composites were modeled by using some of the computation techniques. The developed convolutional neural network (CNN) is used to accurately predict the mechanical properties of these composites. The ground-truth information is used for the training process attained from the finite element analyses below the plane stress statement. After completion of the training process, the developed design is authorized using the invisible data through the training. The optimum microstructural model is identified by a developed model embedded with a genetic algorithm (GA) optimizer. The optimizer converges to conformations with highly enhanced properties. The GA optimizer is used to improve the mechanical properties to have the soft elements in the area adjacent to the tip of the crack.

1. Introduction

In the current situation, industries were mostly focused on the sustainable idea of manufacture to minimize the non-renewable resources procedure and adopt the process of ecofriendly materials by waste reuse or recycling. To prepare composite materials, extensive work is done by the researcher in several areas of the world [1]. Polymer and natural fiber composites have been selected as ideal materials due to necessary characteristics including reusability, recyclability, long-term constancy, and widespread accessibility at a reasonable cost. When compared to synthetic fibers, natural fibers have inferior qualities such as significant water absorption, weak bonding, low durability, and

low mechanical and thermal properties on industrial applications. The optimization and modeling computational engineers employ some approaches to deal with the mechanical difficulties that arise in science and engineering research [2].

Researchers in the field of materials engineering are investigating these computational methods that may be used to model and optimize the many properties of composite materials reinforced with natural fibers. Due to various environmental concerns, the goal is possibly replacing synthetic fibers and environmental considerations [3]. Fiber treatment, nanofilter addition, and hybridization are a few technologies that have been developed to overcome these restrictions. The use of these technologies to manufacture natural fiber composite (NFC) materials has broadened their range of applications such as household, structural, sporting, automobile, aerospace, and other manufacturing applications in recent decades [4].

The process of analyzing the natural fiber's quality and the composites that arise is complicated, which makes it challenging to establish generic methods for modeling and optimizing composite qualities [5]. The use of current computational approaches for studying the characteristics of NFCs has proven to be helpful in the modeling and optimization of composite materials. The shielding process of mechanical properties on natural fiber composites is done by using the electromagnetic interference (EMI). The shielding of EMI efficiency, microstructure, flexibility, tensile, and inner bonding strength of the composites are examined. The EMI excellent shielding performance and mechanical properties use the composite materials in the EMI protection fields. Researchers and producers can easily determine the best mix of constituent materials to balance the strength and cost of the resultant materials by using computational or mathematical models. The analysis of the relationship between the input and output parameters in materials processing is part of composite material modeling.

A deep neural network is inspired by the biological neural network architectures processing the learning data obtained from the user. This network usually has input, hidden, and output layers [6]. The DNN is used to succeed in finite element analysis while solving the optimization problem of graded functionality plates. A DNN for forecasting foamed concrete compressive strength models was trained on a huge number of photos, and then their learning ability was transferred to pavement fracture identification using digitized pavement surface images.

A convolutional neuronal network (CNN) model makes it possible to quantitatively predict the mechanical properties of the compound through maximum fraction space volume [7]. CNNs are a type of DNN, and they were chosen because of their performance in image recognition tasks. In the following sections, taking into account all the volume fractions considerably expands the sample space. Also, from a practical perspective, having a model that forecasts composite performance of actual standards instead of classes list derived from an organization model is more helpful [8]. In addition, using an optimization approach depends on GA with the model CNN created for optimizing mechanical properties in terms of stiff and soft material volume fraction and spatial distribution in the microstructure.

The remaining part of this paper is as follows. Section 2 describes the previous effort that was done by the scholars in this domain with the various experimental tasks; Section 3 offers the materials and methods, Section 4 represents the evaluation and performance of the result and discussion; and Section 5 represents the work achieved in conclusion.

2. Literature Survey

Munde and Ingle (2015) evaluates interest in minimum environmental and inexpensive pollution. This research is focused on biocomposite mechanical properties using the models of available theory and investigational authentication of mechanical properties. Parallel and series, modified Halpin–Tsai, Hirsch model, and Halpin–Tsai are the theoretical models used for mechanical tensile properties evaluation. To prepare the sample specimen by using the compression molding machine, the characterization of the mechanics is performed ASTM D638-01 through the universal test machine. The results compared the assumed modulus of tensile and strength of tensile with the characteristics of mechanical properties [9]. De Araujo Alves Lima et al. (2020) analyzed alkalization influence. By combining the behavior of alkalization and silanization on the adhesion interfacial and intralaminar hybrid composite's mechanical properties, the single tensile fiber examined fragmentation and also performed the tests of the short beam. Finally, the analysis of SEM is used to research the surface chemical influence treatment used on the natural fibers morphology, to improve the fiber tensile strength by the research of chemical treatment and alkaline treatment on fibers such as ramie, curaua, and jute. After the fusion treatment, there are better results from the presented sisal fibers. The best treatment of being superficial for individual types of composites is the alkaline treatment for fibers obtaining better results for the untreated samples [10].

Sridharan and Muthukrishnan (2013) evaluate, during the machining and production, whether biocomposites require less energy. The quality of fiber is enhanced by using different chemical treatments. The process of mercerization is improving the composite mechanical properties significantly. This research compares the machinability of reinforced composite jute fiber organized using processed and untreated alkaline fiber. The value of the hole is depending on a comparison of the delamination factor achieved through digital image processing techniques. The experiments are based on the factorial design conducted at the various levels of feed rate and velocity. The ANOVA (analysis of variance) is used to research the chemical treatment influence on delamination. To find the condition of optimum drilling, the Grey Relational Analysis (GRA) is employed [11]. Sultana et al. (2020) estimate the various soft approaches for computing such as Response Surface Methodology (RSM), Artificial Neural Network (ANN), and Support Vector Regression (SVR) for nonlinear empirical development models to expect the mechanical properties of Jute Fiber Reinforced Concrete

Composites (JFRCC). The water-cement relationship (W/C), the capacity of jute fibers, and the length are the most dependent properties. The data for JFRCC properties are matrix-design-based and these data are used to plan, compare, and estimate the models. Thus, the act of the SVR model is better than RSM and ANN models with different performance and parameters measuring to predict both tensile and compressive strengths [12].

Wang, Wu, and Wang (2010) evaluate the fiber aspect ratio effect on steel fiber reinforced concrete (SFRC) mechanical characteristics. This analysis exposes the aspect ratio of the best parameter for strength in every batch. The steel fibers addition can relatively increase the effect of ductility. The erosion-based algorithm is used for numerically simulated steel projects on two SFRC targets such as perforation and crater. Due to the postyield injury, the behavior of softening model has tabulated the effective plastic strain and effective stress. These results show that the hydrodynamic model described the SFRC responses under effect loading. In addition, the higher appearance ratio of the fiber engages high energy causing reduced craters in the SFRC goal and less remaining rate of the projectile [13]. Table 1 shows the various mechanical properties of natural fiber composites.

3. Materials and Method

The composite material of natural fibers was modeled using certain computation methods in this research. The materials include mechanical properties such as jute, sugarcane, ramie, pineapple, and banana fibers. The various parameters are observed from the mechanical characteristics of natural fiber composites. The natural hybrid composites are fabricated through the process of vacuum-assisted rein transfer molding (VARTM). The composites presented better electromagnetic interference (EMI) shielding performance with better mechanical properties. The properties are inherited from the aluminum sheets and natural fiber composites. Currently, the natural fiber composites have mechanical properties of inferiority when compared to the parts of the synthetic counter [21]. The two or more fibers that are dissimilar are get mixed in a common matrix to create a composite panel in the hybrid composite. The hybridization is achieved by merging the different lengths and dissimilar diameters for small fibers. This method aims to evaluate the mechanical properties and shielding performance of natural fiber composites. Next, the content of the nanofiller is used to overcome the limitations of the composite material that is reinforced in natural fibers to enhance dimensional stability. Figure 1 shows the manufacturing of man-made fibers from raw materials.

3.1. Modeling of Mechanical Properties of Natural Fiber Composites. Modeling the mechanical properties of natural fibers composite materials is considered a complex process due to different parameters including the matrix type, used fiber, overall composition, the process of manufacturing, the process of fabrication, and planned applications. The composites offered electromagnetic interference (EMI) for shielding performance with better mechanical properties. Researchers have been able to build these improved modeling approaches with better precision due to recent advances in processing capacity. The goal is to review some computational modeling methodologies that have been employed in the study of fiber-reinforced composite materials.

3.2. Rule of Hybrid Mixture (RoHM). The Rule of Hybrid Mixture (RoHM) model considers that the structure is made up of more than one fiber embedded in one matrix material as a hybrid composite [22]. Applying the isostrain state condition to a reinforced hybrid composite with the two fibers yields equation (1), where ε_{co}, ε_{m1}, ε_{m2} denote the total material strain, initially fiber strain, and next fiber strain. By assuming no interplay between each type of fiber, the equation of RoHM is modeled to compute the hybrid composite modulus as shown in equation (2). Then L_{co}, U_{r1}, and U_{r2} represent the hybrid composite elasticity and qualified volume fraction of hybrid composite for initial and next fibers.

$$\varepsilon_{co} = \varepsilon_{m1} + \varepsilon_{m2}, \tag{1}$$

$$L_{co} = L_{r1}U_{r1} + L_{r2}U_{r2}, \tag{2}$$

Equations (1) and (2) are under the following conditions: $U_{r1} + U_{r2} = 1$, $U_{r1} = U_{m1}/U_f$, $U_{r2} = U_{m2}/U_f$, and $U_f = U_{m1} + U_{m2}$, where U_f is the complete reinforcement fraction volume upon the $(U_{m1} + U_{m2})$, which is basically used as the volume fraction of reinforcement for the elasticity computation (L_{r1} and L_{r2}) of the both exclusive composites. Tensile strength and density fraction of banana module/sisal fiber in variable ratios using experiments and applying RoHM are considered a predictor tool. The comparison between the exact experimental results and the RoHM tensile strength results is shown in Figures 2 and 3 which allows for concluding the methods.

3.3. Halpin–Tsai Model. The model of Halpin–Tsai is employed to expect the composite material elastic modulus using fiber elasticity, materials of the matrix, and geometry as input parameters [23]. The empirical approach is considered, the field approach of self-consistency from the basic model. The model offers that the modulus of tensile and strength of tensile composite material is given in (3) and (4), where S_a, S_d, I_a, I_d represent the composite elastic moduli, matrix elastic moduli, matrix tensile strength, and composite tensile strength, respectively. U_m represents the volumetric fraction of fibers in composites. The parameter value of $F = J - 1$ and $J = 1 + 2s/t$, where the diameters of fiber and length are denoted as t and s, respectively. The parameter γ is given by equation (5) and (6). The parameter of F measures the geometry of fiber, distribution of fiber, and loading of fiber condition. I_m and S_m represent the moduli of elastic and tensile strength of the fiber, respectively. The

Table 1: List of various mechanical properties of natural fiber composites.

Reference	Fiber	Matrix	Strength of tensile (MPa)	Stiffness (GPa)	Strength of flexural (MPa)	Modulus flexural
[14]	Sisal	Epoxy	212	6	320	27
[15]	Banana	Epoxy	46	8	—	—
[16]	Flax	Up	147	14	198	17
[16]	Hemp	Epoxy	165	17	180	9
[16]	Coir	Epoxy	225	6	—	—
[17]	Jute	PP	74	11	112	12
[18]	Kenaf	PLA	223	23	259	22
[16]	Oil palm	PP	53	2	80	3
[19]	Sisal/Hemp	PLA	60.23	6.1	79.76	6.04
[20]	Jute/Sisal	Epoxy	74.78	6.76	—	—

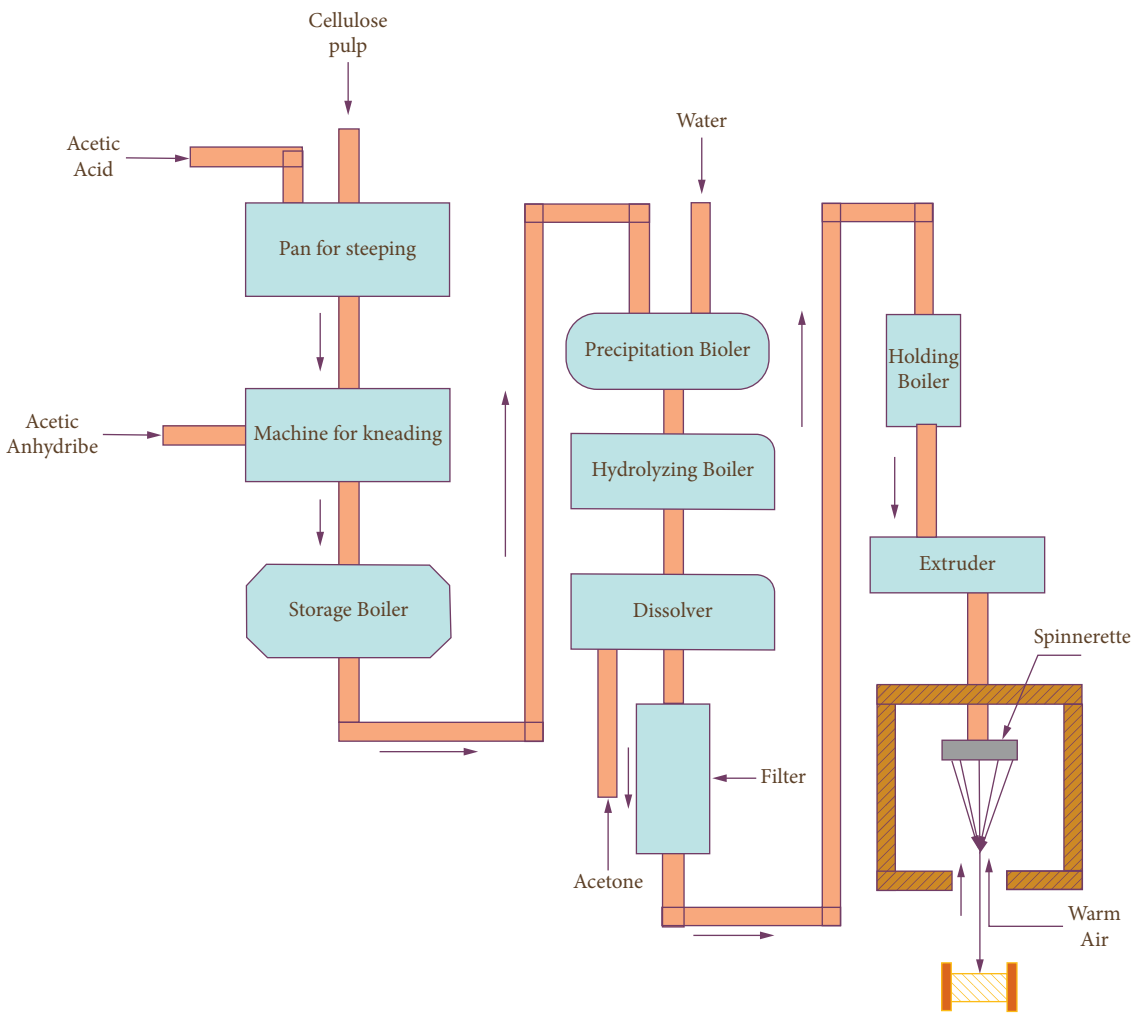

Figure 1: Manufacturing of man-made fibers.

Halpin–Tsai model's essential equations are used to explain the issues analytically to determine the natural occurrence of the structure's fluctuation. The results obtained after using the optimization revealed a higher frequency attained by the hybrid nanocomposites compared with nonhybrid composites.

$$S_a = S_d\left[\frac{1 + F_\gamma U_m}{1 + \gamma U_m}\right], \tag{3}$$

$$I_a = I_d\left[\frac{1 + F_\gamma U_m}{1 + \gamma U_m}\right], \tag{4}$$

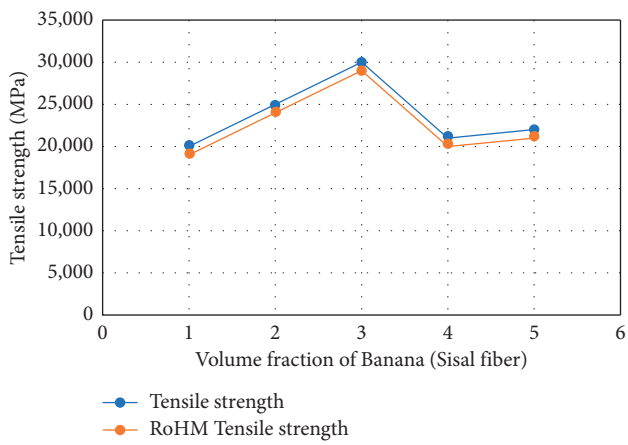

Figure 2: Experimental and RoHM tensile strength of banana/sisal fiber composites results.

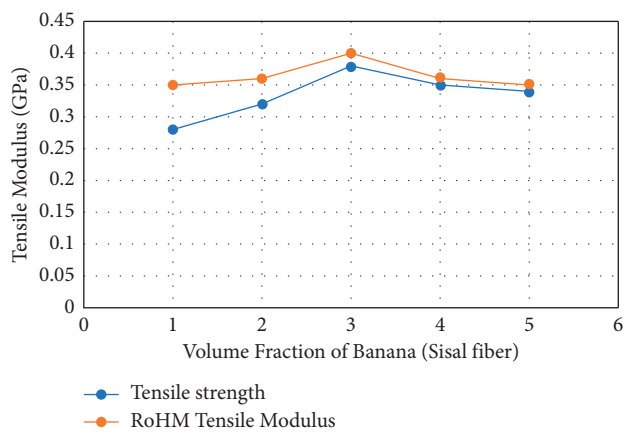

Figure 3: Experimental and RoHM tensile modulus of banana/sisal fiber composites results.

$$\gamma = \frac{S_m/S_d - 1}{S_m/S_d + F}, \tag{5}$$

$$\gamma = \frac{I_m/I_d - 1}{I_m/I_d + F}. \tag{6}$$

3.4. Model of Hirsch. The model is concerned with the sequence stacking and fiber orientation in a matrix material [24]. A diagram of the Hirsch model is given in Figure 4 which shows the parallel and series mixture models. Thus, equation (5) shows the composite characteristics, where I_a, I_d, and I_m represent the composite strength of tensile, matrix material strength of tensile, and fibers tensile strength. U_d denotes the matrix volume fraction and U_m denotes the fraction of fiber volume.

$$I_a = z\left(I_d U_d + I_m U_m\right) + (1 - z)\frac{I_m I_d}{I_d U_m + I_m U_d}. \tag{7}$$

z in the equation indicates a variable amount which gives the load transfer between the fiber and the array. The Hirsch model is used to determine the best characteristics of tensile hybrid composite, which reveals that the mechanical performance is modifiable between the values 0.37 and 0.55.

3.5. Electromagnetic Interference for Shielding Process. Figure 5 shows that A2, A3, A2H11, and A3H12 are investigated using the micro-A1 sheets. The EMI shielding occurs through the radiation reflection. The EMI shielding is the most popular method by using metal sheets and coating. The metal sheets are regularly used, but some suffer from drawback on the bad mechanical properties and resistance corrosion. The metal sheets are converted into the natural fiber composites. The EMI shielding process results from using metal sheets and thus having better mechanical properties given by the natural fiber composites. The metal sheets are protected to avoid the electrochemical corrosion by natural fiber composites. The microstructures of EMI shielding performance and the mechanical properties of the composites are examined.

3.6. Convolutional Neural Network Model. The convolutional neural network model is designed to predict the rigidity, toughness, and strength of two material fibers, one rigid and brittle and the other soft and ductile [25]. The CNN technique model frequently needs important data to provide the exact prediction of fibers. During the training process, it examines new data that is invisible to the model following the formation of the CNN model. The CNN model is based on the data of an FEA (Finite Element Analysis).

The FEA is performed to estimate the interest assets. The replication of the finite elements is motionless when the von Mises (ε_{vs}) deformation at the crack point reaches the corresponding fracture deformation. Then, the von Mises strain is explained as

$$\varepsilon_{vS} = \frac{2}{3}\left(\frac{3}{2}\left(\varepsilon_{11}^2 + \varepsilon_{22}^2 + \varepsilon_{33}^2\right) + \frac{3}{4}\varepsilon_{12}^2\right)^{1/2},$$

$$\varepsilon_{11} = \frac{\sigma_{11}}{V} - \frac{u\sigma_{22}}{V}, \ \varepsilon_{22} = \frac{\sigma_{22}}{V} - \frac{u\sigma_{11}}{V}, \ \varepsilon_{12} = \frac{1+u}{V}\sigma_{12.}. \tag{8}$$

Young's modulus value for stiff fiber is $V = 1$ GPa, and the value of soft fiber material is $V = 0.1$ GPa. The Poisson relationship for both flexible and rigid fiber materials is $u = 1/3$. The break deformation of brittle and rigid fiber materials is 10%, although the break deformation of soft and ductile fiber materials is expected to be 100%. Consider three active qualities of fibers: modulus, strength, and toughness. In FEA, four-node elements were used when the individual section has one point of four quadratures and the individual part has one degree of the two freedoms [26]. The cracked fibers have two dissimilar sizes assumed as 8×8 and 16×16 size systems as examples for the input.

Finite Element Analysis (FEA) is conducted to create data critical to this research. Consider both grid sizes 8×8 and 16×16 as illustrated in Figure 6. The FE approach is used to study a large amount of alternative complex

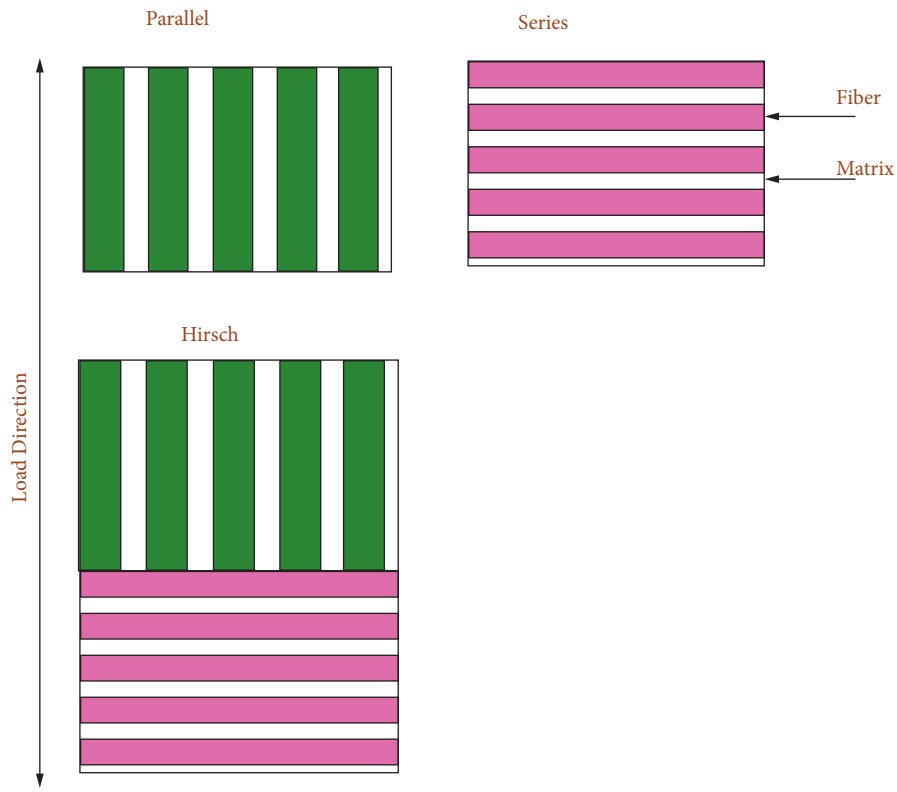

Figure 4: Hirsch model diagram.

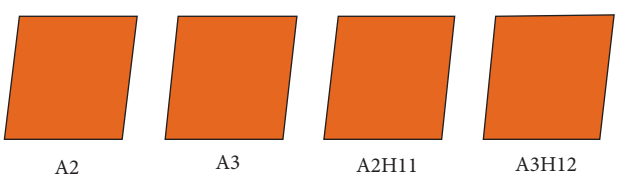

Figure 5: The fabrication composites diagram.

arrangements corresponding to the two grid sizes, and the resultant characteristics within each structure are recorded. The microstructure, containing information on volume fractions and phase spatial distributions, is called configuration. Some preprocessing processes are required after obtaining data from the FEA to make the information for feeding into the CNN model [27]. A matrix is a representation of data in its most basic form from the acquired FEA. The training instances are represented in the rows of that matrix, while the binary distribution of the materials is represented in the columns as 0 for stiffness and 1 for softness. Every learning algorithm has a labeled vector that contains the three material properties: strength, toughness, and strength. Each function is translated into an image by specifying the spatial model for every component to be supplied into the CNN model, whose convolutions could be conducted to develop the CNN model.

The key strategy of a CNN is that the input data are or may be viewed as a picture. As a result, the set of variables is reduced greatly, resulting in speedier processing. In Figure 7, the convolutional layer, pooling layers, fully connected layers, and beginning purposes are the layers that make up a typical CNN. A filter is connected to the input image by an activation function in the convolutional layer, which maintains the interconnections between pixel values. A pooling layer combines the input layer as max-pooling that yields the best accuracy division from every session. Layered and simulation functions in fully linked DNN systems are comparable to those in simple DNN structures [28]. The next layer, such as stall layers, which are the regulation strategies to minimize model overflow, may also be added to CNN. Two CNN architectures were developed in each dimension grid with six fused layers, one exclusion layer, and one fully connected layer in the respective architecture. Each composite layer consists of a 2D convolution layer, a 2D batch stabilization layer, and a corrected linear part activation (ReLU) function. The convolutional layers kernel scopes are varied between the two architectures.

3.7. Evaluation of CNN Model. The mean square error (MSE) cost purpose is used during the formation phase to reduce the residual error among the output data model and the ground-truth data. The average absolute percentage error (MAPE) is used to calculate the model precision. Equations (9) and (10) are used to calculate the mean square and the mean absolute percent error to measure the difference between the actual and projected values.

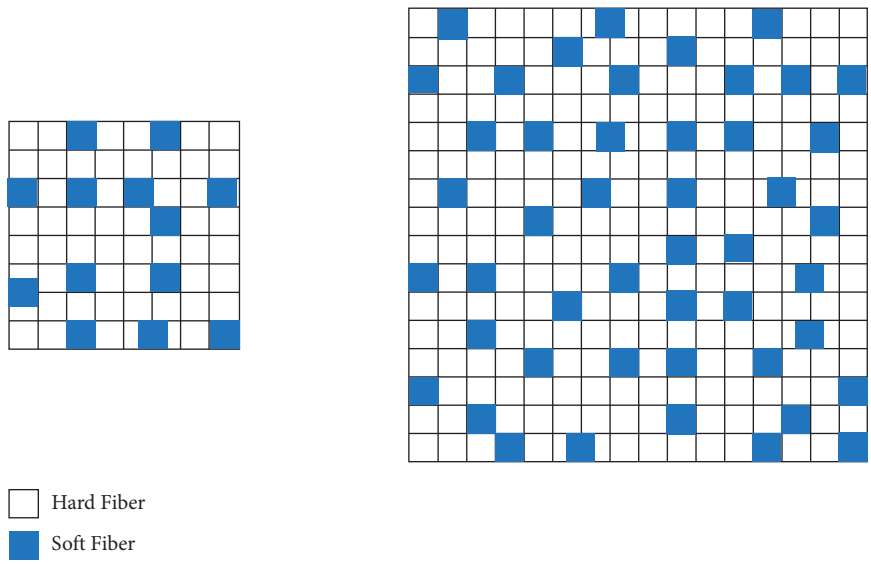

Figure 6: 8 × 8 grid and 16 × 16 grid.

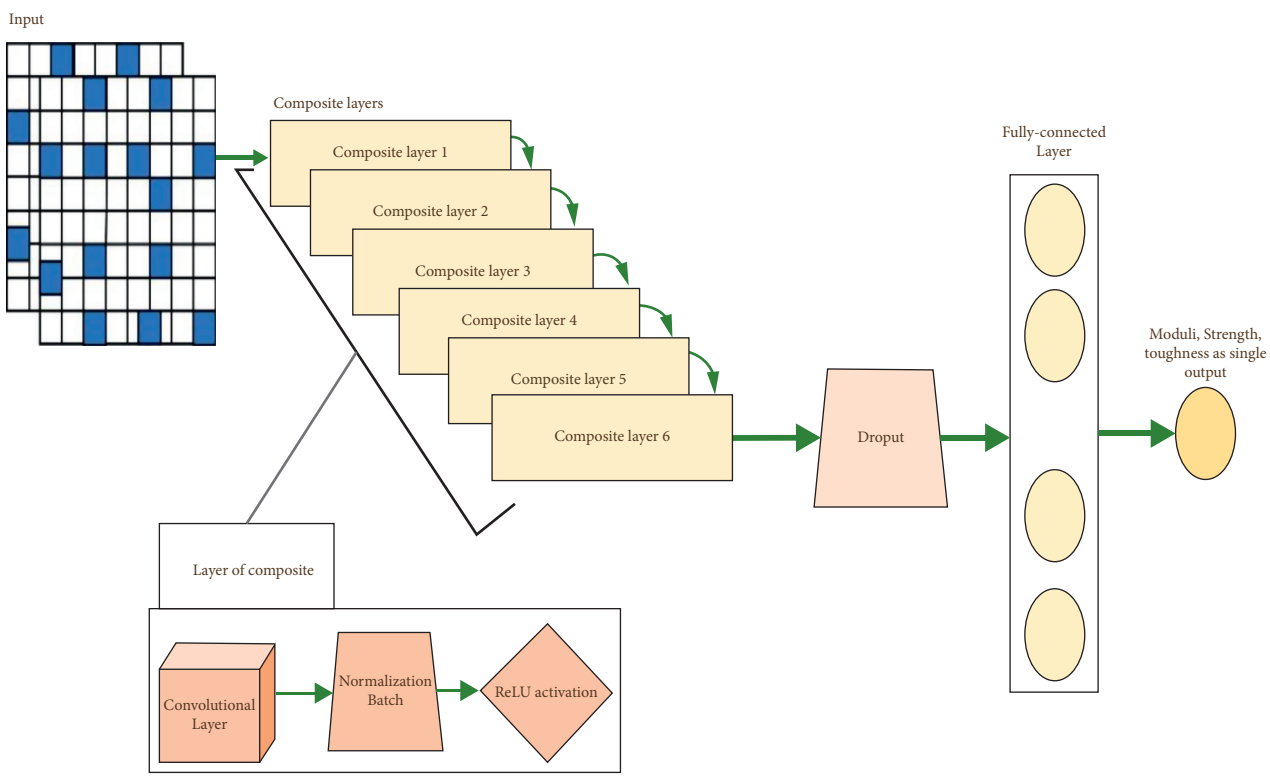

Figure 7: Schematic diagram of CNN model.

$$\mathrm{MSE} = \frac{1}{a}\sum_{n=1}^{a}\left(k_n - \hat{k}_n\right)^2, \tag{9}$$

$$\mathrm{MAPE} = \frac{1}{a}\sum_{n=1}^{a}\left|\frac{k_n - \hat{k}_n}{k_n}\right|, \tag{10}$$

where $\hat{k}_n$ is the prediction found based on the model and k_n is the real value.

3.8. Genetic Algorithm for Optimization. The various bio-inspired operators such as crossover, mutation, and selection are frequently used in GA optimizers to obtain the optimal

solutions. The GA optimizer selects random individuals from the last generation as parents generating offspring for subsequent generations through each optimization process [29]. The roulette wheel mechanism is utilized as the selection operator, with greater fitness values yielding a larger selection probability. The frequency of the optimal solution in an optimization system is called fitness.

A genetic algorithm is a type of computer-based research and optimization algorithm that depends on natural genetics and natural selection mechanics. Other conventional optimization methods are less likely to provide optimal global coverage than the GA. The reason for this is that GA is based on probabilistic criteria and research based on a population of the points in inherited space. Traditional optimization strategies are usually based on deterministic research which uses the idea of the gradient to localize local optima. Each genetic operation cycle is referred to as a developing process. The fitness of every member of the population was assessed in each generation and subsequent generations were formed using the chromosomes of the current population. This entails the mixing and recombination of genes from both parents to produce offspring in the following generation. Reproduction, mutation, and crossover are all parts of the evolution process. The optimization problem as is follows:

$$a_i^{(U)} \leq a_i \leq a_i^{(V)},\ a_i = p_1, p_2. \tag{11}$$

a_i are decoded with this linear mapping rule:

$$a_i = a_i^{(U)} + \frac{\left(a_i^{(V)} - a_i^{(U)}\right)}{2^{ui-1}}\ \textit{is decoded value}\ (t_i), \tag{12}$$

where $a_i = p_1,\ p_2$; (U) = minimum limitation; (V) = maximum limitation; ui = binary bit count; and t_i = equivalent of decimal values.

A chromosome relates to some microstructures that store the material around it to form a specific microstructure element. A uniform distribution is used to choose the first generation at random. The suitability of a microstructure is determined independently of the break of the generational chromosomes. The technique for using the genetic algorithm is shown in Figure 8.

4. Results and Discussion

The efficiency of the linear model is associated with the CNN model. To develop a linear model quantitatively based on the composite properties, the equation in the linear model is given as follows:

$$M = XC + Y, \tag{13}$$

where M is the property of the material and C is the material distribution of the compounds in vector form. X and Y are determined as weights, and X and Y weights are regulated by the training process to suit every physical property. Since composite gratings are of 8×8 and 16×16 sizes, they standardize for every model for all 3 properties of fiber material. The determination of the resulting coefficient (D^2) for the adjusted line is 0.916. Then, the mean absolute error ratio represents the limitations and generalization issues by the linear model; then, the modulus exceeds the mean absolute error percentage (25%), and the toughness and strength are as high as 200% and 40%. As 16×16 grid size, the outcomes of the linear model are determination coefficient (D^2) of 0.928; then, the values of MAPE are maximum with 21%, 32%, and 127% for modulus, strength, and toughness. High error standards are generated from the linear model to explain the CNN for the prediction problem. Figure 9 and 10 show that the ranked weights are determined by the dark color near to the tip crack, the light color is determined by the straight one at the crack tip as positive of soft fiber materials, and then colorless materials are determined by the negative as stiff fiber materials. These composite mechanical properties have high accuracy.

The CNN is used in signal processing and recognition of images and is also utilized to extract geographies from datasets. Before the inference process, CNN models must be developed. The training process is a problem of optimization; then, the MSE is minimalized by the optimal collection of the weight of the model CNN. To begin the training process, it required many examples of dataset; then, the input and output data determine the approximate relationship by optimal mapping. Then, the CNN model uses 200 training periods; it is an iteration of the CNN model training process. A single epoch is concluded when on each training the CNN model is trained with examples in the dataset. The 200 epochs are used meeting the CNN model on each example of training of about 200 times of the set of training data. Figures 11 and 12 show the loss functions of test convergence history and drive for 8×8 and 16×16 grids. The loss function of MSE of all mechanical properties for two sizes of the grid converges with very low standards. The variance between test and training sufferers after the 200 epochs is small and there is no serious overflow occurring. The CNN model developed and produced the best problematic results and predicted the three properties of fiber materials with great precision.

After the process of training, estimate the CNN model performance using the 3 parameters, the mean absolute error ratio, data points percentage, and maximum error with an error maximum of 5%. These parameters are measured by testing the data set that is nongenerated by the CNN during the process of model creation. The performance of the CNN model is illustrated in Tables 2 and 3. Resistance, toughness, and MAPE modulus are less than 5%. A stronger limit for estimating the activity of the CNN is the extreme error. The extreme strength and error in the module are greater than 5%. But the data points' number larger than 5% error is meager, 8×8 grid has 1.7%, and 16×16 has 0.082%.

4.1. Shielding Performance. The EMI samples results A2, A3, A2H11, and A3H12 in a range of 10 GHz are compared and examined as given in Figure 13. The EMI shielding was intensely improved after the A1 sheets are presented because of the good shielding property. The EMI samples A2, A3, A2H11, and A3H12 are 1.0–4.8 dB, 1.4–6.3 dB, 30.7–46.8 dB, and 28.5–53.5 dB as in

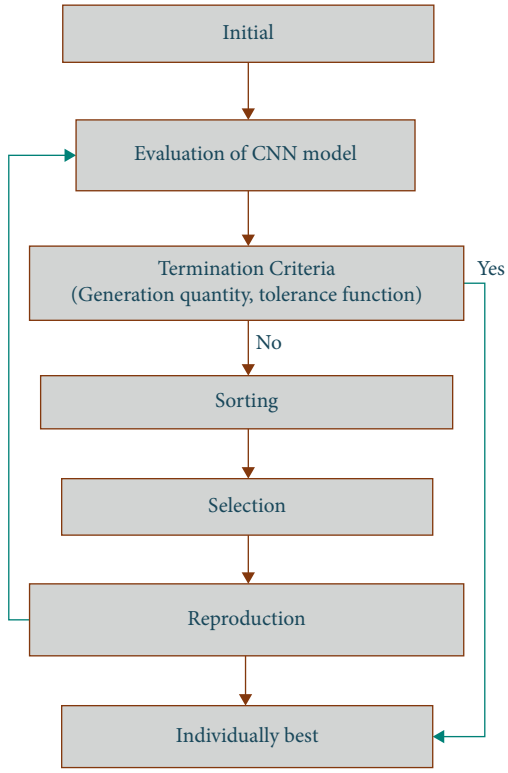

Figure 8: Flowchart of genetic algorithm process.

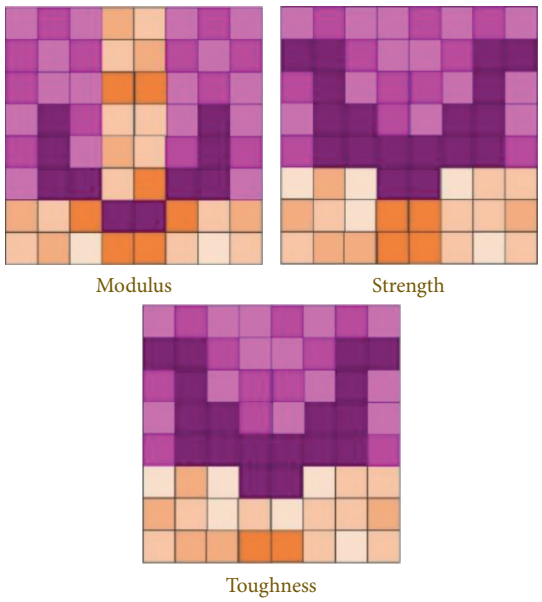

Figure 9: 8×8 grid weights ranking.

Figure 13(a). Comparing the control samples, EMI shielding improves the samples A2H11, and A3H12 are important. The samples EMI shielding performance A2H11 and A3H12 are on the needed values of EMI shielding in applications. Figure 13(b) represents the reflection in EMI of A2, A3, A2H11, and A3H12 composites which were 10.1–17.3%, 17.0–29.8%, 52.6–79.4%, 56.0–80.6%. The EMI shielding values from the absorption and multiple-reflection of the composites were 82.7%–89.9%, 70.2%–83.0%, 20.6–47.4%, and 19.4–44.0%, Figure 13(c). The natural fiber composites have low EMI, while the composites with A1 sheets presented much more reflection. The EMI reflections of A2H11 and A1H12 minimized the A1 sheet measured as 83.7–93.9%. During the reflection and incidence, materials absorb EMI waves; it will reduce the shielding efficiency.

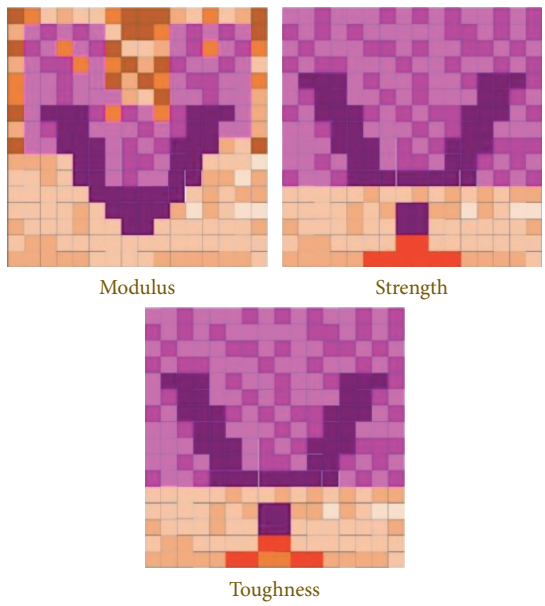

Figure 10: 16 × 16 weights ranking.

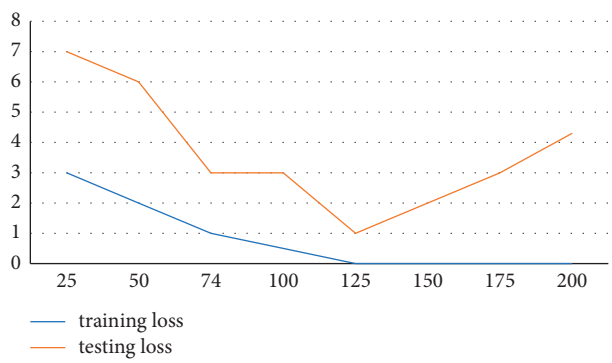

Figure 11: The convergence loss function history of the 8 × 8 grid.

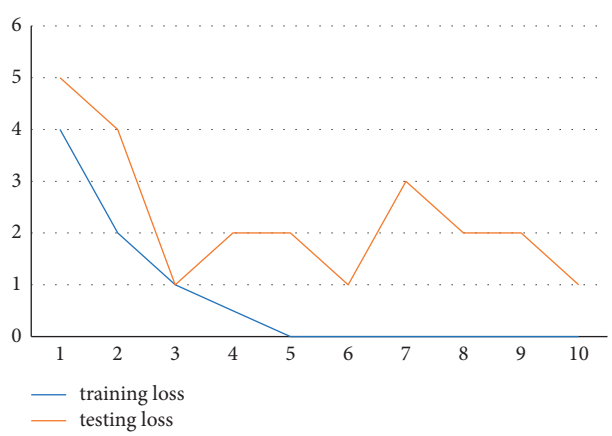

Figure 12: The convergence loss function history of the 16 × 16 grid.

4.2. GA Optimizer. The genetic algorithm optimization method is applied to optimize the maximal tensile strength function with GA. The strains receive the output value of the best tensile strength, the bending strength. The maximum impact force and results were gained during the repetition in the GA method.

Table 2: CNN model performance for 8×8 grid.

	MAPE (%)	Max error (%)	Data points with error % > 5 (%)
Modulus	0.6	0.7	0.0
Strength	0.2	0.4	0.0
Toughness	0.8	38.8	1.7

Table 3: CNN model performance for 16×16 grid.

	MAPE (%)	Max error (%)	Data points with error % >5 (%)
Modulus	0.2	2.4	0.0
Strength	0.4	2.1	0.0
Toughness	2.4	188.7	0.082

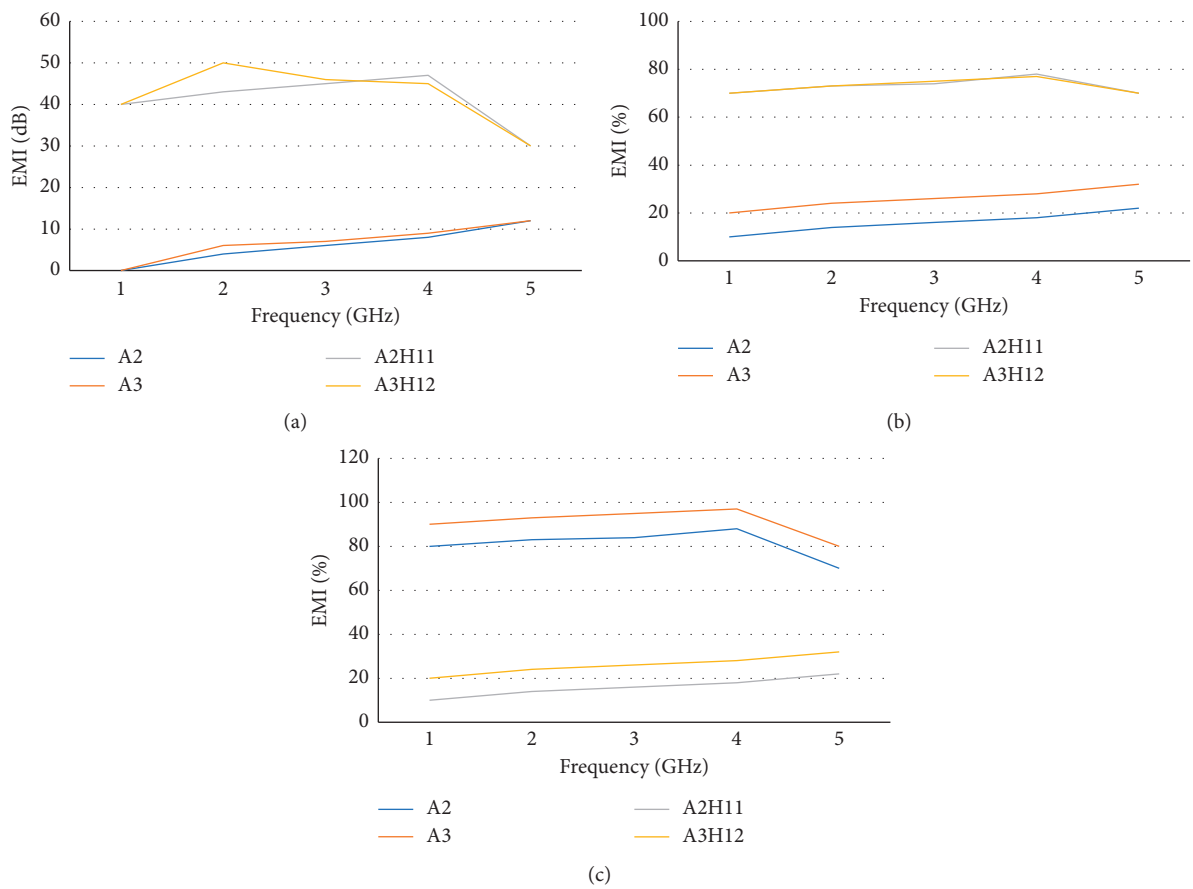

Figure 13: The shielding effectiveness of electromagnetic interference of the A2, A3, A3H11, and A2H12 composites. (a) Reflection contribution, (b) absorption, and (c) shielding efficiency.

Figure 14 shows the mathematical model and GA accuracy. The experimental and expected values were derived from the GA mathematical model:

$$\text{error}(\%) = 100 * \frac{(\text{expected} - \text{experimental})}{\text{predicted}}. \quad (14)$$

The combination of simultaneous optimization has four possibilities: (a) the strength and the module, (b) the toughness and the module, (c) the toughness and the strength, and (d) the toughness of the module and the strength. The objective aggregate function (AOF), which combines the various objects into the scalar function,

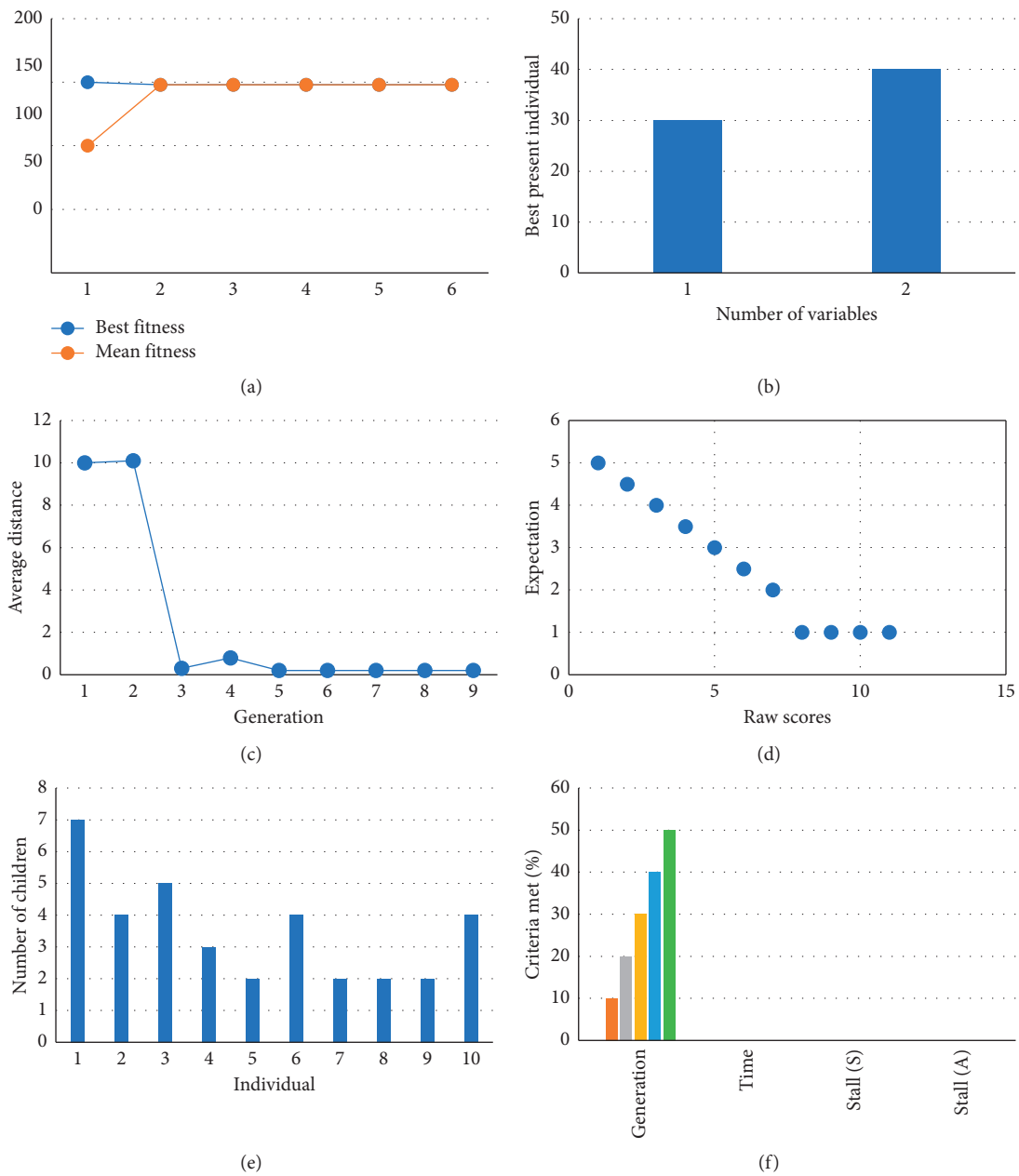

Figure 14: GA optimization method. (a) Best and mean fitness. (b) Present best individual. (c) Average distance between individuals. (d) Scaling fitness. (e) Selection function. (f) Stopping criteria.

depends on the simple biased objective amount that works poorly in the nonvexatious case. One solution is used for programming compromise:

$$\mathrm{AOF} = E_m t_m^x + E_s t_s^x + E_t t_t^x, \tag{15}$$

$$T_m = \frac{\text{modulus}}{\text{maximum modulus}}, \quad T_s = \frac{\text{strength}}{\text{maximum strength}}, \quad T_t = \frac{\text{toughness}}{\text{maximum toughness}}, \tag{16}$$

where x is the objective exponent function, and it is selected to be $x = 4$. Then E_m, E_s, and E_t are the masses of modulus, strength, and toughness. When optimizing two properties, the weight matching to the properties and then optimized for the assigned value is 0.5. Then the third property of the attributed weight value is 0.0. For three properties, the value of each of the three weightings is 0.333. In addition, the various goals have various scales which can cause bias to higher values of the goals. This issue is determined by each normalizing target by its maximum value as shown in (16).

Figure 15 and Table 4 show the outcome result derived from the optimizer GA when the multiobjective is measured with the checkerboard material. From the optimization of

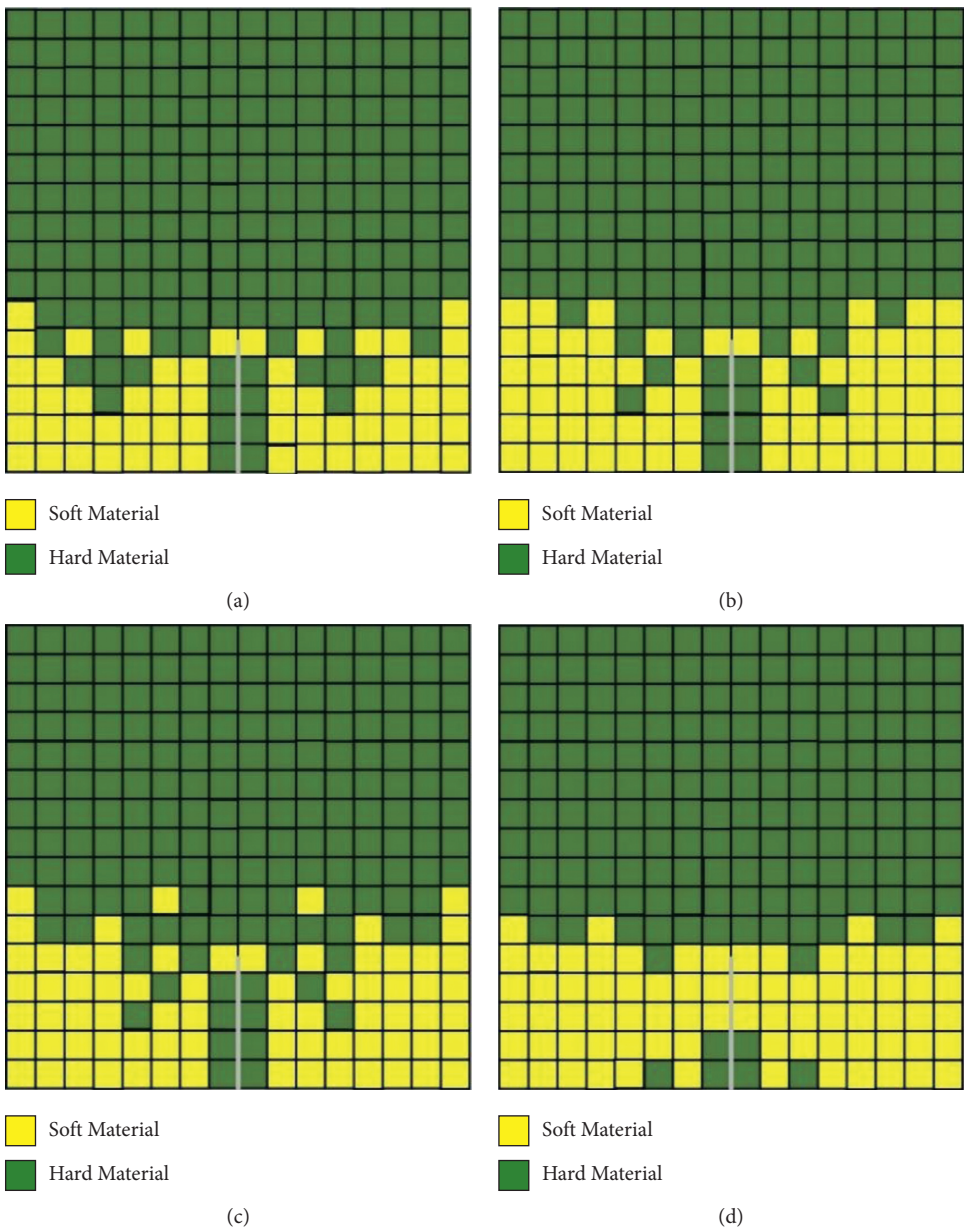

Figure 15: Optimization of multiobjective using GA method.

Table 4: Results of optimization using GA.

Output	Strength and modulus	Toughness and modulus	Toughness and strength	Modulus, strength, and toughness
The fractional volume of soft material (%)	23.4	27.3	28.1	32.8
T_s	0.99	0.99	0.99	0.97
T_m	0.84	0.81	0.79	0.76
T_t	0.86	0.94	0.94	0.97

single-objective, the material is not soft, so the modulus is maximum. But when optimizing toughness or strength in addition to the module, the optimizer allows for equilibrium of the various purposes. The modulus determined from optimization of multiobjective is importantly minimized due to the soft materials, and the soft fiber material volume segment ranges from 23% to 33% depending on the materials that are optimized. Then, the configuration of strength high values and the toughness of fiber materials have a good synchronization. The optimizer inclines to

bundle the flexible fiber material at the location next to the tip of the crack. Therefore, less compromise is required.

5. Conclusion

An approach to analyze the mechanical properties of natural fiber composites for modeling and optimization methods was developed, such as RoHM, CNN, and GA methods to improve properties and usage. The techniques for application modeling in NFC allowing to identify and isolate the various parameters that have an important effect on the outcoming materials are carried out to the optimization. The convolution neural network (CNN) is established to predict the mechanical properties of NFC composites by considering the checkboard of two sizes of 8×8 and 16×16 gird. The grid model is used to determine the module, strength, and tenacity of the material. It has shown the potential for using CNN in hardware and structural study. The composites represent the shielding performance of EMI with better mechanical properties as the structure of EMI shielding materials. The development of the model CNN is combined with a GA optimizer to find the fraction of volume of the composite material configuration to enhance performance. The optimization of GA results from the mechanical property of fiber length and content. There is better agreement between values of experimental and predicted values. CNN models take the accelerating potential of present optimization methods, and they develop the field of material and structural design.

Data Availability

The data used to support the findings of this study are included within the article.

Conflicts of Interest

The authors declare that there are no conflicts of interest regarding the publication of this article.

Acknowledgments

The authors would like to express their gratitude towards Saveetha School of Engineering, Saveetha Institute of Medical and Technical Sciences (formerly known as Saveetha University), for providing the necessary infrastructure to carry out this work successfully.

References

[1] R. Anandkumar, S. Ramesh Babu, and R. Sathyamurthy, "Investigations on the mechanical properties of natural fiber granulated composite using hybrid additive manufacturing: a novel approach," *Advances in Materials Science and Engineering*, vol. 2021, pp. 1–12, 2021.

[2] S. Velumani, P. Navaneetha Krishnan, and S. Jayabal, "Mathematical modeling and optimization of mechanical properties of short coir fiber-reinforced vinyl ester composite using genetic algorithm method," *Mechanics of Advanced Materials and Structures*, vol. 21, no. 7, pp. 559–565, 2014.

[3] S. Ferdous and S. Hossain, "Natural fibre composite (NFC): new gateway for jute, kenaf and allied fibres in automobiles and infrastructure sector," *World J Res Rev*, vol. 5, no. 3, pp. 35–42, 2017.

[4] K. Salasinska and J. Ryszkowska, "The effect of filler chemical constitution and morphological properties on the mechanical properties of natural fiber composites," *Composite Interfaces*, vol. 22, no. 1, pp. 39–50, 2015.

[5] M. Alhijazi, Q. Zeeshan, Z. Qin, B. Safaei, and M. Asmael, "Finite element analysis of natural fibers composites: a review," *Nanotechnology Reviews*, vol. 9, no. 1, pp. 853–875, 2020.

[6] S. Mahesh and D. G. Ramkumar, "Smart face detection and recognition in low resolution images using alexnet CNN compare accuracy with SVM," *Alinteri Journal of Agriculture Sciences*, vol. 36, no. 1, pp. 721–726, 2021.

[7] G. Ramkumar, G. Anitha, S. Suresh kumar, M. Ayyadurai, and C. SenthilKumar, "An effectual underwater image enhancement using deep learning algorithm," in *Proceedings of 2021 5th International Conference on Intelligent Computing and Control Systems (ICICCS)*, vol. 2021, 2021.

[8] Dr Govindaraj, "Face recognition based on spatio angular using visual geometric group- 19 convolutional neural network," *Annals of the Romanian Society for Cell Biology*, vol. 25, pp. 2131–2138, 2021.

[9] Y. S. Munde and R. B. Ingle, "Theoretical modeling and experimental verification of mechanical properties of natural fiber reinforced thermoplastics," *Procedia Technology*, vol. 19, pp. 320–326, 2015.

[10] R. de Araujo Alves Lima, D. Kawasaki Cavalcanti, J. de Souza e Silva Neto et al., "Effect of Surface Treatments on Interfacial Properties of Natural Intralaminar Hybrid Composites," *Polymer Composites*, vol. 41, no. 1, pp. 314–325, 2020.

[11] V. Sridharan and N. Muthukrishnan, "Optimization of machinability of polyester/modified jute fabric composite using Grey relational analysis (GRA)," *Procedia Engineering*, vol. 64, pp. 1003–1012, 2013.

[12] N. Sultana, S. M. Zakir Hossain, and M. S. Alam, M. S. Islam, M. S. Islam, and M. A. A. Abtah, "Soft computing approaches for comparative prediction of the mechanical properties of jute fiber reinforced concrete," *Advances in Engineering Software*, vol. 149, no. November, Article ID 102887, 2020.

[13] Z. L. Wang, J. Wu, and J. G. Wang, "Experimental and numerical analysis on effect of fibre aspect ratio on mechanical properties of SRFC," *Construction and Building Materials*, vol. 24, no. 4, pp. 559–565, 2010.

[14] M. S. Islam, N. A. B. Hasbullah, M. Hasan, Z. A. Talib, M. Jawaid, and M. K. M. Haafiz, "Physical, mechanical and biodegradable properties of kenaf/coir hybrid fiber reinforced polymer nanocomposites," *Materials Today Communications*, vol. 4, pp. 69–76, 2015.

[15] L. Kerni, S. Singh, A. Patnaik, and N. Kumar, "A review on natural fiber reinforced composites," *Materials Today: Proceedings*, vol. 28, pp. 1616–1621, 2020.

[16] K. L. Pickering, M. G. A. Efendy, and T. M. Le, "A review of recent developments in natural fibre composites and their mechanical performance," *Composites Part A: Applied Science and Manufacturing*, vol. 83, pp. 98–112, 2016.

[17] D. K. K. Cavalcanti, M. D. Banea, J. S. S. Neto, R. A. A. Lima, L. F. M. Da Silva, and R. J. C. Carbas, "Mechanical characterization of intralaminar natural fibre-reinforced hybrid composites," *Composites Part B: Engineering*, vol. 175, Article ID 107149, 2019.

[18] A. Subasinghe, R. Das, and D. Bhattacharyya, "Study of thermal, flammability and mechanical properties of intumescent flame retardant PP/kenaf nanocomposites," *International Journal of Social Network Mining*, vol. 7, no. 3, pp. 202–220, 2016.

[19] A. Pappu, K. L. Pickering, and V. K. Thakur, "Manufacturing and characterization of sustainable hybrid composites using sisal and hemp fibres as reinforcement of poly (lactic acid) via injection moulding," *Industrial Crops and Products*, vol. 137, pp. 260–269, 2019.

[20] M. Boopalan, M. Niranjanaa, and M. J. Umapathy, "Study on the mechanical properties and thermal properties of jute and banana fiber reinforced epoxy hybrid composites," *Composites Part B: Engineering*, vol. 51, pp. 54–57, 2013.

[21] K. P. Ashik and R. S. Sharma, "A review on mechanical properties of natural fiber reinforced hybrid polymer composites," *Journal of Minerals and Materials Characterization and Engineering*, no. 5, pp. 420–426, 2015.

[22] N. Venkateshwaran, A. Elayaperumal, and G. K. Sathiya, "Prediction of tensile properties of hybrid-natural fiber composites," *Composites Part B: Engineering*, vol. 43, no. 2, pp. 793–796, 2012.

[23] G. Arani, H. B. Ali, Z. Akbar, and E. Haghparast, "Application of halpin-tsai method in modelling and size-dependent vibration analysis of CNTs/fiber/polymer composite microplates," *Journal of Computational and Applied Mechanics*, vol. 47, no. 1, pp. 45–52, 2016.

[24] S. S. Shinde, A. V. Salve, and S. Kulkarni, "Theoretical modeling of mechanical properties of woven jutefiber reinforced polyurethanecomposites," *Materials Today: Proceedings*, vol. 4, no. 2, pp. 1683–1690, 2017.

[25] G. Ramkumar, R. Thandaiah Prabu, N. Phalguni Singh, and U. Maheswaran, "Experimental analysis of brain tumor detection system using Machine learning approach," *Materials Today: Proceedings*, 2021, In press.

[26] Y.-W. Jung and H.-K. Kim, "Prediction of nonlinear stiffness of automotive bushings by artificial neural network models trained by data from finite element analysis," *International Journal of Automotive Technology*, vol. 21, no. 6, pp. 1539–1551, 2020.

[27] S. Ye, B. Li, Q. Li, H.-P. Zhao, and X.-Q. Feng, "Deep neural network method for predicting the mechanical properties of composites," *Applied Physics Letters*, vol. 115, no. 16, Article ID 161901, 2019.

[28] G. Ramkumar and E. Logashanmugam, "Hybrid framework for detection of human face based on haar-like feature," *International Journal of Engineering & Technology*, vol. 7, no. 3, pp. 1786–1790, 2018.

[29] A. Jaramillo-Botero, S. Naserifar, and W. A. Goddard III, "General multiobjective force field optimization framework, with application to reactive force fields for silicon carbide," *Journal of Chemical Theory and Computation*, vol. 10, no. 4, pp. 1426–1439, 2014.

Hindawi
Advances in Materials Science and Engineering
Volume 2021, Article ID 8122989, 12 pages
https://doi.org/10.1155/2021/8122989

Research Article

A Combination of Coconut Fiber Suture and Tamarind Seed Gel with Dehydrated Human Amnion Membrane for Wound Surgery in Rats

Raghu Babu Pothireddy,[1] Angeline Julius,[2] Manu Thomas Mathai,[1] Ganesh Lakshmanan,[3] and Beimnet Asfaw Hailemariam[4]

[1]*Department of Zoology, Madras Christian College, Affiliated to University of Madras, Chennai 600059, Tamil Nadu, India*
[2]*Centre for Materials Engineering and Regenerative Medicine, Bharath Institute of Higher Education and Research, Chennai 600126, Tamil Nadu, India*
[3]*Department of Anatomy, Asan Memorial Dental College and Hospital, Chennai 603105, Tamil Nadu, India*
[4]*Institute of Biotechnology, Addis Ababa University, Addis Ababa, Ethiopia*

Correspondence should be addressed to Raghu Babu Pothireddy; raghubabu_84@yahoo.com and Beimnet Asfaw Hailemariam; beimnet.asfaw@aau.edu.et

Received 8 July 2021; Accepted 10 August 2021; Published 19 August 2021

Academic Editor: Ravichandran M

Today, there are over 2,000 different biomaterials used for various medical applications, but none of these biomaterials are 100% compatible with all human beings. Coconut fiber is widely available but has not been tested as a safe natural alternative for sutures. Immature coconut fiber is nonabsorbable and is effective for cuts and open wounds when used in combination with dehydrated human amnion membrane (dHAM). Immature coconut fiber, tamarind seed polysaccharide (TSP), and dHAM were prepared to test their combinational effect on wound healing in rats. TSP enhanced cell viability, proliferation, and migration in human skin cells and cured wounds both individually and in combination with dHAM. An antibiotic-free combination of the human amniotic membrane with intact epithelium, tamarind seed polysaccharide, and immature coconut fiber provided faster wound healing. Significantly higher wound healing was seen on the 11th day based on an initial 10 mm biopsy punch surgery in Wistar rats compared to control groups. Histological studies revealed thickened dermis edges with more neutrophil infiltration. Collagen deposition in the dermis was homogeneous across the excised skin tissue in the test group, again attesting to the utility of this procedure. This research signifies the use of TSP gel together with the amnion membrane representing a "smart patch" with wound healing potential, which would encourage further research on the smart patch made using a combination of plant and animal biological materials.

1. Introduction

Wound healing is a natural and complex process of tissue recovery of injured tissues involving growth factors and cytokines, released at the injured site. Delayed or impaired wound healing may occur due to several reasons like chronic medical conditions and medications that inhibit the healing process [1]. Medicinal plants with wound healing properties have been used to treat acute and chronic wounds for the past three decades [2, 3]. Among the world population, 70 to 80% depend on medicinal plants for the management of various ailments since ancient time [3]. Wound dressings made of pectin and collagen enhance wound healing but are highly expensive [4]. Identification of potent and effective natural compounds for wound healing would benefit in the management of wounds in a cost-effective manner.

The present research relates to the use of plant materials and biological membrane together as biocompatible biomaterials for wound healing. Coconut fibers are available plenty in India and are used for different purposes. The scope of this research is to come up with this novel use of immature coconut fiber along with other novel combinations of

biomaterials for cut and open wound healing studies. Coconut fiber of green coconuts is immature and tough because of the presence of lignin [5] and the presence of biodegradable hemicellulose and cellulose that contribute to wound healing [6, 7]. The coconut fiber material has never been thought of as a suture, nor has been used as a cheaper, safer, economically viable, and easily available suture material to date. This green, alternative, nonabsorbable suture (Indian Patent no. 298076) is effective when compared with commercial nonabsorbable sutures such as prolene, silk, and nylon.

Xyloglucans of *Tamarindus indica L.* have been currently explored for its property of wound healing, individually or in combination to heal wounds by enhancing cell viability, proliferation, and migration in human skin keratinocytes [8]. Xyloglucans are polysaccharides, which are the main constituents of the tamarind seed kernel and are rich in xylose and galactoxylose substituents. Due to their mechanical properties, they have a wide application in hydrogel production, films, and as drug delivery agents for slow drug delivery [9]. Xyloglucan is abundantly found in plant cell walls, contains ($\beta 1 \longrightarrow 4$)-linked d-glucan substituted with xylose, possesses mucoadhesive properties mainly due to the mucin-like structure, and belongs to the group of polysaccharides, referred to as hemicelluloses [10]. The mucoadhesive property of xyloglucan has permitted its use as an adhesive with antimicrobial property to prevent bacterial adherence and invasion [11]. Xyloglucans when introduced into nanofibrillated cellulose (NFC) through adsorption and presorption to strengthen the NFC revealed highest adsorption, reinforcement, enhancement of cell growth, and proliferation for wound healing [12].

Hemicellulose films have proved to be haemostatic, absorptive, and bactericidal and have shown effective epithelial wound healing in leukaemia patients with herpes zoster infections [13]. A natural hydrogel from honey in combination with polyvinyl pyrrolidone, polyethylene glycol, and agar solution showed a significant wound healing effect compared to the control groups. The hydrogel demonstrated histopathologically confirmed reduction in wound size and has been recommended for burn injuries due to a high fluid absorption rate [14]. Furthermore, a porous hydrogel (size: 32.8–101.6 μm) from a mixture of chitosan and xyloglucan with good mechanical properties has enhanced the properties of chitosan with the addition of xyloglucan, without affecting its antimicrobial activity for wound dressing [15]. Since xyloglucans have shown positive effects on wound healing [16], hydrogels of xyloglucans could exhibit wound healing action and also act as a vector for slow drug delivery to aid healing. This work focuses on extraction, identification of polysaccharide consisting of xyloglucan from the kernel of tamarind, preparation of the wound gel by crosslinking with epichlorohydrin, and providing a platform for the intervention of efficacious and cost-effective wound healing agent.

The human amniotic membrane (HAM) has been proved to be an excellent source of material for wound therapy [17], since it induces reepithelialization meanwhile processing antiangiogenic and antimicrobial properties. The human amniotic membrane (HAM) lacks immunogenicity and acts as a substrate for growth, adhesion, and migration [18]. The wound healing ability of HAM accounts for the presence of growth factors such as EGF, KGF, and HGF to aid wound healing [19]. The three biomaterials used for the study are biowastes, which were used positively for wound healing, and this research could cause a great impact on the identification of novel biomaterials that could work in combination to provide high healing efficiency.

This study employs plant and animal biomaterials to treat cut and open wounds. Figure 1 illustrates the preparation of immature coconut fiber, tamarind seed polysaccharide, and dehydrated human amnion membrane (dHAM) to test wound healing in rats. The use of plant and human tissue combinations for wound healing and management had made this research novel in its attribute that has not been performed or reported before.

2. Materials and Methods

2.1. Preparation and Evaluation of Physical Parameters of Immature Coconut Fiber

2.1.1. Preparation of Immature Coconut Fiber Suture. The fiber of green coconuts was removed from the shell of the nut and was soaked in water for 24 to 48 hours to allow the fiber to be separated into strands. The fiber strands are then soaked into 70% isopropyl alcohol for decolourization for 5 hours and dried in a hot air oven between 40 and 50°C for 1 hour.

2.1.2. Determination of Tensile Strength of Coconut Fiber Using Universal Testing Machine (UTM). The thickness of each fiber was measured (in diameter) using a dial thickness gauge. The average diameter of the fibers ($n = 3$) was noted to determine the tensile strength. Each fiber was inserted into the universal testing machine and ensured that the ends were gripped symmetrically so that the tension force was distributed uniformly over the cross section. The load cell value was set to zero, and the speed of the moving grip was 10 mm/min. Changes in the test length were noted throughout the test and were continued until the break of the test sample. Three samples of thin and thick immature coconut fibers were taken in comparison with prolene and silk sutures [20].

2.1.3. Skin Holding Effect of Coconut Fiber, Prolene, and Silk Sutures in Rats. Sprague Dawley (SD) rats (14 numbers) were used for the study, and they were anesthetized with ketamine and xylazine and acclimatized for 7 days. Animals were randomly divided into two groups, with 7 animals in each group. Group 1 was tested with thin coconut fiber in comparison with the prolene suture. Group 2 was tested with thick coconut fiber in comparison with silk suture.

Two 3.5 cm long parallel full-thickness skin incisions were made under aseptic conditions on the back of the experimental rat. The incisions were closed immediately by 4 simple sutures (Figure 2). Rats were sacrificed by carbon dioxide inhalation. The skin wounds were removed from the

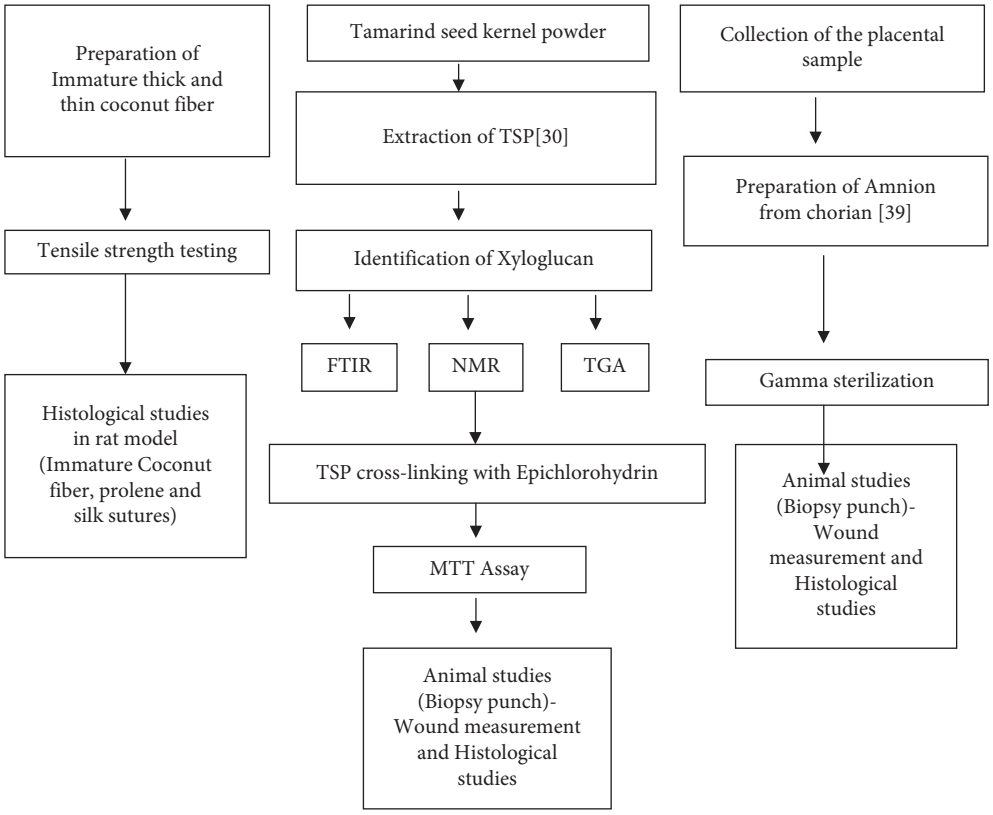

Figure 1: Combination therapy for cut and open wounds. TSP: tamarind seed polysaccharide; FTIR: Fourier-transform infrared spectroscopy; NMR: nuclear magnetic resonance; TGA: thermogravimetric analysis; MTT: 3-(4,5-dimethylthiazol-2-yl)-2,5-diphenyltetrazolium bromide.

Figure 2: SD rat sutured with immature coconut fiber and silk suture.

body after 24, 48, 72, 96, 120, 144, and 168 h ($n = 1$/group/time point). Histopathological analyses were performed using hematoxylin-eosin, Azur, PAS, and van Gieson stained slides.

2.2. TSP Gel Wound Healing Ability in Wistar Rats. Male Wistar albino rats (90 days old) weighing around 200 g to 250 g were used for the study. The animals ($n = 3$) were fed with standard laboratory diet in the pellet form, and the rats had access to drinking water and libitum. Under intramuscular injections of a combination of ketamine (40 mg/kg body weight (b.w) and xylazine (15 mg/kg b.w), the dorsal aspect of the rats was shaved. An excision punch biopsy was done passing through both sides of the lifted midline, achieving two 8 mm diameter excision wound side by side to its spine below the neck region in the dorsal aspect [21, 22]. One side of the excision was treated with the prepared TSP gel (approximately 0.25 ml of thawed gel twice daily for 5 days) and the other side was not treated (control).

Postcreation of the wound, the animals were given a broad-spectrum antibiotic, amoxicillin (0.001 mL/kg b.w, intramuscularly, single dose), and anti-inflammatory/analgesic agent, piroxicam (3 mg/kg b.w, intramuscularly daily for 3 days), and monitored for any signs of active infection for the first two days. At the end of the study period (after 7 days), the animals were euthanized using a gas chamber filled with isofluorane fumes. The wound area with the surrounding tissue was excised to its full depth and fixed in 10% neutral buffered formalin and processed for routine histopathology.

2.3. Combined Wound Surgery with the Prepared Biomaterials in the Rat Model. The wound was created using a 10 mm biopsy punch on animals used for the study. One of the excised wounds was treated with the prepared biomaterials (application of approximately 0.25 ml TSP gel on wound area with dHAM placed on top and sutured with immature coconut fiber). Another excision wound was untreated (control) in Wistar rats of group 1 ($n = 3$). Similarly, one excised wound of group 2 animals ($n = 3$) was treated with TSP gel, applied on the surface of the wound area (approximately 0.25 ml) with dHAM placed on top and sutured

with immature coconut fiber. The other wound incision was treated with the commercial silicone gel membrane and sutured with the commercial silk suture.

Postcreation of the wound, the animals were given a broad-spectrum antibiotic, amoxicillin (0.001 mL/kg b.w, intramuscularly, single dose), and anti-inflammatory/analgesic agent, piroxicam (3 mg/kgb.w, intramuscularly daily for 3 days), and monitored for any signs of active infection for the first two days. At the end of the study period (after 11 days), the animals were euthanized using a gas chamber filled with isofluorane fumes. The wound area with the surrounding tissue was excised to its full depth and fixed in 10% neutral buffered formalin and processed for routine histopathological examinations.

3. Results and Discussion

3.1. Analysis of Immature Coconut Fiber

3.1.1. Mechanical Testing of Immature Coconut Fiber. The tensile strength of the immature coconut fiber was tested using the universal testing machine (UTM).Table 1 lists the parameters for tensile strength estimation.

3.1.2. Histopathological Examination of Sutures in Wistar Rats. The skin sections from all the groups revealed spurs of epithelial cell migration towards the wound edges in the epidermal layer and acute neutrophilic infiltration in the dermis and presence of necrotic myofibers of the injured skeletal muscles in the deepest part of the wounds from day 1 to day 3 with similar severity grades.

On days 4 to 6, the epithelial cell proliferation resulted in a thickened epidermal layer. While in the dermis, neutrophilic infiltrations were largely replaced by macrophages along with the formation and invasion of granulation tissue. Maximal neovascularization and collagen production were observed in all three sutured skin samples.

On day 7, the epidermal layer recovered its normal thickness (re-epithelialization) and differentiation with self-keratinisation for the immature coconut fiber treated groups equal to the silk and prolene treated groups. The dermal layer revealed the remodelling phase with the presence of diffused and organized collagen fibers with granulation tissue formation (Figures 3–6).

3.2. TSP Gel Wound Healing Ability in Wistar Rats. TSP gel application on an 8 mm wound on the right side of the animals ($n = 3$) resulted in gradual wound reduction compared to the nontreated control. The wound site measurement of the control and the treated on the 7th day reveal exceptional wound healing property of TSP. The treated site had its size reduced to 3.5 mm (±0.13) on an average, while the nontreated control had a wound size of 6.5 mm (±0.22), which is almost double the size of the TSP treated site, revealing the wound healing ability of TSP. Difference between the two groups was tested using the students t-test and was found to be statistically significant ($p < 0.001$), revealing the wound healing ability of TSP (Figure 7).

3.3. Histological Investigation. The epidermis of the control animals was thickened at its cut edges. The dermis close to the excision area showed rich polymorph nuclear infiltration. A demarcation line was formed, which separated the necrotic slough tissue from viable tissue. Mild fibroblast proliferation was noted in the dermis region beneath the wound. Neovascularisation in the form of capillary blood vessel formation was noted. However, new collagen formation was minimally seen (Figure 8(a)).

In TSP gel treated animals, the wound edges are approximated and the dermis edges are thickened with more polymorph nuclear infiltration. Fibroblast proliferation is well noted with collagen deposition noted along the wound area. New blood vessel formation was well marked (Figure 8(b)).

3.4. Combination Therapy Involving Natural Biomaterials for Wound Management. Group I animals ($n = 3$), 10 mm wounds, sutured with immature coconut fiber with prepared dHAM and TSP gel in combination, had better healing after 11 days. Profound wound reduction was observed in the treated wound area with a measurement of 2 mm (±0.10), differing much with the nontreated control measuring 6 mm (±0.10) (Figure 9(c)) Difference between the two groups was tested using the Student t-test and was found to be statistically significant ($p < 0.001$). Following the study, the animals were euthanized, and the wound area was processed for histopathological examinations.

Group II animals ($n = 3$) with 10 mm wound excisions treated with dHAM, TSP gel, and immature coconut fiber (Figure 10(a)) were compared with 10 mm wound excisions, treated with silicone gel membrane and silk suture as the positive control. Wound measuring 1.5 mm (±0.17) at the test site (dHAM + TSP gel + coconut fiber) in comparison with the positive control (silicone gel membrane + Silk suture) after 11 days of treatment reveal the wound healing potency of the biomaterials tested (Figure 10(c)). There is no statistical difference between the groups ($p > 0.05$)..

3.5. Histopathology Investigation of Group I Samples. Control animals exhibited thickened epidermis at its cut edges (Figure 11(a)). The dermis close to the excision area showed rich polymorph nuclear infiltration. A demarcation line was formed, which separated the necrotic slough tissue from the viable tissue. Mild fibroblast proliferation was noted in the dermis region beneath the wound. Neovascularisation in the form of capillary blood vessel formation was noted. However, new collagen formation was minimally seen.

In test (dHAM + TSP + coconut fiber treated) animals, the wound edges were thickened with high epithelialization features (Figure 11(b)). The PMNL infiltration was seen in clusters and evenly dispersed across the wound area. Fibroblast proliferation was high in the dermis region with added neovascularisation across the dermis and also in the underlying subcutaneous matrix. The dermis edges are thickened with more polymorph nuclear infiltration. Circular clusters of collagen deposition in the dermis are noted all over the excised skin tissue.

Table 1: Parameters for tensile strength estimation.

Material	Average diameter (mm)	Average length	Rate (Speed) (mm/min)	Tensile strength (N)
Coconut thin fiber (Non absorbable)	0.126	18 cm to 25 cm	10	1.63
Prolene (Non absorbable) monofilament	0.099	45cm	10	1.96
Coconut thick fiber (Non absorbable)	0.248	18 cm to 25 cm	10	7.40
Silk braided (Non absorbable)	0.225	45 cm	10	20.12

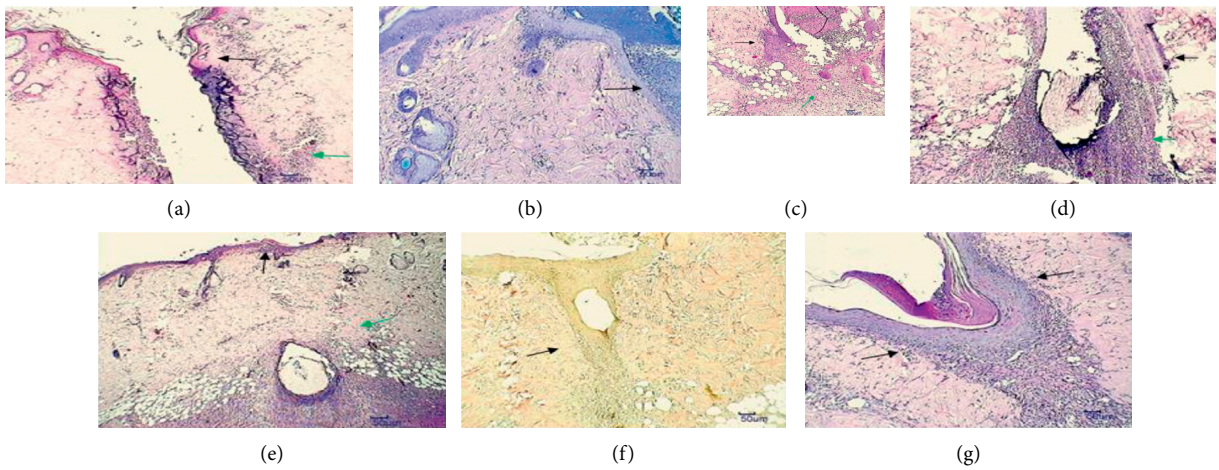

Figure 3: Histopathological indications of immature coconut fiber (multifilament) sutured skin area sections. (a) 24 hrs—hematoxylin and eosin (H and E) 10x, necrosis of epidermal and dermal cells, mild neutrophilic infiltration. (b) 48 hrs—Giemsa 10x, epithelial cell migration and moderate neutrophilic infiltration. (c) 72 hrs—H and E 10x, moderate epidermal proliferation, mild granulation tissue invasion. (d) 96 hrs—H and E 10x, epidermal layer thickening, moderate granulation tissue formation. (e) 120 hrs—H and E 10x, moderate epidermal keratinization, mild collagen proliferation and granulation tissue. (f) 144 hrs—van Gieson 10x, moderate amount of diffuse collagen deposition with granulation tissue formation. (g) 168 hrs—PAS 10x, moderate amount of new blood vessels with granulation tissue.

3.6. Histopathology Investigation of Group II Samples. In the test (dHAM + TSP gel + coconut fiber) treated animals, the wound edges are thickened with high epithelialization features. The PMNL infiltration was seen in clusters and evenly dispersed across the wound area. Fibroblast proliferation was high in the dermis region with added neovascularisation across the dermis and also in the underlying subcutaneous matrix. The dermis edges are thickened with more polymorph nuclear infiltration. Collagen deposition in the dermis is homogeneous and was noted all over the excised skin tissue (Figure 12(a)).

In the positive control (silicone gel membrane + silk suture) treated animals, the edges were in close approximation with a great reduction in wound space. Healing is hastened with a good amount of collagen deposition all over the excision space. PMNL infiltration has started to clear off with signs of thickened epithelium development (Figure 12(b)).

The complex and coordinated process of wound healing involves different factors and steps and requires additional care to prevent the worsening of the wound and abnormal scar development. Though traditional therapies for wound care have shown beneficial effects, there remain certain challenges that require novel therapeutic approaches. Wound closure techniques have evolved initially from suture materials comprising of absorbable and nonabsorbable properties [23]. Noncontaminated and small skin wounds are ideally sealed by topical skin adhesives or glues that are cost-effective to prevent further infection. Topical skin adhesives are also proved to be effectively used along with sutures. Since the degree of healing depends on the affected area, therapeutic process, and compatible material used for treatment, interventions on combination therapy for wound management would be a better option to contain and treat wounds in a multidirectional perspective [24].

Large size wounds pose a serious problem and, preferably, an autograft is installed at the wound site. Minimal or lack of graft tissue for treatment had resulted in the use of allograft human amnion/chorion tissue as an alternative to autografts, which could modulate inflammation and enhance healing of tissues, thus promoting wound healing. Bioavailability of factors of wound healing and the increased shelf life of the naive and immunomodulatory human amnion membrane have been major reasons for its clinical use [25].

Our multidirectional research has employed a combinational treatment approach for cut and open wound management, combining the use of TSP gel, the human amnion membrane, and the novel immature coconut fiber suture.

Though topical therapy is common in wound management, our objective was to provide the best natural

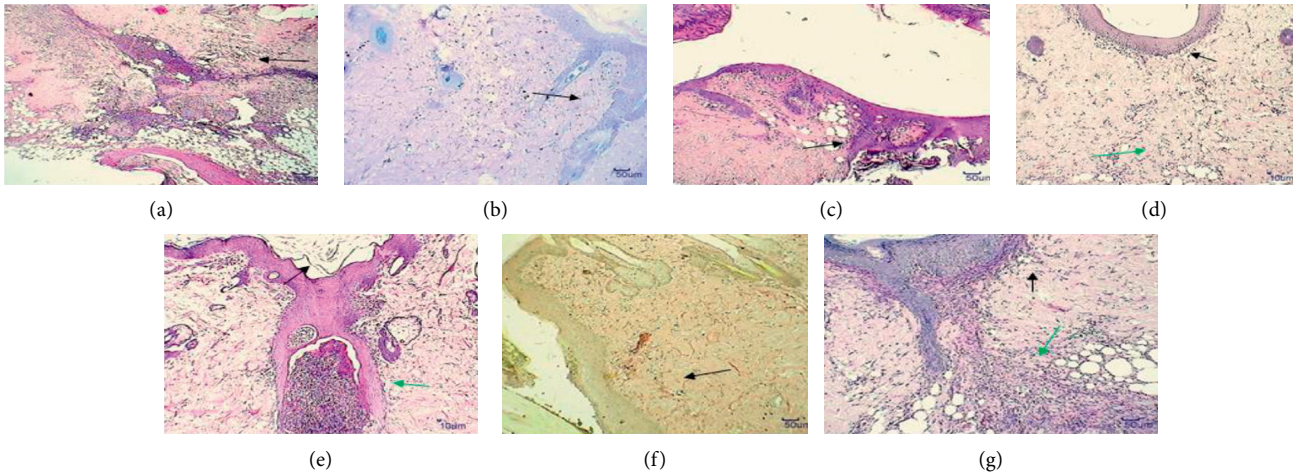

Figure 4: Histopathological indications on immature coconut fiber (monofilament) sutured skin area sections. (a) 24 hrs—H and E 10x, necrosis of epidermal and dermal cells with scab formation and severe neutrophilic infiltration. (b) Epithelial cell migration and proliferation with severe neutrophilic infiltration. (c) 72 hrs—H and E 10x, mild epidermal proliferation with granulation tissue invasion. (d) 96 hrs—H and E 10x, epidermal layer thickening, mild granulation tissue formation. (e) 120 hrs—H and E 10x, severe epidermal keratinization, moderate invasion of granulation tissue. (f) 144 hrs—van Gieson 10x, organized collagen proliferation. (g) 168 hrs—PAS 10x, moderate amount of neovascularization, granulation tissue formation.

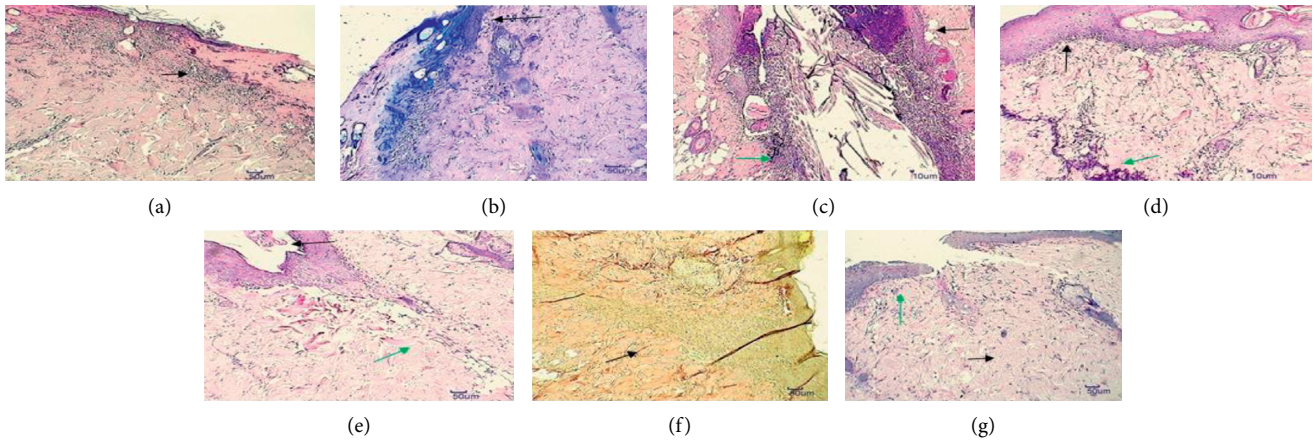

Figure 5: Histopathological indications on braided silk sutured skin area sections. (a) 24 hrs—H and E 10x, necrosis of epidermal and dermal cells with scab formation and mild neutrophilic infiltration. (b) 48 hrs—Giemsa 10x, epithelial cell migration with moderate neutrophilic infiltration. (c) 72 hrs—H and E 10x, epidermal proliferation, mild granulation tissue invasion. (d) 96 hrs—H and E 10x, epidermal layer thickening, mild granulation tissue formation. (e) 120 Hrs—H and E 10x, severe epidermal keratinization, moderate collagen production. (f) 144 hrs—van Gieson 10x, diffuse moderate collagen production. (g) 168 hrs—PAS 10x, severe collagen production, moderate neovascularization in the dermis.

alternative to the available treatment options involving synthetic materials in wound treatment. Porous silicone membranes play a dual role, serving as epidermal barriers and as a scaffold for delivering therapy to the affected area. Collagen-based silicone gel sheet, comprising of a porous silicone sheet coated with collagen, had been proved to heal different grades of the wound in several studies and decreased hypertrophic scarring when applied to surgical wounds [26]. Treatment using topical silicon sheets date back to the early 1980s, where silicone sheets were used to treat hypertrophic and keloids scars [27]. Studies indicate the improvement of hypertonic and keloid scars in 85% of the cases treated with silicone gel sheet [28] though reported with skin irritation, a well-known side effect. dHAM allografts have been employed to heal wounds without any complications or rejection even in elderly individuals. The usage of dHAM further can rule out inconveniences and pain, mainly due to the anti-inflammatory properties of the membrane and its action as a barrier covering the nociceptors [17].

Our research uses three different biomaterials for wound therapy, each having its own medicinal value contributing to the wound healing effect. Our novel study investigates and evaluates the use of combination therapy

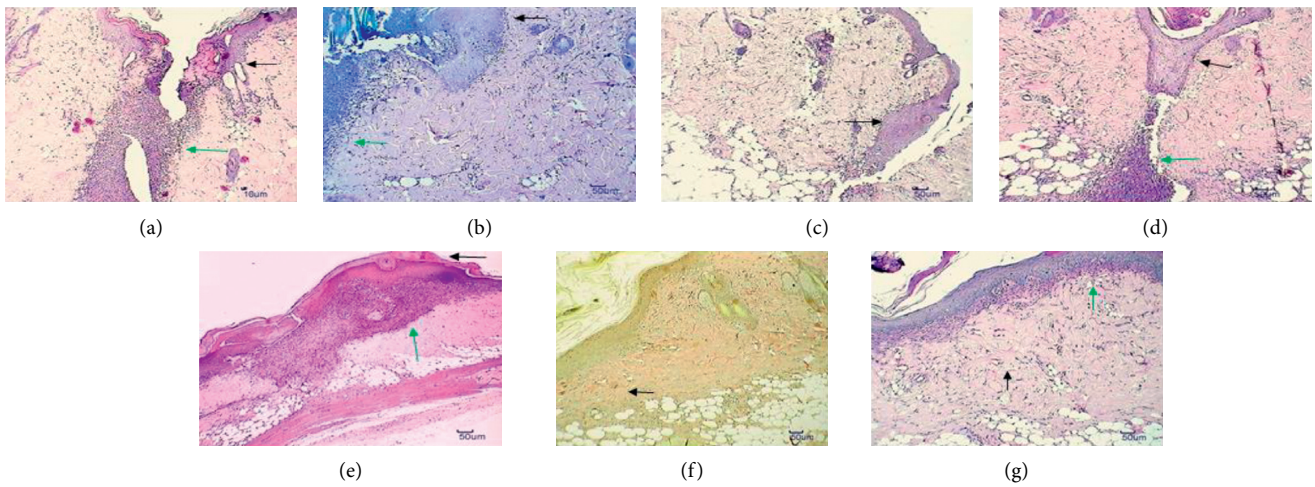

Figure 6: Histopathological indications on Prolene suture skin area sections. (a) 24 Hrs—H and E 10x, necrosis of epidermal and dermal cells, severe neutrophilic infiltration. (b) 48 hrs—Giemsa 10x, epithelial cell migration, severe neutrophilic infiltration. (c) 72 hrs—H and E 10x, moderate amount of epidermal proliferation and thickening. (d) 96 hrs—H and E 10x, epidermal layer thickening, mild granulation tissue formation. (e) 120 hrs—H and E 10x, severe epidermal keratinization, moderate granulation tissue formation. (f) 144 hrs—van Gieson 10x, diffuse fibroblast proliferation in the dermis. (g) 160 hrs—PAS 10x, severe collagen production, maximal neovascularization in the dermis.

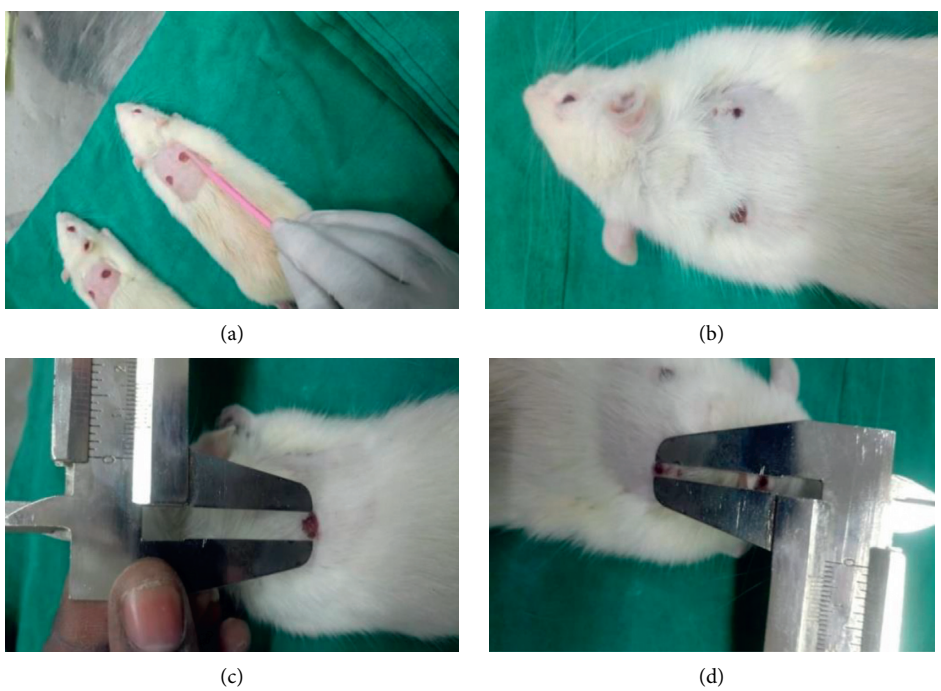

Figure 7: TSP gel wound healing ability in Wistar rats. (a) TSP gel application site (right side), (b) wound site reduction at TSP gel applied site (after 7 days), (c) wound site measurement of control (6.5 mm) at 7th day, and (d) wound site measurement of TSP gel applied site (3.5 mm) at 7th day. Values are expressed as mean ± SE ($n = 3$), where $p \leq 0.001$.

in wound healing and management of cut and open wounds.

Immature coconut fiber, both thin and thick, had satisfying skin holding capacity equal to prolene, a monofilament suture, and silk, a multifilament suture. Neovascularisation, collagen production, and re-epithelialization were observed with the recovery of the epidermal layer to its normal thickness on the 7th day of the study in all three suture treated groups.

Tamarind seed xyloglucan of tamarind seed kernel powder act as a drug vehicle and influence cell viability, cell migration, and gene expression of human skin keratinocytes and fibroblasts [8]. The use of noncarcinogenic TSP in the

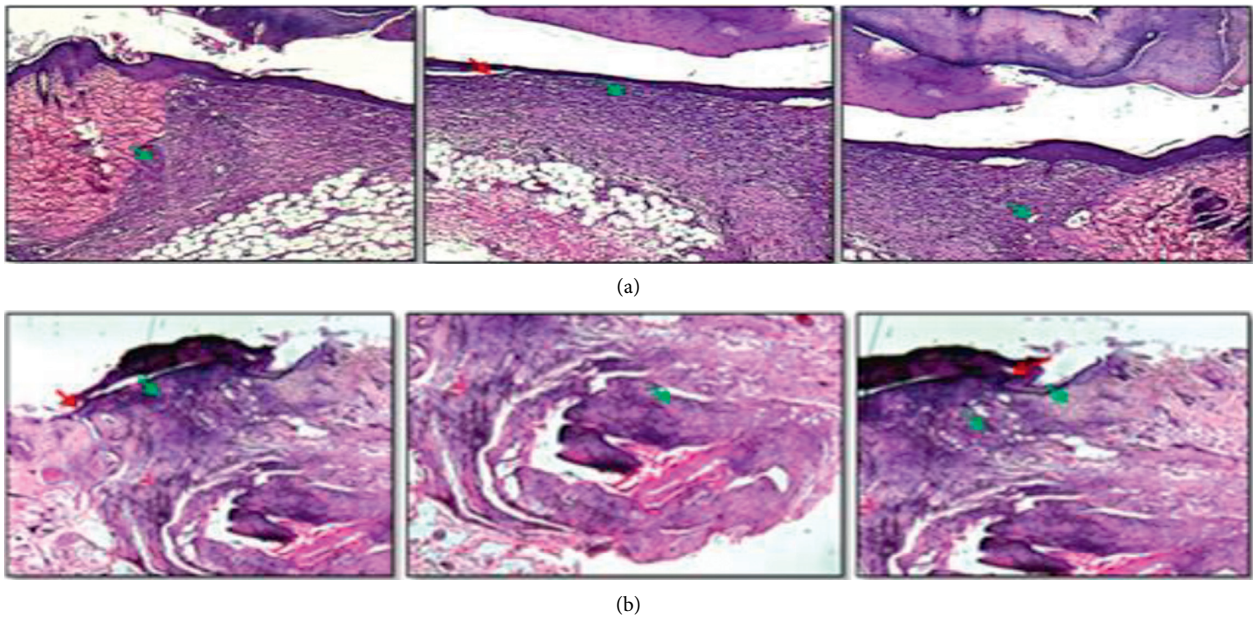

Figure 8: (a) Control (untreated) and (b) TSP gel treated: photomicrographs of H &E-stained images showing the wound edges and wound crater. Epithelialization is marked by a red arrow and collagen formation by green arrows.

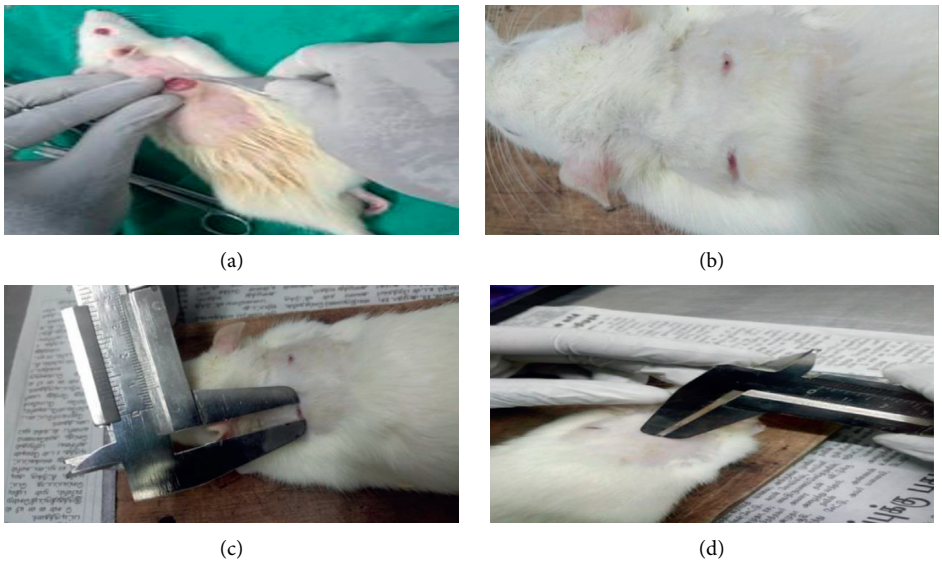

Figure 9: Group I animals tested with a combination of dHAM, TSP gel, and immature coconut fiber compared with untreated (control). (a) dHAM surgery on the right side with TSP gel and coconut fiber suture for 10 mm biopsy punch diameter wound. (b) After 11 days, wound reduction site on the right side is better than the nontreated control. (c) Wound site measurement (6 mm) at the nontreated control site after 11 days. (d) Wound site measurement (2 mm) at the test site (dHAM + TSP gel + coconut Fiber) after 11 days. Values are expressed as mean ± SE ($n = 3$), where $p \leq 0.001$.

drug delivery system accounts for its mucoadhesive property and drug holding ability [29].

The gel-like consistency of TSP, when mixed with water, add additional advantage to its wound healing property in retaining its characteristics during treatment [30]. It also acts as a carrier in drug delivery as reported by several studies [31, 32]. Its slow drug-delivering action ensures proper and timely delivery with its elasticity, mimicking a scaffold that would benefit in gripping of the treatment site. Additionally, its bioadhesive nature has been exploited in the development of polymeric films in the treatment of candida vaginitis using nystatin as the drug [31]. Its high drug holding nature has facilitated its use as carriers to substantiate the sustained release of drugs.

A combination of immature coconut fiber, dHAM, and TSP gel healed wounds much faster than the nontreated control, with wound measurements 2 mm (±0.10) and 6 mm (±0.10), respectively. Similarly, a 10 mm wound treated with

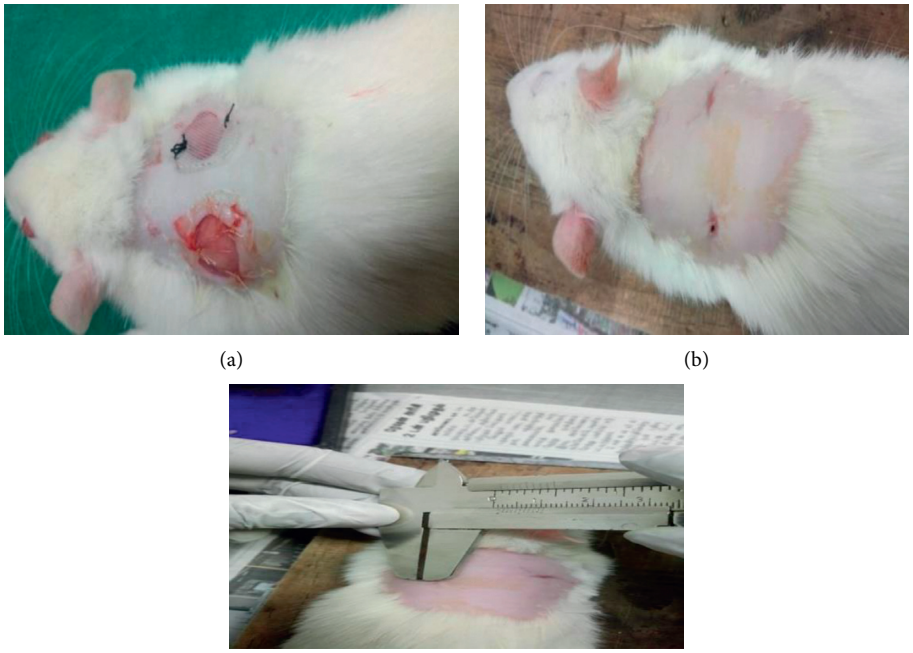

(a) (b)

(c)

Figure 10: Group II animals tested with a combination of dHAM, TSP gel, and immature coconut fiber compared with silk suture and silicone gel membrane (positive control). (a) dHAM + TSP gel + coconut fiber (Left side) and silicone gel membrane + silk suture (right side). (b) After 11 days, the test sample on the left side showed healing in comparison with completely healed positive control on the right side. (c) Wound site measurement (1.5 mm) at the test site (dHAM + TSP gel + coconut fiber) after 11 days. The silicone gel membrane + silk suture site (positive control) was completely healed after 11 days, and hence no measurement was taken. Values are expressed as mean ± SE ($n = 3$), where $p \leq 0.05$).

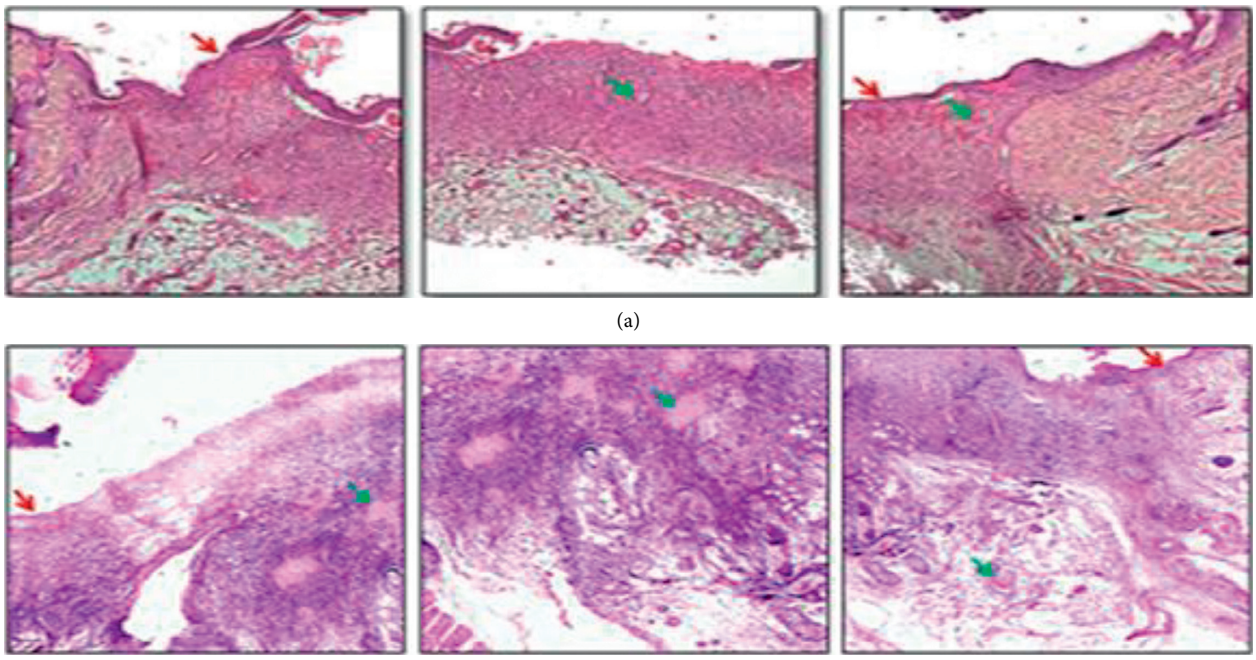

(a)

(b)

Figure 11: (a). Control (untreated) and (b) test (dHAM + TSP gel + coconut fiber): photomicrographs of H and E-stained images showing the wound edges and wound crater. Epithelialization is marked by a red arrow and collagen formation by green arrows.

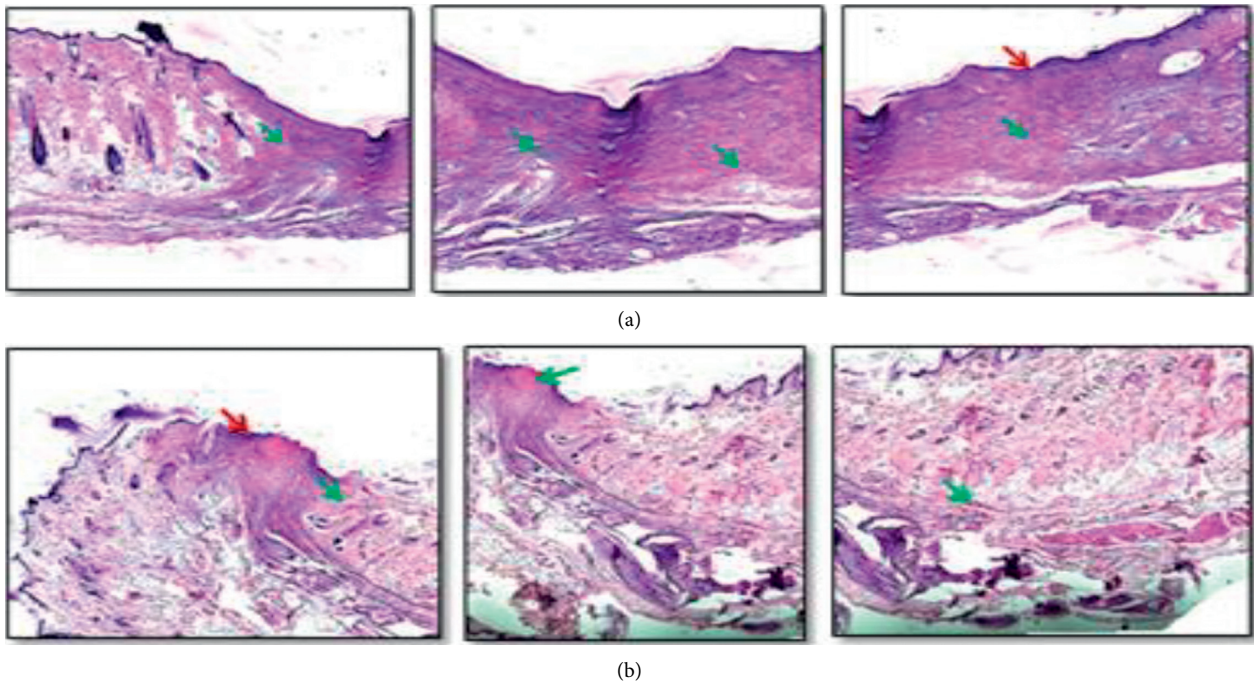

Figure 12: (a) Test (dHAM + TSP gel + coconut fiber) and (b) positive control (silicone gel membrane with silk suture): photomicrographs of H and E-stained images showing the wound edges and wound crater. Epithelialization is marked by a red arrow and collagen formation by green arrows.

the biological preparation had rapid healing, having a wound measurement of 1.5 mm (±0.17), compared to the completely healed wound treated with the positive control, i.e., silk suture with silicone gel membrane. The rigidity, thickness, and the direct pasting of the silicone gel sheet (positive control) during surgery might account for better healing compared to the individual application of test materials (TSP gel and thin dHAM). TSP acts as a carrier for the transport of growth factors and cytokines from the dHAM, and the hydrating potential acts as a shield for preventing skin irritation. Histopathological examinations revealed high epithelialization and thickened wound edges and were similar to the positive control with collagen deposition all over the excised skin tissue. Our study proves the treatment efficiency of the biological preparation comprising of dehydrated human amnion membrane, TSP gel, and fiber suture in wound healing. Animal study results clearly indicate the potency of natural biomaterials in wound healing, resembling treatment with commercial and synthetic biomaterials.

Conventional tissue adhesive patches serve wound management and fixation of medical devices. Tissue adhesives, butylcyanoacrylate and octylcyanoacrylate, were not efficient in decreasing the wound closure time when compared with the tissue bandages [33]. In contrast to the conventional patches, multifunctional smart skin adhesive patches serve multiple functions of being thin, flexible, and incorporate monitoring technology [34]. Smart patches with capabilities of preventing wound infections and the promotion of tissue remodelling are of high value. Recently, smart patches consisting of biomass chitosan microneedle array with responsive drug delivery with the application of hydrogel has been proved beneficial in wound healing [35]. Wound patches with artificial intelligence have wide application in various disciplines, especially it can be used to monitor and promote wound healing [36]. On the other hand, advanced, multifunctional, next generation smart bandages that could deliver and monitor oxygen in the wound site are under research to be made available as a low-cost alternative for quick healing [37].

Smart hydrogel wound patches can act as a carrier for drug delivery with a combination of drugs and also as a wound healing indicator when incorporated with modified pH indicator dyes to monitor the tissue healing process by the colour transition of the hydrogel patch [38]. This research signifies the use of TSP gel together with the amnion membrane representing a "smart patch" with wound healing potential, which would encourage further research on the smart patch made using a combination of plant and animal biological materials.

4. Conclusion

The natural novel combination of biomaterials (dHAM, TSP gel, and immature coconut fiber suture) showed better wound healing ability than nontreated controls and closely similar wound healing activity to commercial biomaterials in animal studies. Natural biomaterials were tested individually and also in combination and compared with commercial biomaterials used in wound management. The materials are safer and are easily available and can be greatly used by the medical/veterinary community in the near future.

The unresolved wound treatment challenges can be solved by using different treatment approaches involving natural substances as substitutes or adjuvant therapy in current wound care procedures. A "smart patch" consisting of natural wound healers is the need of the hour, and the combination of plant and animal biological materials would improve the search for novel natural materials for wound healing.

5. Limitations

The length of the immature coconut fiber suture could not be more than 25 cm, while commercial sutures are available in different lengths. Treatment procedures involved the application of 0.25 ml TSP gel to the wound and can be tried with different volumes for its best use and effectiveness.

Data Availability

Data used to support the findings of this study are available from the corresponding author upon request.

Conflicts of Interest

The authors declare that they have no conflicts of interest.

Acknowledgments

The authors thank Madras Christian College, affiliated to University of Madras for providing research facilities. Department of Scientific and Industrial Research (DSIR), Government of India, provided funds for coconut fiber research: DSIR/tepp/861/2010, Government of India.

References

[1] N. Izzah Ibrahim, S. Wong, I. N. Mohamed et al., "Wound healing properties of selected natural products," *International Journal of Environmental Research and Public Health*, vol. 15, no. 11, p. 2360, 2018.

[2] T. V. A. Lordani, C. E. De Lara, F. B. P. Ferreira et al., "Therapeutic effects of medicinal plants on cutaneous wound healing in humans: a systematic review," *Mediators of Inflammation*, vol. 2018, Article ID 7354250, 12 pages, 2018.

[3] C. Agyare, A. J. Akindele, and V. Steenkamp, "Natural products and/or isolated compounds on wound healing," *Evidence-Based Complementary and Alternative Medicine*, vol. 2019, Article ID 4594965, 3 pages, 2019.

[4] J. S. Boateng, K. H. Matthews, H. N. E. Stevens, and G. M. Eccleston, "Wound healing dressings and drug delivery systems: a review," *Journal of Pharmaceutical Sciences*, vol. 97, no. 8, pp. 2892–2923, 2008.

[5] Y. Yan, "Developments in fibers for technical nonwovens," *Advances in Technical Nonwovens*, Elsevier, Amsterdam, Netherlands, pp. 19–96, 2016.

[6] L. Del Valle, A. Díaz, and J. Puiggalí, "Hydrogels for biomedical applications: cellulose, chitosan, and protein/peptide derivatives," *Gels*, vol. 3, no. 3, p. 27, 2017.

[7] D. Melandri, A. De Angelis, R. Orioli et al., "Use of a new hemicellulose dressing (Veloderm) for the treatment of split-thickness skin graft donor sites," *Burns*, vol. 32, no. 8, pp. 964–972, 2006.

[8] W. Nie and A. M. Deters, "Tamarind seed xyloglucans promote proliferation and migration of human skin cells through internalization via stimulation of proproliferative signal transduction pathways," *Dermatology Research and Practice*, vol. 2013, Article ID 359756, 14 pages, 2013.

[9] V. Gupta, R. Puri, S. Gupta, S. Jain, and G. K. Rao, "Tamarind kernel gum: an upcoming natural polysaccharide," *Systematic Reviews in Pharmacy*, vol. 1, no. 1, 2010.

[10] N. Piqué, M. D. C. Gómez-Guillén, and M. P. Montero, "Xyloglucan, a plant polymer with barrier protective properties over the Mucous Membranes: an overview," *International Journal of Molecular Sciences*, vol. 19, 2018.

[11] K. P. R. Chowdary and Y. Srinivasa Rao, "Mucoadhesive microspheres for controlled drug delivery," *Biological and Pharmaceutical Bulletin*, vol. 27, no. 11, pp. 1717–1724, 2004.

[12] J. Liu, G. Chinga-Carrasco, F. Cheng et al., "Hemicellulose-reinforced nanocellulose hydrogels for wound healing application," *Cellulose*, vol. 23, no. 5, pp. 3129–3143, 2016.

[13] J. Chacon and L. Ferreira, "Hemicellulose dressing for skin lesions caused by herpes zoster in a patient with leukemia-an alternative dressing," *Wounds: A Compendium of Clinical Research and Practice*, vol. 21, no. 1, pp. 10–14, 2009.

[14] R. Mohd Zohdi, Z. Abu Bakar Zakaria, N. Yusof, N. Mohamed Mustapha, and M. N. H. Abdullah, "Gelam (*Melaleuca spp.*) honey-based hydrogel as burn wound dressing," *Evidence-Based Complementary and Alternative Medicine*, vol. 2012, Article ID 843025, 7 pages, 2012.

[15] D. M. Martínez-Ibarra, D. I. Sánchez-Machado, J. López-Cervantes, O. N. Campas-Baypoli, A. Sanches-Silva, and T. J. Madera-Santana, "Hydrogel wound dressings based on chitosan and xyloglucan: development and characterization," *Journal of Applied Polymer Science*, vol. 136, no. 12, Article ID 47342, 2019.

[16] S. Burgalassi, L. Raimondi, R. Pirisino, G. Banchelli, E. Boldrini, and M. F. Saettone, "Effect of xyfoglucan (tamarind seed polysaccharide) on conjunctival cell adhesion to laminin and on corneal epithelium wound healing," *European Journal of Ophthalmology*, vol. 10, no. 1, pp. 71–76, 2000.

[17] A. B. Lyons, L. K. Chipps, R. L. Moy, and J. L. Herrmann, "Dehydrated human amnion/chorion membrane allograft as an aid for wound healing in patients with full-thickness scalp defects after Mohs micrographic surgery," *JAAD Case Reports*, vol. 4, no. 7, pp. 688–691, 2018.

[18] C. Malhotra and A. K. Jain, "Human amniotic membrane transplantation: different modalities of its use in ophthalmology," *World Journal of Transplantation*, vol. 4, no. 2, p. 111, 2014.

[19] N. Koizumi, T. Inatomi, C. Sotozono, N. J. Fullwood, A. J. Quantock, and S. Kinoshita, "Growth factor mRNA and protein in preserved human amniotic membrane," *Current Eye Research*, vol. 20, no. 3, pp. 173–177, 2000.

[20] T. Rihayat, S. Suryani, T. Fauzi et al., "Mechanical properties evaluation of single and hybrid composites polyester reinforced bamboo, PALF and coir fiber," *IOP Conference Series: Materials Science and Engineering*, IOP Publishing, vol. 334, , Article ID 12081, 2018.

[21] S. Lodhi, R. S. Pawar, A. P. Jain, and A. K. Singhai, "Wound healing potential of Tephrosia purpurea (Linn.) Pers. in rats," *Journal of Ethnopharmacology*, vol. 108, no. 2, pp. 204–210, 2006.

[22] S. Murthy, M. K. Gautam, S. Goel, V. Purohit, H. Sharma, and R. K. Goel, "Evaluation of in vivo wound healing activity of Bacopa monniera on different wound model in rats," *BioMed*

Research International, vol. 2013, Article ID 972028, 9 pages, 2013.

[23] L. Al-Mubarak and M. Al-Haddab, "Cutaneous wound closure materials: an overview and update," *Journal of Cutaneous and Aesthetic Surgery*, vol. 6, no. 4, p. 178, 2013.

[24] G. Han and R. Ceilley, "Chronic wound healing: a review of current management and treatments," *Advances in Therapy*, vol. 34, no. 3, pp. 599–610, 2017.

[25] S. Kogan, A. Sood, and M. S. Granick, "Amniotic membrane adjuncts and clinical applications in wound healing: a review of the literature," *Wounds: A Compendium of Clinical Research and Practice*, vol. 30, no. 6, pp. 168–173, 2018.

[26] J. M. Zurada, D. Kriegel, and I. C. Davis, "Topical treatments for hypertrophic scars," *Journal of the American Academy of Dermatology*, vol. 55, no. 6, pp. 1024–1031, 2006.

[27] I. Westra, H. Pham, and F. B. Niessen, "Topical silicone sheet application in the treatment of hypertrophic scars and keloids," *Journal of Clinical and Aesthetic Dermatology*, vol. 9, no. 10, p. 28, 2016.

[28] J. E. Fulton, "Silicone gel sheeting for the prevention and management of evolving hypertrophic and keloid scars," *Dermatologic Surgery*, vol. 21, no. 11, pp. 947–951, 1995.

[29] M. Sano, E. Miyata, S. Tamano, A. Hagiwara, N. Ito, and T. Shirai, "Lack of carcinogenicity of tamarind seed polysaccharide in B6C3F1 mice," *Food and Chemical Toxicology*, vol. 34, no. 5, pp. 463–467, 1996.

[30] R. B. Pothireddy, M. T. Mathai, and A. Julius, "Dual property of tamarind seed polysaccharide aid wound healing," *International Journal of Advanced Science and Technology*, vol. 28, no. 20, pp. 1130–1141, 2019.

[31] P. Bassi and G. Kaur, "Polymeric films as a promising carrier for bioadhesive drug delivery: development, characterization and optimization," *Saudi Pharmaceutical Journal*, vol. 25, no. 1, pp. 32–43, 2017.

[32] A. K. Shukla, R. S. Bishnoi, M. Kumar, V. Fenin, and C. P. Jain, "Applications of tamarind seeds polysaccharide-based copolymers in controlled drug delivery: an overview," *Asian Journal of Pharmacy and Pharmacology*, vol. 4, no. 1, pp. 23–30, 2018.

[33] J. C. Dumville, P. Coulthard, H. V Worthington et al., "Tissue adhesives for closure of surgical incisions," *Cochrane Database of Systematic Reviews*, vol. 11, 2014.

[34] I. Hwang, H. N. Kim, M. Seong et al., "Multifunctional smart skin adhesive patches for advanced health care," *Advanced Healthcare Materials*, vol. 7, no. 15, Article ID 1800275, 2018.

[35] J. Chi, X. Zhang, C. Chen, C. Shao, Y. Zhao, and Y. Wang, "Antibacterial and angiogenic chitosan microneedle array patch for promoting wound healing," *Bioactive Materials*, vol. 5, no. 2, pp. 253–259, 2020.

[36] Y. Wang, M. Guo, B. He, and B. Gao, "Intelligent patches for wound management: in situ sensing and treatment," *Analytical Chemistry*, vol. 93, no. 11, pp. 4687–4696, 2021.

[37] M. Ochoa, R. Rahimi, J. Zhou et al., "Integrated sensing and delivery of oxygen for next-generation smart wound dressings," *Microsystems & Nanoengineering*, vol. 6, no. 1, pp. 1–16, 2020.

[38] L. Liu, X. Li, M. Nagao, A. L. Elias, R. Narain, and H.-J. Chung, "A pH-Indicating colorimetric tough hydrogel patch towards applications in a substrate for smart wound dressings," *Polymers*, vol. 9, no. 11, p. 558, 2017.

[39] R. B. Pothireddy, M. T. Mathai, and A. Julius, "Antibiotic free dehydrated human Amnionmembrane from C-section deliveries to accelerate wound healing," *International Journal of Advanced Science and Technology*, vol. 28, no. 20, pp. 212–217, 2019.